Karlsruhe Institute of Technology

Functional TEMPO-Containing Polymers: Synthesis and Application in Organic Radical Batteries

Zur Erlangung des akademischen Grades eines

DOKTORS DER NATURWISSENSCHAFTEN

(Dr. rer. nat.)

von der KIT-Fakultät für Chemie und Biowissenschaften

des Karlsruher Instituts für Technologie (KIT)

genehmigte

DISSERTATION

von

M. Sc. Wenwen Xue

aus

Shandong, China

KIT-Dekan:	Prof. Dr. Manfred Wilhelm
Referent:	Prof. Dr. Patrick Théato
Korreferent:	Prof. Dr. Michael A. R. Meier
Tag der mündlichen Prüfung:	20.10.2020

Die vorliegende Arbeit wurde im Zeitraum von Oktober 2015 bis September 2020 in der Arbeitsgruppe von Prof. Dr. Patrick Théato am Institut für Technische und Makromolekulare Chemie der Universität Hamburg (von Oktober 2015 bis März 2018) und Institut für Technische Chemie und Polymerchemie des Karlsruher Instituts für Technologie (von April 2018 bis September 2020) angefertigt.

Abstract

As an alternative for conventional inorganic-based electrode materials, organic redox-active polymers have attracted substantial attention due to their high power density, flexible processibility and metal-free characteristics. Organic radical polymers, especially TEMPO (2,2,6,6-tetramethyl-1-piperidinyloxy)-containing polymers represent some of the fastest-charging redox active materials available. Among various synthetic pathways available to obtain TEMPO-containing polymers for energy storage applications, the present thesis focuses on post-polymerization modification (PPM) via activated ester. The high selectivity and versatility of PPM to incorporate TEMPO pendant groups and other functionalities within the polymer chain in precise ratios gives rise to a library of redox polymers allowing for a systematic study of their battery performance.

Since the TEMPO content of poly(2,2,6,6-tetramethylpiperidinyloxy-4-yl) (PTMA) synthesized via conventional post-oxidation method typically varies from 60–80%, the quest for an alternative approach with comparable TEMPO content has been taken and the current thesis focuses on PPM of polymeric pentafluorophenyl (PFP) ester derivatives. Aimed at a high TEMPO content, the reaction parameters such as type of nucleophile, catalyst, solvent, feeding ratio of catalysts and nucleophile, along with reaction time and temperature for aminolysis and transesterification reactions of poly(pentafluorophenyl acrylate) (PPFPA) and poly(pentafluorophenyl methacrylate) (PPFPMA) were investigated. Electron paramagnetic resonance (EPR) spectroscopy and FTIR confirmed the high TEMPO content in five types of TEMPO-containing polymers, particularly poly(2,2,6,6-tetramethylpiperidinyloxy-4-yl acrylamide) (PTAm, 96.2%). Moreover, the electron transfer-promoting effect of the hydrolysis side reaction product (i.e. acrylic acid moieties) on redox reaction of TEMPO was examined. Furthermore, the improvement in battery performance due to the increased TEMPO content was presented by comparing PTAm and PTMA synthesized by conventional post-oxidation method.

In similar manner, electrode processing plays a critical role in battery performance. Recently a vast knowledge has been gained from the preparation of inorganic-based electrode materials, however, this knowledge cannot be directly applied to organic-based materials due to the distinct difference

in the chemical nature (e.g. composition and chemical affinity) between organic and inorganic materials. To fill this gap, the subsequent work investigated the influence of various processing parameters, such as drying temperature, slurry viscosity, carbon forms and calendering on the battery performance (e.g. cycle life and rate capability) of PTMA as the model polymer. With a step-by-step examination of each parameter on the influence of cathode morphology and cycle performance, a well-suitable processing conditions were thus proposed.

Finally, rational structural design of pyrene-functionalized radical (i.e. TEMPO) copolymers for enhanced electrochemical performance was presented for energy storage applications. With a two-step PPM via activated ester, other functionalities, e.g. amide-bonded pyrene and methylene-ester linked pyrene, in addition to TEMPO moieties were efficiently incorporated within the polymer followed by characterization with EPR and UV/vis spectroscopy. Both theory and experiment confirmed the existence of π-π stacking between pyrene moieties and carbon nanotubes. Moreover, amide-bonded pyrene moiety exhibited relatively stable redox reaction than methylene-ester linked pyrene according to cyclic voltammetry analysis. Furthermore, a comparison between low and high content of amide-boned pyrene moieties proved a significantly different effect on the battery performance.

In summary, substantial advances in preparation and understanding of TEMPO-containing polymers were made. As such, the thesis lays a solid foundation of TEMPO-containing polymers for energy storage in future, in addition to possible applications of radical-containing polymers synthesized via PPM.

Zusammenfassung

Als Alternative zu konventionellen Elektrodenmaterialien auf anorganischer Basis haben organische redox-aktive Polymere aufgrund ihrer hohen Energiedichte, flexiblen Verarbeitbarkeit und Metallfreiheit große Aufmerksamkeit erregt. Organische radikalische Polymere, insbesondere TEMPO (2,2,6,6-Tetramethyl-1-piperidinyloxy)-haltige Polymere, repräsentieren einige der am schnellsten ladenden redox-aktiven Materialien, die zur Zeit verfügbar sind. Im Unterschied zu den zahlreich vorhandenen Synthesewegen von TEMPO-haltigen Polymeren für die Anwendung zur Energiespeicherung, konzentriert sich die vorliegende Arbeit auf Post-Polymerisations-Modifikation (PPM) über aktivierte Ester. Die hohe Selektivität und Vielseitigkeit von PPM ermöglicht es TEMPO-Seitengruppen und andere Funktionalitäten in präzisen Verhältnissen in die Polymerkette einzubauen, was zu einer Bibliothek von Redoxpolymeren führt, die eine systematische Studie ihrer Batterieleistung ermöglicht.

Da der TEMPO-Gehalt von Poly(2,2,6,6-tetramethylpiperidinyloxy-4-yl) (PTMA), welches über die herkömmliche Methode der nachträglichen Oxidation synthetisiert wurde, typischerweise zwischen 60–80% variiert, wurde die Herausforderung angenommen einen alternativen Ansatz zu finden, der einen vergleichbaren TEMPO-Gehalt erzielt. Die vorliegende Arbeit konzentriert sich auf die PPM von polymeren Pentafluorophenyl (PFP)-Esterderivaten. Um einem hohen TEMPO-Gehalt zu erzielen, wurden die Reaktionsparameter wie Art des Nukleophils, Katalysator, Lösungsmittel, Zugabeverhältnisse von Katalysatoren und Nukleophilen sowie die Reaktionszeit und Temperaturen für die Aminolyse und Umesterungsreaktionen von Poly(pentafluorophenylacrylat) (PPFPA) und Poly(pentafluorophenylmethacrylat) (PPFPMA) untersucht. Elektronenspinresonanz (engl. electron paramagnetic resonance, EPR)-Spektroskopie und FTIR bestätigten den hohen TEMPO-Gehalt in fünf Arten von TEMPO-haltigen Polymeren, insbesondere Poly(2,2,6,6-tetramethylpiperidinyloxy-4-yl-acrylamid) (PTAm, 96.2%). Darüber hinaus wurde die elektronenübertragungsfördernde Wirkung des Nebenprodukts der Hydrolyse (d.h. Acrylsäuregruppen) auf die Redoxreaktion von TEMPO untersucht. Ferner wurde eine verbesserte Batterieleistung aufgrund des erhöhten TEMPO-Gehalts im Vergleich zu PTAm und PTMA, die durch die herkömmliche Methode der nachträglichen Oxidation synthetisiert wurden, erzielt.

Für die Batterieleistung spielt die Elektrodenverarbeitung ebenfalls eine kritische Rolle. In jüngster Zeit wurde durch die Präparation von anorganischen Elektrodenmaterialien umfangreiches Wissen gewonnen. Aufgrund der ausgeprägten Unterschiede in der chemischen Beschaffenheit zwischen organischen und anorganischen Substanzen (z.B. deren Zusammensetzung und chemische Affinität) kann dieses Wissen jedoch nicht direkt auf Materialien auf organischer Basis angewendet werden. Um diese Lücke zu schließen, wurde in der vorliegenden Arbeit der Einfluss verschiedener Verarbeitungsparameter wie Trocknungstemperatur, Aufschlämmungsviskosität, Kohlenstoffformen und Kalandrierung auf die Batterieleistung (z.B. Zykluslebensdauer und Stromratenfähigkeit) von PTMA als Modellpolymer untersucht. Mithilfe einer schrittweisen Untersuchung jedes einzelnen Parameter auf den Einfluss der Kathodenmorphologie und der Zyklisierungsleistung wurden entsprechend geeignete Verarbeitungsbedingungen vorgeschlagen.

Schließlich wurde ein rationales strukturelles Design von Pyren-funktionalisierten radikalischen (d.h. TEMPO) Copolymeren für eine verbesserte elektrochemische Leistung für Energiespeicheranwendungen untersucht. Mit einer zweistufigen PPM über einen aktivierten Ester wurden zusätzlich zu den TEMPO-Einheiten weitere Funktionalitäten, wie z.B. amidgebundenes Pyren oder Methylen-Ester-verknüpftes Pyren, effizient in das Polymer eingebaut, gefolgt von Charakterisierung mit EPR und UV/vis-Spektroskopie. Sowohl die Theorie als auch das Experiment bestätigten die Existenz von π-π-Wechselwirkungen zwischen Pyren-Einheiten und Kohlenstoff-Nanoröhren. Darüber hinaus zeigte die amidgebundene Pyren-Funktionalität laut der cyclovoltammetrischen Analyse eine relativ stabilere Redoxreaktion als Methylen-Ester-gebundenes Pyren. Ferner zeigte ein Vergleich zwischen niedrigem und hohem Gehalt an amidgebundenen Pyrenanteilen einen signifikant abweichenden Effekt auf die Batterieleistung.

Zusammenfassend lässt sich sagen, dass wesentliche Fortschritte bei der Präparation und dem Verständnis von TEMPO-haltigen Polymeren erzielt wurden. Damit legt die Arbeit ein solides Fundament für TEMPO-haltige Polymere zur Anwendung in zukünftigen Energiespeichern, zusätzlich zu möglichen Anwendungen von radikalhaltigen Polymeren, die mittels PPM synthetisiert werden.

Contents

1. Introduction and Motivation

Due to the worldwide high economic growth, increased access to marketed energy and rapid population growth, the globe is facing an unprecedented high energy demand. Globally, human activity has consumed 583.90 EJ of primary energy in 2019 which increased by 1.3% compared with 2018 [1], and the demand is expected to grow by 50% between 2018 and 2050 [2]. Among diverse energy sources, fossil fuels are the dominant primary energy resources at present, which accounts for more than 80% of the primary energy consumption in 2019 [1]. Although being cheap (typically $0.049–0.174 per kilowatt hour for fossil fuel-fired electricity cost) and reliable with well-developed technologies for extraction and refining [3], fossil fuels are finite energy source (i.e. non-renewable) and bring about climate change due to the copious CO_2 emissions, which took up 67.8% of the total global greenhouse gas emissions in 2018 [4]. To meet the increasing energy demand and prevent the worst consequences of climate change, there is a pressing need for renewable energy, i.e. clean energy, which is energy from sources that are naturally replenishing but flow-limited, such as wind and solar energy. With the pledge made at the 2015 Paris Agreement to keep the global temperature rise within 2°C above pre-industrial level by 2100, the transformation to a sustainable energy system with high shares of renewables is thus more urgent.

As alternative energy resources, renewable energies, including solar, wind, hydro, biofuels and others, are intermittent due to their fluctuating nature, e.g. diurnal or seasonal variations. Energy storage is one way to constrain or even overcome this renewable energy intermittency challenge. Apart from providing flexibility to the energy system, energy storage can generally be deployed quickly and modularly whenever it is needed. While energy storage comes in many forms, including pumped hydro, hydrogen, molten salt and flywheels [5], batteries are the most common ones. Moreover, according to the International Energy Agency, batteries will have a central place in future energy markets [6]. There are a variety of batteries that are currently in use and many more under development. Lithium ion batteries (LIBs) represent the state of art battery technology [7] that satisfies high demands in energy (100–265 Wh kg^{-1}, 3.6 V) and long cycle life (last 15–20 years based on calendar aging) [7–9]. It is worth noting that the 2019 Nobel Prize in Chemistry has been awarded to John B. Goodenough, M. Stanley Whittingham and Akira Yoshino for their

contributions in the development of lithium-ion batteries, a technology that laid the foundation of a wireless, fossil fuel-free society, and are of the greatest benefit to humankind [10].

However, LIBs are based on valuable metals such as lithium (39.7 mg g^{-1}) as well as cobalt (207.9 mg g^{-1}), nickel (29.9 mg g^{-1}) and manganese (18.7 mg g^{-1}), which are sourced solely from mining for the time being [11]. Although recycling these metals from spent LIBs is possible, the recycling process is potentially unsafe, energy-consuming and environmentally undesirable [12]. Furthermore, with reference to the demand and mining capacities, it is predicted that cobalt and nickel shortages are likely to occur by 2030 and mid-2030s, respectively, and even recycling cannot replenish the supplies [9] that are needed. Therefore, new battery technologies with better sustainable feature are required.

Organic electrode materials as an alternative to transition-metal-based materials have attracted great attention over the years by virtue of its feature designable, environmentally benign and cost-effective characteristics [13, 14]. To date, various organic electrode materials have been reported, such as conjugated carbonyl compounds [15], organosulfur compounds [16], radical polymers [17], imine compounds [18] or azo compounds [19]. Among them, radical-containing polymers (RCP) represent one of the most promising candidates due to their excellent rate capability and extraordinary cycle life [14, 20, 21], especially TEMPO-containing polymers. For example, the bimolecular rate constant ($k_{ex,app}$ [M^{-1} s^{-1}]) and the standard reaction rate constant (K^0 [cm s^{-1}]) for TEMPO-based polymers are typically in the order of $\sim 10^5$ and $\sim 10^{-5}$, respectively [22]. The record cyclability so far for a redox polymer-based electrode, which is 6000 cycles with a capacity retention of 92% at a high current density of 2.2 A g^{-1} (20 C-rate) [23], was set by a TEMPO-containing polymer.

Despite its popularity, there are still several major obstacles that hindering the further application of RCP. First of all, as the classic RCP, poly(2,2,6,6-tetramethylpiperidinyloxy-4-yl methacrylate) (PTMA), normally exhibits a TEMPO content of 60–80% from conventional post-oxidation method [24, 25]. Although direct polymerization of TEMPO-acrylate/methacrylate derivatives via anionic or group transfer polymerization can be achieved with a high yield of over 95% [26–28], the synthetic route requires stringent reaction conditions. Therefore, there is a critical quest for alternative suitable synthetic routes that enables a reliable, reproducible and scalable production of the targeted PTMA derivatives. Moreover, radical polymers suffer from poor electrical conductivity, which blocks the efficient electron transfer throughout the electrode layer. For instance, the electronic conductivity of PTMA is only about 10^{-11} S cm^{-1} [29], which is much lower than that of lithium transition metal oxides ranging from 10^{-4} S cm^{-1} (LiCoO$_2$) to 10^{-9} S cm^{-1} (LiFePO$_4$) [30]. Furthermore, RCP are propensity to dissolve in conventional organic electrolytes, e.g. carbonate-

based electrolytes, which might lead to rapid self-discharge and capacity loss. For instance, Nakahara et al. [31] found that 38% of the capacity for PTMA-based cathodes was disappeared after 1 week of storage, which they attributed to the shuttle effect of dissolved PTMA in the electrolyte. It is reported that compared to PTMA with a low number-average molecular weight (M_n = 1.6 kDa, $Đ$ = 1.1), PTMA with a high number-average molecular weight (M_n = 16 kDa, $Đ$ = 1.35) showed a higher specific discharge capacity (16%) and better cycling stability (65% retention at 30 C) due to its relatively low solubility in the electrolyte [25].

Aimed at a simple and feasible synthetic approach for PTMA derivatives with a relatively high or comparable TEMPO content compared with conventional post-oxidation method, the current thesis turned to post-polymerization modification (PPM) via activated ester (namely pentafluorophenyl (PFP) ester), which is an alternative and versatile route to equip polymers with numerous functional groups including stable radicals [32–38]. Owing to the good solubility, high reactivity as well as good traceability via ^{19}F NMR spectroscopy and FTIR, the PFP ester-based polymers were selected as the parent polymers. By reacting the parent poymers with various TEMPO nucleophilic derivatives, diverse TEMPO-containing polymers can be obtained. Moreover, the reaction process can be monitored by FTIR following the decrease of the C=O (PFP ester) band and the aromatic ring C-C stretching band, both of which are quite distinguishable. Furthermore, TEMPO content in the resulting polymer can be detected by electron paramagnetic resonance (EPR) spectroscopy. In addition, to achieve a high TEMPO content, the optimal reaction conditions were investigated by utilizing different solvents, catalysts, feeding ratios, reaction temperatures and times.

To achieve the full potential of TEMPO-containing polymers as cathode materials, the processing of PTMA-based cathodes on battery performance was investigated. Battery performance, including cycling performance and rate performance, was examined for cathodes prepared with different parameters, such as drying temperature, mass fraction of cathode in the slurry, cathode thickness, calendering, and conductive additives.

Moreover, to address the conductivity and solubility issue, specific functionality, i.e. amide-bonded pyrene, was incorporated into the TEMPO-containing polymer as anchor points, which could immobilize the RCP on carbon nanotubes (CNTs) through π-π stacking. With the high selectivity and versatility of PPM, quantitatively and efficiently incorporating both TEMPO and pyrene functionalities into one polymer chain is proposed in the present work. The pyrene and TEMPO content within the copolymer can be determined by UV/vis spectroscopy and EPR measurement, respectively. Furthermore, the π-π stacking could be evidenced by the sedimentation status of CNTs in the suspension containing CNTs and pyrene-functionalized TEMPO-containing polymers. Besides, quantum mechanical calculations can also give a hint by taking graphene flake as the

model material and calculating the adsorption energy between the pyrene monomer and the graphene layer. Due to the high conductivity of CNTs (10^6–10^7 S cm^{-1}) [39] and intramolecular π-π interaction between multiple pyrene and CNTs, a good rate capability and stable cycle life of the resulting cathodes are expected.

The main focus of the present work is schematically summarized in Figure 1.1 as they expand current knowledge and frontiers of radical-based (particularly TEMPO) batteries for energy storage design.
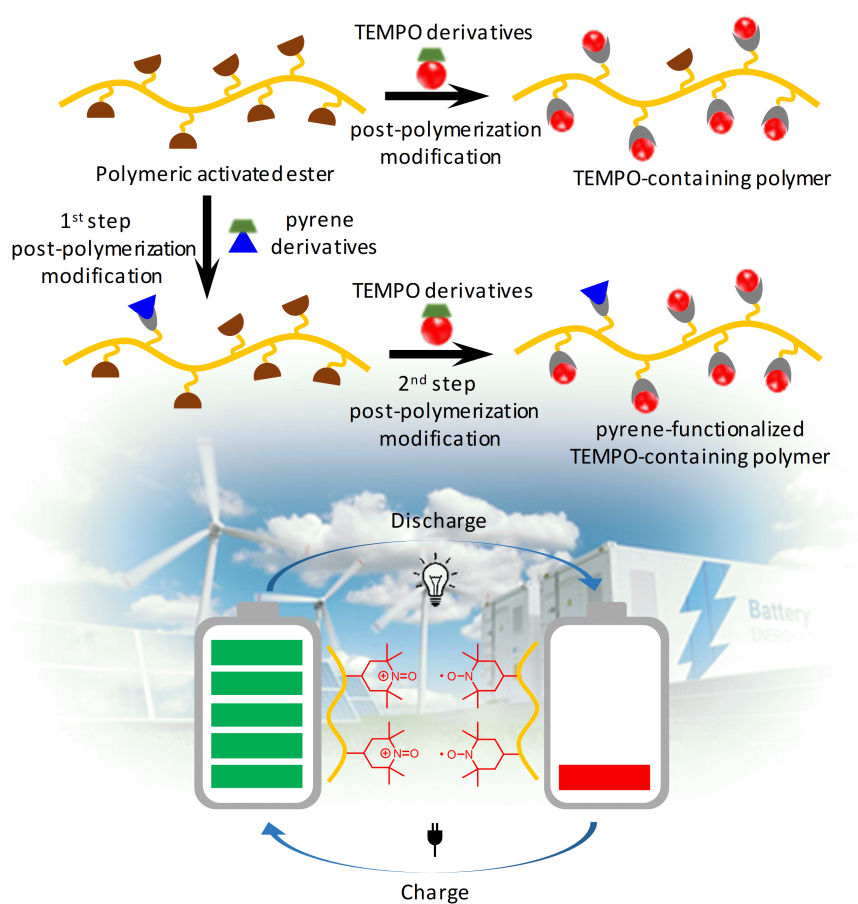
Figure 1.1.: Graphical overview of the different studies included in the current thesis.

2. Theoretical Background

With the increasing worldwide energy consumption demands and environmental problems, renewable energy (or clean energy), that is usually based on natural sources and can be replenished on a human timescale, such as sunlight and wind, offers a sliver of hope for the limited reserves of fossil fuels and pollution therefrom [40–42]. As these renewable energies are intermittent, energy storage, in particularly battery storage, qualifies to be one of the solutions for universal access to clean, reliable and affordable electricity services [43–45].

A battery is based on the concept of an electric cell that transforms chemical energy into electrical energy. Generally, it consists of two electrodes suspended in an electrolyte with a separator placed between them. Both electrodes contain active materials that can undergo respective chemical reactions when the two electrodes are electrically connected. Electrons move from the material with a low redox potential to the material with a high redox potential, thus generating a current. The electrode where oxidation takes place during the process is defined as the anode (i.e. negative electrode with low potential), and the electrode where reduction occurs is designated as the cathode (e.g positive electrode with high potential). If the active material can be restored to its original composition by an external electric current flowing in the opposite direction, then the corresponding cell is called a secondary cell/battery or rechargeable battery, otherwise, it is classified as a primary cell/battery or a galvanic cell, which can only supply electrical power once by sacrificing its electrodes without any rechargeable feature.

With the increasing demands being placed on future batteries, a wide variety of different battery and cell technologies have been investigated, ranging from the established primary batteries such as zinc-carbon (Leclanché), alkaline, silver oxide, mercury, lithium and zinc-air [46], to rechargeable batteries, like lead-acid, NiCd, Nickel metal hydride (NiMH), lithium-ion batteries (LIBs), etc [47]. During the last 200 years, battery technology has seen a rapid development and the major achievements are listed in the timeline, as shown in Figure 2.1 [48]. As the very tip of the iceberg was uncovered in 19th century, battery technology ushered a warm spring in the 20th century, with development of LIBs being the crowning achievement.

1836 Daniell Cell constant electricity	**1899** NiCd battery rechargeable battery	**1954** Solar Cells	**1970** NiMH cells rechargeable battery	**1991** Commercial lithium-ion battery	

1791
Frog Legs conduct
electricity

1866
Carbon-Zinc battery
first dry cell battery

1940
First button cell
Zn/Ag_2O

1959
First commercial
alkaline dry cell

1981
organic battery
conjugated polymers

1800
Voltaic Pile
first wet cell battery

1878
First air cell

1949
Alkaline-Manganese
Battery

1973
First commercial
lithium battery

21st Century
Post-lithium batteries ??

1748
The term battery
being coiled

1859
Lead acid battery
first rechargeable cell

1901
Edison cell
Ni_2O_3/Fe battery

1959
First commercial
alkaline dry cell

1990
Commercial NIMH
Rechargeable battery

Figure 2.1.: Major achievement in battery development.

Entering the 21th century, battery technology continues to thrive, and more varieties of batteries such as organic radical batteries (ORB), lithium-sulfur batteries, sodium/magnesium batteries, etc. are being revealed. Organic based battery that are endowed with the feature of fast charging and long cycle life (typically exceeds 1000 cycles) and consequently, ORB has attracted a lot of attention since its discovery [17]. Accordingly, this chapter mainly focuses on ORB, including the fundamental, working principle and the most prominent electrode material utilized in ORB, i.e. TEMPO (2,2,6,6-tetramethylpiperidin-1-oxyl-4-yl)-containing polymers. Additionally, post-polymerization modification (PPM), which is a versatile approach to functionalize polymers, is also going to be discussed in this chapter, as it is intensively adopted in the present thesis.

2.1. Organic Radical Batteries

LIBs are the state of art battery technology designated for portable devices (dozens of watt-hours), electric vehicles (dozens of kilowatt-hours) and grid applications (tens of megawatt-hours) [7, 49, 50]. Nevertheless, next-generation batteries are expected to provide higher energy density, remarkable rate capability, and excellent cycle life with environmental-friendly and cost-effective features [8, 9, 51, 52]. Due to the relatively limited availability of lithium and cobalt in addition to the large energy cost of battery manufacture and recycling, replacing lithium by more abundant and environmentally benign material is imperative. Hence, organic electrode materials have evolved as alternatives to traditionally metal-based inorganic materials that may fulfill the aforementioned criteria as electrodes in next-generation batteries [13, 14, 53]. First of all, they are environmental benign without the usage of expensive and rare earth metals (e.g. lithium, cobalt,

manganese etc.), as the constitutional elements (e.g. C, H, O, N, S) are naturally recycled within the biosphere. Moreover, their electrochemical properties are designable, for example, in respect of redox potential [54, 55], theoretical capacity [56, 57], rate capability [55, 58], solubility [59, 60] and mechanical properties [61, 62], which in turn can be altered by employing various synthetic routes, thus resulting in sustainable and eco-effective electrodes derived from biomass, such as cellulose and alginate [63, 64]. Furthermore, they provide a superior processability, making printing techniques (e.g. screen printing, inkjet printing), various casting methods (e.g. blade casing) and roll-to-roll manufacturing feasible [65].

Different categories of organic compounds are adopted as electrode active materials over the years as depicted in literature survey. Among the broad toolbox, the following classes can be distinguished: conjugated carbonyl compounds [15], conducting polymers [66], organosulfur compounds [16], radical polymers [20], imine compounds [18], nitrile compounds [67], azo-compounds [19], conjugated *N*-heterocyclic compounds including Hydrazine-Embedded ones and pteridine derivatives [68–70], conjugated carboxylates [71], naphthalene derivatives [72, 73] as well as hydrated dilithium rhodizonate [74], triangulene derivatives [75, 76], antiaromatic norcorroles [77], and tetracyanoquinodimethane [78]. Among them, radical polymers, which contain stable radicals such as open-shell nitroxides moieties, are quite promising as electrode materials owing to their extraordinary rate capability and excellent life performance [24, 79–81].

Batteries with radical polymers as redox-active materials are referred as ORB, which is a relatively new type of rechargeable battery and was initially proposed by NEC in 2001 [17]. The radical in the name of ORB indicates the persistent radical in the molecular structure of the active material, i.e. radical polymer. By far, a variety of stable radicals have been investigated for ORB, such as nitroxyl, phenoxyl, and hydrazyl radicals, as depicted in Scheme 2.1. Among them, most of the stable radicals possess a relatively high redox potential (Scheme 2.1), making them right candidates for cathode active material but not suitable for anode active material.

The first report on ORB was released in 2002 by Nakahara [17], in which poly(2,2,6,6-tetramethyl-piperidenyloxyl-4-yl methacrylate) (PTMA) and lithium were adopted as active materials for cathode and anode respectively. Since lithium meal was also involved in the battery in addition to PTMA, it is actually a metal–organic hybrid cell in a strict sense. The first all organic ORB, featuring radical polymers for both electrodes, was presented by Nishide et al [82] not until 2009. The hybrid ORB generally exhibits a specific capacity below 185 mAh g^{-1} referred to the active material [83], however, an all organic ORB delivers a much lower capacity ($\leqslant$ 64.4 mAh g^{-1} referred to the total amount of active materials) [84]. Although ORB do not excel in capacity, they have great advantages in fast charging and extraordinary cycle stability. In combination with

0.73 V	0.74 V	0.5 V	0.8 V, 1.6 V	0.7 V, -0.6 V	0.52 V

0.76 V	0.66 V

-0.55 V	-0.55 (0.6) V	0.06 V	-0.39 V
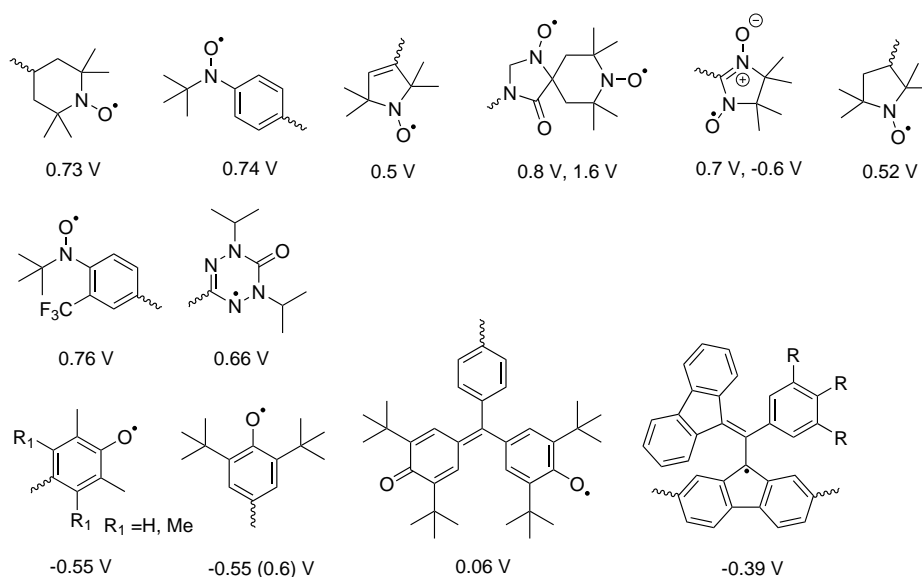
Scheme 2.1: Various stable radicals used as redox-active sites in ORB and their redox potentials (vs. Ag/Ag$^+$).

their good processability and tailor made properties, possible applications can be found in sensors, radio frequency identification tags, intelligent food packages, etc [20, 21].

With regard to the fundamentals and working principles of ORB, such as components, working mechanism, as well as common battery specifications, this section will give an detailed introduction with an focus on TEMPO based ORB.

2.1.1. Components

As the electrode active material, radical polymer possess unique electronic properties, because they can be oxidized (p-type, as cathode material) or reduced (n-type, as anode material) during a charging-discharging cycle. Taking TEMPO (or similar nitroxide) containing polymer as an example, it can undergo either oxidation or reduction to the *N*-oxoammonium cation or the aminoxy anion by either losing or gaining one electron, respectively, as shown in Scheme 2.2. The former process leads to a p-doping of the polymer while the latter induces n-doping. Theoretically, both ORB electrodes can be based on nitroxide radical polymers, however, practically nitroxide radical polymers are mainly used as cathodes since the n-doping process of nitroxide exhibits poor electrochemical stability and reversibility [85]. Therefore, lithium metal is commonly adopted as the anode when nitroxide radical polymers are employed as cathode active materials in battery research. In this respective battery system, during the charging process, the nitroxide is oxidized

to oxoammonium at the cathode while lithium-ion is reduced to lithium at the anode. Upon discharging, this process is reversed and the corresponding nitroxide radicals are regenerated, as indicated in Figure 2.2.
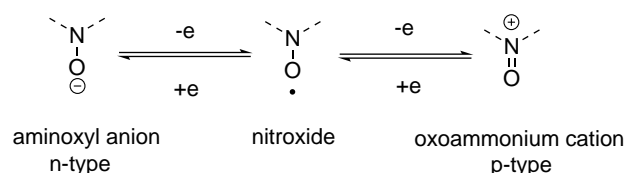
Scheme 2.2: Redox reactions among different nitroxide redox species.
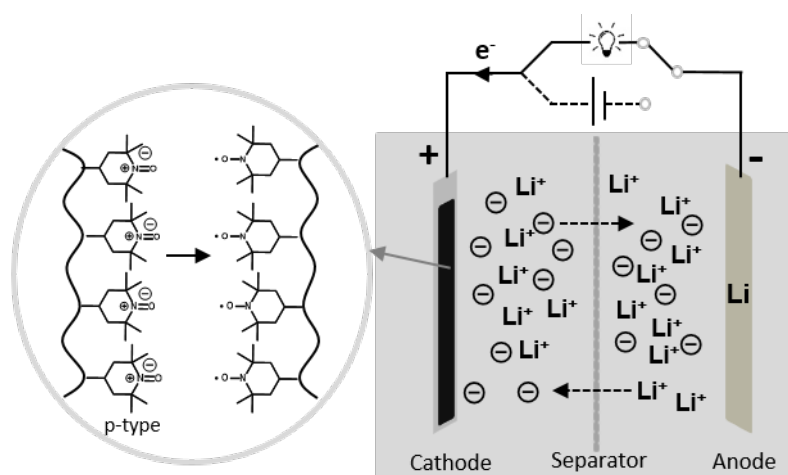
Figure 2.2.: The mechanism of ORB during discharging.

Figure 2.2 shows the typical composition and configuration of an ORB. This configuration permits a closed circuit with an internal ion transportation and an external electron transmission. During charging, anions (e.g. PF_6^-) in electrolyte migrate from the negative electrode through a separator to the positive electrode driven by an external power, while cations (e.g. Li^+) move in the opposite direction. In the meantime, electron flow is generated from the direction of the positive electrode to the negative electrode. Discharging the battery reverses the process, thus causing an electron flow from anode to cathode to provide electricity. The spontaneous ion transportation is driven by the difference of the electromotive force (emf) between the two half-cell reactions, i.e. potential difference (ΔE). Therefore, the reversible conversion between electrical energy and chemical energy is realized when ions shuttle between the two electrodes. With respect to each component of an ORB, a detailed introduction is given in the following section.

Electrodes

An electrode is classified as either a cathode or an anode. The cathode is the positive electrode where active material accepts electrons from the external circuit and get reduced during discharging, displaying relatively high reaction potential. The anode is the negative electrode where active material donates electrons to the external circuit and gets oxidized during the cell discharge, which should exhibit a relatively low reaction potential to obtain a high full-cell voltage. Practically, when radical polymers which generally have an intrinsic low electrical conductivity (e.g. 10^{-11} S cm^{-1} for PTMA) [29] are adopted as active materials, conductive additive and binder are also required in electrodes. The two components are introduced as follows.

Conductive additives are necessary to accelerate electron transfer by constructing a conductive percolation network, thereby increasing the electrical conductivity of the electrode. Furthermore, it could also adsorb and retain part of electrolyte liquid, allowing close contact between ions and active materials. So far, various carbon forms have been reported in literature for ORB, such as carbon black (CB) [86, 87], vapor grown carbon fiber (VGCF) [17], graphene [88], and carbon nanotubes (CNTs) [89, 90] and activated carbon [91].

The selection of carbon species and their mixing with other electrode components are very critical, as the characteristics of the carbonaceous material as well as their respective distribution in the composite electrode may affect the electrochemical properties of the composite electrode. For instance, Liu et al. [87] compared the electrochemical performance of cathodes based on PTMA with Black Pearl 2000 (BP-2000), VGCF and acetylene black (AB) as conductive agent, respectively. They revealed that the specific capacity of the PTMA-BP cathode is 26.7% larger than that of PTMA-VGCF and PTMA-AB cathodes at 1 C rate, and 27.6% and 16.7% higher than that of PTMA-VGCF and PTMA-AB cathodes at 50 C rate, respectively, due to the high specific surface area of BP-2000, which facilitates a thorough contact of PTMA with BP carbon, and thus improve the conductivity of the PTMA-BP composite. Apart from the inherent specific surface and conductivity of the conductive additive, shape also matters. As revealed by Suguro et al. [92], VGCF played a significant role in reinforcing the polymer-carbon composite in the electrodes and promoting the electron transfer, while carbon black additive (e.g. Ketjenblack black and acetylene black) would result in the cracking of electrodes at the same filling amount (15 wt.%). Probably due to the good crack control effect of short fibers (10–20 μm) as well as their good electrical conductivity (10^4 S cm^{-1}) along the fiber direction, VGCF has been adopted as the most common conductive agent for ORB since the radical polymer PTMA was first reported as a cathode active material in 2002 by Nakahara et al. [17]. In addition to the nature of the carbon species, its

distribution within the composite electrode also cannot be underestimated. For example, Choi et al. [93] fabricated a nanocomposite electrode with highly dispersed single-walled carbon nanotubes (SWCNTs) wrapped by PTMA at a molecular level via a combination of ultrasonication and ultracentrifugation. This cathode displayed both high electrical conductivity and excellent rate capability, which was 100 mAh g^{-1} at 1 A g^{-1} and 75 mAh g^{-1} at 60 A g^{-1}, with the content of SWCNTs being only 4 wt.%. This result demonstrates the importance of the even distribution of the conductive agent to form uniform conductive pathways within the composite electrode in realizing quantitative formula-based redox capacity and fast electron transfer.

A binder also plays an important role in composite electrodes, though being inactive. On one hand, it acts as an adhesive to maintain the connection between the electrode materials and current collector [94]. On the other, it keeps the integrity of the composite electrode and imparts mechanical flexibility [95, 96]. An ideal binder should meet the following criteria: (1) Offer high adhesion to both the electrode materials and the current collector; (2) Be electrochemically stable to ensure a superior cycling performance; (3) Be high soluble in the processing organic solvent or water for slurry preparation but insoluble in electrolyte or have a low swelling ratio; (4) Have a high electrical and ionic conductivity; (5) Have a high tensile strength to endow the composite electrode with mechanical flexibility; (6) Be economically effective and environmentally friendly. The most commonly used binders are poly(vinylidene fluoride) (PVdF), poly(tetrafluoroethylene) (PTFE), carboxyl methyl cellulose (CMC) and CMC-SBR (styrene butadiene rubber) in Li batteries as well as in ORB [94, 96, 97]. Nevertheless, these binders do not fulfill all criteria mentioned above. In the search for better binders fulfilling more of the above criteria, other binders have also been reported in the literature [98, 99]. For instance, Komaba et al. [98] adopted polyacrylate binder in PTMA-based cathode and achieved capacity retention of 96% after 1000 cycles at 20 C rates due to the boosted electron-transfer kinetics of TEMPO radical and improved conductivity of the electrode. Casado et al. [99] employed a conducting polymer, poly(3,4-ethylenedioxythiophene) (PEDOT) decorated with TEMPO pendant groups, as a binder as well as partial active material in LiFePO$_4$-nitroxide hybrid electrode. It is worth noting that the addition of a binder in the composite electrode reduces the gravimetric energy density of ORB as a binder does not essentially contribute to the redox reaction while still contributing to the overall weight of the electrode.

The typical form of a radical polymer-based electrode is a laminated film normally prepared by tape casting (or doctor blading) a well-mixed slurry consisting of a suspension based on the three independent components in organic solvent or water. Nonetheless, other forms with various morphologies and architectures, such as a (patterned) planar film [100–102], a three-dimensional porous foam [103, 104] and a non-woven fibrous membrane [105, 106], etc., have also been

attempted. For instance, Lee et al. [100] fabricated a PTMA brushed ITO electrode by grafting PTMA brushes on a patterned ITO glass via surface-initiated atom transfer polymerization (SI-ATRP) to prevent the dissolution of PTMA in the electrolyte. Similarly, they immobilized nitroxide polymer brushes on three-dimensional ordered macroporous (3DOM) polypyrrole via SI-ATRP. The resulting 3DOM nitroxide polymer brush cathodes delivered 40 times higher capacity than that of the planar electrode at 5 C rate, and remained 96.1% of its capacity after 250 cycles [103]. Kim et al. [104] prepared an ordered nanocomposite of polyethylene glycol–organic radical polymer–mesocellular carbon foam by incorporating PTMA into acidified mesocellular carbon foam (MCF) followed by polyethylene glycol coating, and demonstrated a much better cycle performance at 1 C rate with 70% capacity retention after 50 cycles at 50 °C compared to pristine PTMA and PTMA-MCF, whose capacity decreased rapidly to 20% within 7 cycles and 50 cycles, respectively. Kim et al. [105] prepared a micro-fibrous PTMA-based electrode by electrospinning technique. Due to the fibrous microstructure, this cathode showed a quantitative capacity even at 50 C rate, and a remarkable volumetric capacity which is 209 mAh cm^{-3} at 10 C rate.

Concerning <u>fabrication methods</u> for the prevailing laminated electrode, spin coating [82, 107], reactive inkjet printing [108], screen printing [109] and drop-casting [110] have also been reported in addition to doctor blading. For example, the Nishide group prepared a see-through, flexible battery by spin coating poly(galvinoxylstyrene) (n-type) onto an ITO-coated glass or poly(ethylene terephthalate) (PET) substrate with a film thickness of 50–500 nm [82]. Taking advantage of the good dissolution of PTMA in dimethylformamide (DMF) and *N*-methyl-2-pyrrolidone (NMP), the Schubert group [108] prepared an inkjet printable ink, which was a suspension of epoxidized carbon nanopowder in a solution mixture of PTMA, an epoxy-based cross-linker, and a plasticizer (e.g. ethylene carbonate) in DMF and NMP. After inkjet printing on a graphite foil, followed by drying and thermal cross-linking arising from the expoxy-amine reaction between the epoxy-based cross-linker and PTMA bearing residue chemically reactive amine groups from the incomplete oxidation of PTMA precursor, they obtained an inkjet printable cathode. Lin et al. [110] prepared a PTMA/carbon-nanotube-array electrode by drop-casting the solution of PTMA and PVdF in NMP onto a stainless-steel substrate grown with vertically aligned carbon nanotubes array to improve the high-rate charge/discharge performance in ORB.

Electrolytes

Electrolyte serves as an ionic charge carrier in a battery system, which can either be a liquid or a solid. Typically, an ideal electrolyte should meet the following requirements: (1) Having high ionic conductivity but low electronic conductivity with low viscosity to promote ion transportation and minimize self-discharge; (2) Possessing a wide electrochemical stability window to avoid electrolyte degradation within the working potential range; (3) Being thermally stable with the working temperature in between its melting point and boiling point but not close to; (4) Being safe and cost-efficient with low toxicity and less environmental hazards. The common electrolyte in ORB is liquid ones which consist of an organic solvent or water in addition to a conducting salt. Theoretically, the common liquid electrolyte used in LIBs can also be applied to ORB without any further adjustment. Among them, the state-of-the-art electrolytes in commercial LIBs batteries, i.e. lithium hexafluorophosphate $LiPF_6$) in carbonate-based electrolyte (e.g. 1 M $LiPF_6$ in ethylene carbonate/dimethyl carbonate (EC/DMC=50/50, v/v) or ethylene carbonate/diethyl carbonate (EC/DEC=30/70, v/v)) [111,112], is also the most commonly used electrolyte in ORB. Other electrolytes reported in ORB are: 0.1 M NaCl aq. [113], 1 M lithium perchlorate ($LiClO_4$) in EC/DEC (50/50, v/v) [114], $LiPF_6$ or lithium tetrafluoroborate ($LiBF_4$), tetrabutylammonium tetrafluoroborate ($TBABF_4$) or $LiCF_3SO_3$ in PC [115], 1 M lithium bis(trifluoromethanesulfony)imide (LiTFSI) in *N*-butyl-*N*-methyl-pyrrolidiniumbis(trifluoromethanesulfonyl)imide (Py_{14}TFSI) [116], LiTFSI in *N*-butyl-*N*-methylpyrrolidinium bis(trifluoromethylsulfonyl)imide (BMPTFSI) [117], 1 M $LiPF_6$ in EC/DEC/DM (1/1/1, v/v/v) electrolyte [118], lithium bis(fluorosulfonyl) imide (LiFSI) or LiTFSI in EC/DMC (4/6, v/v) [119], 1 M tetraethylammoniumbis(trifluoromethylsulfonyl)imide (Et_4NTFSI) or Pyr_{14}TFSI in PC and neat Pyr_{14}TFSI [120] etc.

The type of electrolyte and its respective concentration are very critical for secondary batteries including ORB [120,121]. Initially, the charge-discharge process is regulated by the chemical and physical properties of an electrolyte, such as ionic conductivity, viscosity, ion-ion and ion-solvent interactions. For instance, Iwasa et al. [119] revealed that LiFSI has a high degree of dissociation and weak interaction with PTMA gel, and the increase in LiFSI concentration from 1.0 M to 1.5 M suppresses the shortage of electrolyte anions at high rate charging, thus improving rate performance. Nakahara et al. [115] experimentally showed that the mobility of anions (e.g. PF_6^- and BF_4^-) strongly influenced charge transfer and electron self-exchange in PTMA. Using *in situ* electrochemical quartz crystal microbalance with dissipation monitoring (EQCM-D) during cyclic voltammetry, Wang et al. quantitatively showed a two-mode doping mechanism of PTMA. It was revealed that the dominate mode is highly depended on polymer–anion, anion–solvent interactions as well as timescale [122]. Secondly, the electrochemical stability of the electrode material at

high potentials and elevated temperature is associated with electrolyte. For example, using float tests, Gerlach et al. [120] found 1 M Et_4NTFSI in PC has a negative effect on the electrochemical stability of PTMA-based electrodes, while 1 M $Py_{14}TFSI$ in PC and neat $Py_{14}TFSI$ not. Moreover, the self-discharge that decreases the shelf life of batteries results from dissolution of electrode material in the electrolyte. For instance, Nakahara et al. [31] found that 38% of the capacity for PTMA-based cathodes disappeared after 1 week of storage, which they attributed to the shuttle effect of the dissolved PTMA in the electrolyte (1 M $LiPF_6$ in EC/DEC (30/70, v/v)). Cheng et al. [117] revealed that the addition of LiTFSI to BMPTFSI electrolytes increased the polarity of the electrolytes, and thus suppressed the solubility of PVDF binder and PTMA active material. Accordingly, the PTMA-based cathode exhibited a good cycle-life performance with 94.5% retention after 200 cycles, when 0.6 M LiTFSI/BMPTFSI electrolyte was utilized. Last but not least, an electrolyte that contains flammable solvent can be a safety hazard for rechargeable batteries [123].

Separators

A separator is a permeable electrical insulating membrane placed between the two electrodes of a battery to prevent an electrical short circuit caused by direct contact of the cathode and anode, allowing ion charge carriers to transport between electrodes. Monolayer and triple-layers (typically 20–30 μm thick) of micro-nonporous (pore size of 30–100 nm) polyolefin derivatives (polyethylene, polypropylene or their blends) with semi-crystalline based separators have been the most widely used separators for ORB, due to their excellent electrochemical stability, high mechanical strength and acceptable cost [124]. However, there are some negative aspects that need to improve, particularly, the poor electrolyte wettability and severe shrinkage at high operating temperatures. The former drawback arising from the surface hydrophobicity of the polyolefin separator could lower the electrolyte uptake and ionic conductivity, and consequently, lead to a high internal ionic resistance and a low rate capability. The latter can result in a short-circuit or thermal runaway, especially at high charge/discharge current. Another type of separator used in ORB is a glass microfiber filter (e.g. Whatman® GF/D) [125, 126], which has been intensively adopted in Li-S and Li-air batteries due to its high porosity, superior wettability and good thermal stability [127]. It is worth noting that as the glass microfibers separators typically have a thickness up to several hundreds of micrometers (e.g. 670 µm for Whatman® GF/D), their applications are mainly limited to the laboratory. Additionally, non-woven fabric membrane based on electrospun poly(vinylidene fluoride-*co*-hexafluoropropylene) (PVDF-HFP) was also attempted as separator and electrolyte for ORB [128]. Owing to the three-dimensional microporous structure (58% porosity and average

diameter of 1μm), this non-woven membrane exhibited a good wettability (240% within 1 min) and sufficient mechanical strength and self-standing properties.

Current Collectors

A current collector is a conductive solid part connected to the electrode with external loading. It mainly has two purposes. One is to support the electrode, and the other is to conduct electrons from inside the electrochemical reaction to the external circuit. It is desired to be chemically and electrochemically stable when it is in contact with the cell components, e.g. electrode active material and electrolyte, within the potential operation window. In practical terms, continuous corrosion of current collectors should be avoided as it increases the internal resistance of cells, causes capacity loss and may even induce short-circuit. Therefore, the choice of material is very critical. Normally thin aluminum foils are used as current collectors at the cathode side while copper foils are employed at the anode side. This can be explained from two aspects, which are passivation and corrosion of current collectors [129]. Aluminum is usually covered with a thin and dense passive oxidation layer, Al_2O_3, which can prevent aluminum from further oxidation. Besides, this passive Al_2O_3 layer has a minor effect on the conductivity of aluminum. Furthermore, at high voltage (3.5–5 V vs. Li/Li^+), the protective passive film of the aluminum can be formed, which could ensure battery performance and safety. However, at low potential (0–1.5 V vs. Li/Li^+), aluminum reacts with lithium ions to form an aluminum–lithium alloy, which may cause battery failure. Therefore, aluminum cannot be used as a current collector on the anode side. On the contrary, copper showed a good stability at low potential (0–3 V), nonetheless, oxidation occurs at high voltage ($>$ 3.6 V vs. Li/Li^+). Accordingly, copper is selected as anode current collectors and not suitable as cathode current collectors. Apart from aluminum and copper, other types of current collectors have also been reported, such as 304 stainless-steel wafer [110], ITO substrate [100], flexible graphite [102] and CNTs [89], etc. Besides, in order to increase the contact area of active material and electrolyte, some current collectors with three-dimensional porous structure were also investigated, for example 3DOM polypyrrole opal [103] and MCF [104].

Similar to LIBs, the above-discussed components can be manufactured into different battery shapes, such as coin cells, cylindrical cells, prismatic cells, and pouch cells. In addition, due to the substantial flexibility of radical polymers, printable batteries are also achievable with the help of conventional printing methods, like screen-printing [130, 131]. This allows the storage of electrical energy without employing metals or metal compounds. Actually, Evonik already stepped forward and made a leap in this field with TAeTTOOz®, a new material technology for

printable batteries, unveiled at the LOPEC trade show 2019 held in Munich, Germany [130, 132]. Attractively, battery cells produced with the TAeTTOOz® technology even do not require liquid electrolytes and therefore cannot leak.

2.1.2. Working Principle

Charge transport in redox polymers is normally driven by band conduction (for conjugated polymers) or electron self-exchange between adjacent redox sites (typically for nonconjugated polymers) [133]. As a non-conjugated redox polymer, a radical polymer is not an exception, and follows the latter mechanism (see Figure 2.3), which is also called diffusive hopping with the existence of electrolytes.

The typical working mechanism of an organic radical polymer based-electrode is considered to consist of two steps: heterogeneous electron transfer between the current collector and the radical sites and homogeneous electron transfer among the radical centers, as shown in Figure 2.3 [79, 134]. In the meantime, physical diffusion of counterions occurred to compensate for the charge change at the radical sites maintain charge neutrality.
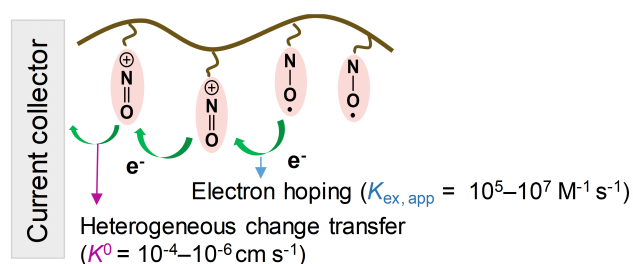
Figure 2.3.: Electron transfer in a non-conjugated redox polymer-based electrode.

In the first step, the electron transfer rate is entirely dependent on the diffusion rate of the radical polymer onto the current collector surface. The standard rate constant (k^0) of heterogeneous electron transfer is found to be on the order of 10^{-4}–10^{-6} cm s^{-1} according to the peak separation of cyclic voltammogram by the method of Nicholson [22, 134, 135].

Unlike conjugated polymers whose charge is transported along pathways of conjugation, charge propagation in the second step is realized in the form of redox diffusive hopping among neighboring redox centers, i.e. self-exchange. In order to make electron diffusion occur through self-exchange, the adjacent redox centers must be in close proximity [22, 136, 137]. Moreover, in respect of different polymer structures, it is suggested that the smaller the intersite distance, δ_{av}, the higher the capacity a radical polymer could deliver, as shown in Figure 2.4 [58]. The effective charge

transfer length of a certain polymer can be predicted by modeling and dynamic simulation. For example, Kemper et al. [136] found the effective electron transfer length for PTMA to be 5.5 Å using atomistic molecular dynamics simulations. Besides, they claimed nearly 85% electron transfer between radical sites occurred on different polymer chains. This result indicates that polymeric chains with a high degree of flexibility and mobility facilitate redox sites contact by diffusion, and accordingly improve the rate capability of ORB. Due to the shielding effect of the surrounding electrolyte, no electric field is present in the bulk electrode; it only exists across the electric double layer (Stern layer and Gouy-Chapman layer) on the electrode surface, hence migration is negligible [138]. The electron hopping follows Fick's law of diffusion and is driven by the concentration gradient of the oxidized species in the film. This electron self-exchange by neighboring redox-active centers decreases the concentration gradient until all present radicals are oxidized. The bimolecular rate constant $k_{ex,\,app}$ for electron self-exchange was estimated to be typically 10^5–10^7 M^{-1} s^{-1} by the Smoluchowski model, which is in the same order of magnitude as that of transition metal-containing polymers such as poly(vinylferrocene) [22, 134, 135, 139]. Owing to the relatively fast electron propagation, a layer of cross-linked polynorbornene with TEMPO pendant groups showed Nernstian adsorbate-like electrochemical behaviors with thicknesses in a submicrometer scale [135]. The apparent electron diffusion coefficient ($D_{TEMPO,\,app}$) as a sum of the contributions from the physical motion of redox centers and electron exchange, is typically ~10^{-8}–10^{-10} cm^2 s^{-1} [22, 140].
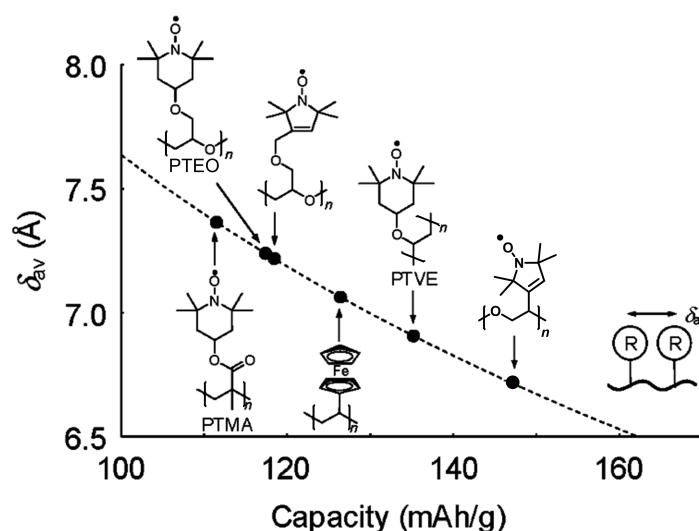
Figure 2.4.: Correlation of the mean intersite distance δ_{av} versus redox capacities for various radical polymers (adapted from ref [58] with permission from American Chemical Society).

In the presence of an electrolyte, the electron hopping is accompanied by the diffusion of counterions. In terms of the counterion migration and doping during the electrochemical process,

a dual doping mechanism is proposed for PTMA: doping by lithium-ion expulsion and doping by anion uptake [122], as shown in Figure 2.5. In the first process, a lithium cation is expelled by an anion (A⁻) that already imbibed into the PTMA dope. Afterwards, an anion from the bulk electrolyte is uptaken to dope PTMA. In the end, PTMA is doped by an anion imbibed in the polymer and another anion from the bulk electrolyte is taken to balance the imbibed lithium cation. The contribution of each doping highly depends on the electrolyte (i.e. salt and solvent) and radical nature of the respective polymer.
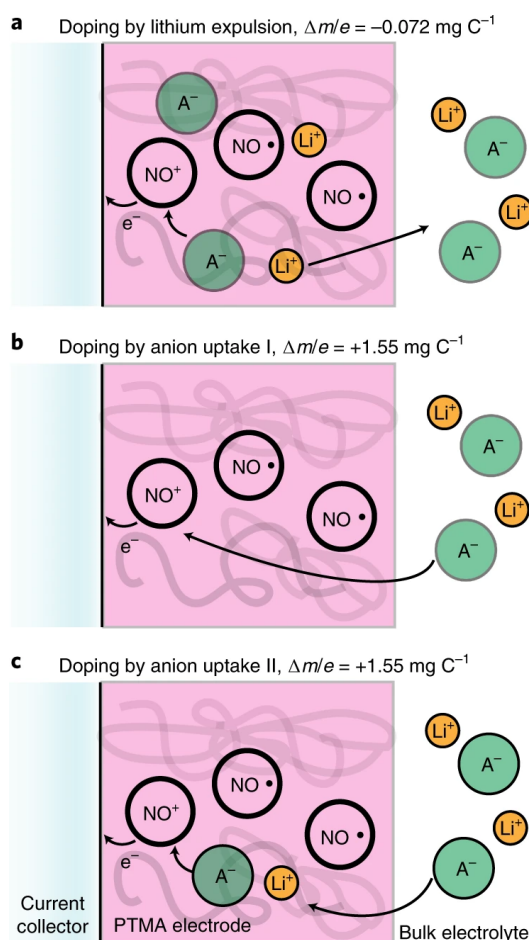
Figure 2.5.: Anionic doping mechanism for a swollen PTMA electrode (reproduced from ref [122] with permission from Springer Nature).

Generally, the ion diffusion process is faster (normally $D_{ion, app} = 10^{-5}$ cm² s⁻¹) than the electron hopping diffusion process (typically $D_{TEMPO, app} = 10^{-8}$–10^{-10} cm² s⁻¹) [22, 141]. Therefore, the physical diffusion of counterions normally is not the main limiting process of charge transfer for many radical polymers. However, there are exceptions. For example, with 0.5 M lithium trifluoromethanesulfonate (LiCF₃SO₃) in propylene carbonate (PC) acting as electrolyte, the

PTMA-based electrode exhibited an electron-diffusion-limited behavior within the scan rate range of 10–100 mV s^{-1} [122]. For a poly(bis-TEMPO-norbornene) film (270 nm) with 0.1 M tetra-*n*-butylammonium hexafluorophosphate in dry acetonitrile (MeCN) as an electrolyte, the physical diffusion coefficient of counterions, $D_{\text{ion, app}}$, was estimated to be on the same order of magnitude as the electron diffusion coefficient,$D_{\text{TEMPO, app}}$, but slightly lower, thus limiting the current at short times/fast charging (e.g. 0.2 s) [142]. To verify whether an electron transfer system is mass-diffusion-limited or electron-diffusion-limited (kinetically-limited), Nicholson model of voltammetry and Laviron's model of voltammetry can be applied [141, 143].

2.1.3. Battery Specifications

- Capacity or Nominal Capacity (Ah) - The amount of charge a battery (cell) contains, which depends on the nature and amount of active materials in a battery. Capacity is obtained by integration the discharge current (in Amps) over the discharge time (in hours), $Q = \int i(t)dt$. It decreases with increasing C-rate.

- Specific capacity (C, mAh g^{-1} or Ah kg^{-1}) - The amount of charge per unit mass that an electrode active material contains. The theoretical capacity of an electrode active material can be calculated according to the Faraday's laws of electrolysis (see Eq. 2.1).

$$Q_{theoretical} = \frac{nF}{(3600 \times M_{\text{w}})} \tag{2.1}$$

  where *n* is the number of charge carrier, *F* is the Faraday constant (96485.3 C mol^{-1}), and M_{w} is the average molecular weight of the active material used in the electrode.

- Cell voltage - The electrical potential difference between the two electrodes of an electro-chemical cell. It usually refers to nonequilibrium conditions, that is when current is flowing through the cell (although this convention is not always followed). Besides, the cell voltage differs from the emf or open-circuit voltage of the cell by the amount of the overvoltage.

- Energy density (Wh kg^{-1} or Wh L^{-1}) - The amount of electrical energy stored per unit weight or volume. Weight-based energy density is often called "specific energy" or "gravimetric energy density". Volume-based energy density is often called "energy density" or "volumetric energy density".

- Power density (W kg^{-1}, W L^{-1}) - The maximum available electrical power per unit weight or volume. Weight-based power density is often called "specific power" or "gravimetric power density". Volume-based power density is often called "power density" or "volumetric power density".

- C-rate (A) - A charge or discharge current is often described as C-rate to normalize against battery capacity. It is a measure of the rate at which a battery is charged or discharged relative to its maximum capacity. A 1C rate means that the discharge current will discharge the entire battery in 1 hour. 1C means fully charge or completely discharge one cell in one hour, and n C corresponding to n^{-1} hours of charge or discharge time.

- Coulombic efficiency or Faradaic efficiency (%) - The percentage of electrical charge restored during discharging after a battery is fully charged.

- Internal resistance (Ω) - The resistance within a battery, normally differs between charging and discharging and also depend on the state of charge. With increasing internal resistance, the battery efficiency decreases as more of the charging energy is converted into heat.

- Cycle life - The number of times a rechargeable battery (or capacitor, especially an electrochemical capacitor) can be cycled before it fails to meet specific performance criteria. Practically, it is related to the C-rate, depth of cycles, as well as temperature and humidity.

2.2. TEMPO-Containing Polymers as Electrode Materials

To act as an electrode material of an ORB, one crucial prerequisite has to be met. In other words, the material should bear redox-active radical groups that can undergo a reversible electrochemical process with stable species in both oxidized and reduced forms. Moreover, this material should not be readily soluble in electrolyte, otherwise severe self-discharge would happen. Small organic molecules which are facilely dissoluble in traditional electrolyte, e.g. carbonate-based electrolyte, are thus mostly inappropriate. Apparently, incorporating radical groups into a polymer structure appears to be the simplest way. Over the years, various polymer backbones, such as poly(methacrylate) [17], polynorbornene [144], polyacetylene [144], polyallene [145] polythiophene [146], polypyrrole [147], polyether [148], poly(vinyl ether) [149], polysiloxane [150], polystyrene [151, 152] polydopamine [153], polytriphenylamine [154] and biomaterials (e.g cellulose derivatives and DNA) [155, 156] have been examined as parental electrode materials.

Besides, a variety of stable organic radicals have been investigated, as depicted in Scheme 2.1. Among them, TEMPO-containing polymers represent one of the most promising electrode materials as a result of rapid electron transfer process and reversible redox reaction between TEMPO and the corresponding oxoammonium [13, 21, 157]. Accordingly, in this section, the electrochemical properties of TEMPO as well as the synthetic methodology towards TEMPO-containing polymers for battery application are discussed.

2.2.1. TEMPO and Its Derivatives

Nitroxides

A free radical is a chemical species possessing an unpaired valence electron except for all paramagnetic salts of transition metals [158]. Generally, it is highly reactive and has a short lifetime due to the open-shell configuration. Chemical reactions like substitution, isomerization, disproportionation, addition and decomposition are typical reactions that take place with the involvement of the free valence. However, there are persistent organic radicals with sterically protected structures around the paramagnetic centers or with resonance stabilization involving the centers, e.g. triphenylmethyl radicals, nitroxides and verdazyl radicals.

Nitroxides, also known as aminoxyl or nitroxyl radicals, are a class of persistent organic radicals with the oxygen radical mainly stabilized by electron donation from the nitrogen lone pair, as depicted in Scheme 2.3. The molecular orbitals (MO) of N-O· are composed of eight filled bonding orbitals including one single occupied molecular orbital (SOMO), as shown in Figure 2.6. This SOMO is an antibonding π^* orbital with the unpaired electron polarized toward the nitrogen atom. On account of the three π electrons and the two resonance structures, (A) and (B), in Scheme 2.3, the N-O bond of the nitroxide has a bond order of 1.5 (one σ bond and a half π bond). The latter is indicated by the bond energy ($\sim$ 100 kcal mol^{-1}), and the bond length, d_{NO}, (1.25 Å $< d_{NO} <$ 1.30 Å), which fits the middle course of a N-OH single bond (53 kcal mol^{-1}; $\sim$ 1.43 Å) and a N=O double bond (145 kcal mol^{-1}; $\sim$ 1.20 Å) [158–160].
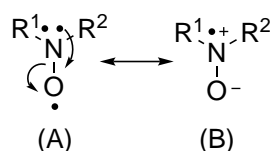
Scheme 2.3: Resonance stablization of nitroxides.
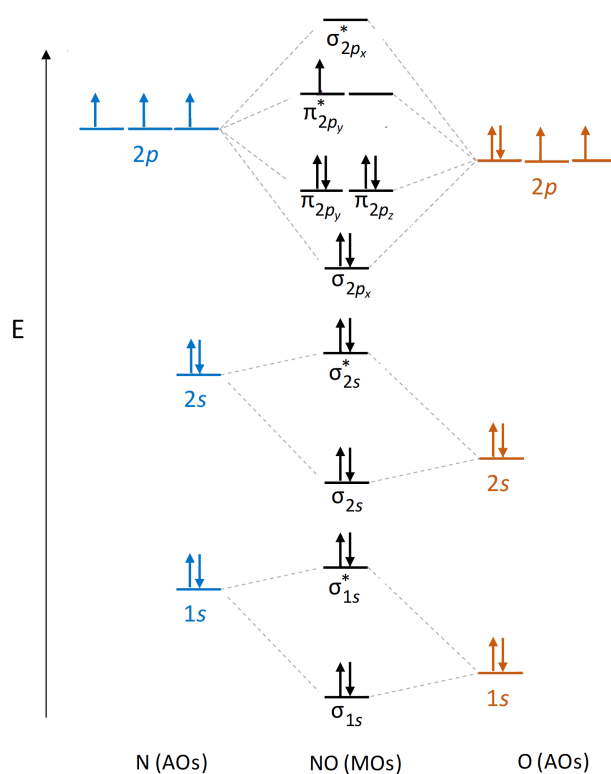
Figure 2.6.: Molecular orbital diagram of NO·.

Based on thermochemical studies, the gain in energy from unpaired electron delocalization between the nitrogen and oxygen atoms was evaluated to be $\sim$ 30.4 kcal for heterocyclic nitroxides [158]. Employing He I/He II photoelectron spectroscopy, this value was reported to be even lower, i.e. 23 kcal mol^{-1} [161]. Whereas, the gain in energy for dimerization of oxygen radicals to form O-O bond was calculated to be $\sim$ 35 kcal mol^{-1}. These results indicate that delocalization is thermodynamically more favorable than O–O dimerization as a system always try to attain maximum stability by minimizing its potential energy, in other words, nitroxides are considerably stabilized. Nonetheless, the persistence of nitroxides depends on the nature of the substituents. For instance, nitroxides with α positions fully substituted or incorporated into the bridgehead position of a bi- or polycyclic framework were suggested to have enhanced stability in general [85], while, nitroxides with α-hydrogen atoms are normally unstable and may undergo disproportionation reactions [162–164], as shown in Scheme 2.4.
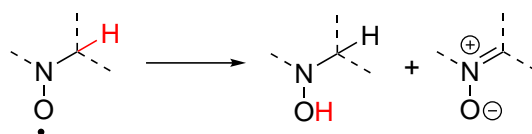
Scheme 2.4: Disproportionation reaction of nitroxide with α-hydrogen atom.

The spin density is mainly distributed on the nitrogen and oxygen atoms with the latter being moderately higher, and slightly allocated to the adjacent alkyl groups. The distribution of spin density between the nitrogen and oxygen atom is strongly dependent on the hybridization preference of the nitrogen atom, e.g. sp^2 (planar) and sp^3 (pyramidal), and the polarity of the solvent [159, 165].

Since the first discovery in 1845 by Edmund Fremy [166], a variety of nitroxides have been prepared as shown in Figure 2.7. As the most prominent member of heterocyclic nitroxides, TEMPO has received great attention due to their inherent paramagnetic feature and unique electronic properties by either losing or gaining one electron to form the corresponding *N*-oxoammonium cation or the aminoxy anion, respectively [80, 85]. So far, widespread applications of TEMPO have been found in analytic techniques, e.g. spin labeling [167], spin probing [168] and spin trapping [169], in chemistry and biology as radical scavengers [170], catalysts for oxidation of alcohols [171], ligands for organometallic catalysis [172], and initiators for nitroxide-mediated radical polymerization (NMP) [173], and battery field as electrode materials [20, 21, 134].

Synthesis of TEMPO Derivatives

TEMPO, an orange-red colored persistent organic radical, was discovered by Lebedev and Kazarnovskii in 1959 [174]. Similar to all nitroxides, TEMPO is stabilized by delocalization of the unpaired electron between the nitrogen and oxygen atom. Moreover, the steric effect from methyl groups at the α position in the six-membered piperidine ring structure (Scheme 2.5) also contributes to the stabilization.
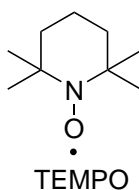
Scheme 2.5: Chemical structure of TEMPO.

TEMPO and its common derivatives with the substituent at 4-position are synthesized from triacetone amine (3), followed by alteration of the ketone group on triacetone amine to other functional groups, and then oxidation of the amine group into a nitroxide functionality, or the other way around, as depicted in Scheme 2.6. Depending on the X and Y functional groups, the resulting TEMPO derivatives (5,8) may also undergo further modifications. The key intermediate,
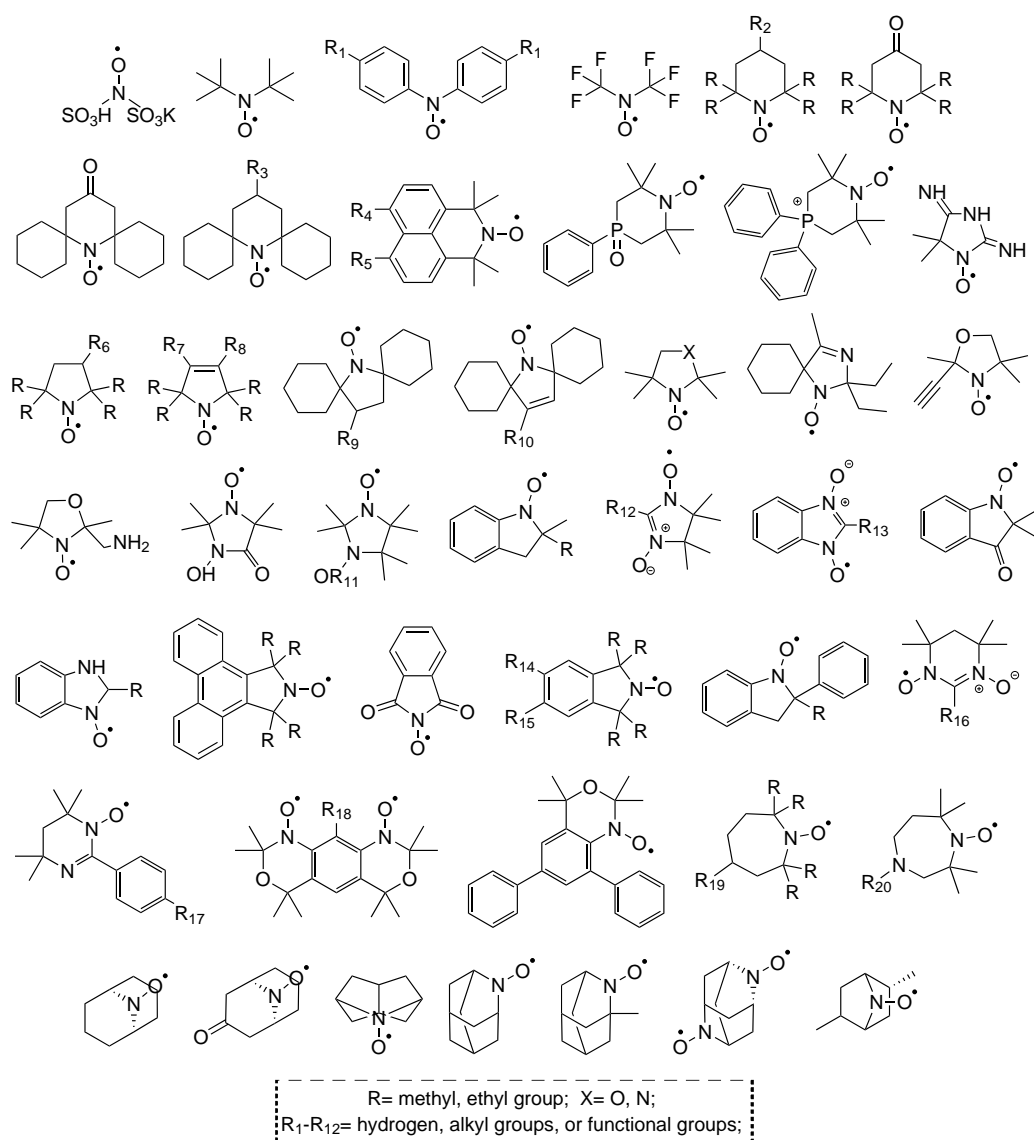
Figure 2.7.: Structures of various nitroxides.

i.e. triacetone amine (3), can be synthesized in several methods. For instance, the most frequently used procedure is the condensation of acetone (1) and ammonia (2) in the presence of an acidic catalyst (e.g. calcium chloride, organic carboxylic acid halide, *p*-nitrotoluene) [175–179]. On similar lines, triacetone amine (3) can also be prepared from phorone (6) and ammonia (2) [180, 181]. Moreover, condensation of 2,2,4,6,6-pentamethyl-1,5-dihydropyrimidine (9) with acetone in the presence of a Lewis acid, such as calcium chloride and ammonium tetrafluoroborate, is another procedure, which was mainly disclosed in patents [182, 183].

Based on triacetone amine (3), 4-oxo-2,2,6,6-tetramethyl-1-piperidinyloxy (4-oxo-TEMPO, 7) can be obtained, which is commonly achieved with hydrogen peroxide and a sodium tungstate
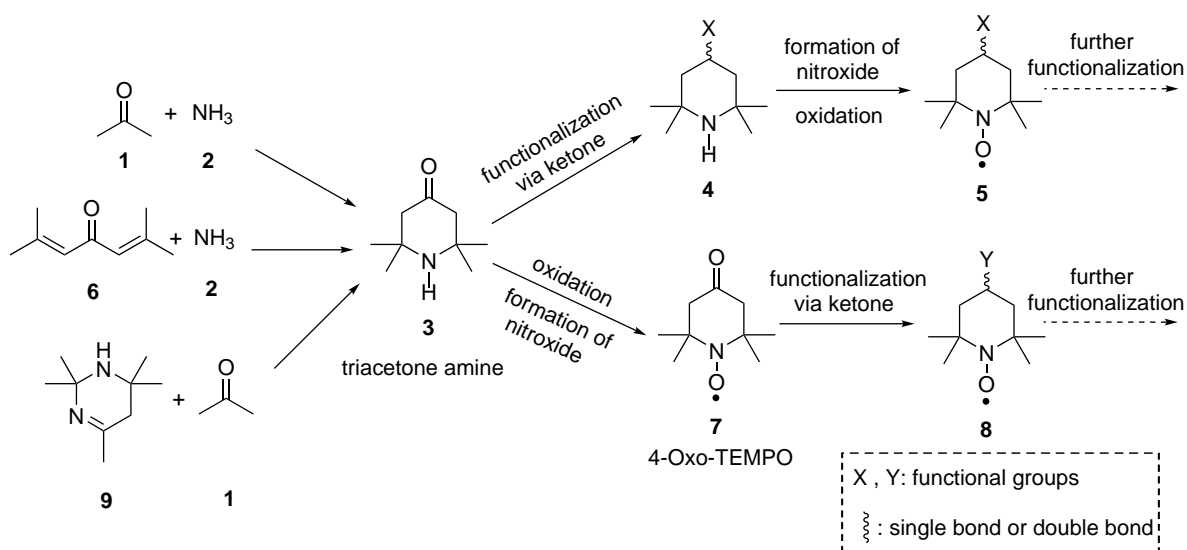
Scheme 2.6: Synthetic procedure for TEMPO derivatives.

catalyst [184]. On top of 4-oxo-TEMPO (7), a variety of TEMPO derivatives can be synthesized, including modifications at 4-position and 3- or 5-positions, as shown in Scheme 2.7. For instance, the ketone (7) can be converted into an imine (10) [185], an amine (11–18, reductive amination) [184, 186–192] or a hydantoin (19, Bucherer–Bergs reaction) by reacting with diverse amines [193]. Through Wolff-Kishner reduction, the carbonyl group can be transformed into a methylene (-CH$_2$-) group, thus forming TEMPO (20) [192]. Through reductive nitrilation of the ketone (7), a cyano-substituted TEMPO derivative (21) can be acquired [194], which could be further hydrolyzed to a carboxylic acid (22). With Corey-Chaykovsky reaction, TEMPO epoxides (23) can be achieved [185]. Via a Witting reaction, an enol ether functionality can be attached to the 4-position of 4-oxo-TEMPO, leading to compound 24 [195], which can be converted to an aldehyde (25) by the application of an acid [195]. Additionally, halogen-substituted TEMPO derivatives can also be obtained either via hydrazone (*in situ* product from condensation of the ketone (7) with hydrazine) iodination at the 4-position (26) [196] or via ketone halogenation at the 3-, 5- position (27, 28) [197, 198] or both (29) [199]. Apart from compounds 27–29, other TEMPO derivatives with modification at 3- or 5- position are also attainable, such as compounds having heterocycles (30, via Mannich reaction) [200], compounds containing double bonds (31–33) [201, 202] and compound with hydroxy group and dimethylacetal group at 3- and 4-position, respectively (34) [203].

Aside from 4-oxo-TEMPO (7), 4-hydroxy-2,2,6,6-tetramethylpiperidine 1-oxyl (35, 4-hydroxy-TEMPO) [186], one member of compound 5, also plays an important role in the preparation of TEMPO derivatives. With a hydroxyl group at the 4-position, 4-hydroxy-TEMPO can participate
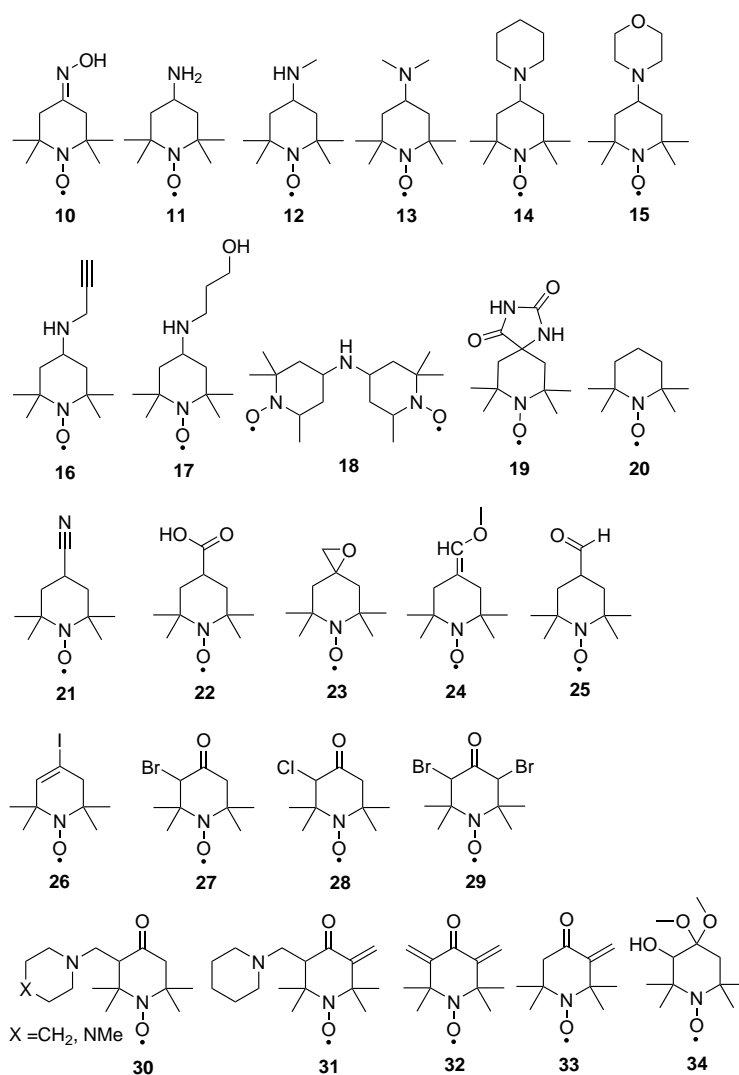
Scheme 2.7: TEMPO derivatives obtained from 4-oxo-TEMPO.

in a broad spectrum of reactions, hence extend the scope of TEMPO derivatives (see Scheme 2.8). For instance, the nucleophilic substitution with the hydroxyl group is one of the most common reactions in which alkyl halides, sulfonyl chlorides, chloro silianes, phosphorous chlorides can serve as electrophiles and result in diverse TEMPO-based ethers (36–48) [190, 204–216]. Electrophilic substitution at oxygen by derivatives of carboxylic acid, sulfonic acid, acyl chloride, chlorophosphate, sulfonyl chloride etc., is also achievable, leading to the formation of various TEMPO-based esters (49–58) [185, 217–228]. Employing a S_N2 reaction with thionyl bromide, TEMPO bromide (59) can be obtained [185]. Moreover, the resulting compounds from these reactions may also bear other functionalities, i.e. unsaturated hydrocarbons, alkyl halides, acids, amines, alkoxysilanes, tosyl/mesyl groups and epoxides, which can be further modified and consequently broaden the scope of TEMPO derivatives.
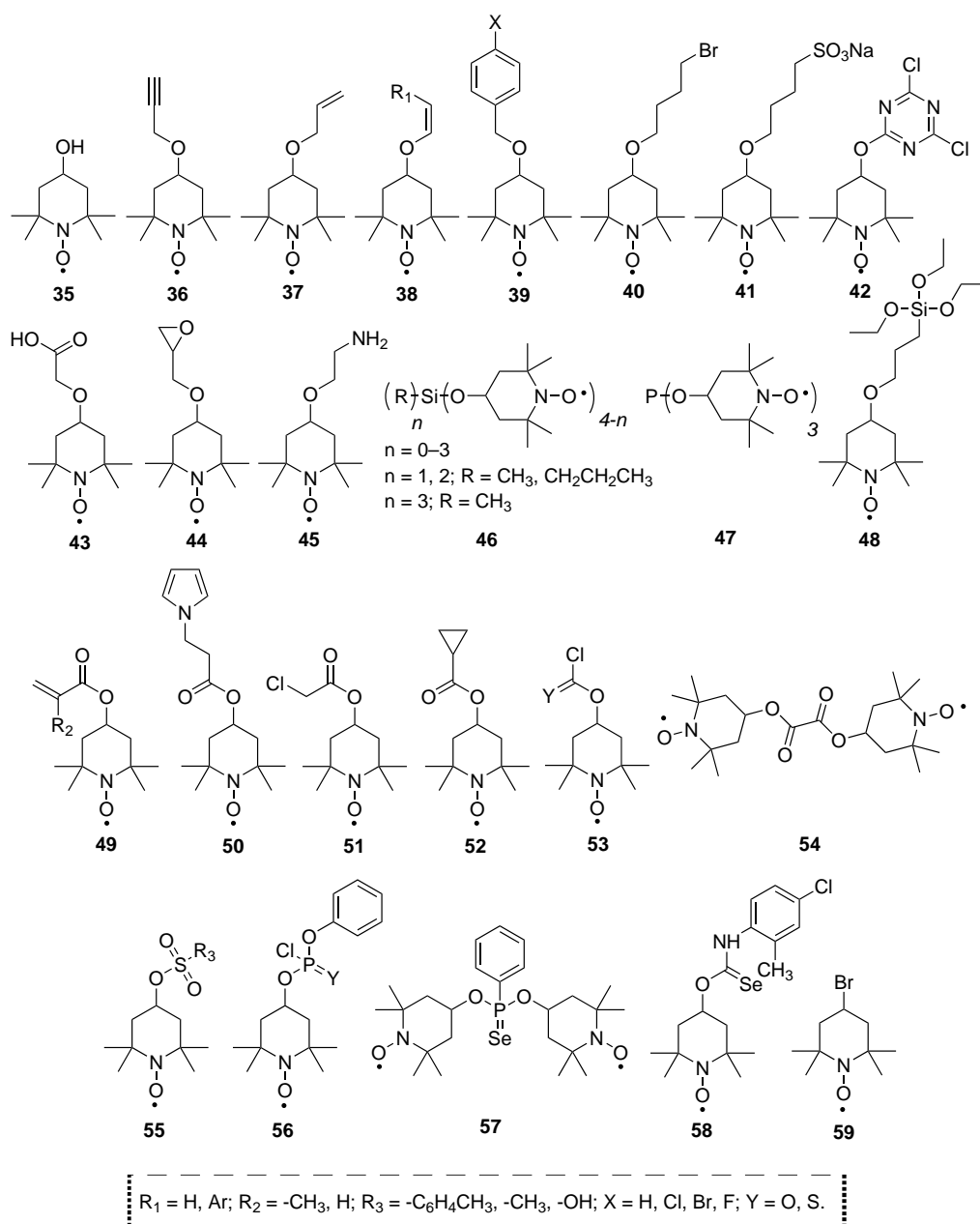
Scheme 2.8: TEMPO derivatives obtained from 4-hydroxy-TEMPO via various modifications.

Electrochemistry of TEMPO Derivatives

1) Electrochemical behavior of TEMPO derivatives and the mechanisms

Shortly after the discovery of TEMPO, the electrochemistry of TEMPO started to be investigated [229]. With linear sweep voltammetry, an electrochemical reversible, one-electron transfer process controlled by diffusion (mass transport to the electrode) with $E_{pa} = 315$ mV, $E_{pc} =$

250 mV vs. Ag/Ag$^+$, was revealed for TEMPO in MeCN (see Figure 2.8A). Other than that, voltammetric studies of TEMPO in aqueous media were also conducted in a combination of UV-visible spectroscopy [230]. Figure 2.8B and 2.8C illustrate the voltammograms of TEMPO in tetraethylammonium perchlorate (TEAP) aqueous solution at pH = 7. A defined, symmetric peak at E_{pa} = 480 mV vs. a saturated calomel electrode (SCE), with a peak width of 94 mV, was observed in the differential pulse voltammogram (DPV) (Figure 2.8B). A pair of redox peaks at E_{pa} = 520 mV and E_{pc} = 460 mV vs. SCE, with i_{pa}/i_{pc} close to unity, and i_{pa} or i_{pc} being proportional to $\nu^{1/2}$, was noted in cyclic voltammogram (CV) (Figure 2.8C). These results confirmed that the electrooxidation of TEMPO in aqueous solution is a diffusion-controlled, reversible, one-electron transfer process, which resembles the reaction in organic media [229]. Whereas, the redox process exhibited at negative potential proved to be irreversible with a poorly defined peak at E_{pc} = -720 mV vs. SCE in DPV, and no anodic peak accompanying the cathodic peak at E_{pc} = -0.62 V showed up in CV. The products from the electrooxidation and electroreduction of TEMPO were monitored by thin-layer spectroelectrochemistry (Figure 2.8D). It was found that the oxidation product at +0.65 V is quite stable and did not change over an observation period of 3hr., while the reduction product at -0.80 V could not be reoxidized even at a potential 200 mV more positive than -0.62 V (E_{pc}). The latter further confirms the complete irreversibility of the reduction process of TEMPO on a platinum electrode.

By utilizing a glassy carbon electrode, the reoxidation peak arising from the anodic sweep of the reduction product of TEMPO was later detected with cyclic voltammetry in both aqueous and aprotic solution [231, 232]. On an oxidized carbon electrode, a smaller peak-to-peak separation for the reduction process was observed in comparison to a glass carbon electrode [233]. At the surface of a hanging mercury drop electrode under basic condition (pH = 12), a practically reversible redox behavior, with a peak separation of 66 mV, was found by Kishioka et al. [234]. These results indicate that the kinetics of the reduction process of TEMPO, notably the reoxidation, is dependent on the characteristics of the electrode, which may due to the catalytic effect related to surface chemistry of the electrode [235, 236].
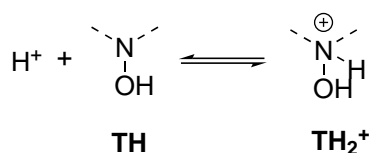
Scheme 2.9: The equilibrium between TEMPO hydroxylamine (TH) and TEMPO hydroxylammonium (TH$_2^+$) under acid conditions.

The mechanism of the irreversible reduction processes for TEMPO derivatives was revealed by
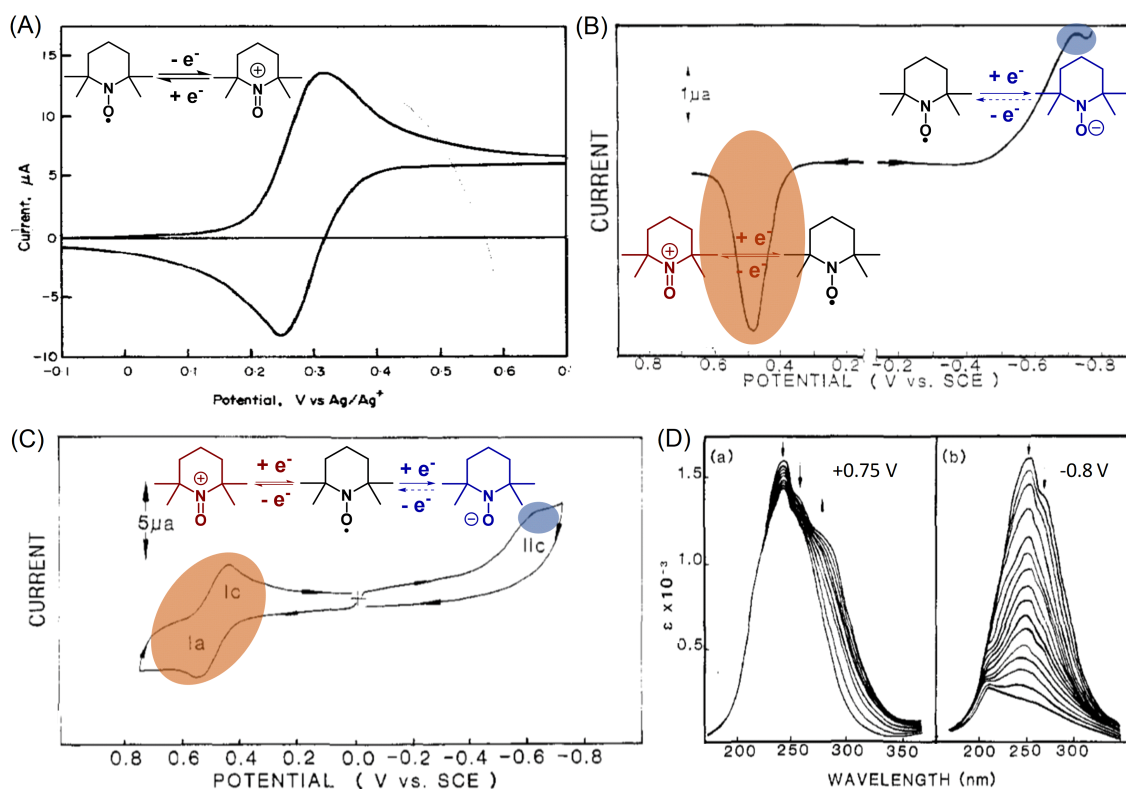
Figure 2.8.: Voltammograms of TEMPO at platinum electrodes. (A) Cyclic votammogram of 0.005 M TEMPO in 0.5 M LiClO$_4$ in MeCN with a scan rate of 92 mV s^{-1} (adapted from ref [229] with permission from Elsevier Science Ltd.); (B) differential pulse voltammograms of 0.0008 M TEMPO in 0.08 M TEAP aqueous solution at a scan rate of 2 mV s^{-1} and amplitude of 20 mV; (C) cylcic votammograms of 0.0008 M TEMPO in 0.08 M TEAP aqueous solution at a scan rate of 100 mV s^{-1}; (D) electronic absorption spectra of 0.000174 M TEMPO in 0.08 M TEAP a) during oxidation at applied potential of +0.75 V, and b) during reduction at -0.80 V (adapted from ref [230] with permission from American Chemical Society).

Kato et al. [231]. The electron transfer process is accompanied by a proton coupling leading to the formation of hydroxylamine. Moreover, according to Nigam et al. [237], under acidic conditions, there exists an equilibrium between the hydroxylamine form (TH) of TEMPO (T*) and its conjugate acid hydroxylammonium (TH$_2^+$), as shown in Scheme 2.9. Therefore, the change in pH of the solution would interfere with the formation of hydroxylammmonium ion (TH$_2^+$) and hydroxylamine (TH), especially under acidic conditions, thus affecting the redox potentials (E_{a2} and E_{c2}, see Figure 2.9A) between TEMPO and hydroxylamine species (T*/TH). As shown in Figure 2.9B and 2.9C [231, 238], with the increase in pH, both E_{a2} (stick marks) and E_{c2} (star marks) shifted downwards for TEMPO as well as for 4-hydroxy-TEMPO. On the contrary, the oxidation product of TEMPO, i.e. oxoammonium cation (T$^+$), is found to be stable over the acidic and most of the basic pH range [237], suggesting less pH-sensitive redox potentials (E_{a1}

and E_{c1}) between TEMPO and oxoammonium cation (T^*/T^+, see Figure 2.9A). As exhibited in Figure 2.9B and 2.9C [231, 238], with the change of pH, E_{a1} and E_{c1} remained relatively the same for both TEMPO ($E_{1/2}^{ox} = 740 \pm 10$ vs. NHE) and 4-hydroxy-TEMPO ($E_{1/2}^{ox} = 825 \pm 15$ mV vs. NHE).
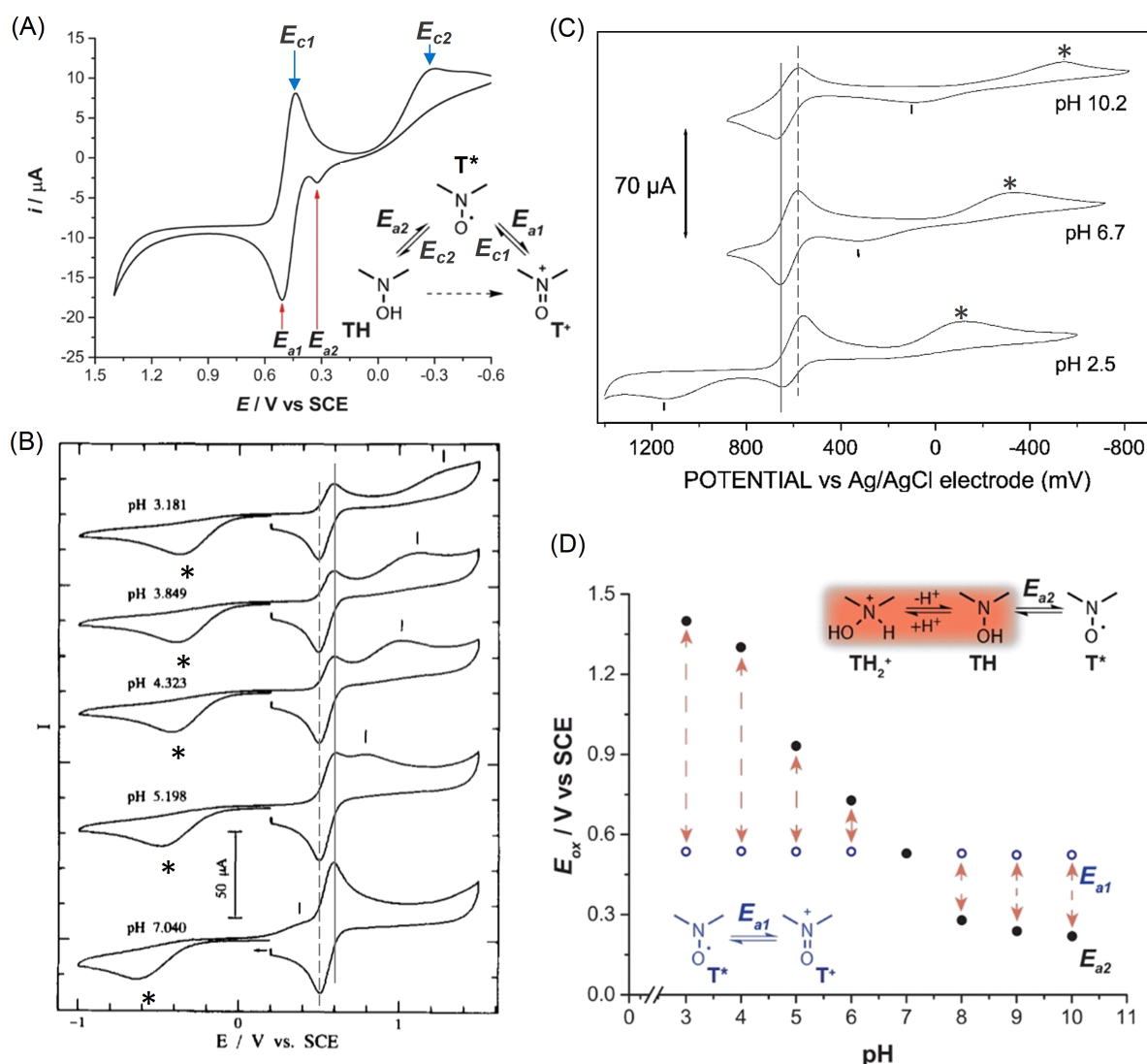
Figure 2.9.: (A) A representative CV of TEMPO with the anodic peak potentials, E_{a1} and E_{a2}, and cathodic peak potentials, E_{c1} and E_{c2}, highlighted. CV of (B) 2.4 mM TEMPO in acetate-borate-phosphate buffer and (C) 4.6 mM 4-hydroxy-TEMPO in 10 mM phosphate buffer measured at various pH conditions at a scan rate of 100 mV s^{-1}; stick marks, star marks, solid lines and dash lines show E_{a2}, E_{c2}, E_{a1} and E_{c1}, respectively. (D) Experimental values of E_{a1} and E_{a2} as a function of pH for 5 mM TEMPO in 150 mM Robinson buffer consisting of equal parts phosphate, acetate, and borate (adapted from ref [231, 238, 239] with permissions from Elsevier Science Ltd. and American Chemical Society).

By tracking the anodic peak potentials, E_{a1} and E_{a2} in CV, followed as a function of pH, Hickey

et al. [239] experimentally showed that E_{a1} is independent of proton concentration, while E_{a2} is inversely proportional to pH, and as a result, exhibited a low value under basic conditions, as presented in Figure 2.9D. On similar lines, the pH dependence of the half-wave potentials, $E_{1/2}^{red}$, between nitroxide and hydrxoylamine redox couples for TEMPO and 4-hydroxy-TEMPO was investigated by Israeli et al. [238]. Fitting curves containing two straight lines with an intersection were obtained in both cases, as shown in Figure 2.10. Furthermore, the slopes of the linear plots below the intersection $E_{1/2}^{red}$ were found to be -51 and -54 mV/pH, corresponding to a 1 e$^-$/1 H$^+$ redox process (T/TH), while the slopes above the intersection $E_{1/2}^{red}$ were -127 and -144 mV/pH, indicating a 1 e$^-$/2 H$^+$ redox process (T*/TH$_2$$^+$), for TEMPO and 4-hydroxy-TEMPO, respectively. Based on the intersection of the two lines, the pK_a values for TEMPO and 4-hydroxy-TEMPO were determined to be 7.5 and 7.1, respectively, which is in agreement with the value determined by kinetic experiments (7.5 and 6.9, respectively), particularly in the case of TEMPO [238].

Figure 2.10.: $E_{1/2}^{red}$ of (A) 4.6 mM TEMPO and (B) 4.6 mM 4-hydroxy-TEMPO in 10 mM phosphate buffer measured in pH range of 2–12 by CV measurement (scan rate = 100 mV s^{-1}) (reproduced from ref [238] with permission from Elsevier Science Ltd.).

In a more detailed study conducted by Samuni and co-workers [233], the redox behavior of TEMPO derivatives within a wide pH range from 0 to 13 were investigated. The mechanism of each section and the structural effects of various TEMPO derivatives were elaborated via Pourbaix diagrams, i.e. potential/pH diagrams, (Figure 2.11). Taken TEMPO for instance (see Figure 2.11B), above pH = 7.34, pKa of hydroxylammonium, the redox reaction for the reduction process takes place between TEMPO and hydroxylamine species (T*/TH), as depicted in Figure 2.11A_a1. Whereas, at 3 < pH < 7.34, the reduction process occurs between TEMPO hydroxylammonium and TEMPO (T*/TH$_2$$^+$) as shown in Figure 2.11A_a2, and its corresponding reoxidation process takes place in the reverse path. At pH < 3, acid-promoted disproportionation of TEMPO goes essentially to completion, and no TEMPO exists under such acidic condition, as shown in Scheme 2.10; hydroxylammonium is thus directly oxidized to oxoammonium (TH$_2$$^+$/T$^+$, see Figure 2.11A_a3).

Concerning the oxidation process of TEMPO, it takes place between TEMPO and oxoammonium (T_*/T^+) redox couples (see Figure 2.11A_a4) in the pH range of 7.34–14.0 (the upper pH limit may differ from literature to literature) [230]. While at pH > 14.0, the redox reaction continues as exhibited in Figure 2.11A_a5, due to the presence of an equilibrium between oxoammonium and hydroxylamine *N*-oxide.

Figure 2.11.: (A) Redox mechanisms for TEMPO derivatives. Pourbaix diagrams of (B) TEMPO, (C) ACT, (D) AMT measured by cyclic voltammetry in the pH range of 0–13. Fitted lines have been constrained to have slopes corresponding to 0, 1, or 2 H^+/e^-, and to intersect at points. Black circles and lines correspond to oxoammonium reduction, red stars and lines correspond to nitroxyl reduction, solid blue lines are pKa values measured spectroscopically, dashed blue lines are pKa values inferred from CV data; dashed red lines are redox potentials inferred from NMR data (adapted from ref [233] with permission from American Chemical Society).

Scheme 2.10: Disproportionation-comproportionation equilibrium between TEMPO (T*) and oxoammonium/ hydroxylammonium (T$^+$/TH$_2$$^+$) under acid conditions.
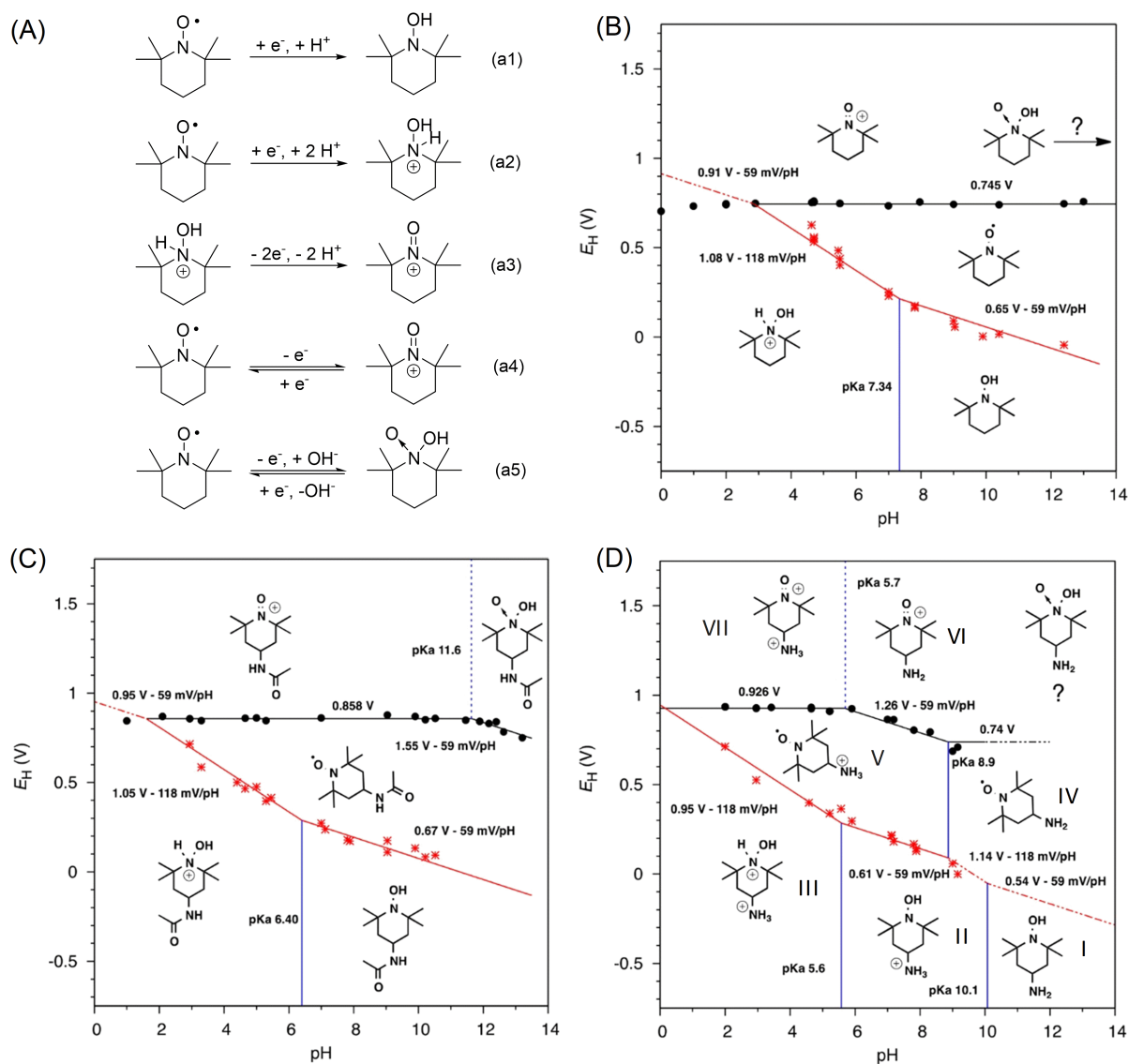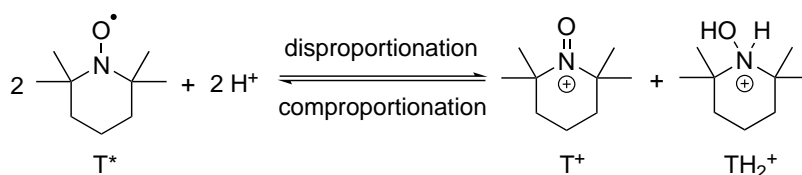
Due to the mild electron-donating effect of the amide substituent (-NHCOMe), 4-(acetylamino)-2,2,6,6-tetramethyl-1-piperidinyloxy (ACT) exhibits an increase in the 1 e$^-$ oxoammonium/nitroxyl and 1 H$^+$/1 e$^-$ nitroxyl/hydroxyamine reduction potentials by 113 mV and 20 mV, respectively, in comparison to TEMPO (see Figure 2.11C). The pKa (6.4) of its corresponding hydroxylammonium ion decreases relative to TEMPO. The critical pH below which hydroxylammonium can be directly oxidized to oxoammonium, also decreases compared to TEMPO. At pH value greater than 11.6, i.e. pKa of the oxoammonium cation, the midpoint potential shifts to a lower potential (i.e. < 0.858 V) and the CV appears more reversible at low scan rates.

Compared to TEMPO and ACT, the redox mechanisms for 4-amino-2,2,6,6-tetramethyl-piperidinyloxyl (AMT) is rather complicated, as the amine substituent features protonation at a wide range of pH (0–10.1), aside from the inherent electron-donating effect to the heterocyclic structure. Except for the protonation of the hydroxylamine site (II → III, Figure 2.11D) at pH < 10.1, each species with a primary amine substituent is involved in a protonation equilibrium at a certain pH range, which is below 10.1, 8.9 and 5.7 for amino-hydrxoylamine (I, Figure 2.11D), AMT (IV, Figure 2.11D) and amino-oxoammonium (VI, Figure 2.11D), respectively. Moreover, because of the amine substituent, the direct oxidation of hydroxylammonium to oxoammonium (III → VII, Figure 2.11D) does not occur even at pH = 0.

It is worth noting that there is a pH-dependent disproportionation-comproportionation equilibrium between TEMPO (T*) and oxoammonium/hydroxylammonium (T$^+$/TH$_2$$^+$) (see Scheme 2.10) [238], which may influence the electrochemical behavior of TEMPO derivatives at various pH conditions. Under acidic conditions, disproportionation dominates, as shown in Figure 2.12A [240]. With the increase in acidity of the media by adding *p*-toluenesulfonic acid (*p*-TSA), the concentration of TEMPO declined to half of its initial concentration, while oxoammonium accumulated. Both concentrations changed in a linear fashion against the concentration of *p*-TSA, with the former changing twice faster as the latter. At pH = 3 (1 mM *p*-TSA), TEMPO disappeared completely, and the concentration of TEMPO oxoammounium reached a plateau with the value being half (0.5 mM) the initial concentration of TEMPO (1 mM). As shown in Figure 2.12B, the

addition of *p*-TSA caused the rest potential of the TEMPO/oxoammonium cation couple to shift in a more positive direction and resulted in a decrease of the peak current in CV (Figure 2.12B_b). The subsequent addition of 2,6-lutidine as a Lewis base promoted the reverse comproportionation and thus made the rest potential and the peak current recover (Figure 2.12B_c and 2.12B_d), indicating the disproportionation-comproportionation reactions of the nitroxides in MeCN are chemically reversible. In aqueous solution, this disproportionation-comproportionation equilibrium also exists [241, 242]. As shown by Grzeszczuk et al. [241] with steady-state voltammograms in Figure 2.12C, at pH $= 7$, an anodic plateau ascribed to TEMPO/oxoammonium (T^*/T^+) was observed, while, at pH $= 0$, the anodic plateau was almost absent with I ≈ 0, and the cathodic current reached maximum which is approximately half of the initial anodic current, implying that the concentration of T^+ is half of the original TEMPO concentration.

Figure 2.12.: (A) Concentration plots of TEMPO and TEMPO oxoammonium as a function of the concentration of *p*-TSA in 0.2 M NaClO$_4$ in MeCN. (B) CV for 1 mM (a) TEMPO, (b) TEMPO with 1 mM *p*-TSA, (c) TEMPO with 1 mM *p*-TSA and 0.5 mM 2,6-lutidine and (d) TEMPO with 1 mM *p*-TSA and 1 mM 2,6-lutidine in 0.2 M NaClO$_4$ in MeCN. (C) Steady-state voltammograms of 1mM TEMPO in 1M NaClO$_4$ (pH $= 7$) and 1M HClO$_4$ (pH $= 0$) aqueous solution (adapted from ref [240, 241] with permissions from Elsevier Science Ltd. and John Wiley & Sons, Inc.).

Under basic conditions, the comproportionation reaction dominates. With rapid-mixing stopped-flow methods in combination of electron paramagnetic resonance (EPR) spectroscopy, Samuni et al. evaluated the rate constants of comproportionation reactions for TEMPO and 4-hydroxy-TEMPO as a function of pH, as shown in Figure 2.13. A similar trend was observed for both TEMPO (Figure 2.13A) and 4-hydroxy-TEMPO (Figure 2.13B): at pH < 7, the rate constant of the reaction is relatively slow, while at high pH (basic condition), the comproportionation reaction indeed speeds up dramatically.

Additionally, the half-wave redox potential, $E_{1/2}^{ox}$, between TEMPO and oxoammonium cation

Figure 2.13.: The pH dependence of the second-order rate constant (k_{app}) for the reaction of oxoammoniums with hydroxylamines derived from TEMPO (A) and 4-hydroxy-TEMPO (B). The values of k_{app} were determined by spectrophotometric measurements (solid symbols) and EPR spectrometry (open symbols). The solid lines reflect the fitting curves. Plateau values represent the rate constants of hydroxylammonium and hydroxylamine. The intersections reflect the pK_a of hydroxylamines (adapted from ref [238] with permission from Elsevier Science Ltd.).

(T^+/T^*) is reported to be insensitive to the identity of the buffering electrolyte, indicating that there is no strong ion pairing between the oxoammonium species and the electrolytes [233], whereas the half-wave redox potential between TEMPO and hydroxylamine (T^*/TH) exhibited some dependence on the anions present in the buffer at pH $\geqslant$ 7.0 [243].

2) Structural effects on the redox properties of TEMPO derivatives

As mentioned in the previous section, substituent effects may affect the redox mechanism of TEMPO derivatives, resulting in distinctive electrochemical behavior. Generally, the half-wave potential is susceptible to the inductive constants or Hammett constants of the substituents. In 1991, Morris et al. [244] found that $E_{1/2}^{red}$ for hydroxylamine/nitroxide redox couple increased as a function of inductive substituent constant in a linear fashion (see Figure 2.14A), indicating electron-donating substituents lead to a more negative $E_{1/2}^{red}$. However, no such trend was observed for the anodic potential of nitroxide/oxoammonium (see Figure 2.14B). By screening thirteen TEMPO derivatives electromagnetically, Zhang et al. [245] recently revealed the linear correlation between the anodic potential for nitroxide/oxoammounium and the Hammett constant, δ_p. As shown in Figure 2.15A, with an increase of δ_p, the anodic potential for nitroxide/oxoammounium increased. The latter can be explained by the ability of various substituents to electrostatically stabilize/destabilize the oxoammonium cation. The substituent R can electrostatically interact with both the polarized N-O· bond in nitroxide and the formal charge in oxoammonium ($+N=O$). When the charge-dipole is dominant, the favorable charge-dipole interaction with the R substituent would stabilize the oxoammonium cation, thereby resulting in a lower anodic potential. Conversely, the

poorly aligned charge-dipole interaction with R substituent would destabilize the oxoammonium cation, thus leading to a higher anodic potential (see Figure 2.15B).

Figure 2.14.: (A) Correlation between inductive constants and half-wave potentials (vs. SCE) for various hydroxylamine/nitroxide redox couples measured in phosphate butter (pH = 7.2–7.4) on a Hg drop electrode. (B) Oxidation potentials (vs. SCE) of nitroxide/oxoammonium redox couples measured on a glass carbon electrode (adapted from ref [244] with permission from American Pharmacists Association).

Figure 2.15.: (A) Correlation between oxidation potentials (vs. Fc/Fc$^+$) for various TEMPO derivatives with the Hammett constants (δ_p). (B) Oxidation of nitroxide radical with differing remote (non-conjugated) substituent dipole orientations (adapted from reference [245] with permission from the PCCP Owner Societies).

Additionally, the substituent moiety can also affect the electrochemical stability of TEMPO derivatives. For instance, at high pH, AMT displays irreversible oxidation, possibly arising from oxidation of the amino group [233]. At moderate pH (4.63), degradation of the oxoammonium cation for 4-oxo-TEMPO is expected [233].

3) Electron-transfer kinetics of TEMPO derivatives

The kinetics of electrochemical behavior for TEMPO derivatives are of great importance for the potential applications of TEMPO derivatives [81]. As both the oxidation and reduction process of TEMPO derivatives exhibit diffusion-controlled behavior, the diffusion coefficient, D, thus can be determined by cyclic voltammetry in combination with Randles-Sevcik equation (Eq. 2.2) [81, 246–249]. Generally, the measured diffusion coefficients for the oxidation process of TEMPO derivatives in aqueous solution (pH = 7) are on the order of 10^{-5}–10^{-6} cm^2 s^{-1} [246, 248, 250]. Whereas diffusion coefficients in low viscosity organic solvents, like MeCN, are typically in the regime of 10^{-5} cm^2 s^{-1} [81], and in high viscosity media, like ionic liquids, are around 10^{-7} cm^2 s^{-1} [247, 249]. Compared with the oxidation process of TEMPO derivatives, the diffusion coefficients for the reduction process are typically slower, for instance, 10^{-7} cm^2 s^{-1} in ionic liquids, which is one order less than the oxidation process [249].

$$i_p = 0.4463nFAC\left(\frac{nF\nu D}{RT}\right)^{\frac{1}{2}} \tag{2.2}$$

Where i_p refers to the current maximum in amps, n denotes to number of electrons transferred in the redox event, A refers to the electrode area in cm^2, F is Faraday constant in C mol^{-1}, D is the diffusion coefficient in cm^2 s^{-1}, C refers to the concentration in mol cm^{-3}, ν refers to scan rate in V s^{-1}, R is gas constant in J K^{-1} mol^{-1}, T refers to the temperature in K.

The heterogeneous or standard electron-transfer rate constant (k^0) can be estimated by the Nicholson method [81, 249]. For the oxidation process, it is reported to be $\sim 10^{-3}$ cm s^{-1} in aqueous solution (pH = 7) [246, 248], 10^{-1}–10^{-2} cm s^{-1} in organic electrolyte [81], and 10^{-4}–10^{-5} cm s^{-1} in ionic liquids [249]. For the reduction process, k^0 is relatively slow with k^0 being one or two orders of magnitude less in comparison to the oxidation process [249].

2.2.2. Synthetic Approaches Towards TEMPO-Containing Polymers

Generally, a radical polymer consists of a polymer backbone with populated organic stable radicals as pendant functional groups. When TEMPO is adopted as the persistent organic radical pendent group, this radical polymer is usually referred to as a TEMPO polymer, TEMPO-containing polymer or TEMPO functionalized polymer. Such polymers are generally prepared in three ways: (1) conventional post-oxidation of a polymer precursor decorated with N-H moieties instead of N-O moieties; (2) post-polymerization deprotection/oxidation of polyalkoxyamine precursors; (3) direct polymerization of a TEMPO bearing monomer; and (4) post-polymerization modification

(PPM) of a functionalized polymer with low-molecular-weight TEMPO derivatives.

1) Conventional post-oxidation method

TEMPO-containing polymers are generally prepared by either polymerizing TEMPO precursor monomers with secondary amine groups, followed by oxidation of the secondary amine moieties into nitroxide radicals. The first radical polymer synthesized by this means was introduced in 1972 [251]. As shown in Scheme 2.11, 4-methacryloylamino-or-oxy-2,2,6,6-tetramethylpiperidines were employed as precursor monomers, based on which homopolymers having piperidine groups in addition to copolymers containing either styrene or methyl methacrylate were prepared by free-radical polymerization (FRP), and then post-oxidized with hydrogen peroxide (H_2O_2) in the presence of ethylenediaminetetraacetic acid (EDTA) and sodium tungstate (Na_2WO_4), leading to the successful synthesis of TEMPO-containing homopolymers as well as copolymers. Aside from FRP [24, 251], the synthesis of polymer precursor with secondary amine moieties, e.g. poly(2,2,6,6-tetramethyl-4-piperidyl methacrylate) (PTMPMA), has also been successfully synthesized by living/controlled radical polymerization (LRP) techniques, such as ATRP [29, 252, 253], reversible addition–fragmentation chain transfer-mediated (RAFT) polymerization [29, 252, 254, 255] and single electron transfer-living radical polymerisation (SET-LRP) [25, 256], in order to acquire well-defined polymers with a narrow molar mass distribution [252]. The best results on number-average molecular weight (M_n) and dispersity ($Đ$) for PTMPMA synthesized from the aforementioned LRP techniques are listed in Table 2.1. NMP technique has also been attempted [252], however, it failed to achieve a controlled polymerization kinetics.
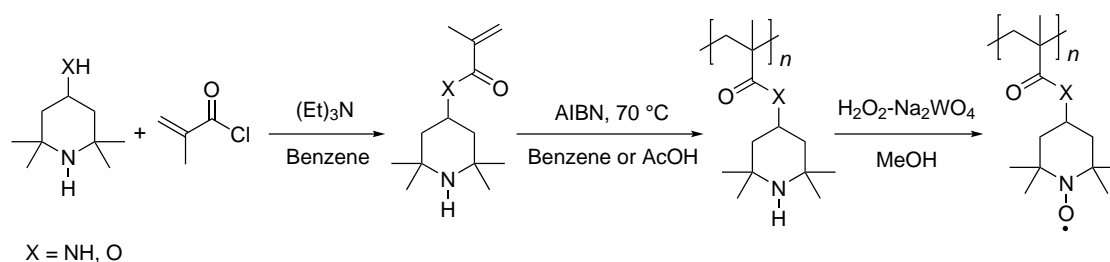
Scheme 2.11: Synthetic routes towards TEMPO based methacrylate and methacrylamide monomers and their respective polymers via conventional post-oxidation.

In terms of the oxidation process, there are two commonly used methods. The first one employs *m*-chloroperbenzoic acid (*m*CPBA) as oxidant and proceeds in an inert solvent such as dichloromethane (DCM) or chloroform [24]. The second one utilizes a $Na_2WO_4 \cdot 2H_2O$/EDTA/H_2O_2 combination and conducts in methanol [251]. With regard to PTMA, the former method was found to result in a narrow polymer dispersity ($Đ = 1.31$) compared with the latter ($Đ = 4.31$), which

Table 2.1.: M_n and $Đ$ based on size exclusion chromatography (SEC) data for PTMPMA/PTMA/PMPEOT synthesized by controlled radical polymerization techniques.

Sample	Polymerization technique	M_n (Kg mol^{-1})	$Đ$	Ref
PTMPMA[a]	RAFT	25.2	1.31	[252]
PTMPMA[b]	ATRP	48.2	1.28	[253]
PTMA[c]	SEC-LRP	131.6	1.35	[25]
PMPEOT[d]	ATRP	55.2	1.20	[217]

SEC were carried out in dimethylacetamide (DMAc), chloroform/2-propanol/triethylamine (94/2/4), THF and THF for a-d, respectively; Data were analyzed with polystyrene (PS), poly(methyl methacrylate) (PMMA), PS and PMMA as standards for a-d, respectively.

may result from the relatively complex work-up procedure for the former method to remove the by-product *m*-chlorobenzoic acid. Moreover, PTMA synthesized from the former method (oxidized with *m*CPBA) showed a slightly lower radical concentration than the latter, which may due to side reactions between *m*CPBA and nitroxides [255, 257, 258]. Besides, both methods suffered from incomplete oxidation of amino groups into nitroxide moieties and sometimes cross-linking of PTMA may accompany [25, 27]. Therefore, post-oxidation results in PTMA with TEMPO content typically in the range of 60–80% as calculated via EPR measurement [24, 25, 29, 254].

2) Post-polymerization deprotection/oxidation method

Similar to the conventional post-oxidation method, post-polymerization deprotection/oxidation is also accomplished in two steps. First, polymerization of a protected TEMPO monomer is applied to obtain a polymer precursor. Then, this polymer precursor is deprotected /oxidized to attain the final TEMPO-containing polymer. Using alkoxyamines as protected precursor groups for nitroxides, Eckert and co-workers [217] presented an approach toward PTMA. As depicted in Scheme 2.12A, PTMA was obtained from oxidative cleavage of the C-ON bonds on the precursor polymer, i.e. polyMPEOT (PMPEOT), which was polymerized from 4-methacryloyloxy-1-((1'-phenylethyl)oxy)-2,2,6,6-tetramethylpiperidine (MPEOT, 1) via ATRP. Since the nitroxide is protected by alkoxyamine, ATRP of MPEOT proceeded straightforwardly without nitroxide exchange reaction with Br happened, and the isolated PMPEOT exhibited a high number-average molecular weight of 55.2 kDa (see Table 2.1). Recently, a thermally robust methoxyamine-protecting group was employed for the synthesis of PTMA by Blinco and co-workers [259], as depicted in Scheme 2.12B. Facile polymerization of the corresponding monomer, i.e. methyl-TEMPO methacrylate, has been demonstrated via FRP and RAFT polymerization. Cleavage of the methoxyamine functionality was accomplished by oxidative treatment with *m*CPBA.
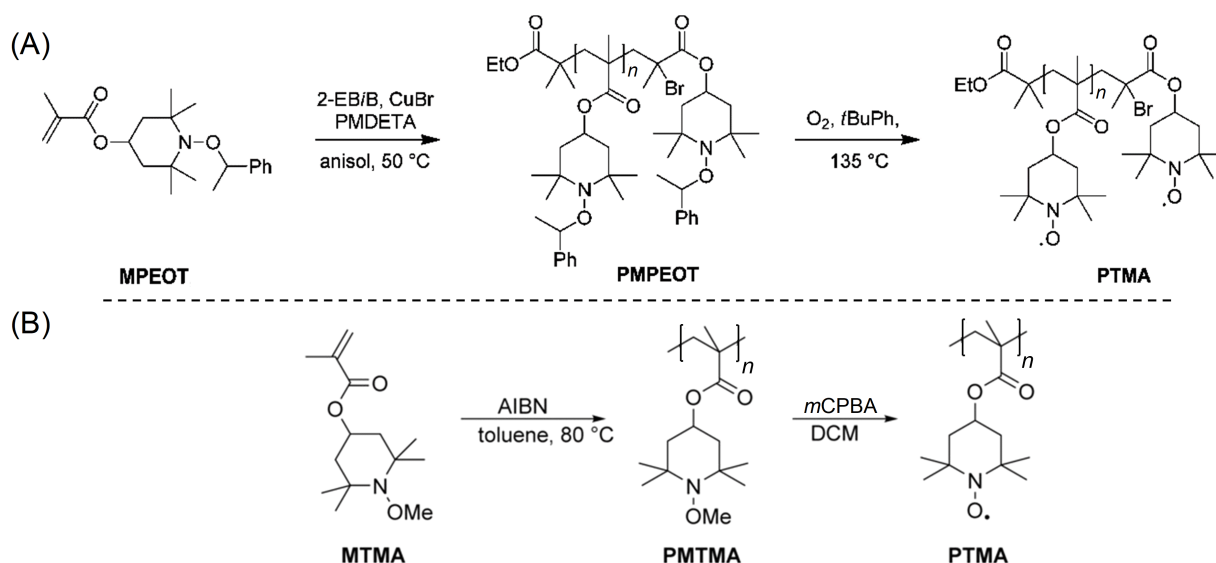
Scheme 2.12: Synthesis of PTMA via post-polymerization deprotection with (A) alkoxyamine and (B) methoxyamine protecting groups.

3) Direct polymerization of TEMPO monomers

Direct polymerization of TEMPO monomers represents a straightforward methodology to obtain TEMPO-containing polymers. So far, several polymerization methods have been applied, such as ionic polymerization and metathesis polymerization.

i) Ionic polymerization

As ionic polymerization does not involve any radical species during the polymerization process, nitroxide functionalities incorporated in the monomers could remain intact. The widely used ionic polymerization techniques for the direct synthesis of TEMPO-containing polymers include carbanionic, oxyanionic, metal-coordinated anionic and cationic polymerizations.

The first TEMPO-containing polymer, to be precise, oligomer ($M_n = 1050–1950$ g mol^{-1}), was synthesized via carbanionic polymerization in 1967 [260]. In the presence of phenylmagnesium bromide, a Grignard reagent, PTMA was directly synthesized from 2,2,6,6-tetramethyl-4-piperidyl methacrylate (TMPMA) (see Scheme 2.13, path 1). This method was later found to result in a partially cross-linked polymer structure, which may result from side reaction between the Grignard reagent and the nitroxide radical center [98].

Both *sec*-butyllithium and 1,1-diphenylhexyllithium (DPHLi) have been reported as initiators for the anionic polymerization of PTMA (Scheme 2.13, path 2 and 3) [27, 261]. However, carbanion attacking radical centers of nitroxides were observed in both cases, resulting in relatively low

TEMPO contents, which were 0.81 and 0.70 radicals per repeating unit, respectively. Owing to the moderate nucleophilicity, bulky structure and reduced basicity, methyl methacrylate-capped 1,1-diphenylhexyllithium (DPHLi/MMA) was found to be an appropriate initiator for the carbanionic polymerization of TMPMA, which can effectively suppress the side reaction with the nitroxide radical moiety (Scheme 2.13, path 4) [27]. The resulting PTMA showed a high TEMPO content of 99% with number-average molecular weight of 19 kDa and the dispersity of 1.04. In similar manner, the initiator lithium,(3-methyl-1-phenylpentyl)benzene capped with *tert*-butyl methacrylate also facilitated the anionic polymerization of TMPMA, resulting in PTMA with M_n = 13.5 kDa and $Đ$ = 1.04 [262].
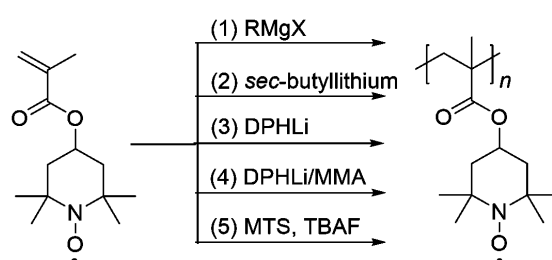
Scheme 2.13: Direct synthetic methods (1-5) of PTMA via carbanionic and group-transfer polymerizations, respectively.

Group-transfer polymerization (GTP), which can be categorized as a type of anionic polymerization, is another reported method for the synthesis of PTMA (Scheme 2.13, path 5) [26]. Although (1-methoxy-2-methyl-1-propenyloxy)-trimethylsilane (MTS) as an initiator in conjunction with tetrabutylammonium fluoride (TBFA) as catalyst worked excellently for GTP of benzyl methacrylate ($Đ < 1.1$). Whereas the GTP of TMPMA did not proceed in a living/controlled manner. The GTP-PTMA showed a number-average molecular weight of 18 kDa and a dispersity of 3.15. Nonetheless, the TEMPO content was determined to be 100% by UV/vis spectroscopy. Moreover, it is revealed that there is a correlation between spectroelectrochemical behavior and microstructural features of GTP-PTMA, which consists of 84% of isotactic triads, 12% of heterotactic triads, and 4% of syndiotactic triads, respectively [28]. A cross-linked copolymer with ethylene glycol dimethacrylate was also attainable in $\sim$ 69% yield with some low molecular weight, non-cross-linked PTMA involved.

Ionic polymerization of TEMPO monomers with epoxy or oxetanyl functionalities has also been attempted. As early as 1993, Endo et al. [263] investigated both the anionic and cationic polymerizaiton of 4-(glycidyloxy)-2,2,6,6-tetramethylpiperidine-1-oxyl (4-glycidyloxy-TEMPO). With potassium *tert*-butoxide (^{t}BuOK) as an initiator (Scheme 2.14, path 1), the anionic polymerization in bulk resulted in polymers with TEMPO contents close to 100%, although

the resulting polymer exhibited a low number-average molecular weight, which was below 6.6 kDa. Similar to the anionic homopolymerization, copolymerization of 4-glycidyloxy-TEMPO with equimolar glycidyl phenyl ether was also attempted in the same study with a 91% yield (M_n = 6.1 kDa). Whereas, the cationic polymerization was not successful with only < 5% conversion obtained. Following the same path in bulk, Nishide et al. [148] later synthesized a TEMPO-containing polymer with high number-average molecular weight (M_n = 32 kDa, $Đ$ = 1.8) and high radical content (84%) in relatively good yield (88%). The obtained polymer was insoluble in any common organic solvents but slightly swollen in chloroform, tetrahydrofuran (THF), and the electrolyte solution (e.g. 1 M $LiPF_6$ in EC/DMC). Similar anionic polymerization was carried out in solution with THF as the solvent. The resulting polymer exhibited a TEMPO content (90%) and a narrow polymer dispersity ($Đ$ = 1.4), but in poor yield (57%) with a relatively low number-average molecular weight (M_n = 3.6 kDa), compared with the bulk one. With $ZnEt_2$/H_2O adopted as an initiator (Scheme 2.14, path 2), the coordinated anionic ring-opening polymerization in bulk was allowed to react at room temperature, however, no apparent improvement on yield (62%), number-average molecular weight (M_n = 25 kDa, $Đ$ = 2.1) and radical content (62%) was observed compared to the anionic polymerization in bulk with ^{t}BuOK as an initiator [264].
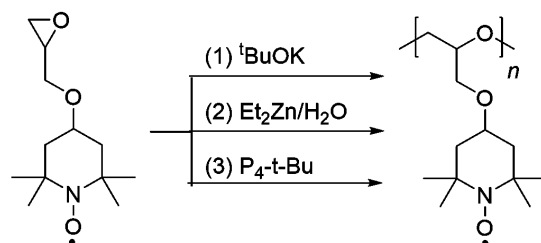
Scheme 2.14: Reported anionic polymerization methods (1-3) of 4-glycidyloxy-TEMPO.

By utilizing potassium 2-(2-methoxyethoxyl) ethoxide as an initiator, anionic copolymerization of 4-glycidyloxy-TEMPO and ethylene oxide were accomplished by Jia and co-workers with a yield of 95% [265]. The resulting copolymer exhibited a number-average molecular weight of 5.4 kDa when the molar ratio between 4-glycidyloxy-TEMPO and ethylene oxide was $\sim$ 1:5. Via anionic ring-opening polymerization of 4-glycidyloxy-TEMPO and 1,4-butanediol diglycidyl ether, Nishide and co-workers [90] synthesized a cross-linked polymer bearing TEMPO pendant groups at room temperature by adopting P_4-t-Bu, a strong base with low nucleophilicity, together in the presence of an alcohol (e.g. 3-phenyl-1-propanol, pentaerythritol) as a monofunctional and a quadruply-branched initiator. Besides, with P_4-t-Bu as the initiator (Scheme 2.14, path 3), homopolymerization of 4-glycidyloxy TEMPO was also achievable, while showing a relatively low yield (80%) compared with the copolymer synthesis. The resulting homopolymer exhibited a

number-average molecular weight of 9.3 kDa ($Đ = 1.5$).

In terms of the TEMPO-substituted oxetanes, anionic ring-opening polymerization is incompatible, as it requires heating up to 180 °C arising from the smaller ring-distortion energies, and consequently, resulting in thermal decomposition of nitroxides. Attempts on a cationic polymerization with Lewis acidic BF_3 or other cationic initiators were also made but no promising results were obtained, due to undesired oxidation of the radical pendants (i.e. TEMPO) [264].

Apart from cyclic ether monomers, ionic polymerization has also been applied to 2,2,6,6-tetramethylpiperidine-*N*-oxyl-4-vinyl ether (4-vinyloxyl-TEMPO) with $BF_3 \cdot Et_2O$ as an initiator [149] (see Scheme 2.15). The resulting polymer, i.e. poly(2,2,6,6-tetramethylpiperidine-*N*-oxyl-4-vinyl ether) (PTVE), was hardly soluble in organic solvents, such as THF, chloroform, and DMF. Nevertheless, the TEMPO content within the polymer was determined to be 100%, which preserved intact for more than a year when stored under aerobic conditions at room temperature.
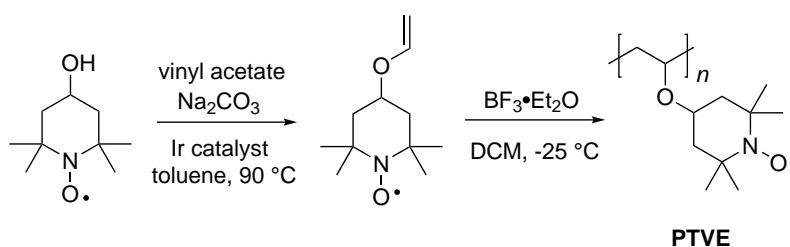
Scheme 2.15: Synthesis of 4-vinyloxyl-TEMPO and its cationic polymerization.

ii) Ring-opening metathesis polymerization(ROMP)

ROMP is another polymerization technique that does not involve any radical initiating or propagating species, therefore it is considered as one of the promising candidates for direct polymerization of TEMPO monomers. Cyclic-ene substituted TEMPO derivatives, such as TEMPO-containing norbornenes and 7-oxanorbornenes, are the desirable monomers suitable for ROMP.

As shown in Scheme 2.16, a series of TEMPO-containing monomers have been polymerized with ruthenium-based metathesis catalysts (Grubbs catalyst, second- and third-generation) via ROMP [144, 266–269]. Among them, poly[2,3-bis(2',2',6',6'-tetramethylpiperidin-1'-oxyl-4'-oxycarbonyl)-5-norbornene] (PTNB) is the first reported and most investigated one [144]. Its polymerization proceeded very fast under mild conditions (30 °C in DCM within 45 min) in 59% (*endo, exo*) and quantitative (*endo, endo*) yields. The obtained polymer was soluble and exhibited a molecular weight of 185 kDa (*endo, exo*) and 137 kDa (*endo, endo*), with dispersity being 1.92 and 2.31, respectively. Katsumata et al. [268] later revealed that unlike its other *endo-endo* and *endo-exo*
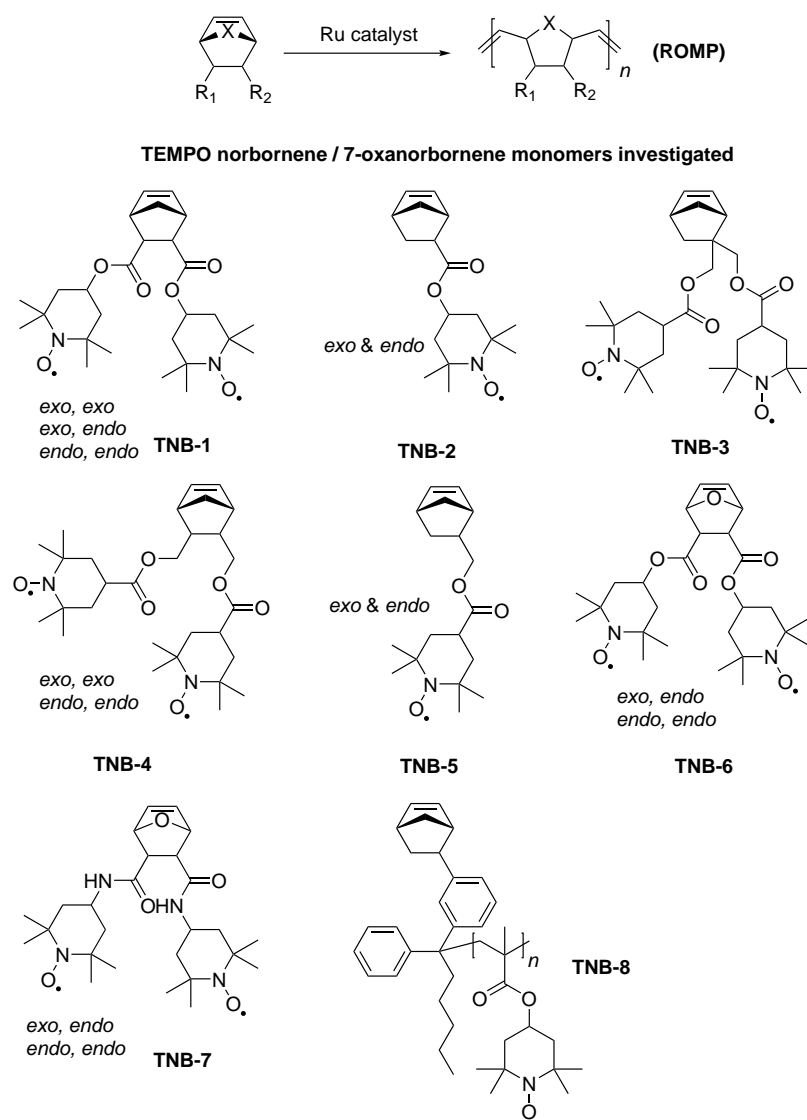
Scheme 2.16: TEMPO-containing norbornenes and 7-oxanorbornenes applicable in ring-opening metathesis polymerization (ROMP).

isomers, ROMP of 5-norbornene-*exo*,*exo*-2,3-dicarboxylic acid bis[4-(2,2,6,6-tetramethylpiperidine-1-oxy)] ester resulted in a polymer insoluble in any common organic solvents, although its TEMPO content was slightly higher (2.0 ± 0.1) than the other two isomers. With regard to TNB-2 to TNB-5, insoluble polymer gels were obtained in the end due to very high molecular weight or cross-linking side reaction.

Using norbornene-substituted diphenylhexyllithium as an initiator, Nishide and co-workers synthesized a norbornene-terminated PTMA macro-monomer (TNB-8) via ionic polymerization, followed by ROMP with Grubbs third-generation catalyst (Dichloro[1,3-bis(2,4,6-trimethylphenyl)-2-

imidazolidinylidene](benzylidene)bis(3-bromopyridine)ruthenium(II)), and finally acquired TEMPO-crowded bottlebrush polymers [267]. Additionally, copolymerization of TNB-2 with glycol-modified norbornene, TNB-1 with aniline-substituted norbornene or imidazolium-containing norbornene, etc., have also been attempted for various applications [270–273] such as supported catalyst for alcohol oxidation [270], efficient electrical conducting path [271] and organic resistive memory material [272].

On similar lines, TEMPO-containing 7-oxanorbornene monomers, e.g. TNB-6 and TNB-7, were polymerized via ROMP using a ruthenium carbene catalyst. Monomers TNB-6 (*exo, endo*) and TNB-7 (*exo, endo*) gave polymers with high number-average molecular weights of 80.1 kDa and 112 kDa in 85 and 96% yields, respectively. Whereas, the polymerization of their *endo-endo* isomers did not afford high molecular weight polymers even at high monomer concentration (2M), especially in the case of TNB-7 (*endo, endo*), owing to the strong steric selectivity of ROMP with ruthenium-based catalyst.

iii) Transition metal catalyzed polymerization of TEMPO substituted acetylenes and alkenes

Apart from ROMP polymerizations, Rhodium-based transition metal catalyst plays an important role in the direct polymerization of TEMPO-containing acetylenes and alkenes, as it is more robust than other transition metal catalyst systems such as W and Mo based ones, in the presence of a nitroxyl radical [274]. Similar to ROMP, the reaction condition for Rhodium catalyzed polymerization is rather mild (30 °C in dry toluene, chloroform, DCM or THF for 24 hr. with $(nbd)Rh^+[(\eta^6\text{-Ph})B\text{-Ph}_3]$ or $[(nbd)RhCl]_2\text{-Et}_3N$.

As depicted in Scheme 2.17, a variety of TEMPO substituted acetylenes and alkenes have been subjected to transition metal catalyzed polymerization with Rhodium-based transition metal catalyst, e.g. $(nbd)Rh^+[(\eta^6\text{-Ph})B\text{-Ph}_3]$, $[(nbd)RhCl]_2\text{-Et}_3N$ or $[RhCl(COD)]_2$. [144, 274–276]. TA-1 was first attempted by Dulog et al. [274] with $[RhCl(COD)]_2$ at 70 °C in dry methanol (MeOH). The resulting polymer exhibited a low number-average molecular weight of 2.3 kDa (Đ = 1.30) with a TEMPO content of 79%. Among mono TEMPO monomers, TA-3 and TA-5 represent the most successful ones with the resulting polymers exhibiting number-average molecular weights of 47 kDa (Đ = 2.01) in 66% yield and 92.7 kDa (Đ = 2.91) in 82% yield, respectively [144, 275]. Polymerization of TA-7 (X = NH), which has a long spacer with amide linkage compared with TA5, did not yield a polymer with $(nbd)Rh^+[(\eta^6\text{-Ph})B\text{-Ph}_3]$, while a low number-average molecular weight (M_n = 7.5 kDa) oligomer mixture was obtained when $[(nbd)RhCl]_2\text{-Et}_3N$) was adopted [276]. In terms of monomers containing two or multi TEMPO
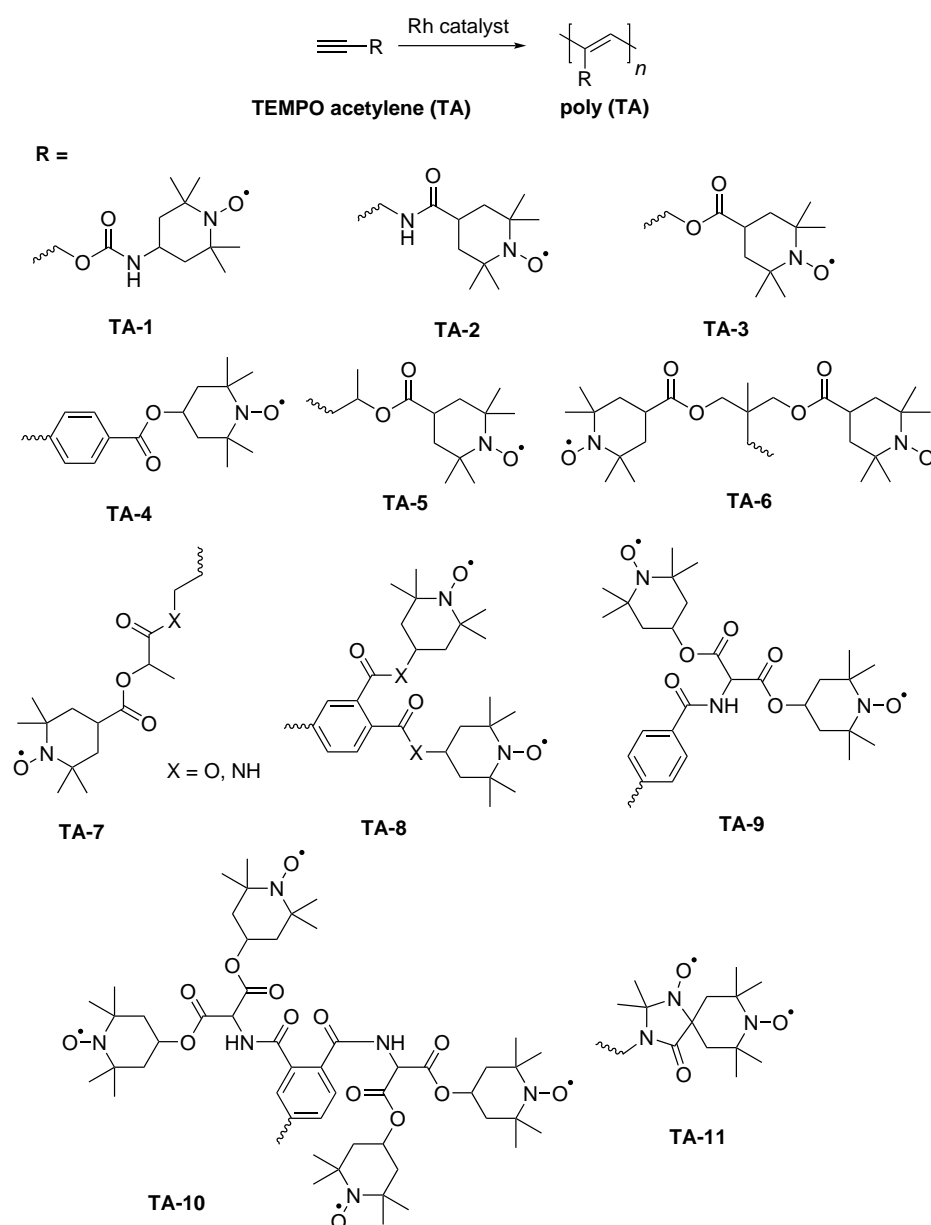
Scheme 2.17: Transition metal catalyzed polymerization of TEMPO-containing acetylenes.

moieties, polymers with number-average molecular weights of 10–137 kDa in 62–99% yield were obtained except for TA-8 with ester functionality, which resulted in gelation similar to the case of TA-2 [275].

Polymerization of spirobisnitroxide acetylene and alkene (TA-11) with Rhodium-based transition metal catalyst was also attempted. Polymerization of the acetylene monomer produced a TEMPO-containing polymer with M_n = 42.9 kDa ($Đ$ = 2.7) in 89% yield. With the addition of a cross-linker (*N,N'*-diprop-2-ynyl-oxalamide) to the alkene monomer system, a polymer gel was

afforded in quantitative conversion [277].

4) Post-polymerization modification

Post-polymerization modification (PPM) of activated ester-containing polymers has emerged as an alternative and versatile route to equip polymers with numerous functional groups including stable radicals [32]. Indeed, early in the 1970s, Kálal and co-workers [33, 34] were the first who employed this strategy in preparing nitroxide-containing polymers, by utilizing a series of copolymers of *N*-(2-hydroxypropyl)methacrylamide with the activated ester monomers 4-nitrophenyl esters (4-NPE) of ω-methacryloylamino acids, which were subsequently converted with 4-amino-2,2,6,6-tetramethyl-piperidinyloxyl (4-amino-TEMPO) yielding the spin labeled copolymers. However, the yield of aminolysis was very low with 60-80%, probably owing to the steric inaccessibility of the 4-nitrophenol ester of methacrylic acid in the copolymer. Next, Bergbreiter et al. [35] incorporated nitroxyl groups into poly(*N*-isopropylacrylamide) (PNIPAM) copolymers to generate 'smart' polyacrylamide copolymers showing redox-sensitive LCST (the lower critical solution temperature) behavior by substitution reaction of polymers derived from *N*-acryloxysuccinimide (NAS) monomers, as shown in Scheme 2.18A. While this post-polymerization strategy is considerably mild, it is often accompanied by side reactions, such as succinimide ring-opening or the formation of *N*-substituted glutarimide groups [36]. Alternatively, pentafluorophenyl (PFP) esters have recently become an increasingly utilized reactive moiety in the modification of polymers with radicals by preserving the integrity of these pendant radicals and polymer backbone. For instance, the group of Théato has recently modified poly(pentafluorophenyl acrylate) (PPFPA) prepared by RAFT polymerization with 4-amino-TEMPO to obtain triple stimuli-responsive copolymers that featured thermo-, light- and redox-responsive characteristics [37] (Scheme 2.18B). Likewise, Suga and colleagues [38] utilized the same PPFPA-motif to prepare a copolymer featuring TEMPO and ionic imidazolium sites, which were further evaluated as organic resistive memory devices.

Poly(acrylic acid) (PAA) is another functional polymer that can be post modified with TEMPO derivatives, such as 4-amino-TEMPO [278–280], 4-hydroxy-TEMPO [281] and 4-glycidyloxy-TEMPO [282]. For instance, Pelton et al. [279] grafted TEMPO moieties onto PAA in the presence of 1-ethyl-3-(3-(dimethylamino)propyl)carbodiimide (EDC) and *N*-hydroxysulfosuccinimide sodium salt (sulfo-NHS), as depicted in Scheme 2.18C. The final TEMPO-containing polymer is an amphoteric polymer, which is soluble at pH values less than 2 and above 4.5. Besides, it exhibited a reversible phase separation under acid conditions (pH = 2–4.5), which is suggested to be driven by electrostatically driven association of polymer molecules. Besides, cellulose derivatives can also be functionalized into TEMPO-containing polymers. Masuda et al. [155] modified ethylcellulose and cellulose acetate with 4-carboxy-2,2,6,6-tetramethylpiperidine 1-oxyl (4-carboxy-

TEMPO) in the presence of EDC·HCl (condensation agent) and 4-dimethylaminopyridine (DMAP, base) and obtained TEMPO-containing cellulose derivatives with high TEMPO content, which is 75% and 99%, respectively (Scheme 2.18D). Recently, Zhang and co-workers [283] converted poly(ethylene-alt-maleic anhydride) (PEM) to TEMPO-containing polymer via transesterification with 4-hydroxy-TEMPO, as shown in Scheme 2.18E. The resulting polymer is hardly soluble in carbonate-based electrolyte, but easily soluble in THF and NMP; moreover, the Curie-Weiss plots revealed a TEMPO content of 97%, making it an extraordinary candidate as the cathode material. Indeed, this material delivered a capacity of 88 mAh g^{-1} and exhibited an excellent rate capacity with 94% retention after 1000 cycles.

Besides, linear poly(ethylenimine) (LPEI) and poly(methylhydrosiloxane) (PMHS) can also act as functional polymer for PPM, as depicted in Scheme 2.18F and 2.18G. For example, Minteer et al. [284] prepared a TEMPO-containing polymer TEMPO-LPEI by simply mixing LPEI with 4-glycidyloxy-TEMPO at room temperature. This TEMPO-LPEI polymer was then cross-linked onto the surface of a carbon electrode and used for electrocatalytic oxidation of alcohols, which resulted in a dramatic enhancement in the catalytic current density when compared with an analogous homogeneous TEMPO catalyst. Suguro et.al [150] modified PMHS with 4-allyl-2,2,6,6-tetramethylpiperidine-*N*-oxyl ether (4-allyl-TEMPO ether) and 4-hydroxy-TEMPO, respectively, in the presence of a platinum- or rhodium-catalyst. The hydrosilylation ratio of PMHS with 4-allyl-TEMPO-ether was determined to be 76%, and the dehydrogenative alcoholysis ratio with 4-hydroxy-TEMPO was 77%, according to elemental analysis.
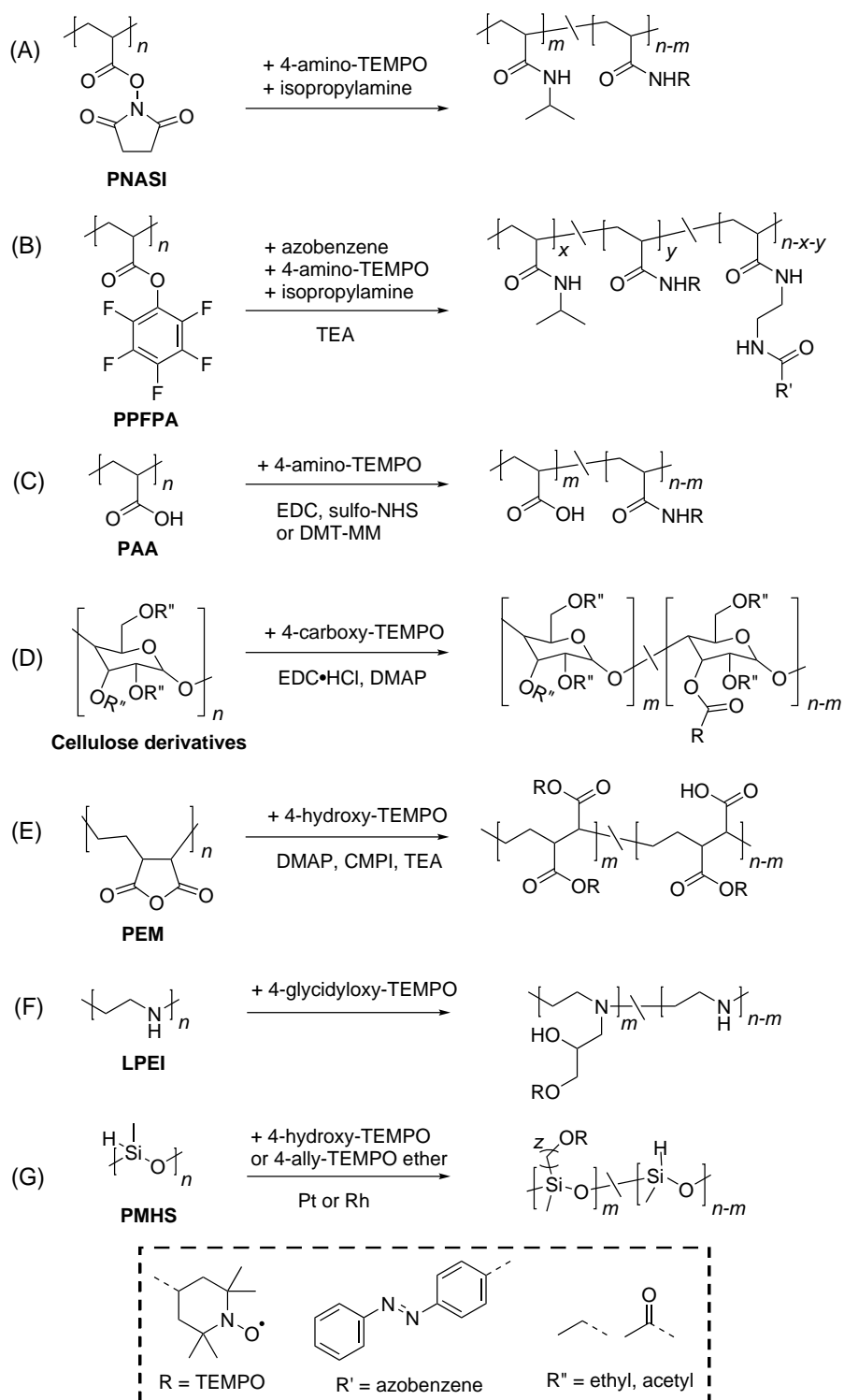
Scheme 2.18: Post-polymerization modification for the synthesis of TEMPO-containing polymers with (A) PNASI, (B) PPFPA, (C) PAA), (D) Cellulose derivatives, (E) PEM, (F) LPEI and (G) PMHS as functional polymers.

2.2.3. TEMPO-Containing Polymers as Electrode Materials

By virtue of the stable and reversible redox reaction between nitroxide and oxoammonium, TEMPO-containing polymers that are endowed with the unique characteristics of nitroxide, have thus found application in ORB as active cathode materials [17]. An efficient battery material is expected to provide high energy density, fast charge and discharge capability, and long cycle life with cost-effective feature [8, 9, 51, 52]. To improve the battery performance concerning the aforementioned properties, great efforts have been made in preparing various TEMPO-containing polymers as electrode materials including ingenious composite architecture with the toolbox of chemistry [97, 285].

2.2.3.1. TEMPO-Containing Polymers Aimed at High Energy Density

Regarding an electrode material, e.g. TEMPO-containing polymer, energy density is proportional to the theoretical capacity and inversely correlated with the mass of the material. Theoretically, tuning the structure of the redox polymer by incorporating as much redox sites within a polymer as possible and adopting low-molecular-weight repeat unit would lead to a high energy density. In terms of a electrode composite, which consists of active material, binder and conductive agent, energy density also depends on mass of the binder and conductive agent. Therefore, decreasing the amount of binder and conductive agent involved in the cell should help in improving energy density. In respect of a whole cell, which contains not only electrodes, but also electrolyte solution, energy density is thus related to the amount of electrolyte solution as well. Hence, methods to minimize the volume or amount of electrolyte solution would be desirable. Based on the design principle, four categories can be classified, as discussed in the following sections.

1) Improving TEMPO content within the polymer

Tremendous efforts have been made in search for a suitable synthetic methodology to convert or preserve as much TEMPO moieties as possible. Since conventional post-oxidation route results in a polymer with typically 60–80% TEMPO content (based on EPR measurement) [24, 25, 29, 254], direct polymerization such as ionic and group transfer polymerization [26, 27], post-deprotection [217, 259] and PPM [286] were accordingly attempted, resulting in TEMPO contents that exceed 90% within the corresponding polymers. In terms of the detailed information for each synthetic method are found in section 1.2.2.

Incorporating more than one TEMPO moiety per repeating unit is another strategy. For instance,

Masuda and co-workers [144, 268] equipped two TEMPO moieties on one norbornene-based monomer (TNB-1) and polymerized it via ROMP, leading to a polymer (PTNB) containing approximately two TEMPO moieties in each repeating unit. When used as cathode active material, this polymer delivered a capacity of 109 mAh g^{-1}, which reached the theoretical value.

2) Adopting simple polymeric structures

Polymers having a simple structure are favorable as cathode materials [144, 149, 268], owing to their relatively low molecular weight of the repeating unit (Figure 2.16). Nishide and co-workers [149, 287] synthesized PTVE via cationic polymerization and used it as cathode active material in ORB. As PTVE is comprised of the simplest backbone, i.e. vinyl, in general purpose, and contains one of the simplest linkages between the polymer chain and TEMPO moieties, it exhibits a much higher theoretical capacity (135 mAh g^{-1}) than other reported TEMPO-containing polymers, as shown in (Figure 2.16). Indeed, it delivered a discharge capacity of 114 mAh g^{-1} at a current density of 0.1 mA cm^{-2} with lithium anode, and approximately 131 mAh g^{-1} with Zinc anode in an aqueous electrolyte at a C-rate of 60 C.
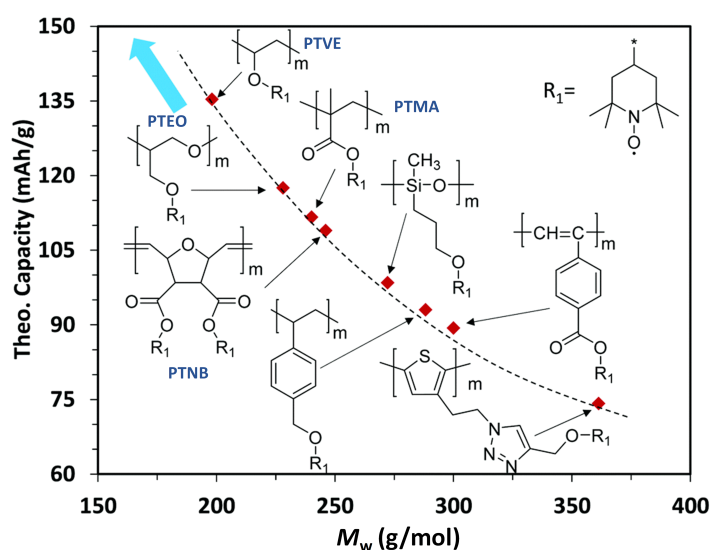
Figure 2.16.: The correlation between theoretical capacities and molecular weights of the repeating units of diverse TEMPO-containing polymers (reproduced from ref [285] with permission from The Royal Society of Chemistry).

3) Fabricating binder-free electrodes

A TEMPO-containing polymer that can act as both active material and binder is also favorable. To this end, many researchers made efforts on fabricating binder-free electrodes. One strategy is to anchor polymer brushes on surfaces via *in situ* polymerization method. For instance, Lee et

al. [114] grafted PTMA brushes onto silica nanoparticles and prepared a binder-free electrode comprising of PTMA brushes/silica nanoparticles and carbon black. The immobilized PTMA brush exhibited a discharge capacity of 84.9–111.1 mAh g^{-1} at 10 C rate and capacity retention of 96.3% after 300 cycles resulting from the insoluble nature of PTMA brushes/SiO$_2$. Kim et al. [102] took another step and fabricated a flexible electrode film by directly bonding PTMA onto a graphite paper via *in situ* polymerization and subsequent oxidation approach, achieving 100 wt.% active material loading without any additives. Together with polyimide-based gel electrolyte and lithium anode, the assembled full-battery displayed almost twice higher energy density (470 Wh kg^{-1}) than the commercial graphite/NCM (LiNi$_{1/3}$Co$_{1/3}$Mn$_{1/3}$O$_2$) battery. Another strategy is to incorporate the redox sites, i.e.TEMPO, into a polymer with a binding feature. For example, Zhang et al. [283] synthesized poly(ethylene-*alt*-TEMPO maleate) by attaching TEMPO to PEM whose analogue poly(isobutylene-*alt*-maleic anhydride) has been adopted as a binder in LIBs [288]. By blending this TEMPO-containing polymer with CB, they fabricated a binder-free cathode which showed a comparable electrochemical performance compared to the cathode with PVdF binder.

4) Switching to cation migration

As mentioned in section 1.1.1, during charging, nitroxide loses an electron and forms oxoammonium, in the meantime, anions in the electrolyte, e.g. PF$_6^-$ migrate to the positive electrode to maintain charge neutrality. Upon discharge, the process is reversed. Therefore, it is the anion migration during the charging-discharging process from the mechanism perspective, which is different from the rocking chair mechanism of LIBs. However, the anion migration results in a change in the salt concentration, hence, the excess amount of electrolyte salt is required for ionic conduction. To dissolve the excess amount of salt, a large volume of solvent is in demand, leading to a low energy density. Contrarily, cation migration helps to minimize the electrolyte volume, due to the "rocking-chair-type" mechanism (Scheme 2.19).

Inspired by the self-doping concept in conducting polymers, zwitterionic pendant design was proposed, as shown in Scheme 2.19. Anionic groups with a large potential window like sulfonate anion, and anionic groups having a high degree of dissociation such as TFSI$^-$ have been attempted to incorporate into polymeric structures of TEMPO-containing polymers [289–291]. For instance, TMPMA was copolymerized with potassium 4-styrenesulfonyl(trifluoromethanesulfonyl)imide, followed by oxidation of the precursor polymer to afford P(TMA-*ran*-TFSI). Owing to the self-charge compensation of TEMPO with TFSI– uniformly tethered to the polymer chain, the P(TMA-*co*-TFSI) layer electrode exhibited a high discharging voltage of 3.7 V and good rate performance with 83% capacity retention at 30 C relative to 5 C [291].

P (TMA-*ran*-TFSI)
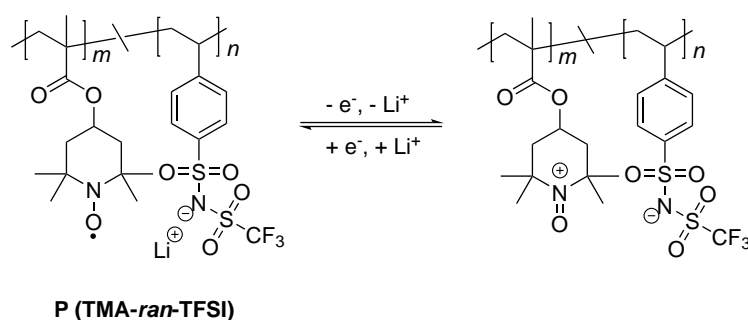
Scheme 2.19: Zwitterionic pendant design for "rocking-chair-type" cation migration.

2.2.3.2. TEMPO-containing Polymers Aimed at Good Rate Performance

1) Tuning electrical conductivity

Generally, radical polymers exhibit poor electrical conductivity [122, 292]. For instance, solid-state PTMA was shown to be electrically insulating (on the order of 10^{-11} S cm^{-1}) over the length scale of micrometers [29], although there are reports showing different values (10^{-5}–10^{-6} S cm^{-1}) [142, 254, 255, 293]. Owing to the flexible backbone and linker, poly(4-glycidyloxy-2,2,6,6-tetramethylpiperidine-1-oxyl) (PTEO) was found to have an electrical conductivity of up to 28 S cm^{-1} over channel lengths up to 600 nm, while a compromised conductivity ($\sim 10^{-4}$ S cm^{-1}) was observed at channel length scale over 700 nm [292]. The poor electrical conductivity would limit electron transfer during charging-discharging process, thus having a negative impact on the discharge capacity as well as the rate performance of the cell.

In order to construct efficient conductive pathways within the composite electrode and improve the electron transfer property of the active material, tremendous efforts have been involved in the aspect of ingenious molecular engineering as well as innovative processing solutions. Thoroughly mixing of TEMPO-containing polymers with conductive carbon for a homogeneous electrode composite is one of the options. Vald et al. [294] proposed a solvent-free, melt-polymerization process of TMPMA with *in situ*-incorporated carbon black nanoparticles, which results in a cross-linked, insoluble PTMA-carbon composite with carbon homogeneously dispersed at the nanoscale. The resulting electrode exhibited a competitive electrochemical performance at a low carbon content of 10 wt.%, achieving ca. 50% of its nominal capacity at 10 C rate with ca. 85% retained after 1200 cycles. Selecting conductive agents with high surface area and good conductivity is another path. Choi et al. [93] employed SWNTS as a conductive additive and wrapped it with PTMA at a molecular level through sonication in dichlorobenzene. This cathode exhibited a good rate capability with 70% capacity retention at a current density of 60 A g^{-1}.

Molecular-level anchoring of radical polymers on carbonaceous materials, such as CNTs [23, 89] and graphene [295, 296], has also been attempted. Gohy et al. [89] grafted PTMA onto multiwalled carbon nanotubes (MWCNTs) via SI-ATRP methods, and constructed a core-shell morphology with a MWCNTs mass loading of 40 wt.%. This MWCNT-*g*-PTMA showed a good capacity retention (87%) after 200 cycles at 2 C. In addition to the molecular-level anchoring of redox polymer onto CNTs or graphene through covalent bonds, efforts have also been made based on intramolecular π-π stacking by incorporating pyrene moieties into the redox polymeric structure [23, 253, 296]. Via NRC reaction, Jia and co-workers [23] attached pyrene moieties to PTMA polymer chain and utilized this TEMPO-pyrene copolymer as cathode active material with CNTs as the conductive agent in sodium-ion batteries. Benefiting from the structural merits (π-π stacking), the nanocomposite exhibited an excellent cyclability with 92% capacity retention at a high current density of 2.2 A g^{-1} after 6000 cycles, and remarkable rate capability (78 mA h g^{-1} at 5.5 A g^{-1}).

2) Tuning polymer mobility

Polymeric chains with a high degree of flexibility and mobility are suggested to facilitate redox sites contact by diffusion, and accordingly improve the rate capability of ORB [22, 136]. For instance, nitroxide-substituted polyether, i.e. PTEO, was synthesized via anionic ring-opening polymerization and used as a cathode-active material for a secondary battery [148]. Due to the flexible polyether backbone and its high compatibility with the carbonate-based electrolyte, the corresponding cathode maintained the same discharge capacity when the loading amount of active material increased from 10–20 wt.% to 30 wt.% even at 10 C rate, while PTMA-based cathode decreased.

Poly(2,2,6,6-teteramethylpiperidine-4-yl acrylamide) (PTAm), a hydrophilic radical polymer, has been fabricated into a fully organic-based rechargeable battery as a cathode active material, together with cross-linked polyviologen hydrogel or poly(tripyridiniomesitylene) (PTPM) acting as anode material, in an aqueous electrolyte [297]. This organic-based cell demonstrated extraordinary high-rate charging/discharging characteristics which allowed the battery to be fully charged and discharged in 30 s (120C) while maintaining long cycle stability (over 2000 cycles) with relatively high voltages (1.1 and 1.5 V, respectively). To enhance the swellability of PTAm in aqueous electrolytes and its stickiness to electrodes as well as other substrates, while maintaining the fast electron self-exchange feature, an acrylic acid moiety was introduced into the polymeric structure of PTAm via PPM (Scheme 2.18C) [280]. The resulting P(TAm-*ran*-AA) copolymer exhibited a two times higher diffusion coefficient (2.2×10^{-10} cm^2 s^{-1}) than the corresponding homopolymer, i.e. PTAm, in an aqueous solution (0.1 M NaCl), indicating an enhanced polymer chain mobility. The P(TAm-*ran*-AA) copolymer exhibited an exceptionally high current density

(up to 1 A cm^{-2}) and high areal capacity ($\sim$ 3 mAh cm^{-2}) when hybridized with SWCNTs and employed as a cathode in a totally organic-based secondary battery together with cross-linked poly(anthraquinone-substituted ethyleneimine) (PAQE)/SWCNTs hybrid as anode and 3 M NaCl as an electrolyte, as shown in Figure 2.17A [298]. Moreover, the P(TAm-*ran*-AA)/SWCNTs hybrid could also be fabricated into highly stretchable (over 700%) and ultrathin (100 nm) electronic devices capable of supplying large current density (0.4 mA cm^{-2} and 41 A g^{-1}) [299] (Figure 2.17B).
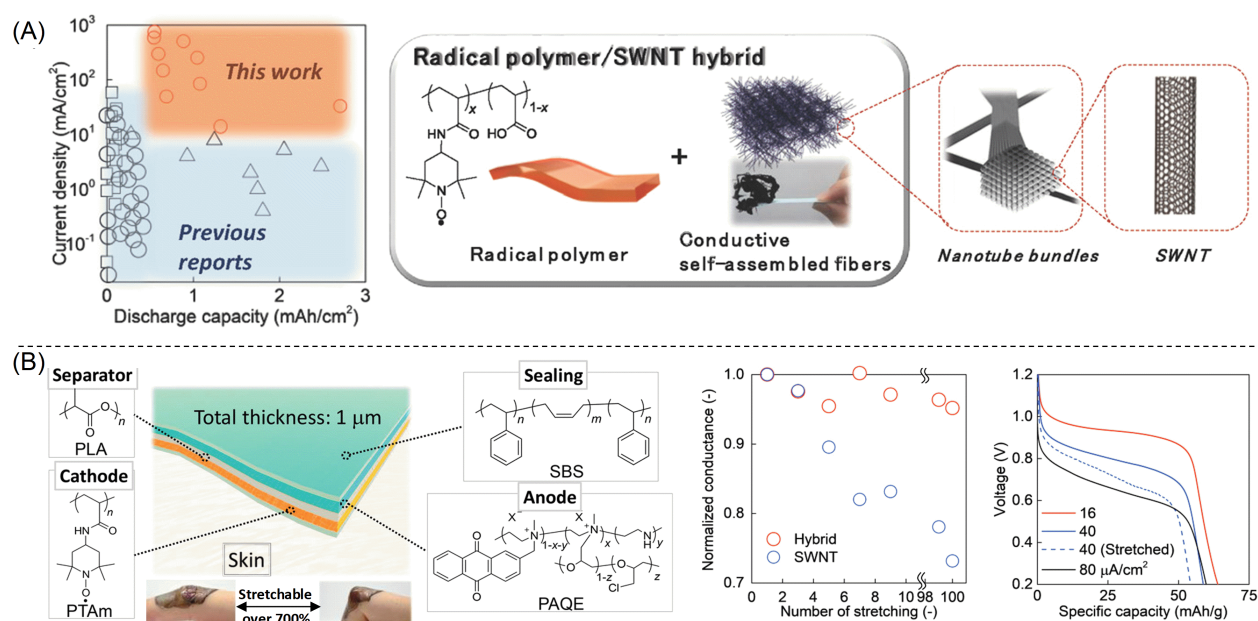
Figure 2.17.: (A) P(TAm-*ran*-AA)/SWCNTs hybrid electrode with ultrahigh output; (B) ultrathin flexible electronic devices with P(TAm-*ran*-AA)/SWCNTs hybrid cathode and PAQE/SWCNTs hybrid anode (adapted from ref [298, 299] with permissions from John Wiley & Sons, Inc.).

2.2.3.3. TEMPO-containing Polymers Aimed at Stable Cycle Life

One of the major drawbacks for TEMPO-containing polymers as electrode materials lies in their dissolution in conventional organic electrolytes, e.g. carbonate-based electrolytes, which might lead to rapid self-discharge and capacity loss. For instance, Nakahara et.al [31] found that 38% of the capacity for PTMA-based cathodes was disappeared after 1 week of storage, which they attributed to the shuttle effect of dissolved PTMA in the electrolyte. It is reported that compared to PTMA with a low number-average molecular weight (M_n = 1.6 kDa, $Đ$ = 1.1), PTMA with a high number-average molecular weight (M_n = 16 kDa, $Đ$ = 1.35) showed a higher specific discharge capacity (16%) and better cycling stability (65% retention at 30 C) due to their relatively low

solubility in the electrolyte [25].

In order to address the dissolution issue of the active material into electrolyte, diverse strategies have been developed. One strategy is to include non-dissolving blocks or moieties (in electrolyte) into the polymeric structures of TEMPO-containing polymers. For instance, Hauffman et al. [300] synthesized PTMA-*b*-poly(styrene) block copolymer with poor solubility in electrolyte (1M LiPF$_6$ in EC/DMC, v/v = 1/1) via ATRP. Zhang et al. [283] functionalized PEM with 4-hydroxy-TEMPO via transesterification and prepared a TEMPO-containing polymer that was hardly soluble in carbonate-based electrolyte, as a result of the partially close packing of TEMPO moieties on each adjacent carbon backbone. The corresponding cathode displayed a superior cycle life with only 6% capacity loss after 1000 cycles.

Constructing covalently cross-linked polymer networks is another path that can be accomplished by various synthetic methods, such as chemical cross-linking (during polymerization process) [26, 277, 301], photocross-linking [107] and thermal curing [59, 60, 108]. For example, Nishide and co-workers [107] photocross-linked PTNB with bis(azide) on an ITO substrate in the presence of a photo-mask, after subsequent workup, they obtained a patterned cross-linked film (50–500 nm), which preserved all its redox sites and was slightly swollen in organic solvents. In a similar manner, they photo-cross-linked PTNB with bis(azide) in a well-mixed solution with carbon nanofiber, and adopted the composite film (polymer thickness of 200 nm) as cathode in a rechargeable battery. The electrode exhibited excellent cycle stability with no significant deterioration in capacity after 1000 cycles. Lutkenhaus group [59] polymerized TMPMA with a relatively low amount (1%, 3% and 5%) of glycidyl methacrylate (GMA) which served as a cross-linker, and afterwards converted secondary amine into nitroxyl via post-oxidation. The obtained copolymers were then photocross-linked or thermally cured to be used as cathode active material. It is found that the sample with 3% GMA cross-linker and submitted to thermal curing led to the best capacity retention (99.6%), which was higher than uncross-linked ones by 5.6–13.6%. It is worth noting that the cross-linking polymer network prepared during polymerization might compromise the solution processability of the electrodes, while post-cross-linking, e.g. thermal curing, which can carry out after the polymer is mixed into the electrode slurry, is more desirable.

Immobilized TEMPO-containing polymers onto current collectors [100], porous substrates [104], nanoparticles [114] or conductive additives [23, 23, 89, 253, 295, 296, 296] were also attempted. For instance, Lee et al. [103] immobilized nitroxide polymer brushes on 3DOM polypyrrole through SI-ATRP. The resulting 3DOM nitroxide polymer brush cathodes delivered 40 times higher capacity than that of the planar electrode at 5 C rate and remained 96.1% of its capacity after 250 cycle. It should be noted that this strategy is versatile since it not only improves cycle stability but also

have other benefits. Firstly, it may avoid the addition of binder as discussed in section "Fabricating binder-free electrodes", and thus help gain a high energy density. Moreover, it may facilitate electron transfer by anchoring on carbonaceous material as mentioned in section "Tuning electrical conductivity", and consequently afford a high rate capability.

2.3. Post-Polymerization Modification via Activated Esters

The rapidly growing demand for functional polymers in diverse interdisciplinary areas of research has highlighted the need for modern synthetic tools to develop advanced polymers featuring a wealth of functional groups. Coincided with the development of modern chemistry, such as LRP and click reactions, post-polymerization modification (PPM), also termed as 'polymer analogous reaction', found its ample scope for abilities to facilely prepare functional polymers including copolymers, especially after the 1990s.

2.3.1. Brief Introduction of Post-Polymerization Modification

Modern polymer chemistry toolbox offers a variety of polymerization methods for the direct synthesis of functional polymers. Some even allow the precise control over polymer composition, molecular weight as well as architecture. However, there are still many functional groups that hinder polymerization or undergo side reactions during the polymerization process, which pose a significant challenge for the direct synthesis of polymers bearing specific functional groups. PPM, is an alternative and versatile approach to overcome these limitations. It is based on the direct polymerization or copolymerization of monomers bearing reactive groups that are inert towards the polymerization conditions but can be quantitatively substituted by a broad range of other functional groups in a subsequent reaction step. Apart from polymerizing monomers that are intractable for direct polymerization, polymers with diverse properties can also be obtained from the same starting polymer by reacting with different reagents or by varying the distribution of the second functional group along the polymer chain. Moreover, in combination with LRP techniques, such as ATRP, RAFT, NMP and SEC, PPM allows the fabrication of a wide variety of well-defined functional polymer architectures.

Many reactive groups, as well as several chemoselective coupling reactions, provided the foundation for PPM (Figure 2.18), such as activated ester, epoxide, anhydride, oxazoline, isocyanate groups, copper-catalyzed azide/alkyne cycloaddition (CuAAC), thiol-ene addition, Michael addition, Diels-

Alder cycloaddition, thio-dissulfide exchange, etc., due to their relatively high reactivity and selectivity, as well as quantitative conversions under mild conditions [302].
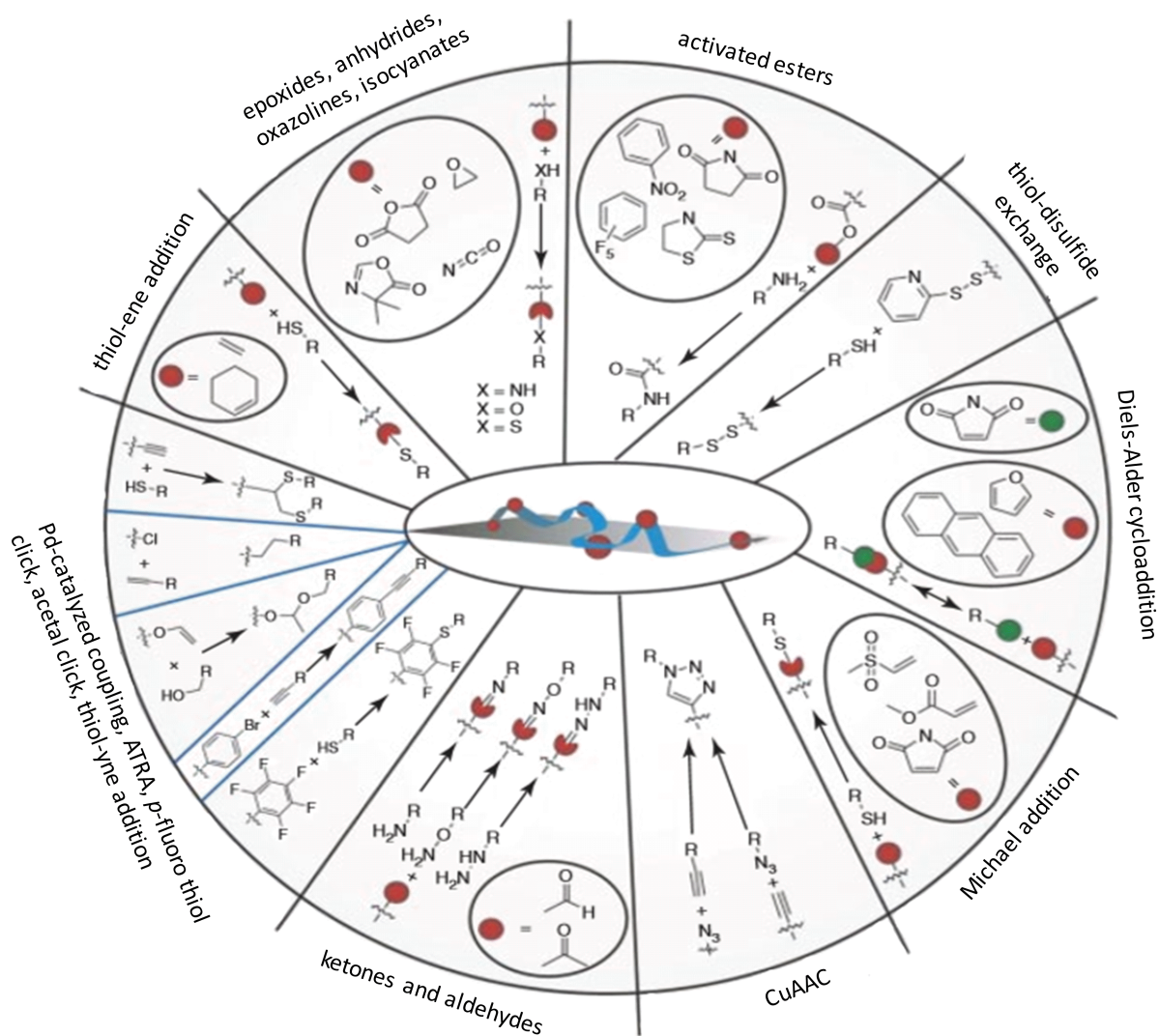
Figure 2.18.: Common reactions utilized in post-polymerization modification (adapted from ref [302] with permission from John Wiley & Sons, Inc.).

2.3.2. Post-Polymerization Modification via Activated Esters

Among the various reactions for PPM, nucleophilic ester cleavage (aminolysis and transesterification) based on activated esters is a conventional method with manifold advantages. First of all, there is abundant availability of most amines and alcohols from natural or commercial

sources when compared with other abiotic synthons (e.g. azides and alkynes). Furthermore, activated esters are useful derivatives for covalent attachment of functional amines based on a stable amide bond formation that is the basis of most biological systems. It is presumed that judicial application of this chemistry can potentially mimic the synthesis of many biostructures and help to comprehend their functions [32]. Similarly, degradable ester bond side chain linkage can also be maintained by PPM with alcohols [303]. Additionally, PPM via transesterification could expand the pool of functional groups attached to the polymer, such as acids, aldehydes and α, β-unsaturated carbonyl derivatives, due to the good tolerance and coexistence of alcohols with those functional groups [303]. Last but not least, it does not involve toxic metal catalysts during the PPM process, and thus is promising for biomedical applications [32]. On the downside, nucleophilic ester cleavage is a substitution reaction, which requires the removal of the released alcohol afterwards, as shown in Scheme 2.20. Nevertheless, the removal of small molecular compounds from polymers is a routine work-up procedure via precipitation and allows recycling of the activating alcohol.
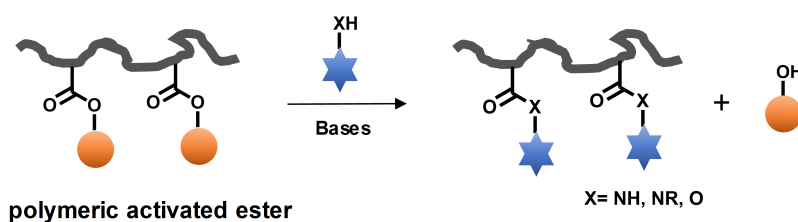
Scheme 2.20: Schematic representation for the synthesis of functional polymer by post-polymerization modification via activated ester.

Activated ester chemistry was first introduced by Ringsdorf [304] and Ferruti [305] in the 1970s. Soon after, various activated ester-based monomers that could be readily polymerized under moderate conditions were discovered, such as *N*-hydroxysuccinimide (NHS) ester monomers [306] and pentafluorophenyl (PFP) ester monomers [307], 4-nitrophenol ester monomers [308] and acetone oxime ester monomers [309], etc., among which the former two are the most explicitly investigated ones.

NHS-ester-based reactive polymers, e.g. poly(*N*-hydroxysuccinimide acrylate) (PNAS) and poly(*N*-hydroxysuccinimide methacrylate) (PNMAS) are quite (yet not fully) resistant to hydrolysis [310], and could be subjected to nucleophilic aminolysis with primary and secondary amines under mild reaction conditions to generate functionalized polyacrylamide derivatives [304, 305]. Under identical reaction conditions, PNAS was found to be more reactive than PNMAS [304]. By aminolysis of PNAS with allylamine, linear poly(*N*-allylacrylamide) which could not be directly polymerized from the corresponding monomer, is affordable [305]. However, the poor solubility of

PNAS and PNAMS in most organic solvents, except for DMF and dimethyl sulfoxide (DMSO), limited their application as homopolymers. Hence, NAS and NMAS are commonly copolymerized with other monomers to enhance the solubility of the resulting copolymers in a wide range of solvents, which allows amines with varying polarity to participate in the aminolysis reaction via PPM. Besides, side reactions, such as ring-opening of the succinimide functionality and formation of *N*-substituted glutarimides by attack of amides on neighboring activated esters, were reported during the aminolysis step [36]. The side reactions associated with NHS-ester-based polymers could be overcome by carrying out PPM at high temperature and in an excess of amine or proton scavengers such as triethylamine (TEA) or DMAP [311].

Subsequently, PFP ester-based reactive polymers were developed, e.g. PPFPA and PPFPMA (poly(pentafluorophenyl methacrylate)). Unlike PNAS/PNMAS, whose solubility is limited to DMSO and DMF, PPFPA and PPFPMA were found to be soluble in a wide range of organic solvents, such as DCM, THF, dioxane and DMF [307]. Moreover, PFP-ester-based polymers were found to be slightly more reactive than the NHS-ester-based polymers. Similar to NHS-ester-based polymers, PFP ester-based polymer with acrylate backbone, i.e. PPFPA, show a higher reactivity in comparison with the methacrylate analogue (PPFPMA) [307]. Besides, the reactivity of PPFPA towards primary amines is found to be relatively higher than secondary amines, while both PPMs showed much higher conversions than PPM with aromatic amines and alcohols. The low reactivity towards alcohols was later combated by adopting DMAP, a powerful aprotic Lewis base, and a polar solvent(DMF) at a relatively high temperature (80 °C) [303]. Additionally, the PPM of the PFP ester-based polymers can be conveniently monitored by ^{19}F NMR spectroscopy due to the existence of fluorine on the PFP leaving group. In respect of PPM via PFP-ester, the Théato group did intensive investigation over the years and released an influential review (Chem. Rev. 2016) in the area of PPM via activated ester [32].

It is worth noting that non-activated ester-based polymer can also be modified at elevated temperatures with the addition of suitable catalysts or bases. For instance, Yang and Birman [312] suggested that 1,2,4-triazole anion could serve as an effective active acyl transfer catalyst suitable for both aminolysis and transesterification of esters. On top of this, our group adopted 1,8-diazabicyclo [5.4.0]undec-7-ene (DBU) and 1,2,4-triazole (Tz) as organo-activating agents at elevated temperatures (120 °C) for the aminolysis of stable polyacrylates [313]. Impressively, high conversions (> 70%) were achieved for the PPM of poly(phenyl methacrylate), poly(2,2,2-trifluoroethyl methacrylate) and poly(methyl methacrylate) with 2-ethylhexylamine.

3. Post-Polymerization Modification via Activated Esters for the Synthesis of TEMPO-Containing Polymers
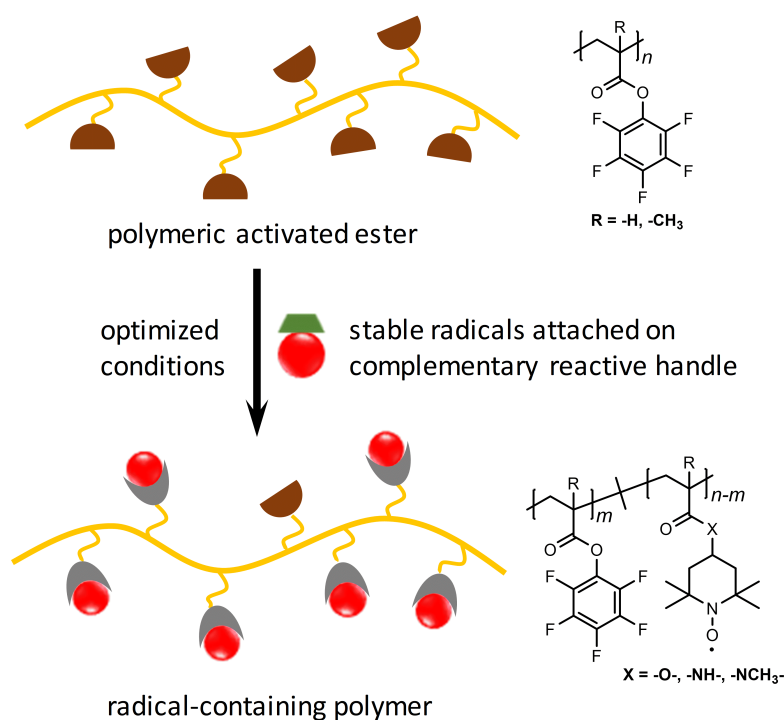
3.1. Prologue

Due to the superior reversibility and ultrafast kinetics of the redox reaction between TEMPO and the corresponding oxoammonium cation [22, 80, 81, 85, 134], TEMPO-containing polymers which are endowed with characteristics of TEMPO, found their facile application in organic radical batteries as cathode materials [314–316]. As TEMPO is the active site, theoretically a higher TEMPO content within the polymeric active material would lead to a higher specific capacity of the cell. Therefore, the purpose of this chapter is to synthesize TEMPO-containing polymers with high TEMPO contents for energy storage application.

The first and representative TEMPO functionalized polymer used in organic radical batteries is poly(2,2,6,6-tetramethylpiperidinyloxy-4-yl methacrylate) (PTMA) due to its excellent rate capability and cycle stability [17, 24]. Generally, PTMA derivatives are synthesized either via post-oxidation (Scheme 3.1A) [17] or by reacting functional polymers with low-molecular-weight TEMPO derivatives [33, 317]. However, the conventionally post-oxidation method only results in a TEMPO content of 60–80% based on electron paramagnetic resonance (EPR) measurement [24, 25] arising from the incomplete oxidation of amino groups to nitroxide moieties in addition to side reactions, e.g. over-oxidation and cross-linking [27, 255]. While reacting functional polymers with low-molecular-weight TEMPO derivatives were only applied to the preparation of copolymers with relatively low TEMPO contents ($\leqslant$ 83%) [280]. Although direct polymerization of TEMPO-acrylate/methacrylate derivatives via anionic or group transfer polymerization have been recognized as efficient alternative synthetic approaches with high yield ($>$ 95%) [26–28], the stringent experimental requirements make the method rather synthetically demanding. Thus, there is a critical quest for alternative suitable synthetic routes that enables a reliable, reproducible and scalable production of the targeted PTMA derivatives.

In order to prepare PTMA derivatives with a high TEMPO content in a more simple and reliable manner, post-polymerization modification (PPM) via polymeric pentafluorophenyl (PFP) ester was proposed. Different form other reports on the preparation of TEMPO-containing polymers via PFP ester [37], a detailed study on the significant influence of critical parameters, such as nature of the solvent, the type of the catalyst, feeding ratio of catalyst and nucleophile, reaction temperature and reaction time, upon the PPM of PFP unit with different types of TEMPO nucleophiles has been performed. Therefore, based on the seminal work of the Théato group on noticeable reactivity difference between poly(pentafluorophenyl acrylate) (PPFPA) and poly(pentafluorophenyl methacrylate) (PPFPMA) during PPM, herein the present chapter systematically screens the PPM of the two classes, polymethacrylates and polyacrylates, respectively, with three different TEMPO

(A) Conventional Post-oxidation Method

- -
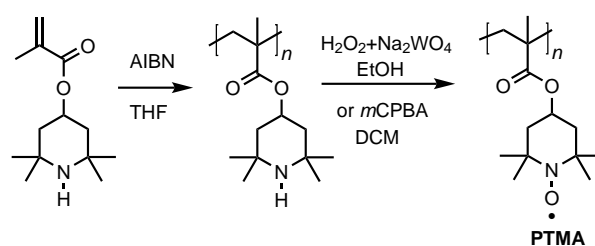
(B) One-step Post-polymerization Modification via Activated Ester
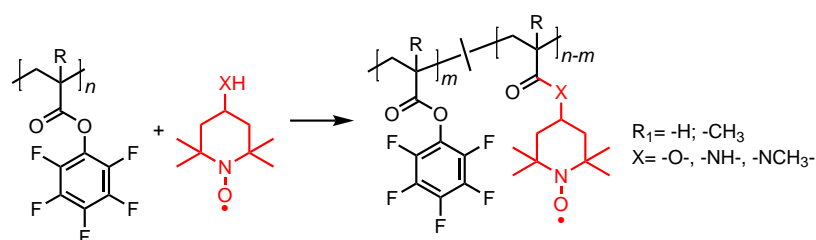
Scheme 3.1: Synthetic routes for TEMPO-containing polymers.

nucleophiles (i.e. 4-hydroxy-TEMPO, 4-amino-TEMPO and 4-methylamino-TEMPO) to prepare the respective TEMPO-functionalized polymethacrylates, polyacrylates, polymethacrylamides, and polyacrylamides (Scheme 3.1B). Noteworthy, aiming at polymers with a high radical density will allow for a study of the structure-property relationships of the various TEMPO polymers in respect to their electrochemical properties.

3.2. Optimization of the Reaction Conditions

The six types of TEMPO-containing polymers were synthesized by reacting 4-hydroxy-TEMPO, 4-amino-TEMPO and 4-methylamino-TEMPO and with PPFPMA and PPFPA respectively (Scheme 3.1B). Aimed at a high TEMPO content within the polymeric structure, the optimal reaction conditions were investigated by using different solvents, catalysts, feeding ratios, reaction temperatures and reaction times for each reaction. The progress of the PPM was monitored by FTIR spectroscopy following the decreasing absorption of the PFP ester C=O band at 1782 cm^{-1}, increasing absorption of newly formed ester C=O band at 1725 cm^{-1} for P_{MA}-O and P_A-O, or newly formed amide C=O band at 1630–1670 cm^{-1} for P_{MA}-A, P_A-A, P_{MA}-MA and P_A-MA. Depending on the reaction conditions, carboxylic acid C=O band at 1722 cm^{-1} may also be detected which resulted from the hydrolysis of polymeric activated ester. In the presented work, the acyl transfer yield was estimated following Eq. 3.1, assuming that PFP ester C=O band, the

newly formed ester C=O band, amide C=O band and acid C=O band (from hydrolysis) have the same absorption coefficient.

$$Conversion\ (\%) = I_x/((I_{ae} + I_{ne} + I_{am} + I_{ac})) \tag{3.1}$$

Where I_{ae}, I_{ne}, I_{am} I_{ac} are the absorption intensity of activated PFP ester C=O band, new formed ester C=O band, amide C=O band and acid C=O band (from hydrolysis), respectively. For P_{MA}-O and P_A-O, I_x represents I_{ne}, while for for P_{MA}-A, P_A-A, P_{MA}-MA and P_A-MA, I_x represents I_{am}.

Depending on the type of the polymeric activated ester, this section is divided into two parts: post-polymerization modification of poly(pentafluorophenyl methacrylate) (PPFPMA) and post-polymerization modification of poly(pentafluorophenyl acrylate) (PPFPA). In each section, detailed synthetic optimization of reaction conditions will be discussed.

3.2.1. Post-Polymerization Modification of Poly(pentafluorophenyl methacrylate)

Considering the different synthetic routes for PTMA in the literature [17, 26, 27, 217], it would be worth optimizing initially the transesterification of PPFPMA with 4-hydroxy-TEMPO, as shown in Scheme 3.2. PPFPMA was synthesized by conventional free-radical polymerization (FRP) of pentafluorophenyl methacrylate (PFPMA) using azobisisobutyronitrile (AIBN) as the initiator yielding a polymer with M_n = 15.4 kDa and $Đ$ = 2.40. The progress of the subsequent transesterification was monitored by FTIR spectroscopy following the disappearance of the PFP ester C=O band at 1782 cm^{-1} and appearance of the newly formed ester C=O band at 1725 cm^{-1} (Figure 3.1, P_{MA}-O_7).
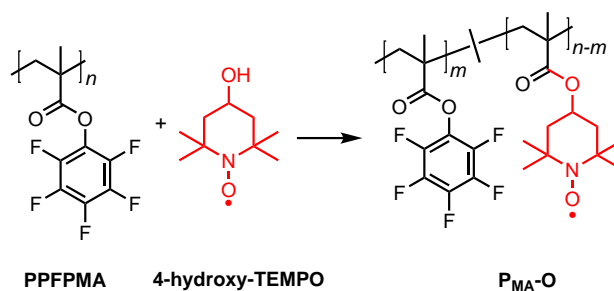
Scheme 3.2: Synthetic route towards P_{MA}-O.

Table 3.1.: PPM for the synthesis of P_{MA}-O.

Entry	Solvent	Catalyst	Molar ratio ester/alcohol/cat.	Temp.	Time	Acyl transfer yield[a]	TEMPO content[b]
				°C	h	%	%
1	DMF	DMAP	1.0/1.3/0.2	60	15	15.0	3.9
2	DMF	DMAP	1.0/1.3/0.2	80	15	20.7	11.5
3	DMF	DMAP	1.0/1.3/0.2	120	15	45.0	[c]
4	DMF	DMAP	1.0/2.0/2.0	80	23	72.2	62.9
5	DME	DMAP	1.0/2.0/2.0	80	23	63.6	51.1
6	DME	Tz/DBU(1/1)	1.0/2.0/2.0	80	6	94.2	62.2[d]
7	DME	Tz/DBU(1/1)	1.0/2.0/2.0	60	6	85.6	73.4
8	DMF	DMAP	1.0/2.0/0.2	80	23	11.7	1.3

[a] Calculated from IR spectra based on the absorption peaks of C=O from activated ester and the newly formed ester at 1782 cm^{-1} and 1725 cm^{-1}, respectively, by assuming them having the same infrared absorption coefficient;
[b] Determined by EPR;
[c] Poor solubility;
[d] Obtained by neglecting the slightly insoluble part.
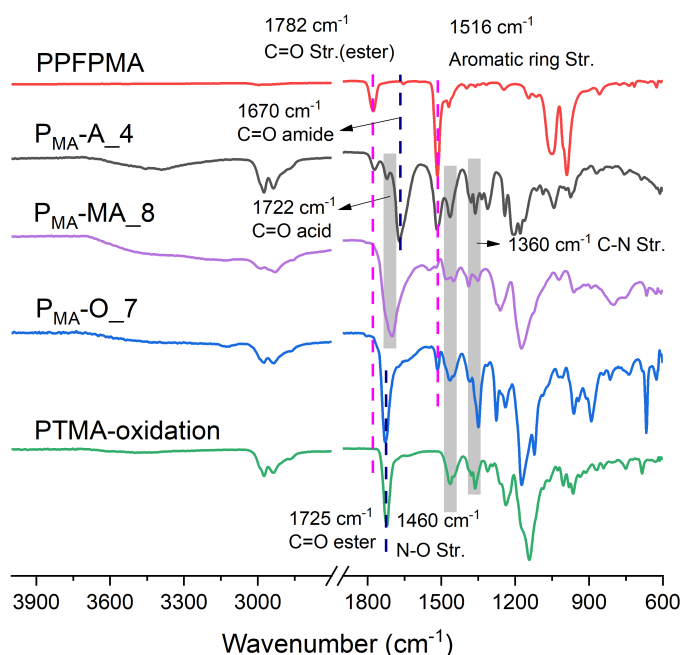
Figure 3.1.: IR spectra of P_{MA}-O_7, P_{MA}-A_4, P_{MA}-MA_8 and PTMA-oxidation. P_{MA}-O_7, P_{MA}-A_4, P_{MA}-MA_8 and PTMA-oxidation represent TEMPO-containing polymers from Table 3.1, Entry 7; Table 3.2, Entry 4; Table 3.3, Entry 8 and PTMA synthesized by conventional post-oxidation method, respectively.

The reactivity of PPFPMA toward 4-hydroxy-TEMPO was screened by adopting slightly modified conditions of previous reports by the Théato group and other groups [303, 318]. Accordingly, the first PPM was conducted by reacting PPFPMA with a 1.3-fold molar excess (relative to PFP ester group) of 4-hydroxy-TEMPO in the presence of a Lewis base catalyst (e.g. 4-dimethylaminopyridine (DMAP), 0.2 eq.) at 60 °C in dimethylformamide (DMF) for 15 hrs. (Table 3.1, Entry 1). DMF was the solvent of choice, since it not only solubilizes both the TEMPO derivative and the polymer, but also actively participates in the transesterification reaction [303]. Nevertheless, these conditions were rather inefficient, leading to only 15.0% conversion according to FTIR analysis, while EPR disclosed only 3.9% of TEMPO moieties within the post-modified polymer, which is dramatically lower than the value estimated by IR spectroscopy. This may result from anhydride side reaction (Scheme 3.3), as evidenced by the stretch band at 1830 cm^{-1} in IR spectra of P$_{MA}$-O (Figure 3.2), which partly contributed to the calculated acyl transfer yield. Conducting the reaction at elevated temperature of 80 °C (Table 3.1, Entry 2) resulted in a slightly higher content of TEMPO radicals (11.5% by EPR). Yet, further increasing the reaction temperature to 120 °C gave rise to an insoluble polymer (Table 3.1, Entries 3). With a 2.0-fold molar excess of 4-hydroxy-TEMPO and DMAP at 80 °C resulted after 23 hrs. of reaction time in a dramatically increased content of side-chain radical concentration of 62.9% (Table 3.1, Entry 4). Since side reaction occurred in all DMF involved reactions (Table 3.1, Entry 1-4) and the ultimate goal of this work is to optimize reaction conditions for the synthesis of radical containing polymers for use in ORB applications, it was worthwhile to investigate the PPM in 1,2-dimethoxyethane (DME), which is utilized in batteries as an aprotic solvent [319]. It is interesting to note that replacing DMF with DME, under otherwise identical reaction condition, resulted in a lower radical content of 51.1%, as determined by EPR (Table 3.1, Entry 5). The difference in TEMPO loading on the post-modified P$_{MA}$-O is presumably due to the polarity of the solvent and the conception that DMF does actively participate in the transesterification.

Due to the benign nature of DME and its broad applicability in battery applications [320], we aimed to boost the efficiency of the post-polymerization reaction in DME by an anionic mode of catalysis based on 1,8-diazabicyclo [5.4.0]undec-7-ene (DBU) and 1,2,4-triazole (Tz). In fact, this organo-activating agent system has been recently employed by the Théato group as a powerful tool for the facile amidation of non-activate polyacrylates and polymethacrylates yielding the respective poly(meth)acrylamides [313]. Hence, in accordance with previous reports, we evaluated the PPM at 80 °C under similar conditions as Entry 5 in Table 3.1. Intriguingly, within 6 hours of reaction time, distinct transesterification of PFP ester with 4-hydroxy-TEMPO was observed in the presence of an equal molar equivalent of Tz and DBU (Table 3.1, Entry 6). The resulting polymer was slightly insoluble in dimethylacetamide (DMAc), yet EPR revealed a radical content
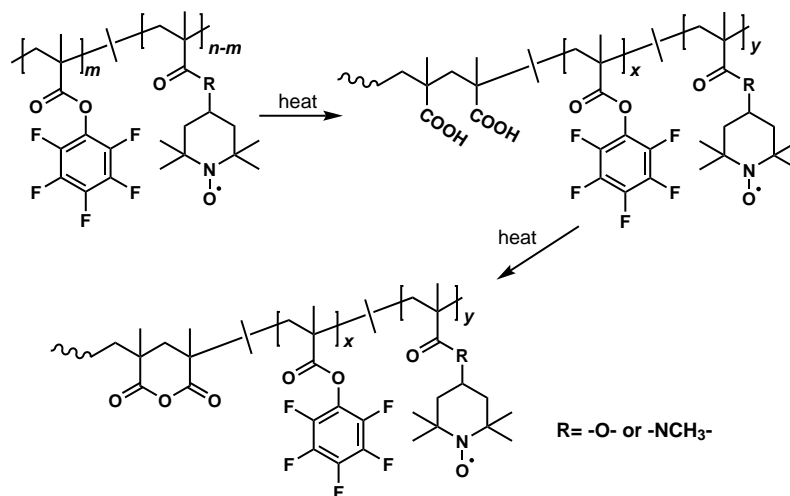
Scheme 3.3: Anhydride side reactions.
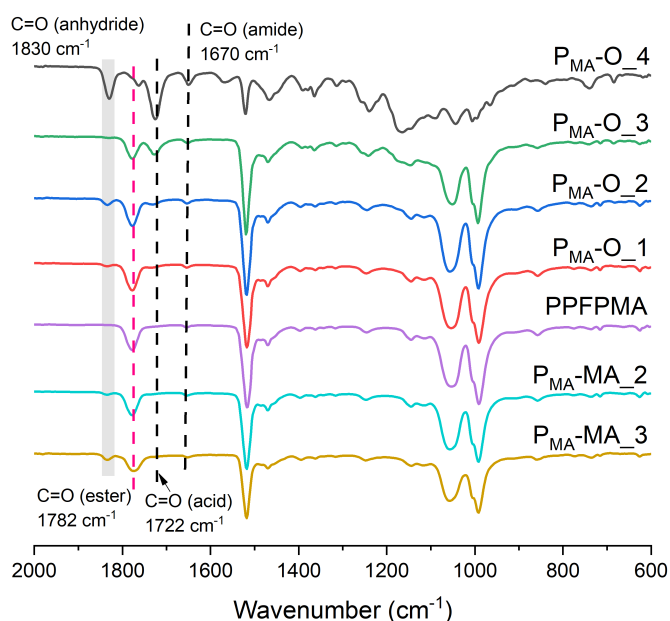
Figure 3.2.: Comparative IR spectra of P_{MA}-O_1 to P_{MA}-O_4, P_{MA}-MA_2 and P_{MA}-MA_3. P_{MA}-O_1 to P_{MA}-O_4 represent resulting polymers from Table 3.1, Entry 1 till Entry 4; P_{MA}-MA_2 and P_{MA}-MA_3 represent resulting polymers from Table 3.3, Entry 2 and Entry 3, respectively.

of 62.2% by neglecting this slightly insoluble part, while IR showed a 94.2% conversion. Owing to the big difference between the estimated acyl transfer yield from IR measurements and TEMPO content from EPR spin count, which also accounts for side reaction like TEMPO quenching or an accompanied hydrolysis, the PPM was conducted a lower temperature of 60 °C, resulting in an increased TEMPO content of 73.4% by EPR (Table 3.1, Entry 7). This is very similar to the active TEMPO content in reference PTMA synthesized by post-oxidation method (66.6%).
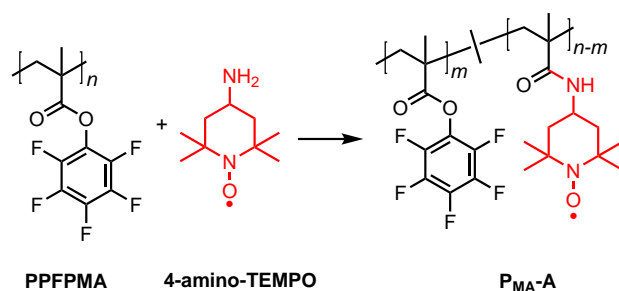
Scheme 3.4: Synthetic route towards P_{MA}-A.

Table 3.2.: PPM for the synthesis of P_{MA}-A.

Entry	Solvent	Catalyst	Molar ratio ester/alcohol/cat.	Temp.	Time	Acyl transfer yield[a]	TEMPO content[b]
				°C	h	%	%
1	THF	TEA	1.0/1.5/1.5	55	96	17.0	[c]
2	DMF	DMAP	1.0/1.2/0.2	60	15	34.7	30.9
3	DMF	DMAP	1.0/2.0/2.0	60	24	55.4	51.9
4	NMP	DMAP	1.0/2.0/2.0	60	24	65.9	64.1
5	NMP	DMAP	1.0/2.0/2.0	80	12	63.1	63.3
6	DME	Tz/DBU(1/1)	1.0/2.0/2.0	80	6	64.3	63.6
7	NMP	DMAP	1.0/2.0/0.2	60	24	56.0	62.7

[a] Calculated from IR spectra based on the absorption peaks of C=O from ester and amide at 1782 cm^{-1} and 1670 cm^{-1}, respectively, by assuming them having the same infrared absorption coefficient;
[b] Determined by EPR;
[c] Poor solubility.

Inspired by the PPM of PPFPMA with 4-hydroxy-TEMPO, we transitioned from transesterification to amylolysis using 4-amino-TEMPO and 4- methylamino-TEMPO, which led to P_{MA}-A and P_{MA}-MA, respectively (Scheme 3.4 and 3.5). P_{MA}-A was synthesized in attempts by reacting PPFPMA with 4-amino-TEMPO in THF with triethylamine (TEA) as catalyst at 55 °C for 96 hrs. (Table 3.2, Entry 1), similar to literature known conditions [37], however, only a very weak C=O amide band at 1670 cm^{-1} showed up in the IR spectrum of the isolated polymer (Figure 3.3), corresponding to 17.0% acyl transfer yield. Other than that, the resulting polymer precipitated out after reacting for 2 days and it is only partly soluble even in solvents with high polarity like DMF. In order to achieve high TEMPO content, a more polar solvent DMF together with a stronger Lewis base DMAP at a slightly higher reaction temperature 60 °C were adopted, leading to a much higher TEMPO content of 30.9% according to EPR (Table 3.2, Entry 2). Subsequently, the feeding ratio of nucleophile and catalyst with regard to PFP moieties was increased from

1/1.2/0.2 to 1/2.0/2.0, the reaction time was extended to 24 hrs., and *N*-Methyl-2-pyrrolidone (NMP), another polar solvent, was examined (Table 3.2, Entry 3-4). It was found that NMP, which is commonly used in preparation of electrode composite slurries, was more effective than DMF with around 10% higher TEMPO amount by both IR and EPR. However, further increasing the reaction temperature to 80 °C resulted in a similar TEMPO content of 63.6% according to EPR (Table 3.2, Entry 5). Further, the use of the catalyst Tz/DBU did also not result in an increase of the TEMPO content within P_{MA}-A (Table 3.2, Entry 6). As shown in Figure 3.1, the IR spectrum of P_{MA}-A_4 (Table 3.2, Entry 4) shows a significantly decreased C=O (activated ester) stretching vibration band at 1782 cm^{-1} and aromatic ring stretch band at 1516 cm^{-1} from PFP, while new bands at 1670 cm^{-1}, 1460 cm^{-1} and 1360 cm^{-1} appeared that are ascribed to the C=O, N-O and C-N (amide) stretching vibrations, respectively [255, 263, 321].
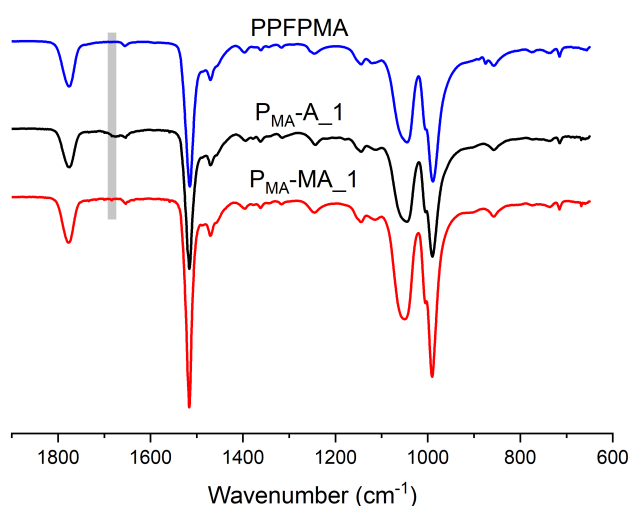
Figure 3.3.: Comparative IR spectra of P_{MA}-A_1 and P_{MA}-MA_1. P_{MA}-A_1 and P_{MA}-MA_1 represent resulting polymer from Table 3.2, Entry 1 and Table 3.3, Entry 1, respectively.

On account of the structural similarity of P_{MA}-MA and P_{MA}-A, the conditions for the synthesis of P_{MA}-A were applied to the synthesis of P_{MA}-MA. Unlike P_{MA}-A, a lower acryl transfer yield (6.3%) was observed for P_{MA}-MA when THF and TEA was used (Table 3.3, Entry 1) due to the steric hindrance from the secondary amine of the TEMPO derivative and the methyl group at the PPFPMA backbone (Figure 3.3). Besides, the resulting polymer P_{MA}-MA-1 also had a low solubility in DMF even after reacting for 96 hrs. Thus, the use of more polar solvents like NMP and DMF, and a stronger base DMAP were investigated (Table 3.3, Entry 2, 3), however, side reactions occurred in both cases as a stretch band at 1830 cm^{-1} corresponding to anhydride showed up in the IR spectra (Figure 3.2, P_{MA}-MA_2 and P_{MA}-MA_3). Therefore, DME was chosen as the solvent for the following reactions. With a higher excess of 4-methylamino-TEMPO

and DMAP (increasing from 1.2-fold to 2.0-fold), the incorporated TEMPO content increased from 2.2% to 10.8% according to EPR (Table 3.3, Entry 4-7), which could be further increased to 17.9% by utilizing the organo-activator Tz/DBU at 80 °C when reacted for 6hr. (Table 3.3, Entry 8).
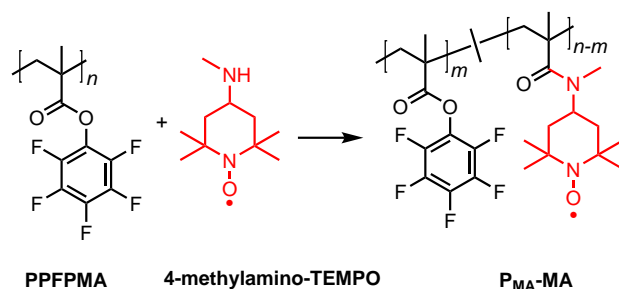
Scheme 3.5: Synthetic route towards P$_{MA}$-MA.

Table 3.3.: PPM for the synthesis of P$_{MA}$-MA.

Entry	Solvent	Catalyst	Molar ratio ester/alcohol/cat.	Temp.	Time	Acyl transfer yield[a]	TEMPO content[b]
				°C	h	%	%
1	THF	TEA	1.0/1.5/1.5	55	96	6.3	[d]
2	NMP	DMAP	1.0/1.5/1.5	60	24	[c]	[d]
3	DMF	DMAP	1.0/1.5/1.5	60	45	[c]	[d]
4	DME	DMAP	1.0/1.2/1.2	60	45	18.6	2.2
5	DME	DMAP	1.0/1.5/1.5	60	45	17.4	4.4
6	DME	DMAP	1.0/1.7/1.7	60	45	17.8	5.9
7	DME	DMAP	1.0/2.0/0.2	60	45	23.5	10.8
8	DME	Tz/DBU(1/1)	1.0/2.0/2.0	80	6	∼ 100	17.9
9	DME	DMAP	1.0/2.0/0.2	60	45	15.8	3.2

[a] Calculated from IR spectra based on the absorption peaks of C=O from ester and amide at 1782 cm^{-1} and 1670 cm^{-1}, respectively, by assuming them having the same infrared absorption coefficient;
[b] Determined by EPR;
[c] Not sure because of unknown side reaction with 1830 cm^{-1} showing up in IR spectra;
[d] Poor solubility.

3.2.2. Post-Polymerization Modification of Poly(pentafluorophenyl acrylate)

Based on the achievements for the alternative synthesis of P_{MA}-O by transesterification, a similar synthetic approach for polyacrylate P_A-O was investigated (Scheme 3.6). Again, temperature, feeding ratio, reaction time as well as catalytic effect were varied and the results are summarized in Table 3.4. In contrast to the transesterification to yield P_{MA}-O, in the reactions of P_A-O, no anhydride vibration band was observed at 1830 cm^{-1} in IR spectra when DMF was used as solvent. Consequently, DMF was chosen as a standard solvent for all P_A-O reactions. Remarkably, PPM of P_A-O could even proceed at room temperature, resulting in a polymer with a TEMPO content of 18.4% (Table 3.4, Entry 1), which is higher than that of P_{MA}-O reacted at 80 °C (Table 3.1, Entry 2) under the same condition. With increasing temperature, the TEMPO content first increased, reaching the highest conversion at 80 °C (53.1%), and afterwards decreased at 120 °C (Table 3.4, Entry 1–5). Noteworthy, at 120 °C, the resulting polymer (Table 3.4, Entry 5) showed a great deviation between acyl transfer yield (100.0%) and actual TEMPO loading (24.6%), which suggested a dominating side reaction at 120 °C. With the purpose of obtaining a much higher TEMPO content, 80 °C was adopted for the following reactions. Unlike the reactions of P_{MA}-O, a 2.0-fold molar excess of nucleophile and catalyst and longer reaction time of 23 hrs. did not result in an obvious increase in TEMPO content (Table 3.4, Entry 6). The resulting polymer exhibited only a TEMPO content of 57.1% which is similar to P_A-O obtained from Table 3.4, Entry 4, even though the characteristic C=O band at 1782 cm^{-1} indicates the nearly disappearance of activated ester (Figure 3.4, P_A-O_6). With the optimized reaction conditions (Table 1, Entry 7 for P_{MA}-O), P_A-O showed a poor solubility after 4 hrs. (Table 3.4, Entry 7).

PPFPA   4-hydroxy-TEMPO P_A-O
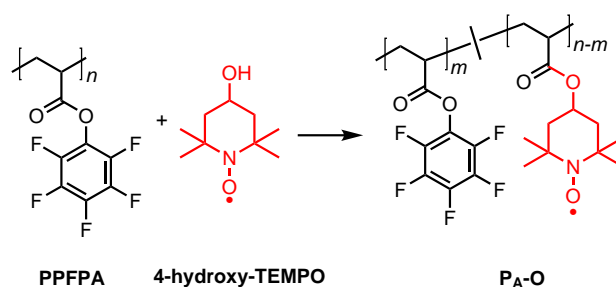
Scheme 3.6: Synthetic route towards P_A-O.

Owing to the high reactivity of the PFP ester of PPFPA towards primary amines, PPM of PPFPA was conducted with 4-amino-TEMPO to yield P_A-A (Scheme 3.7 and Table 3.5). In this case, a quantitative conversion was observed by IR spectroscopy for the TEA catalysed reaction and EPR

Table 3.4.: PPM for the synthesis of P_A-O.

Entry	Solvent	Catalyst	Molar ratio ester/alcohol/cat.	Temp. °C	Time h	Acyl transfer yield[a] %	TEMPO content[b] %
1	DMF	DMAP	1.0/1.2/0.2	rt	15	37.5	18.4
2	DMF	DMAP	1.0/1.2/0.2	40	15	42.5	34.2
3	DMF	DMAP	1.0/1.2/0.2	60	15	58.1	46.0
4	DMF	DMAP	1.0/1.2/0.2	80	15	60.6	53.1
5	DMF	DMAP	1.0/1.2/0.2	120	15	100	24.6
6	DMF	DMAP	1.0/2.0/2.0	80	23	100	57.1
7	DMF	Tz/DBU(1/1)	1.0/2.0/2.0	60	4	100	c
8	DMF	DMAP	1.0/2.0/0.2	80	15	59.4	30.9

[a] Calculated from IR spectra based on the absorption peaks of C=O from activated ester and new ester at 1782 cm^{-1} and 1725 cm^{-1}, respectively, by assuming them having the same infrared absorption coefficient;
[b] Determined by EPR;
[c] Poor solubility.
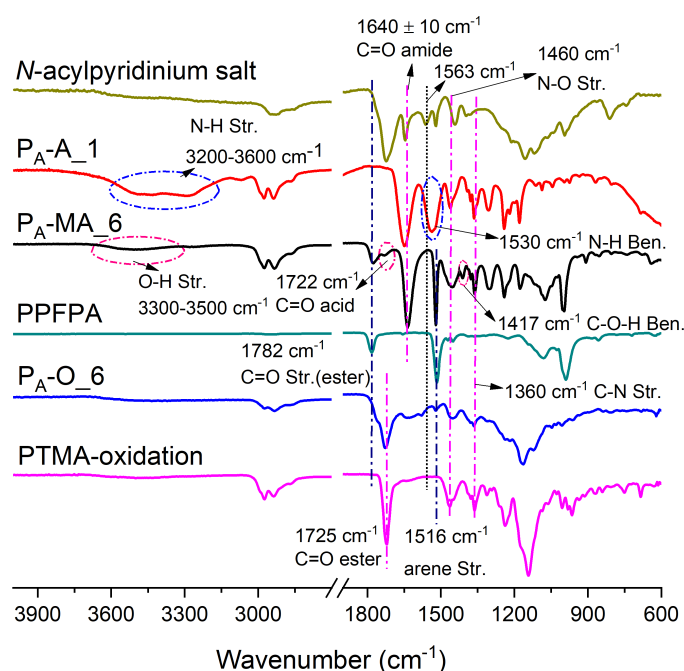
Figure 3.4.: IR spectra of P_A-O_6, P_A-A_1, P_A-MA_6 and PTMA-oxidation. P_A-O_6, P_A-A_1, P_A-MA_6 and PTMA-oxidation represent TEMPO-containing polymers from Table 3.4, Entry 6; Table 3.5, Entry 1; Table 3.6, Entry 6 and PTMA synthesized by conventional post-oxidation method, respectively.

also revealed a very high TEMPO content of 96.2%. According to IR spectroscopy, the indicative bands of PFP ester (1782 cm^{-1} for C=O and 1516 cm^{-1} for PFP) were completely gone and converted to amide bonds represented by the C=O amide band at 1650 cm^{-1} (Figure 3.4, P$_A$-A_1). Though TEA is a weaker Lewis base compared to DMAP, a 96.2% TEMPO content could still be obtained even at a 50 °C within 3 hrs. This is a 30% higher TEMPO content compared to the reference PTMA synthesized by conventional post-oxidation. Besides, no hydrolysis occurred during the reaction. This result is quite promising because P$_A$-A has a theoretical specific capacity of 118 mAh g^{-1}, which is slightly higher than PTMA (111 mAh g^{-1}), and found application in aqueous electrolyte based batteries and skin contacting electronic devices [113, 299].

PPFPA   **4-amino-TEMPO**   **P$_A$-A**
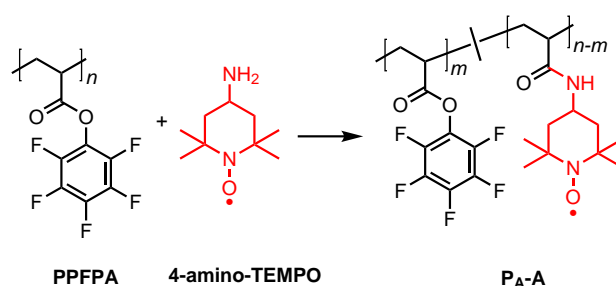
Scheme 3.7: Synthetic route towards P$_A$-A.

Table 3.5.: PPM for the synthesis of P$_A$-A.

Entry	Solvent	Catalyst	Molar ratio ester/alcohol/cat.	Temp.	Time	Acyl transfer yield[a]	TEMPO content[b]
				°C	h	%	%
1	DME	TEA	1.0/2.0/2.0	50	3	100	96.2

[a] Calculated from IR spectra based on the absorption peaks of C=O from ester and amide at 1782 cm^{-1} and 1650 cm^{-1}, respectively, by assuming them having the same infrared absorption coefficient;
[b] Determined by EPR;

Similar to the synthesis of P$_{MA}$-MA, the influence of solvent was first investigated in efforts to synthesize P$_A$-MA (Table 3.6, Entry 1-3). While the solvents DME and NMP resulted in polymers with a TEMPO content of 62.4% and 65.9% according to EPR, respectively, which is quite similar to acyl transfer yield based on IR, PPM with DMF as the solvent yielded a 13% lower TEMPO content in the isolated polymer according to EPR. Though all three reactions did not show a quantitative conversion, the activated ester bonds were quantitatively cleaved, as observed by the complete disappearance of characteristic C=O activated ester band at 1782 cm^{-1} in the IR spectra (Figure 3.5, P$_A$-MA_1, P$_A$-MA_2 and P$_A$-MA_3). The latter was also confirmed by ^{19}F NMR spectroscopy, which revealed no peaks (Figure 3.6). In the IR spectra (Figure 3.5), apart from

the C=O amide stretching band at 1630 cm^{-1}, another band at 1722 cm^{-1} showed up, which can be ascribed to the C=O band of carboxylic acids. This result indicates that a partial hydrolysis happened during PPM, which is a known side reaction also reported for other activated ester based post-polymerization modifications [322, 323].
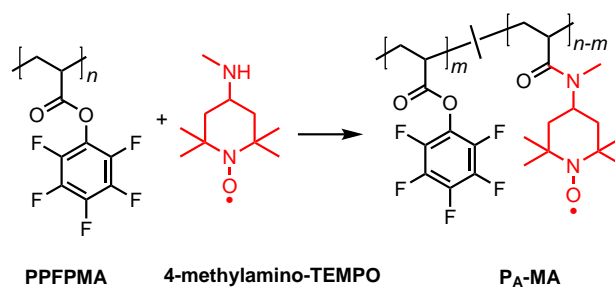
Scheme 3.8: Synthetic route towards P$_A$-MA.

Table 3.6.: PPM for the synthesis of P$_A$-MA.

Entry	Solvent	Catalyst	Molar ratio ester/alcohol/cat.	Temp.	Time	Acid content[a]	Acyl transfer yield[b]	TEMPO content[c]
				°C	h	%	%	%
1	DMF	DMAP	1.0/2.0/2.0	60	24	34.9	65.1	52.4
2	NMP	DMAP	1.0/2.0/2.0	60	24	36.9	63.1	65.9
3	DME	DMAP	1.0/2.0/2.0	60	24	32.2	67.8	62.4
4	DME	DMAP	1.0/2.0/2.0	60	3	54.3	45.7	42.2
5	DME[d]	DMAP	1.0/2.0/2.0	60	24	20.7	57.6	52.8
6	NMP	DMAP	1.0/2.0/0.2	60	24	8.7	75.4	85.5
7	DME	TEA	1.0/2.0/2.0	60	24	∼0	25.0	-

[a] Resulted from hydrolysis side reaction;

[a,b] Calculated from IR spectra based on the absorption peaks of C=O from ester, amide and acid at 1782 cm^{-1}, 1630 cm^{-1} and 1722 cm^{-1}, respectively, by assuming them having the same infrared absorption coefficient;

[c] Determined by EPR;

[d] Extra dry solvent.

It is worth noting that all polymers (P$_{MA}$-A, P$_{MA}$-MA and P$_A$-MA) obtained from amidation reactions with DMAP as catalyst showed carboxylic band at around 1722 cm^{-1} in IR spectra (Figure 3.1, and Figure 3.4). However, this band was particularly intensive for all P$_A$-MA polymers, reaching almost half of the amide band (Figure 3.5 and Table 3.6). The latter resulted from the relatively high reactivity of PPFPA compared to PPFPMA as well as the high basic character of 4-methylamino-TEMPO among all three TEMPO derivatives used in this work.
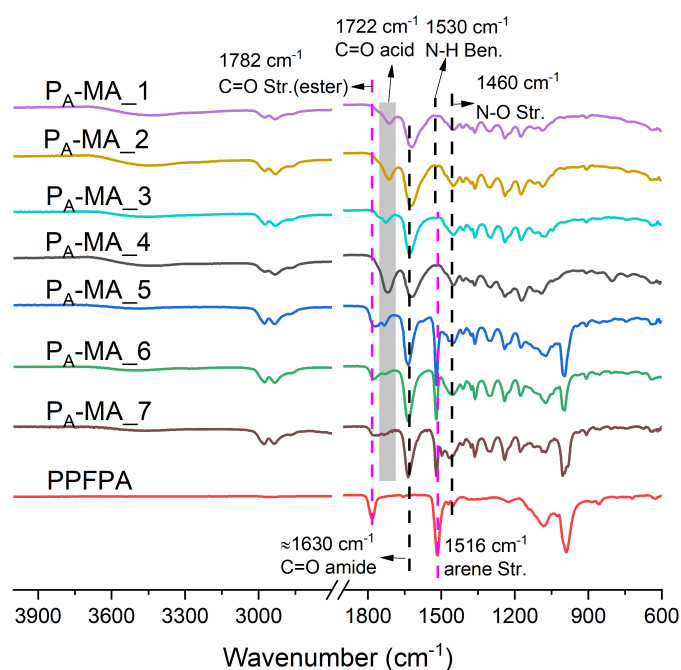
Figure 3.5.: IR spectra of P_A-MA. P_A-MA_1 to P_A-MA_7 represents TEMPO-containing polymer from Table 3.6, Entry 1-7, respectively.
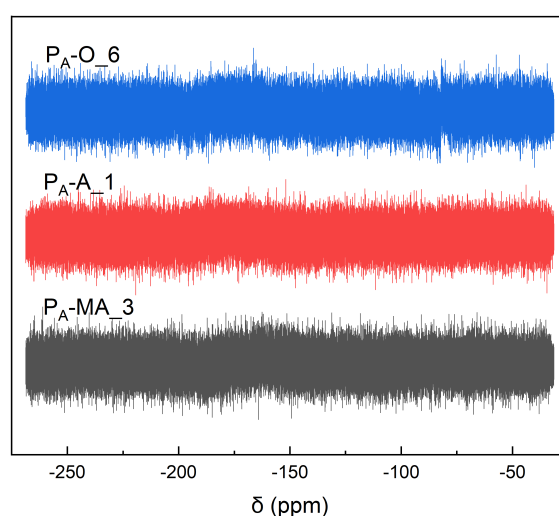
Figure 3.6.: Comparative ^{19}F NMR spectra of P_A-O_6, P_A-A_1 and P_A-MA_3, respectively. P_A-O_6, P_A-A_1 and P_A-MA_3 represent TEMPO-containing polymers from Table 3.4, Entry 6; Table 3.5, Entry 1 and Table 3.6, Entry 3, respectively.

In order to track the progress of the reactions for P_A-MA by IR measurements as well as the cleavage of ester bonds, DME was chosen as solvent because of its high volatility and lack of amide bonds in its molecular structure. It turned out that a reaction time of 3 hrs. was sufficient to result in a 100% cleavage of PFP ester bonds in the resulting polymer, yet the resulting polymers

showed strong hydrolysis in the range from 32.2% to 54.3% (Table 3.6, Entry 3 and Entry 4).

It appears that trace amounts of water from normal analytical grade solvent involved in the reaction and high DMAP loading amount leads to a very noticeable hydrolysis side reaction. To gain a further insight, extra dry DME (Table 3.6, Entry 5) was utilized in comparison to normal analytical grade DME solvent (Table 3.6, Entry 3). As a result, the PFP ester C=O band at 1782 cm^{-1} still remained in the isolated polymer, as observed from the IR spectrum (Figure 3.5, P$_A$-MA_5) and the percentage of ester moiety, amide moiety and acid were 21.7%, 57.6% and 20.7% from IR, respectively, assuming that these three C=O bonds exhibit the same infrared absorption coefficient. Aside from the decrease in acid content, also a 9.6% reduction in TEMPO content was detected by EPR compared to Entry 3 in Table 3.6.

The Lewis base DMAP acted as an activator in the amidation reactions in the present study, however, DMAP has a pKa of 9.6 in water and the more alkaline the solution becomes, the more likely a hydrolysis is to happen. Therefore, the choice of catalyst is important to tune the reaction. When TEA was used as catalyst for the synthesis of P$_A$-MA at a high feeding ratio of 2.0 molar equivalent to PFP ester units, a hydrolysis side reaction barely occurred (Table 3.6, Entry 7) with no peak showing up at 1722 cm^{-1} corresponding to carboxylic acid C=O in IR spectra (Figure 3.5, P$_A$-MA_7), contrary to 32.2% of carboxylic acid formation when DMAP was employed (Table 3.6, Entry 3). The latter suggested that reactions catalyzed by DMAP are more prone to trigger hydrolysis side reactions compared to TEA.

Not only the choice of catalyst, but also the catalyst feeding ratio as well as reaction substrates have an influence on the reaction. Since 4-methylamino-TEMPO has a relatively higher pKa compared to 4-amino-TEMPO and 4-hydroxy-TEMPO, the feeding ratio of DMAP was lowered from 2.0 to 0.2 with respect to activated ester moieties, and at the same time NMP was chosen as the solvent, as it showed the highest TEMPO content among the three solvents (DMF, NMP and DME; Table 3.6, Entry 1-3). Consequently, the hydrolysis side reaction for P$_A$-MA was dramatically suppressed as the acid content significantly decreased from 36.9% to 8.7% while TEMPO content within the isolated polymer increased from 65.9% to 85.5% according to EPR. Based on this result, the same feeding ratio of DMAP to PFP ester unit was applied to other PPM of P$_{MA}$-O, P$_A$-O, P$_{MA}$-A and P$_{MA}$-MA (Table 3.1, Entry 8; Table 3.4, Entry 8; Table 3.2, Entry 7 and Table 3.3, Entry 9), however, the TEMPO content in all 4 polymers did not increase compared to their counterparts prepared with 2.0 molar equivalent DMAP (Table 3.1, Entry 4; Table 3.4, Entry 6; Table 3.2, Entry 4 and Table 3.3, Entry 7, respectively). These results indicate that the use of DMAP in post-polymerization modification of activated ester is quite tricky, as it not only depends on the DMAP concentration but also on the nature of reaction substrates.

As reported in literature, PFP esters can react with DMAP even in the absence of an alcohol or amine to form an *N*-acylpyridinium salt [303, 324, 325]. To investigate if *N*-acylpyridinium salt units were also incorporated into the resulting P_A-A and P_A-MA polymer structures, polymeric *N*-acyl-4-dimethylaminopyridinium salt was formed quantitatively upon mixing PPFPA and DMAP (2.0 molar equivalent to PFP ester units) at 60 °C. This polymeric salt is readily soluble in DMSO and DMF, but less soluble in DCM and chloroform. This salt of P_A-A and P_A-MA also exhibited stretching bands at around 1722 cm^{-1} and 1630 cm^{-1}, respectively, in IR spectra (Figure 3.4, *N*-acylpyridinium salt), however, polymeric *N*-acyl-4-dimethylaminopyridinium salt showed a peak at 1563 cm^{-1}, which was absent in P_A-A and P_A-MA. This revealed that the *N*-acyl-4-dimethylaminopyridinium adduct was an intermediate, which was hydrolyzed during work up. We further noted that the acyl transfer yield of P_{MA}-O and P_{MA}-A of the transesterification reactions calculated by IR were in general higher than the calculated TEMPO content from EPR data, while for polymers P_{MA}-A, P_A-A, and P_A-MA that were prepared by amidation reactions exhibited a similar acyl transfer yield based on IR and EPR analysis (within the range of $\pm10\%$), with the exception of P_{MA}-MA. The relatively higher acyl transfer yield calculated by IR for P_{MA}-O and P_{MA}-A was contributed to the hydrolysis reaction as the newly formed ester C=O band at about 1725 cm^{-1} overlapped with the carboxylic acid C=O band at around 1722 cm^{-1} in IR spectra. Therefore, for P_{MA}-O and P_A-O, I_x in Eq. 3.1 refers to the sum of I_{ne} and I_{ac}, representing the absorption intensity of newly formed ester C=O bands and carboxylic acid C=O bands, respectively. However, for amidation reactions, the acyl transfer yield was calculated only based on the absorption intensity of the C=O amide band I_{am}. Regarding to P_{MA}-MA, the big deviation between acyl transfer yield by IR and EPR most probably resulted from the big tolerance range as the absorption intensity of amide bonds was too low. Other than that, a big deviation could also occur when either of the C=O absorption intensity involved in Eq. 3.1 were too low, like P_A-MA from Table 3.6, Entry 6.

3.3. EPR and Electrochemical Characterization

Figure 3.7 shows the EPR spectra of the six polymers with the highest TEMPO content in this work. P_{MA}-O_7, P_A-O_6, P_{MA}-A_4, P_A-A_1 and P_A-MA_6 exhibited a classic Lorentzian shape similar to PTMA that was synthesized by traditional post-oxidation. This indicated a strong intermolecular spin-exchange (radical-radical) interaction arising from a close spatial proximity between the paramagnetic units in the polymer [137, 326], which is indicative for a high TEMPO content within the polymer. The small shoulder observed in EPR of P_{MA}-O_7 was due to a

small fraction of low molecular weight oligomers in the sample for which end effects may be more prominent [25, 137], rather than residual monomer incorporated in the polymer. Particularly, it is evident from comparative IR spectra there there was no characteristic peak at 3406 cm^{-1} corresponding to –OH (free) functionality that should arise from the monomer, which is 4-hydroxyl-TEMPO (Figure 3.8). In contrast, the EPR spectra of P_{MA}-MA_8 (with a relatively low TEMPO content of 17.9%) showed a triplet splitting due to coupling of the unpaired electron with the ^{14}N nucleus. Noteworthy, the EPR spectra are different because of the influence of radical-radical interaction, since paramagnetic TEMPO units were not densely arranged along the polymer backbone to induce a broad singlet split by radical-radical exchange coupling [137]. From this perspective, the shape of the EPR spectra for most TEMPO-containing polymers could act as an indicator for TEMPO content within the polymer.
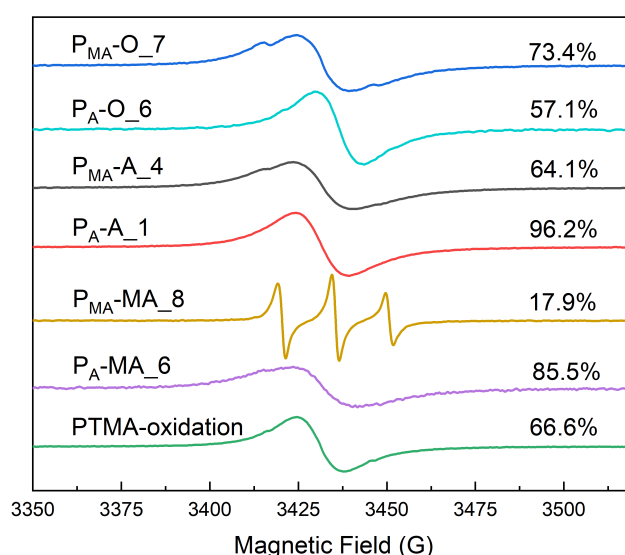
Figure 3.7.: EPR spectra of six types of TEMPO-containing polymers with the highest TEMPO content from PPM via activated ester. PTMA-oxidation represented PTMA synthesized by post-oxidation method; P_{MA}-O_7, P_A-O_6, P_{MA}-A_4, P_A-A_1, P_{MA}-MA_8 and P_A-MA_6 represent TEMPO-containing polymers from Table 3.1, Entry 7; Table 3.4, Entry 6; Table 3.2, Entry 4; Table 3.5, Entry 1; Table 3.3, Entry 8 and Table 3.6, Entry 6, respectively.

As one of the aimed application for TEMPO-containing polymers is as electrode material, it is necessary to check if the hydrolysis side reaction would influence the electrochemical properties of TEMPO-containing polymers. In this regard, P_A-A was chosen as the model polymer together with poly(acrylic acid) (PAA) and investigated by cyclic voltammetry, which is a powerful tool to probe reactions involving electron transfer. There are two reasons for the choice of P_A-A as the model polymer. On one hand, it can achieve nearly 100% TEMPO content under mild conditions in a fast fashion. On the other hand, it bears a secondary amide group along the polymer chain
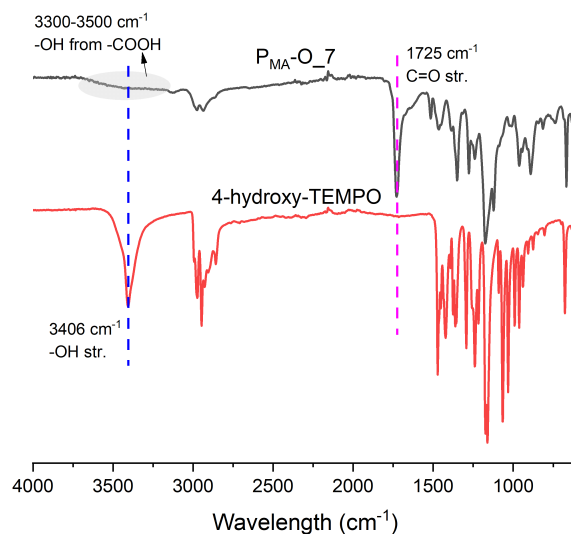
Figure 3.8.: Comparative IR spectra of P_{MA}-O_7 and 4-hydroxyl-TEMPO.

which is quite active, and should be electrochemically the most vulnerable one among all six TEMPO-containing polymers.

Cyclic voltammetry of pure PAA (5 mg) and the mixture of P_A-A and PAA (5 mg/5 mg) were carried out on a potentiostat system in 0.1 M $LiClO_4$ electrolyte in acetonitrile (MeCN, 10 mL) with a scan rate of 100 mV s^{-1} ranging from 0–1.0 V vs. Ag/Ag$^+$ at 25 °C. A glass carbon electrode, a Pt-wire electrode and an Ag/AgCl electrode were used as working electrode, counter electrode and reference electrode, respectively. Both cyclic voltammograms exhibited both oxidation and reduction peaks at the same potential, while the peak current got increased in the presence of PAA (Figure 3.9). Since all cyclic voltammetry was measured under the same condition which means electrode area (A), TEMPO concentration in solution (C), scan rate (ν) and temperature (T) are the same, based on Randles-Sevcik equation (Eq. 1.1), the only reason for the increase of peak current (i_p) could be the increase in electron transfer numbers (n) within the measuring time. This suggested that the existence of acrylic acid units along P_A-A polymer chain does not negatively impact its performance as it would not silent the TEMPO redox reaction, on the contrary it could facilitate an ion transfer. Therefore, though most of the TEMPO-containing polymers presented in this work only achieved a similar TEMPO content as PTMA synthesized by conventional post-oxidation method, and the reactions are often accompanied by a hydrolysis side reaction, the formed carboxylic acid units might have a positive contribution for the electrochemical properties of TEMPO-containing polymers.

Last but not the least, the battery performance based on P_A-A_1 at 5 C-rate in the voltage range of 3.0–4.1 V was investigated in comparison to the PTMA-oxidation synthesized by post-oxidation
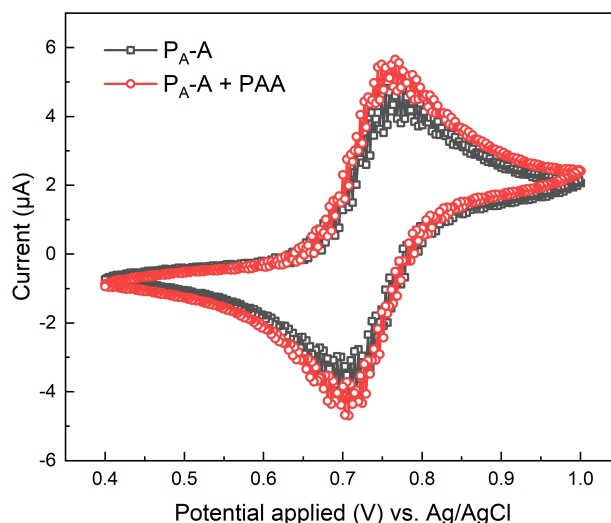
Figure 3.9.: Cyclic voltammetry curves of P_A-A and the mixture of P_A-A and PAA.

method (Figure 3.10). The cathode was prepared by mixing the TEMPO-containing polymer (10 wt.%), poly(vinylidene difluoride) (PVdF, 10 wt.%), and carbon black Super P (CB-SP, 80 wt.%) in NMP, afterwards blade coating the slurry onto an aluminium foil, followed by drying at 80 °C in an oven. The coin cell (CR2032) was assembled by stacking of the polymer based cathode, lithium metal anode and two pieces of separator films (PP/PE/PP) with 1.0 M $LiPF_6$ in EC/DMC (v/v = 50/50, 150 μL) electrolyte in an argon filled glove box. P_A-A_1 showed an initial specific capacity of 89.4 mAh g^{-1}, which was about 12 mAh g^{-1} higher than that of PTMA-oxidation. The capacity of PTMA-oxidation dropped dramatically within the first 30 cycles to around 62 mAh g^{-1} probably due to the broader polydispersity of PTMA-oxidation ($Đ = 4.3$) in comparison to P_A-A_1 ($Đ = 2.3$), as shown in Table 3.7. The latter enlarges the capacity gap between P_A-A_1 and PTMA-oxidation the maximum which is 22 mAh g^{-1}, the capacity of P_A-A_1 decreased only slightly during the subsequent 250 cycles to a capacity of 75 mAh g^{-1}. Subsequently, both cathodes degraded similarly with a specific capacity loss of 23.5% and 27.5% after 500 cycles for P_A-A_1 and PTMA-oxidation, respectively. Notably, as evidenced UV/vis (Figure 3.11) and IR spectra (Figure 3.4), the resulting PTMA-oxidation polymer should not contain any reduction or oxidation states (e.g. hydroxylamine and oxoammonium, respectively), as there was no characteristic UV/vis absorption at 476 nm, which arises from and no +N=O, in addition that there was not any characteristic peak at $\sim$1540 cm^{-1} in IR spectra, which in turn is characteristic for hydroxylamine derivative of nitroxide bond. In this regard, the theoretical specific capacity for PTMA-oxidation should be around 74 mAh g^{-1} (66.6% $\times$ 111 mAh g^{-1}). This is in agreement with its initial capacity (77 mAh g^{-1}) in Figure 3.10. It is worthy to note that poly(2,2,6,6-tetramethylpiperidinyloxy-4-yl acrylamide (PTAm) and PTMA, which are polymers

bearing one radical site in each repeating unit, have practically the same specific capacity, which is 111 mAh g^{-1} and 118 mAh g^{-1}, respectively. Although the two polymeric active materials for comparison in battery performance, i.e. P$_A$-A_1 and PTMA-oxidation, differ in structure as well as in TEMPO content, the cathode based on PTMA-oxidation reached its theoretical capacity, while the cathode P$_A$-A_1 delivered a 12–22 mAh g^{-1} higher capacity at 5 C-rate in the course of 500 cycles than PTMA-oxidation. This result indicates that the enrichment in TEMPO moieties for P$_A$-A_1 accounts for the relatively higher capacity.
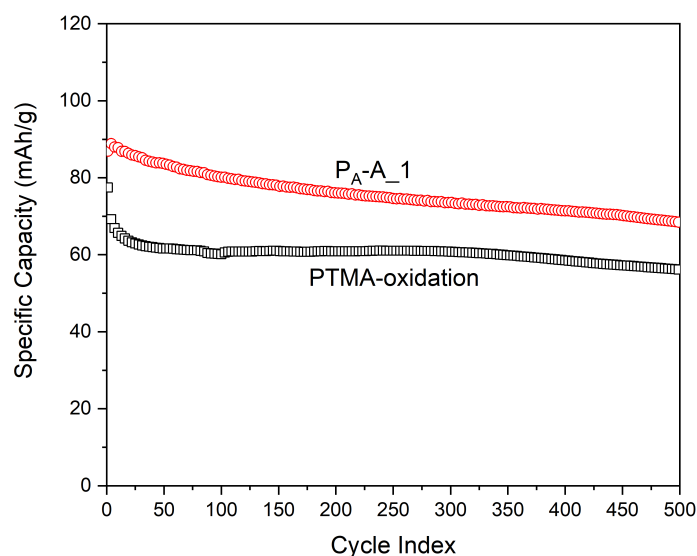
Figure 3.10.: Cycling performance of TEMPO-containing polymers.
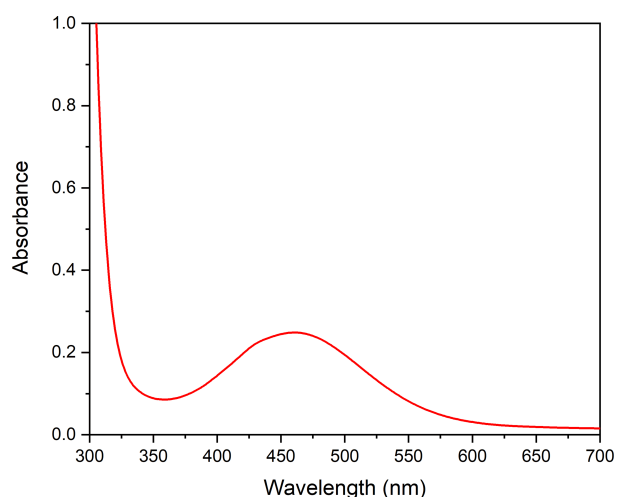
Figure 3.11.: UV/vis spectrum of PTMA-oxidation in DCM (1.0 mg mL^{-1}).

However, during the cathode processing process, it was found that both cathodes fabricated from PTMA-oxidation and P$_A$-A_1 suffered from cracking issue. Moreover, for cathodes from

Table 3.7.: Comparative molecular weight data of P_A-A_1 and PTMA-oxidation.

	P_A-A_1	PTMA-oxidation
M_n (kDa)	61.0	40.1
Đ	2.3	4.3

the same active material, e.g. PTMA-oxidation, different processing parameters, such as slurry viscosity, drying temperature, etc. resulted in apparently different battery performance, implying the processing of electrodes is also of significant importance for battery performance. As the processing of organic-based electrodes differs from the inorganic-based electrodes, which involves different formulations and configurations due to the chief distinctions in both chemical affinity and electrical conductivity between organic and inorganic compounds, further investigation on the processing of polymer-based electrodes is required. With respect to this scientific question, chapter 4 is going to give an insight.

In addition to processing issue, both P_A-A_1 and PTMA-oxidation are found to be soluble in electrolyte (1 M LiPF$_6$ in EC/DMC (v/v = 50/50)), as shown in Figure 3.12, which may account for the capacity loss of 23.5% and 27.5% after 500 cycles, respectively. In terms of this challenge, chapter 5 is going to give a solution by incorporating another functional group into the polymeric structure via a two-step PPM methodology.
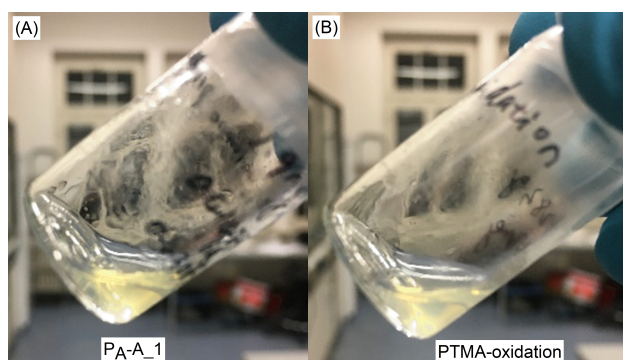
Figure 3.12.: Solubility of (A) P_A-A_1 and (B) PTMA-oxidation in 1 M LiPF$_6$ in EC/DMC (v/v) with a concentration of 4 mg mL^{-1}

3.4. Summary

In this chapter, six types of TEMPO-containing polymers were synthesized by post-polymerization modification (PPM) of PPFPA and PPFPMA with 4-hydroxy-TEMPO, 4-amino-TEMPO and

4-methylamino-TEMPO, respectively. It turned out that PPM via PFP ester is a feasible and versatile way to synthesize TEMPO-containing polymers with various TEMPO derivatives. For each TEMPO-containing polymer, the optimal reaction conditions were investigated by utilizing different solvents, catalysts, feeding ratios, reaction temperatures and reaction times. Among them, post-polymerization functionalization of PPFPA with 4-amino-TEMPO revealed an excellent functionalization degree with a TEMPO content of 96.2% within 3 hrs. under considerably mild conditions.

Moreover, it was shown that the type of catalyst and its respective loading played an important role in reaction orientation. While DMAP facilitated efficient ester bonds cleavage independent of the polymer precursor, side reactions like hydrolysis could take place because of its high basicity. In addition, high loading of DAMP (i.e. 2 eq. per activated ester) is more likely to result in hydrolysis of activated ester even with traces of water from the solvent, especially in the reaction of PPFPA with 4-methylamino-TEMPO.

Furthermore, the influence of the solvent (i.e. polarity) as well as reaction temperature and reaction time were investigated, indicating that dipolar aprotic solvents, such as NMP and DMF, were efficient irrespective the type of the PPM (e.g. amidation or transesterification), whereas high reaction temperature like 120 °C and longer reaction time like over 45 hrs. could lead to quenching of TEMPO as well as polymer solubility problems. Moreover, though most of the TEMPO-containing polymers, except P_{MA}-MA, synthesized via PPM exhibited similar TEMPO contents as the traditional post-oxidation route.

Other than that, although side reaction like hydrolysis may occur in PPM via PFP ester, which depends on the reaction conditions, the existence of carboxylic acid group arising from hydrolysis side reaction actually could promote ion transfer as least in the case of P_A-A_1, as confirmed by CV analysis.

Additionally, due to its high TEMPO content of P_A-A (96.2%), the corresponding cathode exhibited a significantly higher specific capacity (12–22 mAh g^{-1}, 12–36%) compared to PTMA-oxidation at 5 C-rate in the course of 500 cycles.

Last but not least, apart from material perspective, processing of electrodes is of great importance for battery performance, which requires further investigation. Solubility of active polymer into electrolyte was observed which may account for the relatively large capacity loss of 23.5% and 27.5% after 500 cycles in the case of P_A-A_1 and PTMA-oxidation, respectively. Owing to the versatility of PPM to incorporate various functional groups into a polymeric structure, the

solubility issue may also be addressed via PPM methodology.

4. Investigation on the Processing of Radical Polymer-Based Electrodes
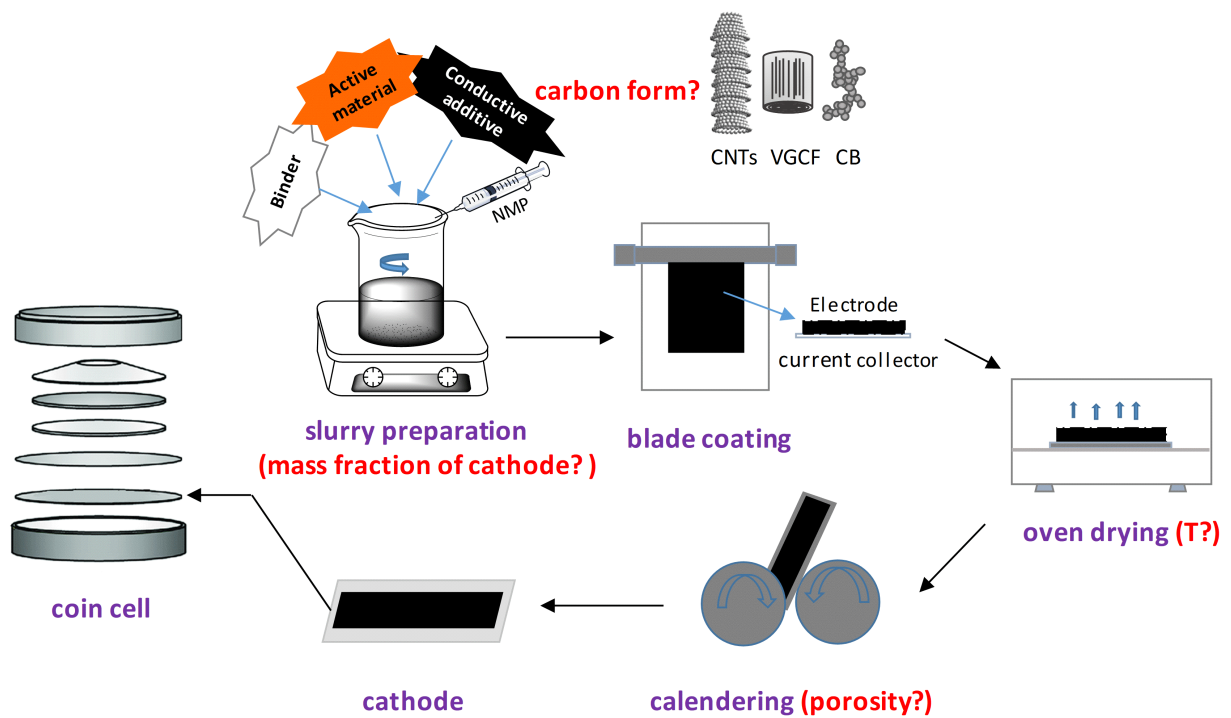
---

4.1. Prologue

Unlike inorganic-based electrodes, organic-based electrodes involve different formulations and configurations due to the chief distinctions in both chemical affinity and electrical conductivity between organic and inorganic compounds. In the case of poly(2,2,6,6-tetramethylpiperidinyloxy-4-yl methacrylate) (PTMA), it exhibits an electronic conductivity of $\sim 10^{-11}$ S cm^{-1} [29], which is much lower than that of lithium transition metal oxides ranging from 10^{-4} S cm^{-1} (LiCoO$_2$) to 10^{-9} S cm^{-1} (LiFePO$_4$) [30]. To increase the electrical conductivity of PTMA-based electrodes, large amounts (i.e. typically, 60–80 wt.%) of conductive additives in form of various carbon species, such as vapor grown carbon nanofibers (VGCF) [17], carbon black (CB) [86,87], carbon nanotubes (CNTs) [110], graphene [295], or activated carbon [327], are added during electrode preparation. Even though there are reports limiting the content of conductive agent to 45 wt.% or even lower (e.g. 30 wt.%, 32 wt.%, 10 wt.% and 4 wt.%) by gaining a homogeneous polymer composite with the conducive agent [31,86,294], or anchoring/wrapping redox polymers onto CNTs [89,93], or even encapsulating radical polymers into CNTs [328], either the battery performance and cathode thickness (e.g. 580 nm) were compromised, or the fabrication process was considerably complicated.

With a high content (e.g. over 60 wt.%) of conductive carbon additive, e.g. carbon black, cracks were more likely to be generated over the course of drying arising from capillary forces [329], thus affecting the subsequent battery performance [330–332]. Owing to the good crack control effect of short fibers (10–20 μm) as well as their good electrical conductivity (10^4 S cm^{-1}) along the fiber direction, VGCF have been adopted as the most common conductive agent since PTMA was first reported as a cathode active material in 2002 by Nakahara et al. [17]. As revealed by Suguro et al. [92], VGCF played a very important role in reinforcing the polymer-carbon composite in the electrodes and promoting the electron transfer, while carbon black additives (e.g. Ketjenblack black and acetylene black) would result in cracking of electrodes at the same filling amount (15 wt.%). Indeed, fibers have long been used for crack control and reinforcement of composites, e.g. cement and clay soils, especially during drying processes, as they can bridge cracks in the matrix and hence distribute and share evenly the generated crack stress [333,334]. In addition to the improvement in cracking resistance, the fibrous morphology results in a high flexural modulus and a low coefficient of thermal expansion, and thus endows the composite material with an increased flexibility and mechanical stability.

Although VGCF and carbon nanotubes have unique advantages, CB is more desirable in practice as a conductive additive in the field of battery application due to the following points. As

the conventional conductive agent in lithium-ion batteries (LIBs), CB facilitates charge transfer because of its large specific surface area, which could enhance electrolyte adsorption and increase the contact area with the active material [335]. Besides, the agglomeration of CB particles can form a percolated conductive structure within the active material, thus maintaining a relatively high electrical conductivity even at a packed form [39]. Also, CB is not as hazardous as carbon nanofibers (CNF) and CNTs, which on the contrary, may pose a respiratory hazard [336]. Furthermore, CB has a higher dispersibillity and better coating processability in pure solvents (e.g. dimethyl sulfoxide, *N,N*-dimethylacetamide, and *N,N*-dimethylformamide) and polymer matrices than CNF and CNTs, as the latter two are supplied in the form of heavily entangled bundles, hence require a high inherent debundling energy [337, 338]. Aside from the inherent debundling difficulties in dispersions, CNTs are also characterized by a small diameter on the nanometer scale (typically 0.4–40 nm) with high aspect ratios ($>$ 1000), thus extremely large surface areas (theoretically 1315 m^2 g^{-1} for single-walled CNTs) [339]. Additionally, CB is economically more favorable than VGCF and CNTs owing to its mature and less complex manufacturing process. Nevertheless, CB has been less reported as conductive additive in radical polymer-based electrodes probably as a result of the cracking issue at high filling amounts. Therefore, the development of novel electrode fabrication processes for radical polymer-based batteries is of critical importance.

The battery performance not only depends on the electrode materials, but also on the preparation process of electrodes. Nevertheless, most reported studies have focused on material aspect, such as synthesis [340–342], chemical structure [343, 344] and electronic properties [345, 346] of electrode materials. In fact, with respect to the complex fabrication of both inorganic and organic-based electrodes, several process factors, like slurry-mixing [346–350], slurry consistency [348, 351], drying condition [352–355], content of binder [356, 357], shape of the carbon particles [358, 359], and electrode film thickness [360, 361] have to be taken into account.

Regarding the processing of anodes, except for a limited number of reports on slurry properties, which are closely correlated with mixing methods and slurry composition [362–364], most reports focused on the drying step of anodes due to the high content of graphite used (over 90 wt.%). For example, Baunach et al. [352] reported that the adhesion force for anode films of LIBs was strongly dependent on the drying temperature. For instance, drying the anode at 55 °C gave rise to a 41% lower adhesion force than drying at 30 °C. In a similar manner, Kwade et al. [354] revealed that increasing the drying temperature from 80 °C to 130 °C caused a 29 % decrease in the adhesion strength and a simultaneous increase by 75% in resistance, owing to binder demixing in the course of drying for graphite anodes.

Compared to anodes, quite a number of reports can be tracked on processing of cathodes. For

example, Oh et al. [347] revealed that a multi-step mixing with a stepwise addition of *N*-methyl-2-pyrrolidone (NMP) into the mixture of $LiCoO_2$ powder, carbon and poly(vinylidene fluoride) (PVdF) led to a more uniform dispersion of solid ingredients in comparison with a one-step process. Besides the mixing sequence, Kuratani et al. [350] took one step further and investigated the correlation between dispersion state of particles in the slurry and the electrode performance. They demonstrated that the rate performance of $LiCoO_2$-based cathodes that are fabricated from excessively dispersed slurry was inferior as compared to one without using high shear flow. In regard to the influence of drying temperature and film thickness on cracking for $LiNi_{1/3}Mn_{1/3}Co_{1/3}O_2$ (NCM)-based cathodes prepared from aqueous slurries, Mukherjee et al. [355] revealed that cracking worsens with increased electrode thickness (11, 15, and 23 mg cm^{-2}) and elevated drying temperatures ranging from 20 °C to 70 °C, thus resulting in a decrease in battery performance in terms of specific capacity.

Critically, all the aforementioned reports are focusing on inorganic-based electrodes for LIBs. However, fewer reports are related to organic-based cathodes [13, 97]. Intriguingly, by virtue of the difference in slurry composition, the optimized processing parameters applicable for inorganic-based electrodes are not necessarily suitable to be directly utilized for organic-based cathodes, including organic radical polymer materials. Thus, in order to fill this gap, and quite importantly, to accomplish a better battery performance in a simple preparation approach, in the present study, a systematically investigation was carried out on various processing parameters for the fabrication of cathodes with PTMA as the model polymer. These parameters include the drying temperature, the mass fraction of electrode materials in the slurry, carbon particle shape and calendering. To overcome electrode cracking in a severe case, the electrode was prepared with a high content up to 80 wt.% of conductive carbon.

4.2. Influence of Different Processing Parameters on Battery Performance

To investigate the influence of processing conditions for PTMA-based cathodes on the resulting battery performance, different parameters, such as drying temperature, mass fraction of cathodes in the slurry, χ_c, coating thickness, carbon species, TEMPO content and calendering were examined.

PTMA was synthesized by post-oxidation method [25], as shown in scheme 4.1. By controlling the oxidation time, two model PTMAs with different contents of (2,2,6,6-tetramethylpiperidin-1-yl)oxyl

(TEMPO) were obtained (M_n = 40.1 kDa, $Đ$ = 4.3). Based on Electron Spin Resonance (EPR) measurements, the TEMPO contents were determined to be 66.2% and 55.2%, respectively. The samples were named as PTMA-66 and PTMA-55 accordingly, and their theoretical capacities were 73 mAh g^{-1} and 61 mAh g^{-1}, respectively. Owing to the systematic error in EPR quantification, usually close to 8–10% [365], a systematically slightly higher or lower experimental capacity is reasonable.
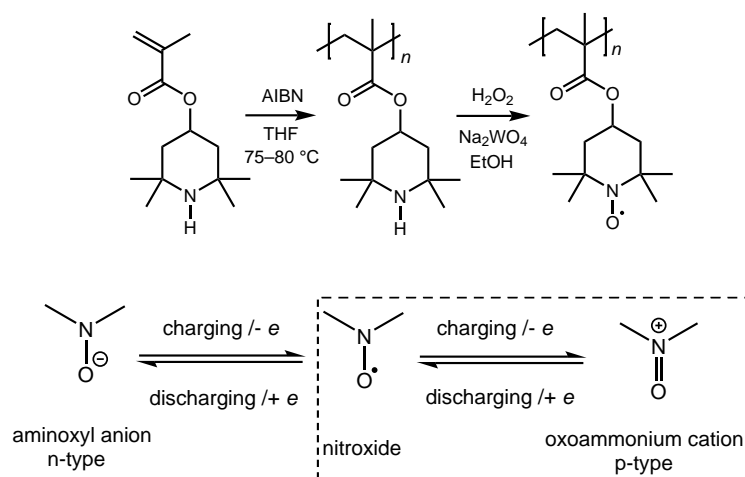
Scheme 4.1: Synthesis of PTMA and the its redox reaction during charging and discharging.

In order to control the slurry composition in a quantitative way, the mass fraction of cathode materials in the slurry, χ_c, was defined as Eq. 4.1,

$$\chi_c = m_{cathode}/m_{NMP} \tag{4.1}$$

where $m_{cathode}$ refers to the mass of cathode in mg, including PTMA, conductive additive and PVdF, and m_{NMP} is the mass of NMP in g within the slurry. The viscosity of a slurry can be reflected by χ_c.

The cathode slurry was prepared by grinding PTMA (10 mg, 10 wt.%) and conductive carbon (80 mg, 80 wt.%) in a mortar for 5 minutes, subsequently transferring the mixed powder into a vial and adding NMP. After mixing on a magnetic stirrer for 2 hrs. to completely solubilize PTMA and coat it on the surface of conductive carbon, a PVdF (10 mg, 10 wt.%) solution in NMP (10 wt.%) was added, followed by stirring the mixture overnight. The slurry was blade coated on aluminum foil (thickness 30 μm) and dried in an oven overnight at varying temperatures. Afterwards, the middle area of the coating film was chosen and punched out as disk shaped cathodes (ϕ = 14 mm). Some samples were calendered at 50 °C before punching with a calendering roll to reduce

32% of the original thickness.

Coin cells (CR2032 type) were assembled by stacking lithium anode, two pieces of separator films (PP/PE/PP) and PTMA-based cathode with 1.0 M LiPF$_6$ in EC/DMC = 50/50 (v/v) as electrolyte in an argon filled glove box, where both O$_2$ and H$_2$O contents were less than 2 ppm.

The coin cells were cycled galvanostatically in the voltage range of 3.0–4.1 V vs. Li/Li$^+$ at a charging and discharging rate of 5 C for 1000 cycles. Rate performance against the cycle number was evaluated for the PTMA-based cathodes at a variable C-rate of 0.5–10 C in the voltage range of 3.0–4.0 V vs. Li/Li$^+$. Cyclic voltammetry measurements of coin cells were performed between 3.0–4.1 V vs. Li/Li$^+$ at a scan rate of 0.1 mV s^{-1}.

To increase the data reliability and minimize the error caused by different weight/thickness of cathodes, for each coating sample, cycling performance tests were carried out on three coin cells per sample except calendering related samples which were carried out on four coin cells, and the mass tolerance of cathodes was below 0.4 mg within the sample. The difference of average cathode mass loading among all samples was less than 0.3 mg unless otherwise noted. The loading of cathode for each coin cell can be referred to Table B.1 under appendix. The detailed processing conditions for each cathode as well as their influence on the resulting battery performance, to be precise, cycling performance and rate performance, are going to be discussed in the following subsections.

4.2.1. Influence of Drying Temperature

As reported in the literature [92], high amount of carbon black (e.g. 80 wt.%) incorporated in PTMA-based cathodes led to cracking of the coating film due to shrinkage during drying. The latter occurs as a result of the large specific area of CB and its remarkable solvent adsorption capacity. When large amount of solvent is present in a slurry, a relatively strong capillary force, as the main driving force for electrode cracks, would generate during the solvent evaporation. Therefore, the drying process has a strong impact on the cracking and microstructure of cathodes. Since drying temperature is one paramount parameter to control drying process, its influence on physical electrode properties is necessary to be investigated. To examine the influence of drying temperature on the morphology and battery performance of PTMA-based cathodes, coating sample #1 (PTMA66-T50) and sample #2 (PTMA66-T80) were prepared at a drying temperature of 50 °C and 80 °C, respectively (see Table 4.1). As organic-based electrodes might be sensitive to high temperature in air, a drying temperature above 80 °C was not included in this study.

Table 4.1.: Processing parameters for coating sample #1 and #2 at different drying temperatures.

Sample ID	#1	#2
Drying temp. (°C)	50	80
Ave. mass$_{cathodes}$ (mg)	2.8	3.1
χ_c (mg g^{-1})	62.5	62.5
Conductive additive	CB-SP	CB-SP
Active material	PTMA-66	PTMA-66
Calendering	No	No

Figure 4.1A and 4.1B present the samples dried at 50 °C that possessed deeper cracks with over 10 μm larger width and 0.03 mm^2 piece^{-1} bigger spacing than samples dried at 80 °C (Table 4.2). This suggests that cathodes dried at 80 °C had a better cohesion than the samples dried at 50 °C. Moreover, SEM images (Figure 4.2A and 4.2B) indicate that, compared to sample #2 (PTMA66-T80) with the identical CB, the CB particle size in sample #1 (PTMA66-T50) is distinctively larger (mainly in 50–80 nm) with a smoother surface and less porosity, which may arise from polymer coating and agglomeration of CB. Presumably because a low drying rate at 50 °C may decrease the interparticle distance of carbon black and form a consolidation layer with a polymer-rich supernatant. Whereas, drying at higher temperatures (80 °C) led to a higher diffusion and thus more effectively equalizing the concentration gradient [352, 365]. Figure 4.3 reveals that the cathodes dried at 80 °C (sample #2) achieved an average initial capacity of 78 mAh g^{-1}, reaching essentially its theoretical capacity (73 mAh g^{-1}), while cathodes dried at 50 °C (sample #1) exhibited only an average initial capacity of 57 mAh g^{-1}, which was about the specific capacity of 80 °C-dried-cathodes after 1000 cycles. Besides, both samples showed a similar degradation tendency with a capacity loss of about 23% within 1000 cycles at 5 C. In summary, drying at 80 °C leads to a better cycling performance with a more homogeneous and less cracking cathode film than drying at 50 °C. Noteworthy, this result is converse to reports on inorganic-based electrodes both cathodes and anodes of LIBs [351, 354, 355].

Table 4.2.: Crack spacing (mm^2 piece^{-1}) for the coating samples #1–#5 and #9, respectively.

Sample ID	#1	#2	#3	#4	#5	#9
Crack spacing (mm^2 piece^{-1})	0.14	0.11	0.10	0.13	-	0.28
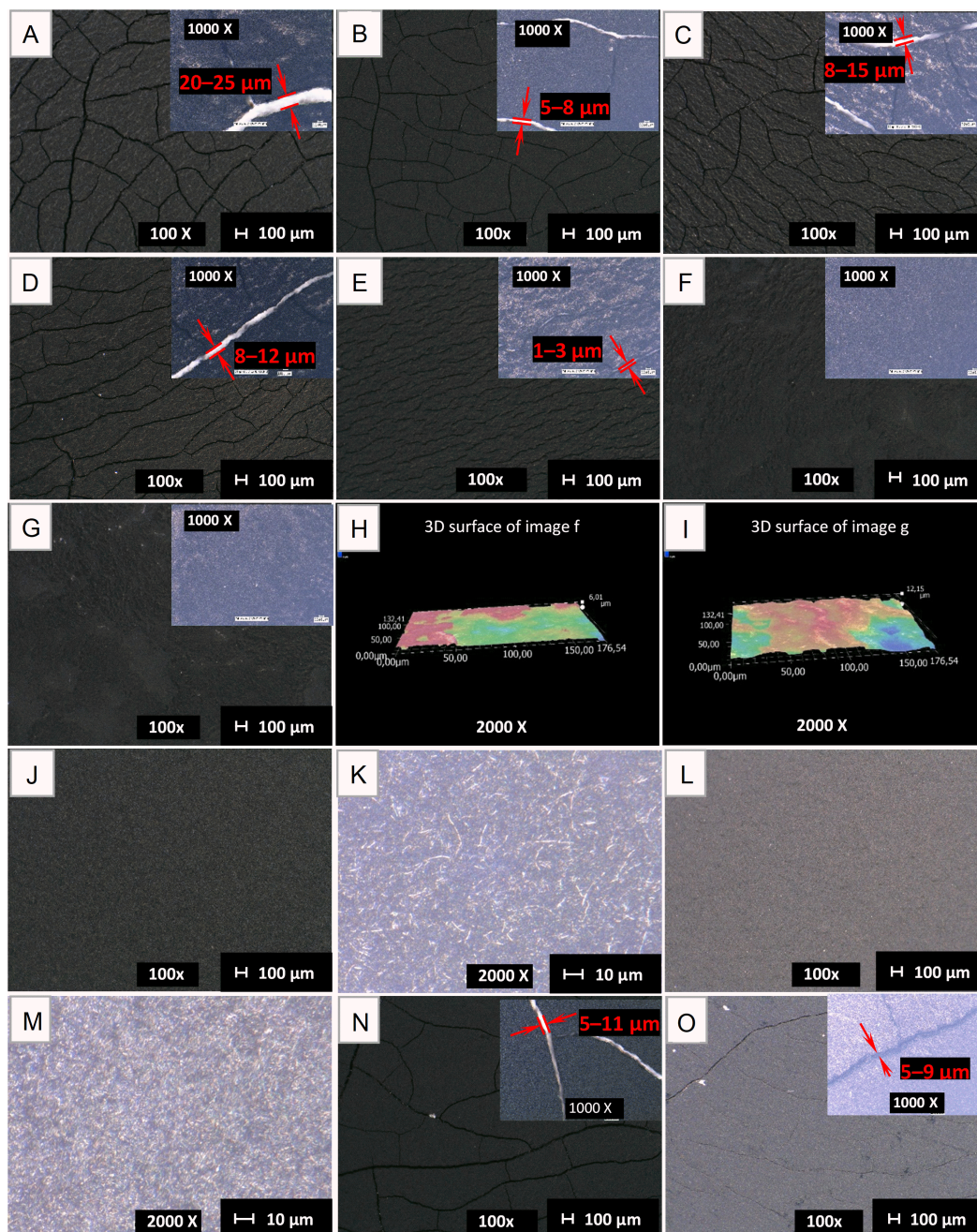
Figure 4.1.: Optical microscope images of various PTMA-based cathodes. (A) Sample #1 (PTMA66-T50); (B) sample #2 (PTMA66-T80); (C) sample #3 (PTMA66-χ76.5); (D) sample #4 (PTMA66-χ70.8); (E) sample #5 (PTMA66-χ62.5); (F) sample #6(PTMA66-χ54); (G) sample #7(PTMA66-χ46.2); (H) sample #6 (PTMA66-χ54), 3D surface; (I) sample #7 (PTMA66-χ46.2), 3D surface; (J) sample #8 (PTMA66-CB&CNF), magnification = 100 x; (K) sample #8 (PTMA66-CB&CNF), magnification = 2000 x; (L) sample #11 (PTMA55-VGCF), magnification = 100 x; (M) sample #11 (PTMA55-VGCF), magnification = 2000 x; (N) sample #9 (PTMA55-NC); (O) sample #10 (PTMA55-C).
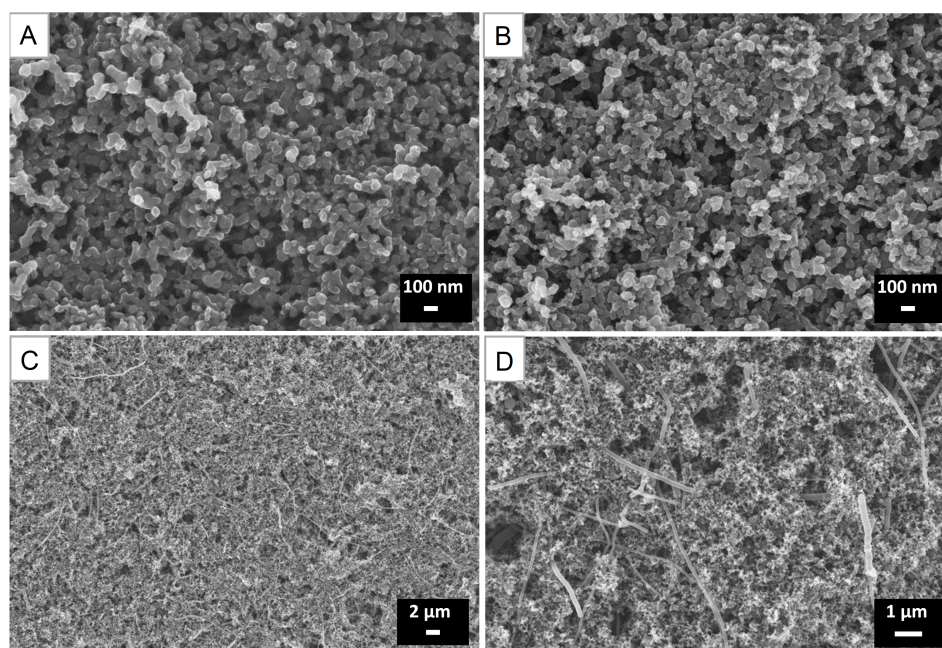
Figure 4.2.: SEM images of various PTMA-66-based cathodes. (A) sample #1 (PTMA66-T50), magnification = 100000 x; (B) sample #2 (PTMA66-T80), magnification = 100000 x; (C) sample #8 (PTMA66-CB&CNF), magnification = 5000 x; (D) sample #8 (PTMA66-CB&CNF), magnification = 200000 x.
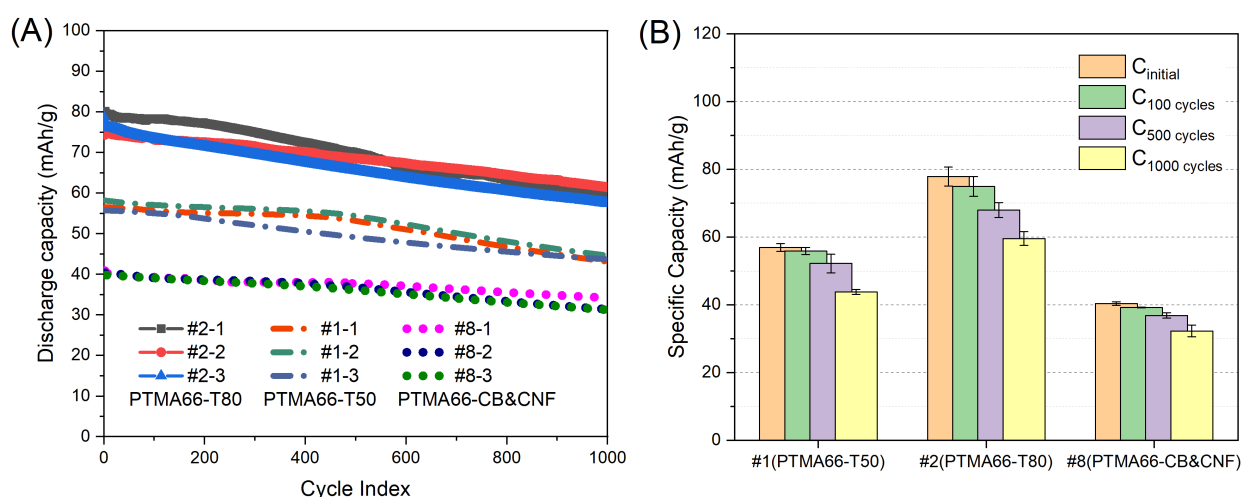
Figure 4.3.: Influence of drying temperature of the coating film and conductive additive on battery performance. (A) Life cycle curves of coin cells based on sample #1 (PTMA66-T50), #2 (PTMA66-T80), and #8 (PTMA66-CB&CNF), each sample contains three specimens, which are named as sample #2–1, #2–2, #2–3 in sample #2's case, so are sample #3 and #8; (B) average specific capacity on specified cycles.

4.2.2. Influence of Mass Fraction of Cathodes in the Slurry

It is known that thick films from colloidal dispersions are more likely to crack under drying [329]. Theoretically, there exists a critical thickness for a certain coating film above which the film would crack spontaneously [366]. The critical thickness is dependent on many factors, such as particle nature and size, solid mass fraction as well as solvent-air interfacial tension. The latter implies that surface morphology varies with different mass fraction of cathode materials in the slurry (χ_c) at a certain thickness. Therefore, with the aim to suppress the cracking, slurries with various χ_c were prepared and dried at 80 °C (see Table 4.3). In addition to morphology of cathodes, the resulting battery performances were also investigated. Due to the high fluidity of the low-viscous slurry for sample #6 (PTMA66-χ54) and #7 (PTMA66-χ46.2), it is impractical to obtain a coating film with desired thickness via a doctor blading, and thus the average mass loading of cathodes from both samples was rather low in comparison with other samples.

Table 4.3.: Processing parameters for coating sample #3–#7 with varying χ_c.

Sample ID	#3	#4	#5	#6	#7
χ_c (mg g^{-1})	76.5	70.8	62.5	54.0	46.2
Ave. mass$_{cathodes}$ (mg)	2.5	2.2	2.2	1.5	0.6
Drying temp. (°C)	80	80	80	80	80
Conductive additive	CB-SP	CB-SP	CB-SP	CB-SP	CB-SP
Active material	PTMA-66	PTMA-66	PTMA-66	PTMA-66	PTMA-66
Calendering	No	No	No	No	No

Optical microscopy images (Figure 4.1, C–I) show the change of morphology from sample #3 (PTMA66-χ76.5) to #7 (PTMA66-χ46.2) corresponding to χ_c varying from the highest to the lowest. In other words, as χ_c decreased from 76.5 (sample #3) to 62.5 mg g^{-1} (sample #5), the crack width was getting smaller in value (8–15 μm, 8–12 μm and 1–3 μm, respectively) (Figure 4.1, C–E). Moreover, from sample #3 (PTMA66-χ76.5) to sample #5 (PTMA66-χ62.5), the cracks were becoming less interlaced and the fracture direction occurred in a more oriented fashion with an average angle deviation being 12.5° for sample #5 (PTMA66-χ62.5). As χ_c was continually lowering (sample #6 to #7), the slurry became more flowable, and the coated films exhibited rougher surfaces (Figure 4.1, F and G). By means of 3D surface measurement at 2000 x magnification (Figure 4.1, H and I), sample #7 (PTMA66-χ46.2) displayed a much coarser surface than sample #6 (PTMA66-χ54), which is reflected by the more colorful image of sample #7. However, at a magnification of 100000 x via SEM, all five samples in Table 4.3 exhibited similar porous microstructures without appreciable differences (Figure 4.4).
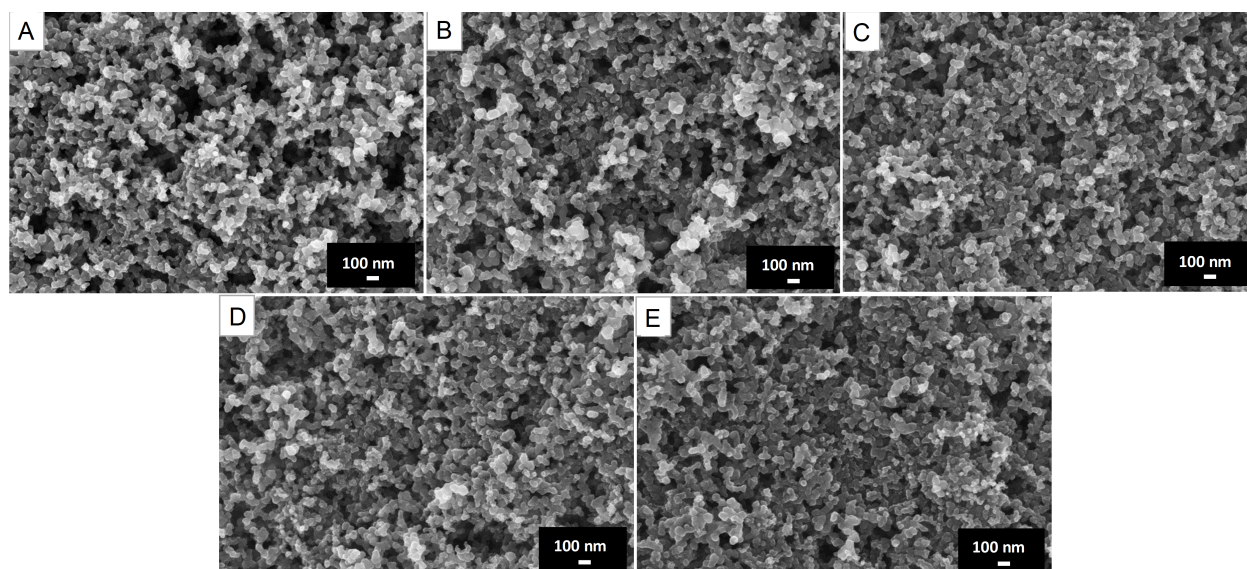
Figure 4.4.: SEM images of various PTMA-66-based cathodes with a magnification of 100000 x. (A) sample # 3 (PTMA66-χ76.5); (B) sample #4 (PTMA66-χ70.8); (C) sample #5 (PTMA66-χ62.5); (D) sample #6(PTMA66-χ54.0); (E) sample #7 (PTMA66-χ46.2).

Due to the thin coating layer and severe cracking, the capacity of cathodes fabricated from sample #3 (PTMA66-χ76.5) and sample #4 (PTMA66-χ70.8) dropped within the first 100 cycles dramatically by 38% and 32%, respectively, while, the other three samples only showed a capacity loss of 4% –13% within the first 100 cycles (Figure 4.5). The data of initial capacity ($C_{initial}$) and capacity at 100/500/1000 cycles ($C_{100\ cycles}$/$C_{500\ cycles}$/$C_{1000\ cycles}$) shown in Figure 4.6 indicates an enhancement in battery performance as χ_c is reduced from 76.5 mg g^{-1} to 62.5 mg g^{-1}. The further decrease of χ_c led to a considerable drop of the electrochemical capacity. Consequently, the cathodes fabricated from sample #5 (PTMA66-χ62.5) showed the best battery performance. For instance, cathodes from sample #5 depicted not only the highest specific capacity in all the tested cycles, but also a relatively low capacity loss within 1000 cycles at 5 C (28%, 46% and 51% for sample PTMA66-χ62.5, PTMA66-χ70.8 and PTMA66-χ76.5, respectively). It is noteworthy that the very thin slurry used for sample PTMA66-χ54 (#6) and PTMA66-χ46.2 (#7) resulted in a big capacity deviation (23–26 mAh g^{-1}) among the cathode specimens because of the inhomogeneity of the composite electrode. Overall, $\chi_c = 62.5$ mg g^{-1} was found to be a better slurry viscosity, nevertheless, either higher or lower values would impair the battery performance.
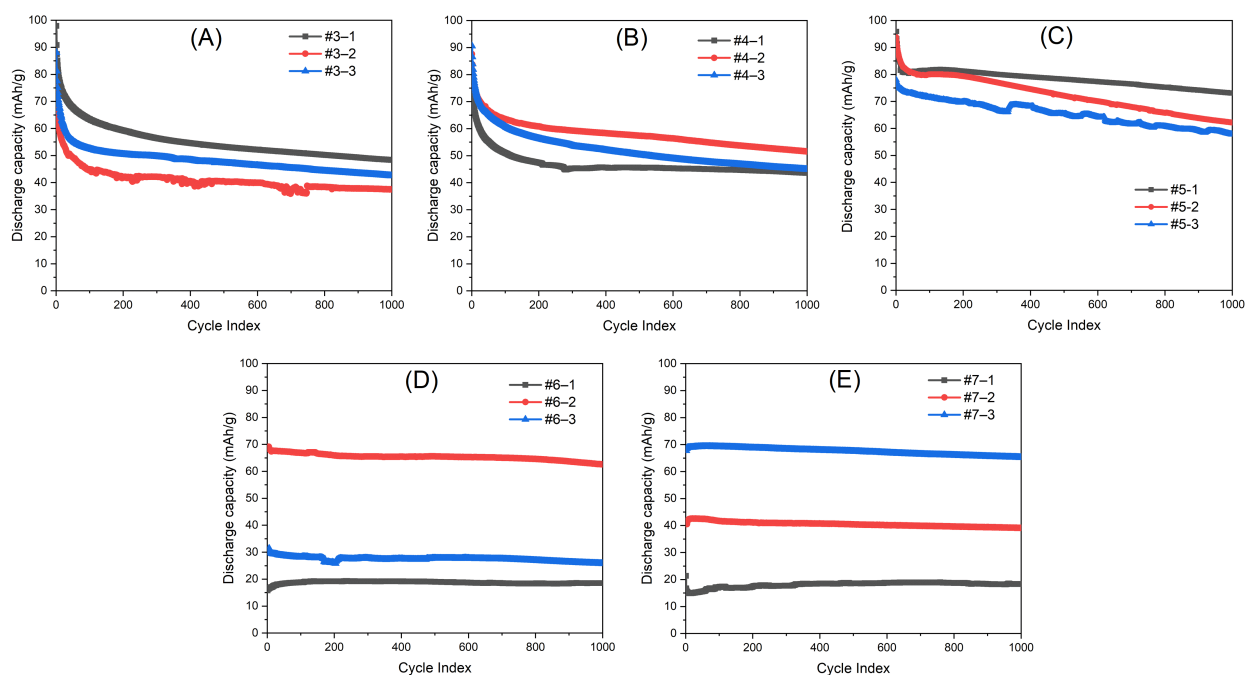
Figure 4.5.: Cycle performances of coin cells based on (A) sample #3 (PTMA66-χ76.5), (B) sample #4 (PTMA66-χ70.8), (C) sample #5 (PTMA66-χ62.5), (D) sample #6 (PTMA66-χ54.0) and (E) sample #7 (PTMA66-χ46.2). Each sample was texted with three specimen, e.g. #3-1, #3-2, #3-3 represent the three specimens for sample #3.
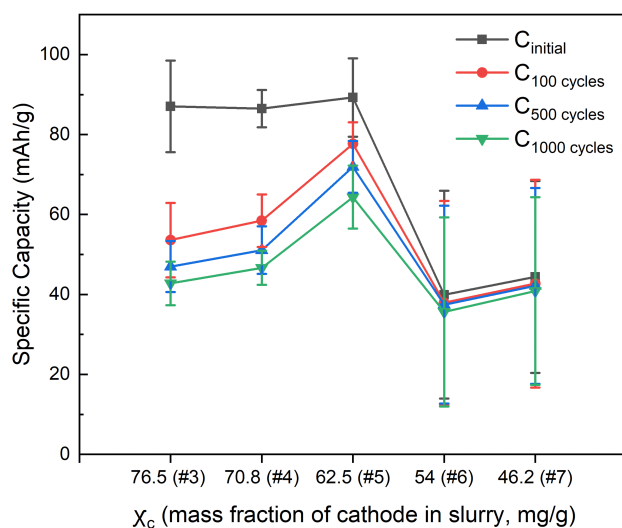
Figure 4.6.: Influence of mass fraction of cathode in slurry, χ_c, on battery performance.

4.2.3. Influence of Cathode Thickness

To investigate the influence of cathode thickness on the coating morphology and battery performance, sample PTMA66-T80 (#2, $\chi_c = 62.5$, $\sim$60 μm) and PTMA66-χ62.5 (#5, T =

80 °C, $\sim$41μm) were compared when prepared using the above-mentioned more-suited conditions, which were dried at 80 °C and has a χ_c value of 62.5 mg g^{-1}. Sample PTMA66-T80 (#2) and PTMA66-χ62.5 (#5) were prepared from the same batch but coated into cathode films with different thickness, which was 60 μm and 41 μm, respectively (Table 4.4). The thin coating film, sample #5, indeed mitigated cracking by 4–5 μm in width, as shown in Figure 4.1B and 4.1E, respectively. Compared to the thick coating film (#2), cracks in the thin coating film (#5) did not interconnect with each other and were more aligned with the average angle deviation being 12.5°. The film thickness of sample #5, which was 41 μm, was close to the critical thickness for such slurry formulation. Nevertheless, regarding cycling performance, both cathodes reached the theoretical capacity of 73 mAh g^{-1} at the initial cycle as shown in Figure 4.7. Besides, both samples presented a good cycling stability with a small degradation rate within 1000 cycles (24% and 28% for sample #2 and #5, respectively) at 5 C (see Figure 4.7 and Table 4.5). Compared to sample #2 (60 μm), cathodes from sample #5 (41 μm) exhibited a 1–3 times larger capacity deviation in the course of 1000 cycles and a 9.6% higher capacity loss in the first 50 cycles (see Figure 4.5C), which may result from the fast dissolution of active material in electrolyte owing to the thin coating layer. Besides, the thin cathodes displayed a slightly higher specific capacity by 5–11 mAh g^{-1} within the tested 1000 cycles than the thick cathodes. The latter can be attributed to the faster ion transportation and diffusion within the thin cathodes.

Table 4.4.: Processing parameters for coating sample #2 and #5 with different cathode mass.

Sample ID	#5	#2
Ave. mass$_{cathodes}$ (mg)	2.2	3.1
χ_c (mg g^{-1})	62.5	62.5
Drying temp. (°C)	80	80
Conductive additive	CB-SP	CB-SP
Active material	PTMA-66	PTMA-66
Calendering	No	No

Table 4.5.: Capacity loss (%) of cathodes #2, #5 and #8–#11, respectively, prepared under different conditions.

Sample ID	#2	#5	#8	#9	#10	#11
100 cycles (%)	3.8	13.0	3.0	2.1	1.6	1.9
500 cycles (%)	12.7	19.5	8.7	12.7	10.2	13.2
1000 cycles (%)	23.5	27.9	20.0	23.9	23.4	24.0
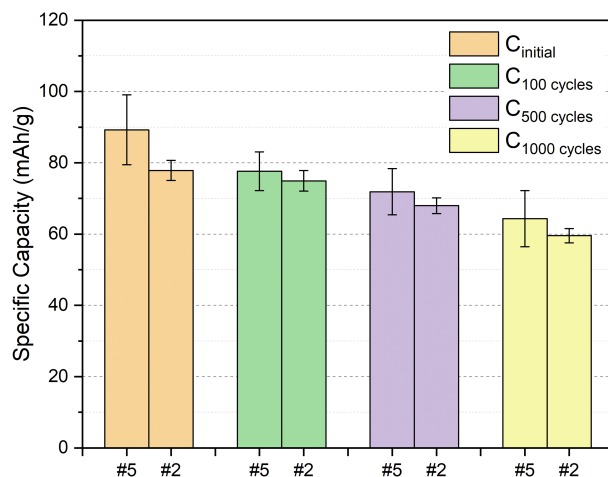
Figure 4.7.: Influence of cathode thickness on battery performance. The thickness of sample $\#5$ (PTMA66-χ62.5) and sample $\#2$ (PTMA66-T80) is 41 μm and 60 μm, respectively.

4.2.4. Influence of Carbon Nanofibers

Although CNF (VGCF excluded) can be used to reinforce constituents in a composite, their uneven electrical conductivity between longitudinal and transverse directions and coating barrier due to fiber aggregation and entangled bundling limit their extensive use in battery research. Therefore, sample $\#8$ (PTMA66-CB&CNF) was designed with a combination of CB and CNF (CB:CNF = 9:1, w/w) as a conductive additive (Table 4.6). With 10 wt.% CB being replaced by CNF, only negligible decrease of through-plane resistance was observed, as shown in Figure 4.8 (sample $\#2$ and $\#8$, respectively). At an average mass loading of 3.4 mg, which is 0.3 mg higher than cathodes from sample 2 (PTMA66-T80), a crack-free coating film was obtained, as can be seen in Figure 4.1J and 4.1K. The detailed SEM images of the morphology (Figure 4.2C and 4.2D) support the bridging and reinforcing effect of CNF in the matrix. By virtue of the homogeneous and crack-free morphology, all three cathodes fabricated from sample PTMA66-CB&CNF displayed an approximately identical discharge capacity with the maximum standard deviation being 1.7 within 1000 cycles at 5 C (Figure 4.3). Additionally, a slightly slower degradation rate was observed, which was about 4% less than sample $\#2$ (PTMA66-T80), during the first 500 cycles (see Table 4.5). Nonetheless, the average capacity of sample PTMA66-CB&CNF, which was in the range of 32–40 mAh g^{-1} over 1000 cycles, was almost half of the capacity delivered by sample $\#2$ (PTMA66-T80), which may due to the lower specific surface area of CNF (39 m^2 g^{-1}) compared to CB (62 m^2 g^{-1}). The low specific area of CNF would limit electrolyte adsorption and decrease the contact area with the active material, thus reducing the charge transfer during the charge and discharge process, while the high active surface area of CB coated with PTMA can shorten the

distance of charge transport and physical diffusion of the redox centers.

Table 4.6.: Processing parameters for coating sample #2 and #8 with different conductive additives.

Sample ID	#2	#8
Conductive additive	CB-SP	CB:CNF = 9:1
χ_c (mg g^{-1})	62.5	56.6
Drying temp. (℃)	80	80
Ave. mass$_{cathodes}$ (mg)	3.1	3.4
Active material	PTMA-66	PTMA-66
Calendering	No	No
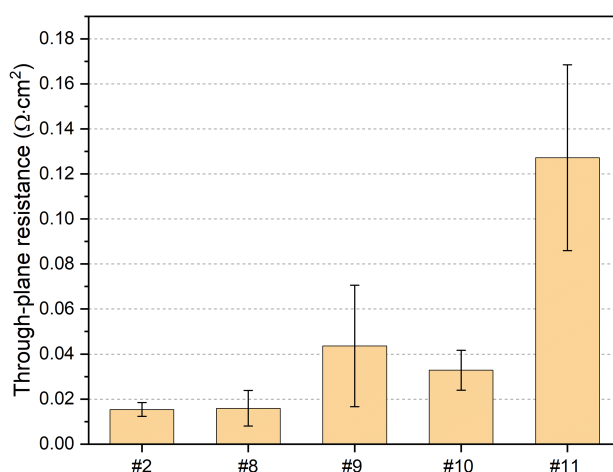
Figure 4.8.: Through-plane resistance of samples #2, #8, #9, #10 and #11. Sample #2, #8, #9, #10 and #11 represent PTMA66-T80, PTMA66-CB&CNF, PTMA55-NC, PTMA55-C and PTMA55-VGCF, respectively.

4.2.5. Influence of TEMPO Content

Two types of PTMA with different TEMPO content were prepared in this study. The names are designated as PTMA-66 and PTMA-55, indicating a TEMPO content according to EPR measurements of 66.2% and 55.2%, respectively. Hence, their theoretical capacities are 73 mAh g^{-1} and 61 mAh g^{-1}, respectively.

Based on the abovementioned analysis, the best processing conditions for PTMA-66-based cathodes were obtained at a drying temperature of 80 ℃ and χ_c = 62.5 mg g^{-1}. In a similar manner, TEMPO containing polymer, PTMA-55, was also processed under the conditions mentioned

above to verify whether the cathode can still reach its theoretical specific capacity of 61 mAh g^{-1} (Table 4.7). Compared to sample PTMA66-T80, sample PTMA55-NC also displayed cracking, but with a larger crack spacing corresponding to about 2.5 times the size of cracks in sample PTMA66-T80 (see Table 4.2), as shown in Figure 4.1B and 4.1N. Cathodes fabricated from sample PTMA55-NC exhibited an average initial capacity of 63 mAh g^{-1} at 5 C, which represents its theoretical capacity (Figure 4.9A). Theoretically, PTMA-55 has a lower capacity than PTMA-66 by 12 mAh g^{-1} (17%). In practical terms, with reference to cathodes from sample PTMA66-T80, a lower capacity of 10–13 mAh g^{-1} (15%–17%) was observed for cathodes from sample PTMA55-NC in the course of the 1000 cycles, which is in consistency with the theoretical value. Besides, both samples exhibited a similar degradation rate which was 4%/13%/24% and 2%/13%/24% at 100/ 500/1000 cycles for sample#2 and sample #9, respectively (see Table 4.5). Hence, the cathode processing conditions of choice seem indeed suitable for the preparation of cathodes from PTMA polymers independent of their active TEMPO content without hindering their final electrochemical properties.

Table 4.7.: Processing parameters for coating sample #2 and #9.

Sample ID	#2	#9
Active material	PTMA-66	PTMA-55
χ_c (mg g^{-1})	62.5	62.8
Drying temp. (℃)	80	80
Ave. mass$_{cathodes}$ (mg)	3.1	3.1
Conductive additive	CB-SP	CB-SP
Calendering	No	No

4.2.6. Influence of Calendering

Calendering is a common technique to improve the mechanical properties, increase the conductivity, and reduce the porosity of electrodes [367, 368]. Therefore, in the present study, calendering was applied to cathodes fabricated from sample PTMA55-C. Sample PTMA55-C and PTMA55-NC are from the identical slurry coated with the same film thickness, except that the former was laminated through a calender roll by 32% in thickness, while the latter was not (see Table 4.8). After calendering, the majority of cracks were fused, leaving only few big cracks, that are still visible with a smaller crack width (5–9 μm) (Figure 4.1N and 4.1O). The through-plane resistance of cathodes was reduced after calendering by 24.7% (Figure 4.8). Moreover, the deviation of through-plane resistance between the tested specimens was smaller for sample PTMA55-C,
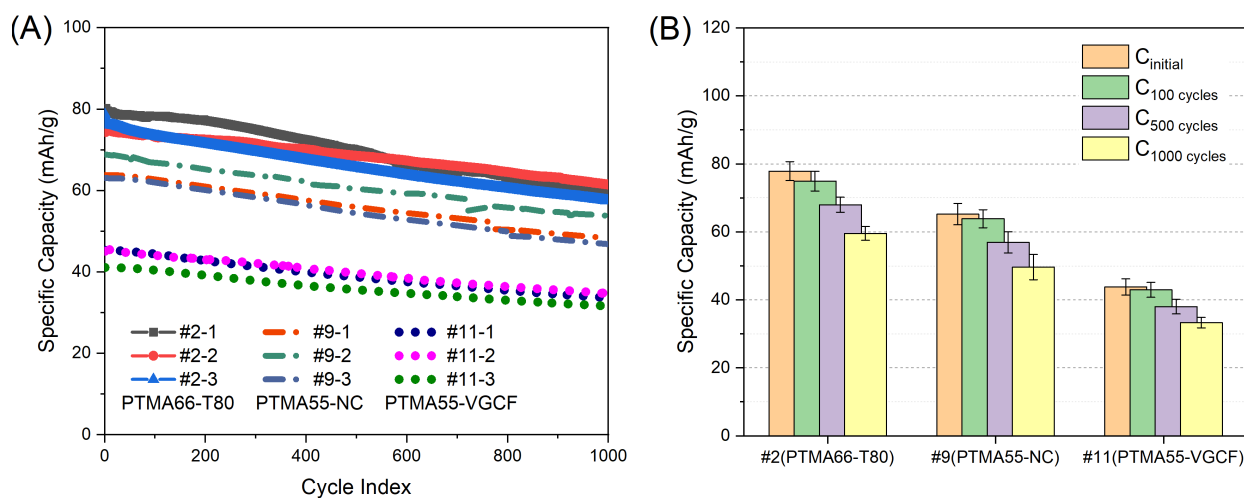
Figure 4.9.: Influence of TEMPO content and carbon forms on battery performance. (A) Life cycle curves of coin cells based on sample #2 (PTMA66-T80), #9 (PTMA55-NC) and #11 (PTMA55-VGCF), each sample contains three specimens, which are named as sample #2–1, #2–2, #2–3 in sample #2's case, so are sample #9 and #11; (B) average specific capacity on specified cycles.

indicating a more homogeneous morphology after calendering. Nevertheless, the improvement on cycling performance compared to sample PTMA55-NC was insignificant (Table 4.5) with the standard deviation getting even bigger (Figure 4.10). The latter implies that calendering with a thickness decrease of 32% does enhance adhesion, but it does not necessarily improve long time cycle performance and would impair the homogeneity of the sample. The latter may result from ion transportation barriers caused by the particle deformation and reduced porosity [368].

Table 4.8.: Processing parameters for coating sample #9 and #10.

Sample ID	#9	#10
Calendering	No	Yes
χ_c (mg g^{-1})	62.8	62.8
Drying temp. (℃)	80	80
Ave. mass$_{cathodes}$ (mg)	3.1	3.3
Conductive additive	CB-SP	CB-SP
Active material	PTMA-55	PTMA-55
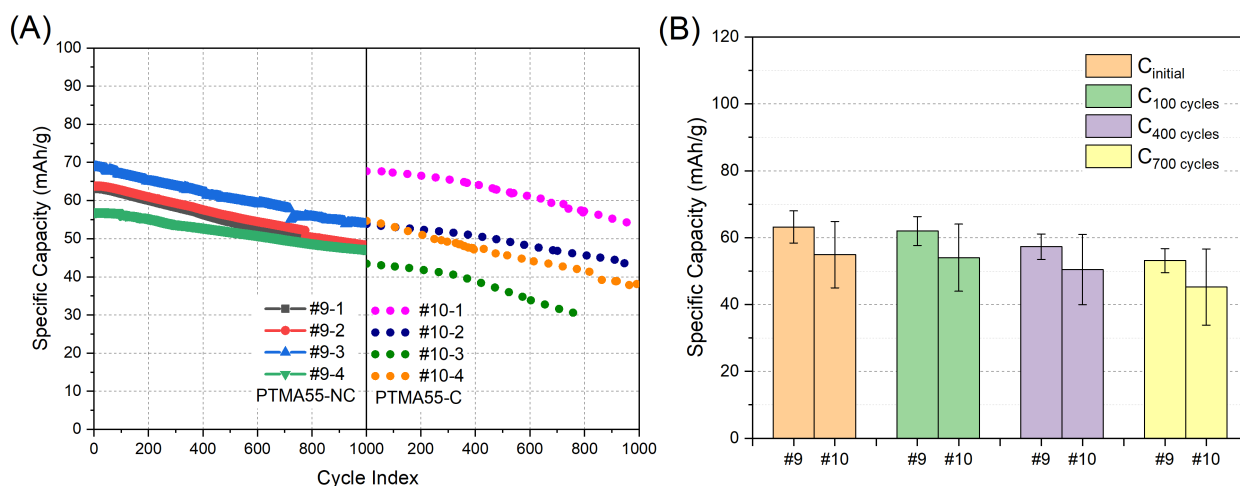
Figure 4.10.: Influence of calendering on battery performance. (A) Life cycle curves of coin cells based on sample #9 and #10, each sample contains three specimens, which are named as sample #9–1, #9–2, #9–3 in sample #9's case, so is sample #10; (B) average specific capacity on specified cycles.

4.2.7. Influence of Vapor Grown Carbon Nanofibers

Sample #11 (PTMA55-VGCF) was prepared by employing VGCF and adopting the processing condition of sample PTMA66-T80 and PTMA55-NC (drying temperature of 80 °C and $\chi_c = 62.5 \pm 0.3$ mg g^{-1}) (see Table 4.9). Indeed, VGCF is the most commonly used conductive agent in radical polymer-based electrodes, instead of CB as conductive agent. A crack-free coating film was obtained (Figure 4.1L and 4.1M), which is in line with other reports [92]. The three cathode specimens from sample PTMA55-VGCF (#11) showed a comparable cycling performance with the standard deviation in the range of 1.5 –2.4 within 1000 cycles (see Figure 4.9). Furthermore, a similar degradation rate of 2%/10%/23% at 100/500/1000 cycles was observed compared to cathodes from sample PTMA55-NC (#9) which was 2%/13%/24% (Table 4.5). However, its average capacity was about 33% (16–21 mAh g^{-1}) lower than that of cathodes from sample PTMA55-NC (#9) in the course of 1000 cycles. The latter can be explained by the higher through-plane resistance of the VGCF-based coating (Figure 4.8, sample #9, sample#11), whose average resistance was 2.9 times of the coating using CB, i.e. sample #9 (PTMA55-NC). The high through-plane resistance of sample PTMA55-VGCF resulted from the poor electron transportation in the radial direction of tubular-shaped VGCF [369], thus, demonstrating that CB appears to be a better conductive agent than VGCF, when the processing parameters for electrode preparation are appropriately selected.

Table 4.9.: Processing parameters for coating sample #9 and #11.

Sample ID	#9	#11
Conductive additive	CB-SP	VGCF
χ_c (mg g^{-1})	62.8	62.3
Drying temp. (℃)	80	80
Ave. mass$_{cathodes}$ (mg)	3.1	3.4
Active material	PTMA-55	PTMA-55
Calendering	No	No

4.2.8. Rate Performance

As the aforementioned cycling performances were carried out at 5 C, the impact of varying the C-rate was investigated for sample #2 (PTMA66-T80), sample #8 (PTMA66-CB&CNF), sample #9 (PTMA55-NC) and sample #11 (PTMA55-VGCF), respectively. From 0.5 C to 10 C, sample #2 exhibited the highest discharge capacity, followed by sample #9 and sample #11, whereas sample #8 showed the lowest discharge capacity (see Figure 4.11A). Besides, sample #2 (PTMA66-T80) also showed the highest retention (71–96%) when running at higher C-rates than 0.5 C (see Figure 4.11B). Unexpectedly at 10 C, the retention of sample #2 could reach 71%, while the values for the other three samples dropped dramatically with less than 60% capacity remaining. Intriguingly, sample #8 (PTMA66-CB&CNF) showed about 32–36 mAh g^{-1} lower discharge capacity than sample #2 at each test C-rate, although only 10 wt.% of the conductive agent being CNF while the rest 90 wt.% being CB in sample #8. The latter implies the poor effect of CNF as a conductive additive on improving PTMA-based battery performance. On the contrary, sample #11 (PTMA55-VGCF) exhibited a similar capacity retention below 5 C as sample #2, which was about 4–8% higher than sample #9 (PTMA55-NC). At 10 C, a 12% lower capacity retention was observed in comparison to sample #2, which was still 15% higher than sample #9. Additionally, 94% of the capacity was recovered for sample #11 and sample #2 when cycled back at 0.5 C for the last 5 cycles, demonstrating a good stability of the cathodes. The latter indicates that VGCF indeed plays a certain role in enhancing rate performance, despite that the corresponding cathodes did not reach the theoretical capacity (61 mAh g^{-1}). Compared to sample #2 (PTMA66-T80), sample #9 (PTMA55-NC), which has 11% less TEMPO content (12 mAh g^{-1}) in the PTMA active material, showed a 7–13 mAh g^{-1} lower capacity at C-rate below 5 C; nevertheless, a significant capacity gap by 27 mAh g^{-1} was observed at 10 C. This may be due to the 1.8 times higher through-plane resistance of sample #9 compared to sample #2 (see Figure 4.8), which would limit the efficient electron transfer, especially at high C-rates.
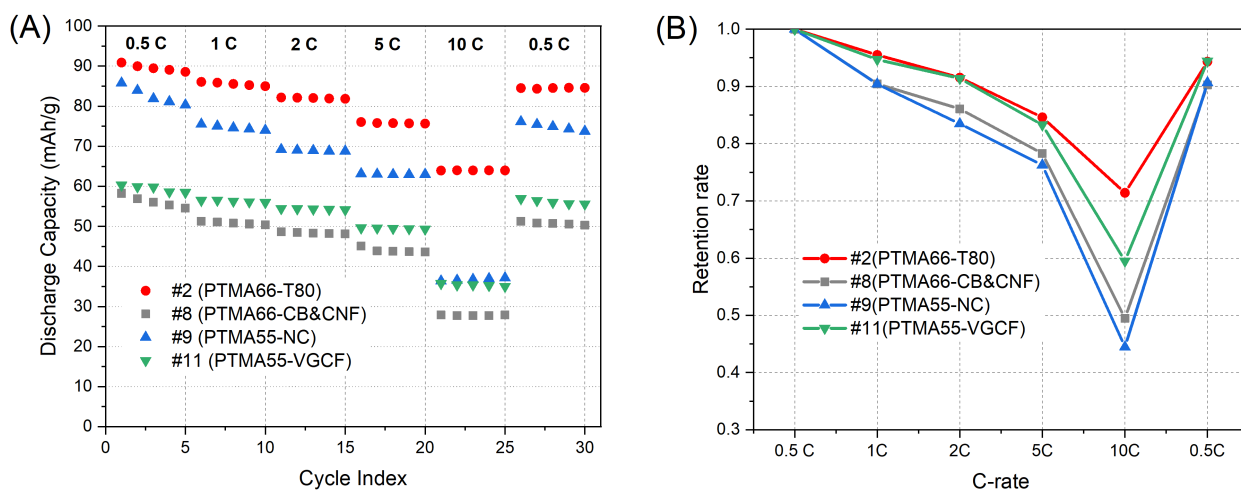
Figure 4.11.: Rate performance of sample #2, #8, #9 and #11. (A) Discharge capacity at different C-rate; (B) capacity retention at different C-rate.

It is worth noting that at 5 C the discharge capacity of sample #2 and #9 reached the theoretical capacity of PTMA-66 and PTMA-55, respectively. However, at lower C-rates both samples showed higher capacity than the theoretical value. This was attributed to the two electron redox reaction of PTMA (see scheme 4.1) with the corresponding redox potential at 2.8–3.1 V (aminoxy anion to radical, n-type) and 3.5–3.7 V (radical to an oxoammonium cation, p-type) vs. Li/Li$^+$ [370]. The galvanostatic charge/discharge curve of sample #2 (see Figure 4.12A) reveals that aside from the distinct voltage plateau at 3.6 V corresponding to the redox reaction between nitroxide and oxoammonium, another voltage plateau at around 3.1 V was also detected when the sample was tested at 0.5 C, 1 C and 2 C, which in turn additionally contributed to the overall discharge capacity. The appearance of the second plateau at 3.1 V can also be confirmed by potentiostatic cyclic voltammetry curve of sample #2 (see Figure 4.13). At C-rate higher than 5 C, the second voltage plateau at around 3.1 V disappeared, which indicates the discharge capacity was fully ascribed to p-type redox behavior. Likewise, sample #9 and #11 also exhibited a similar phenomenon (see Figure 4.12C and 4.12D, respectively). However, sample #8 exhibited a low columbic efficiency especially at 0.5 C and 1 C, which were 65% and 83%, respectively (see Figure 4.12B). This result further proves the advantage of CB over CNF on improving battery performance as a result of the large specific area and extensive electron percolation network within PTMA matrix. It is relevant to note that due to the poor reversibility of n-type redox process in conventional organic electrolytes [249], in the present work, all cycling performance were carried out at 5 C in order to eliminate the redox effect of n-type redox behavior of the TEMPO units with PTMA.
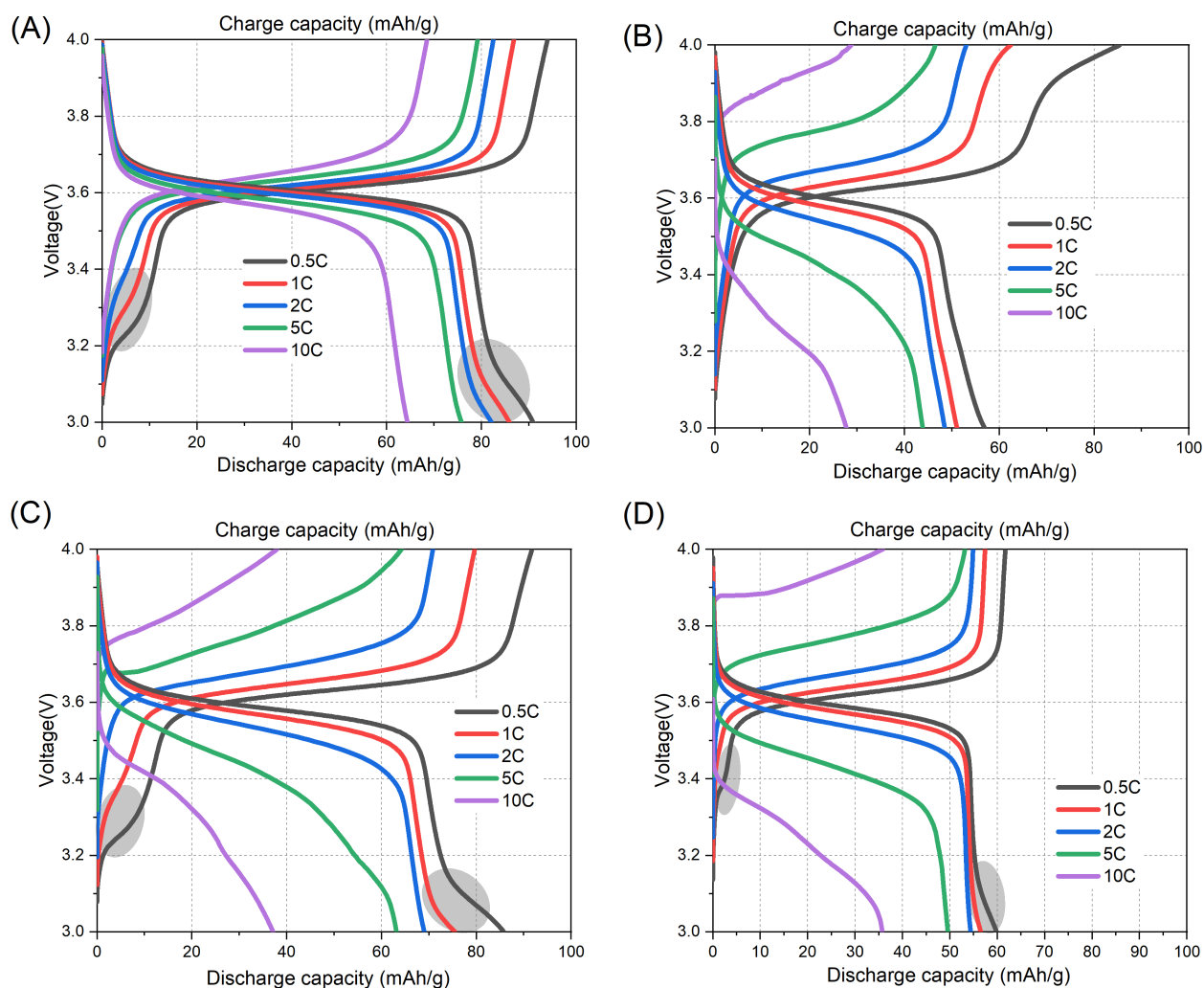
Figure 4.12.: Galvanostatic charge/discharge curves of PTMA66- and PTMA55- based cathodes. (A) sample #2 (PTMA66-T80); (B) sample #8 (PTMA66-CB&CNF); (C) sample #9 (PTMA55-NC); (D) sample #11 (PTMA55-VGCF). The area marked in grey circle indicates the n-type redox process of TEMPO.

4.3. Summary

While there is growing interest towards the development of organic-based batteries, there is still a tremendous lack of knowledge on engineering of organic-based electrodes. Therefore, in an effort to achieve a better battery performance for PTMA-based electrodes with a simple stirring approach, in the present study, different processing parameters including the drying temperature, the mass fraction of electrode materials in the slurry, carbon forms and calendaring, were investigated. To overcome electrode cracking in a severe case, up to 80 wt.% of conductive carbon was incorporated into the fabricated cathodes.
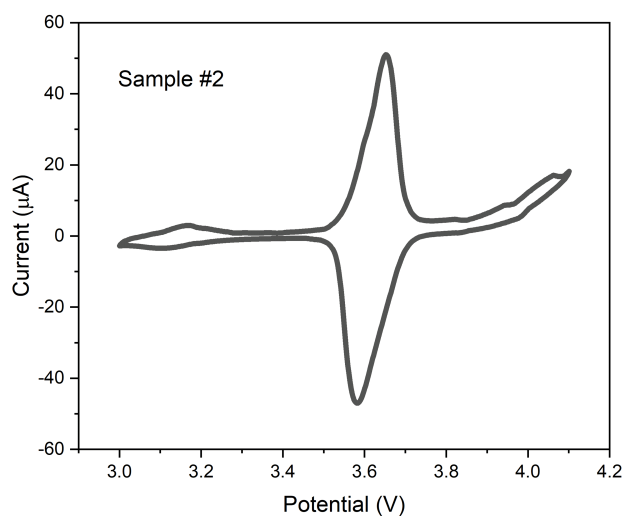
Figure 4.13.: Potentiostatic cyclic voltammetry of coin cells based on sample #2 (PTMA66-T80) at a scan rate of 0.1 mV s^{-1} in the voltage range of 3.0–4.1 V vs. Li/Li$^+$.

The well-suited processing conditions could be summarized as follows: drying temperature of 80 °C and mass ratio between cathode and NMP in the slurry (χ_c) being around 62.5 mg g^{-1} regardless of TEMPO content. Under these optimal conditions, it is postulated that CB is a better conductive agent than VGCF and CNF in the fabrication of PTMA-base cathodes, as it not only results in the highest discharge capacity, but also exhibits the best rate performance, although VGCF and CNF have bridging and reinforcement effect on the composite electrode. Moreover, the critical thickness under these conditions is close to the thickness (41 μm) of sample #5 (PTMA66-χ62.5), which has a cathode loading mass of 2.2 mg. Contrary to reports on inorganic-based electrodes of LIBs [352, 354], cathodes dried at 80 °C exhibited a better cycling performance with a more homogeneous and less cracking morphology than the ones dried at 50 °C. As χ_c decreased from 76.5 to 62.5 mg g^{-1}, the cracking phenomena alleviated and the battery performance showed an increase in terms of specific capacity. While, the continuous decrease of χ_c led to inhomogeneous cathodes formulations with coarse surfaces and strongly deteriorated specific capacity. Carbon nanofibers were effective to reduce cracking for coating films even when replacing only 10 wt.% of CB, however, the discharge capacity was greatly compromised, and the capacity contribution from n-type doping was observed even at a low dicharge rate of 0.5 C, which differs from the other two carbon additives. Additionally, calendering with a compression of 32% does enhance adhesion, but does not also necessarily improve the long term cycling stability and even leads to bigger performance deviation of cathodes.

Therefore, it can be concluded that the processing of cathodes is an important part to be reckoned within the expanding research field of organic batteries. Indeed, knowledge about the optimal

conditions, like slurry viscosity and drying temperature for PTMA-based cathodes, is critical for reducing the crack density as well as improving the cell charge-discharge property and cycling life. Nevertheless, this study paves the way for the fabrication of organic-based electrodes without hindering the electrochemical properties of active materials, especially in the aspect of developing and testing organic-based electrodes in lab research.

5. Structural Design of Pyrene-Functionalized TEMPO-Containing Polymers for Enhanced Electrochemical Storage Performance

---

5.1. Prologue

Although radical-containing polymers (RCP), e.g. poly (2,2,6,6-tetramethylpiperidinyloxy-4-yl methacrylate) (PTMA) have received substantial attention due to their excellent rate capability and extraordinary cycle life [20, 21], two major downfalls are hindering their further application as electrode materials. On one hand, the poor electrical conductivity of RCPs (e.g. 10^{-11} S cm^{-1} for PTMA) [29], which impedes the electron transport throughout the electrode layer, results in low charging/discharging capacity. On the other hand, solubility of RCPs in conventional organic electrolytes, e.g. carbonate-based electrolytes, lead to a rapid self-discharge and capacity loss [25, 31].

To tackle the aforementioned problems, various strategies have been attempted including synergistic approaches, such as covalently binding of RCP onto the surface of highly conductive carbon agents (HCAs), e.g. carbon nanotubes (CNTs) and graphene [89, 295] and molecular-level anchoring of the multiple pyrene-functionalized RCPs on HCAs via π-π stacking between the pyrene functional groups and HCAs [23, 253, 296]. Since the former method is synthetically tedious and may result in electrodes with impaired conductivity [253, 371, 372], the "molecular glue" strategy based on non-covalent π-π interactions is more appealing. In fact, recently two types of hydrophobic polymeric structures with covalently bound pyrene and TEMPO units have been reported [253, 296]. Both synthesis methods rely on the conventional post-oxidation method of the parent piperidine derived polymers synthesized via controlled radical polymerization. In both cases, TEMPO conversions were in the typical range of 60–80% [25], and the pyrene moiety was separated from the polymer backbone via a methylene-ester group linker of the type –(CH$_2$)–(CO)–O–.

As an inertness and robust structural linkage with propensity for hydrogen bonding, amides not only play an important role in both living systems (e.g. proteins) and materials science and engineering (e.g. Nylon), but also act as useful handle for the transmission of electronic effects via cross conjugation [373]. Nevertheless, the understanding of the effects of amide bonds as tethering spacers on the characteristics of TEMPO-pyrene copolymers has remained unrevealed. Thus, in order to gain an insight, in the following sections polyacrylamide-based radical polymer derivatives, i.e. poly[(1-pyrene acrylamide)-*ran*-(4-TEMPO acrylamide)] (P(PyAm-*ran*-TAm), P1 and P2 in Scheme 1) decorated with varying amide-bonded pyrene were synthesized and the respective electrochemical properties were investigated by comparing with poly[(1-pyrenemethyl acrylate)-*ran*-(4-TEMPO acrylamide)] (P(PyMA-*ran*-TAm), P3 in Scheme 1), in which the pyrene moiety was inserted through a methylene-ester linker, in order to permit the evaluation of the spacer effect in the absence of strong electronic coupling with the aromatic unit. The copolymers

(P1-P3) were further fabricated into electrodes through noncovalent π-π stacking between pyrene groups and the planar surface of CNTs in order to reveal their potential as energy storage materials.
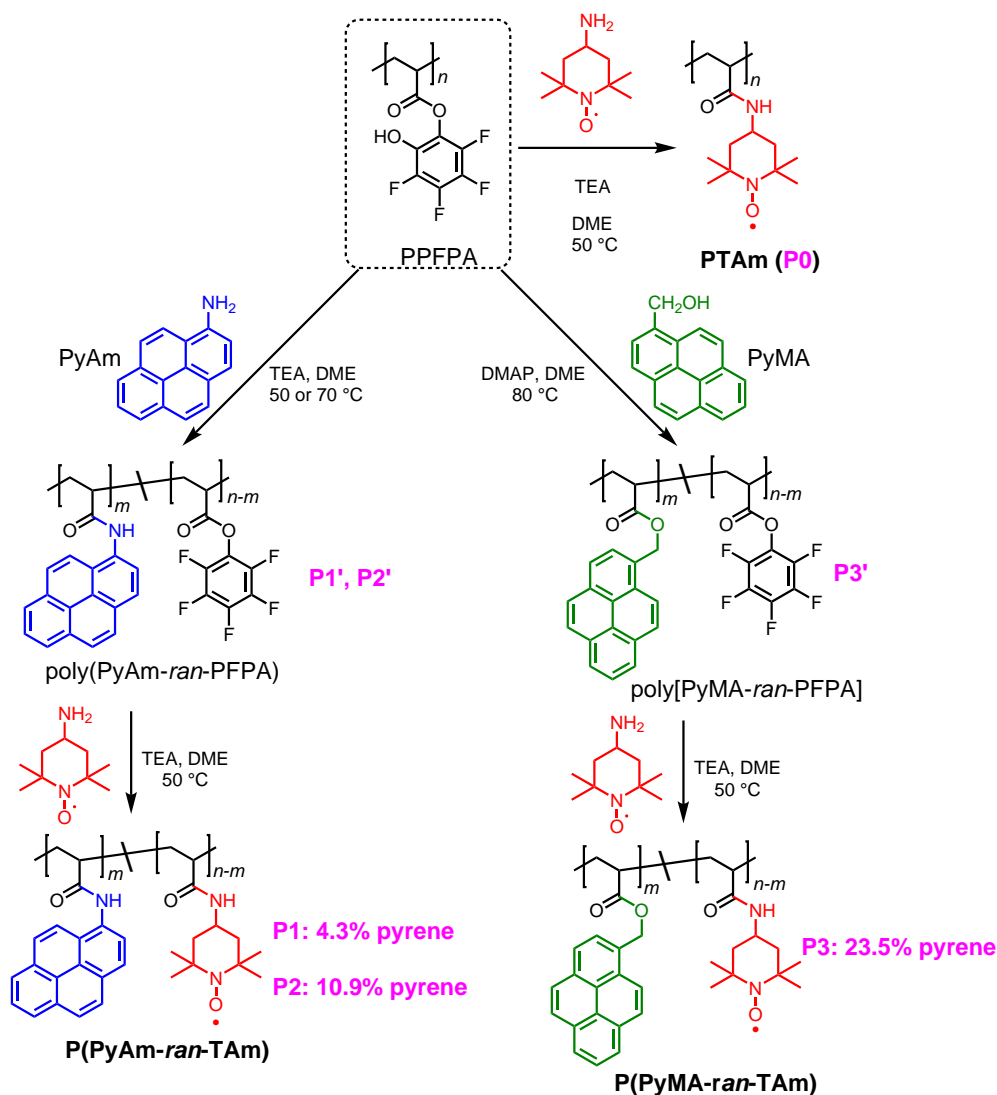
Scheme 5.1: Synthetic route towards (A) PTAm (P0), (B) P(PyAm-*ran*-TAm) (P1, P2) and (C) P(PyMA-*ran*-TAm) (P3), respectively.

5.2. Synthesis and Characterization of Pyrene-Functionalized TEMPO-Containing Polymers

To efficiently incorporate TEMPO and different pyrene moieties (e.g. 1-pyrene acrylamide, PyAm, and 1-pyrenemethyl acrylate, PyMA) into the polymeric structure, while keeping the degree
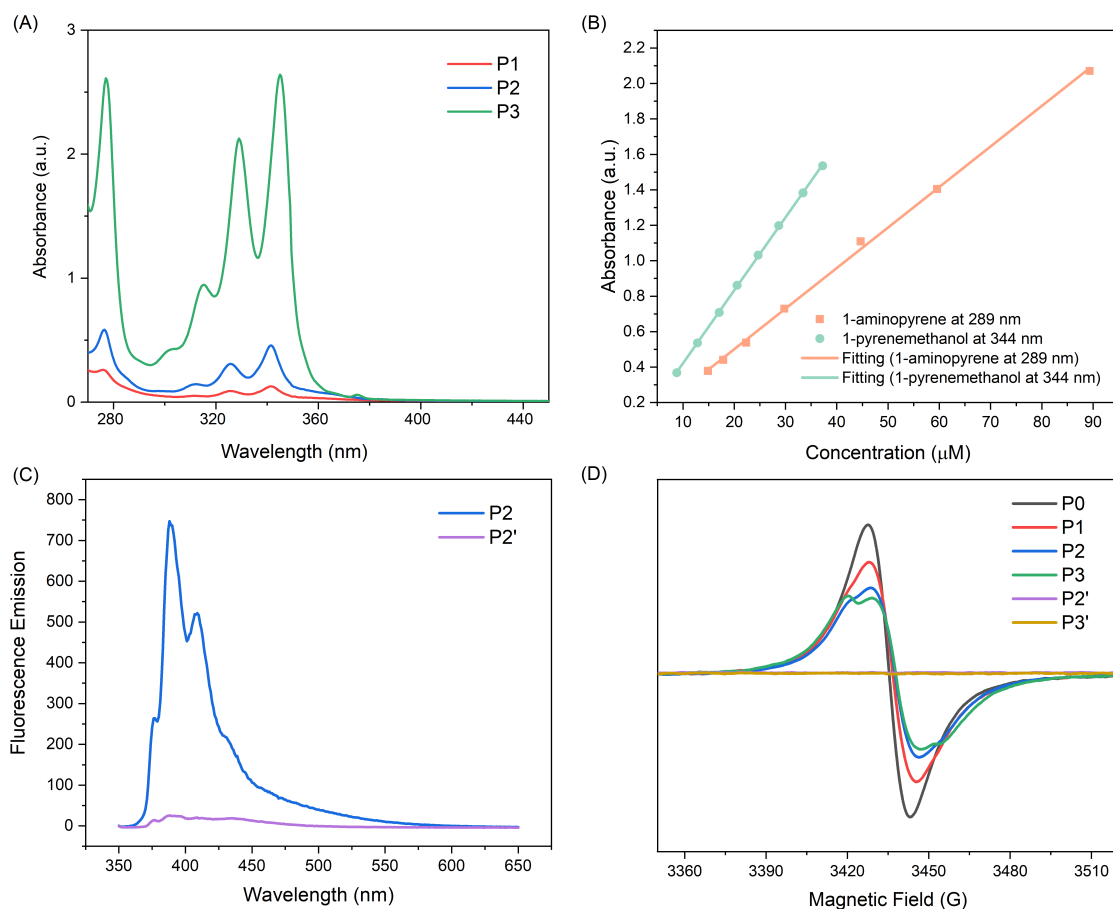
Figure 5.1.: (A) UV/Vis spectra of multiple pyrene functionalized TEMPO-containing polymers (P1-P3, c = 0.05 mg mL^{-1}). (B) UV/Vis absorption calibration curves of pyrene derivatives. (C) Fluorescence spectra of P2 and P2'. (D) EPR spectra of P0–P3 and PPFPA-based copolymers with pyrene moieties (P2' and P3', c = 0.99 mg mL^{-1}). All spectra were recorded in DMAc at ambient temperature.

of polymerization and dispersity in principle the same, post-polymerization modification via activated ester (namely pentafluorophenyl (PFP) ester) was employed (Scheme 5.1). In the first step, poly(pentafluorophenyl acrylate) (PPFPA) with number-average molecular weight (M_n) of 23.3 kDa and dispersity ($Đ$) of 2.2, was synthesized via free-radical polymerization. In order to emphasize the influence of the amide-bonded pyrene moiety on the final material properties, initially only polyacrylamide backboned homopolymer, PTAm (Scheme 5.1, P0) [286], with high radical content (96.2%) has been prepared by reacting PPFPA homopolymer with 4-amino-TEMPO. Further, multi-pyrene PTAm samples (P1 and P2) have been prepared via sequential one-pot post-modification of PPFPA with 1-aminopyrene and 4-amino-TEMPO. Random copolymer structures were targeted to favor the π-π interactions with the CNTs. By varying the reaction temperature during the aminolysis step (50 ℃ and 70 ℃, respectively) of PPFPA with 1-aminopyrene, the

pyrene content within the resulting P(PyAm-*ran*-TAm) could be altered. As shown in Figure 5.1A, the UV/vis absorbance maxima for P2 solution (0.05 mg mL^{-1}) in dimethylacetamid (DMAc) at 276 nm ($S_0 \rightarrow S_2$), 326 nm ($S_0^{\nu = 0} \rightarrow S_1^{\nu = 1}$) and 342 nm ($S_0^{\nu = 0} \rightarrow S_1^{\nu = 0}$) corresponding to the two electronic transition moments of pyrene group was higher than that of P1. Based on the calibration plot of UV/vis absorption at 289 nm for 1-aminopyrene (Figure 5.1B) and Beer-Lambert Law, the amide-bonded pyrene content within P1 and P2 is determined to be 4.3% and 10.9%, respectively (Table 5.1). Whereas for P3, the pyrene content was regulated via the molar feed ratio between 1-methanolpyrene nucleophile and PPFPA, and was assessed to be 23.5% (Table 5.1) based on the calibration plot of 1-pyrenemethanol at 344 nm (Figure 5.1B). Fluorescence quenching of the pyrene group was observed when TEMPO moieties were introduced, as shown in Figure 5.1C with P2 as the example. Nevertheless, for all samples (e.g. P1-P3), the content of radical (i.e. TEMPO), was also calculated according to the spins recorded on an electron paramagnetic resonance (EPR) spectrometer (see Table 5.1) in DMAc solutions (0.99 mg mL^{-1}), which was in agreement with the results of UV/vis analysis. Whereas, both P0 and P1 exhibited a classic Lorentzian shape (Figure 5.1D) due to the strong intermolecular spin-exchange (radical-radical) interaction arising from the close spatial proximity between the paramagnetic units. P1 displayed a relatively low intensity compared to P0, indicating a lower TEMPO content. Apart from the domain broad Lorentzian-like component, P2 and P3 revealed a triplet splitting, particularly in the case of P3. The latter clearly implies a decrease in average radical-radical spacing induced by an increase in pyrene unit along the polymer chain.
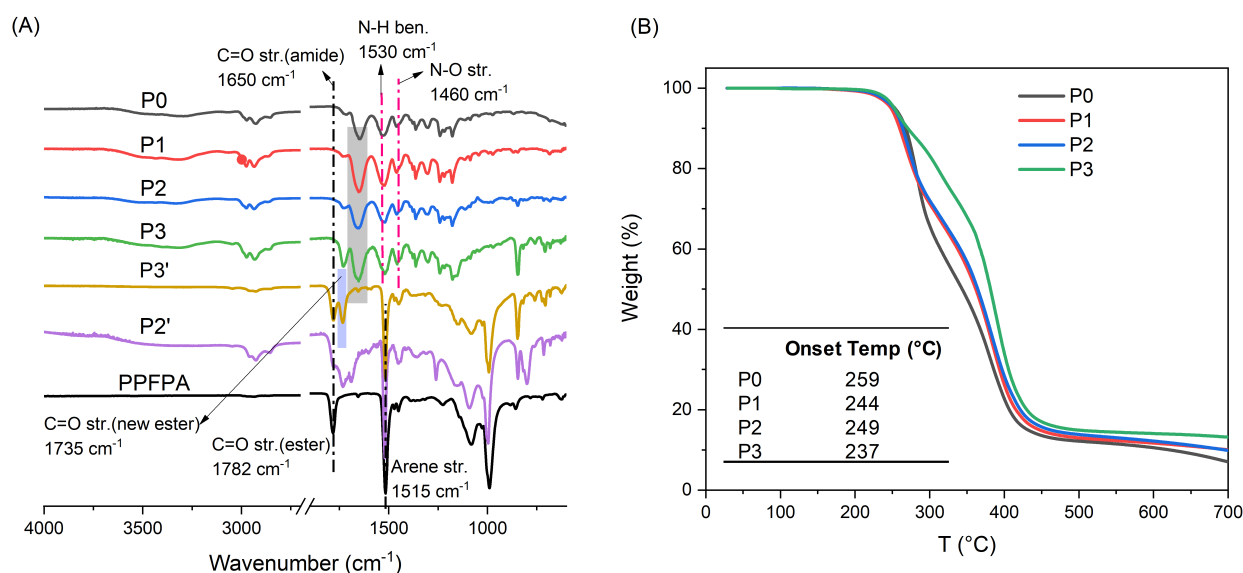
Figure 5.2.: (A) FTIR spectra of P0-P3 and PPFPA-based copolymers with pyrene moieties (P2', P3'). (B) TGA curves showing the mass loss of P0-P3 under N$_2$.

Table 5.1.: Molecular composition, molecular weight and dispersity as well hydrodynamic size in DMAc for PPFPA and P0–P3.

Sample	Pyrene content[a]	TEMPO content[b]	M_n[c]	$Đ$[c]	R_H[d]
	%	%	kDa		nm
PPFPA	-	-	23.3	2.2	6.5
P0	0	96.2	48.5	3.0	4.2
P1	4.3	92.5	37.8	3.1	5.6
P2	10.9	87.3	30.9	2.8	3.6
P3	23.5	71.5	34.1	3.0	3.1

[a] determined by UV/vis spectroscopy;
[b] determined by EPR spectroscopy;
[c] determined by size exclusion chromatography in DMAc and calculated with PMMA as the calibration standard;
[d] based on number-size distribution from DLS measurement.

Importantly, it should be noted that all polymers analyzed within in this work were derived from the same PPFPA parent polymer, thus possessing the same chemical and analytical information in regard to polymer backbone structure with the same degree of polymerization and dispersity (Table 5.1). Indeed, as exhibited in FTIR spectra (Figure 5.2A), the characteristic C=O band at 1782 cm^{-1} and arene C-C band at 1515 cm^{-1} for PFP ester disappeared completely in P0-P3. Meanwhile, new peaks at 1460 cm^{-1}, 1530 cm^{-1}, 1650 cm^{-1}, 1735 cm^{-1} corresponding to the vibrations of N-O stretch, N-H bending, C=O (amide) stretch (P0-P2), and C=O (new ester) stretch (P3), respectively, were observed as indication for the successful polymer modification. In comparison, P(PyAm-*ran*-PFPA) (P2') and P(PyMA-*ran*-PFPA) (P3'), which is the direct precursor polymer of P2 and P3, respectively, exhibited decreased infrared absorption at 1782 cm^{-1} (C=O, activated ester) aside from the appearance of amide C=O (1650 cm^{-1}) and new formed ester C=O (1735 cm^{-1}) characteristic bands, respectively. The thermal stability of P0-P3 were investigated by thermogravimetric analysis (TGA). Figure [?]B showed that under inert condition (i.e. N$_2$) all samples were stable with onset temperature up to 237 °C. Moreover, amide-bonded pyrene samples (P1, P2) exhibited slightly higher onset temperature than methylene ester-bonded pyrene samples (P3). These results demonstrates the good thermal stability of pyrene-functionalized TEMPO-containing polymers as electrode materials.

5.3. π-π **Interaction**

The evolution of the size distribution for the relevant polymer solutions in DMAc was determined via dynamic light scattering (DLS, Figure 5.3A). PPFPA showed number-weighted distribution of 6.5 nm (Table 5.1), while P0 exhibited a smaller size by 2.3 nm, which may result from the hydrogen bonding between the adjacent amide bond in each repeating units. With 4.3% of amide-bonded pyrene content, assessed via UV/vis analysis, P1 displayed extended chain conformation as a result of the randomly incorporated amide-bonded pyrene moieties, and hence showed number-weighted distribution of 5.6 nm. Intriguingly, as the pyrene content increased from 4.3% to 23.5%, the size of the polymer coil gets smaller, which was 3.6 nm and 3.1 nm for P2 (with amide bonded pyrene) and P3 (with methylene ester-bonded pyrene), respectively (Table 5.1). The latter indicated that the entanglements of polymer chains were locked by multiple π-π interactions of the pendant pyrene groups, which induced and maintained a coiled structure.
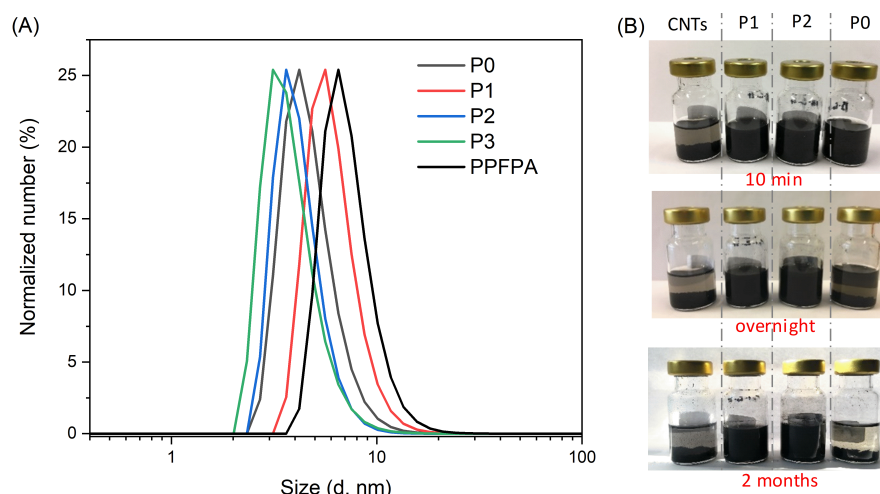
Figure 5.3.: (A) DLS traces of PPFPA and P0–P3. All traces were recorded in DMAc (c = 0.67 mg mL^{-1}) at ambient temperature. (B) Composite suspensions of P0–P2 (3.0 mg) and CNTs (3.0 mg) in THF (4.5 mL) prepared with a homogenizing mixer; suspensions at the leftmost is the blank sample with CNTs (3.0 mg) in THF (4.5mL).

As the next step is to fabricate the TEMPO-pyrene copolymers into electrodes through noncovalent π-π stacking between pyrene groups and CNT, the existence of such π-π interaction between pyrene moieties and CNTs was examined. As shown in Figure 5.3B, with the aid of a homogenizer, CNTs were well dispersed in the two amide-bonded pyrene copolymer (P1, P2) solutions, without apparent sedimentation even after 2 months. Conversely, a rapid settling of CNTs was observed within minutes after homogenizing. For P0 solution, the suspension state could only be maintained for a bit more than one hour. Taken together, these results suggest that the introduction of

pyrene moieties into PTAm-based polymer structure indeed assists intramolecular π-π interaction with CNTs, which may facilitate the effective immobilization of polymer chains on the surface of CNTs.

To compare the interaction between each type of functional group on the polymer and CNTs, quantum mechanical calculations based on Mϕller–Plesset perturbation theory were performed. The graphene flake was modeled as a large aromatic hydrocarbon with 130 carbon atoms and the edges terminated with hydrogen atoms. TEMPO, 1-aminopyrene, and 1-pyrenemethanol molecules were located in the center of the graphene flake to avoid the electronic influence from the edge carbons. The interaction energy (ΔE) between the molecular and graphene flake was defined as the energy difference between the graphene/molecular complex and infinitely separated fragments (graphene/ 1-aminopyrene, 1-pyrenemethanol and 4-amino-TEMPO). Indeed, both 1-aminopyrene and 1-pyrenemethanol, which prefer to lie almost flat on the graphene flake (Figure 5.4F and 5.4G), showed much higher interaction with CNTs compared to 4-amino-TEMPO (Table 5.2). Besides, 1-aminopyrene displayed more affinity towards graphene layer than 1-pyrenemethanol with interaction energy, ΔE, values of -0.022 eV and 0.006 eV, respectively. The latter implies that, theoretically, 1-aminopyrene/CNTs possess a stronger interaction than 1-pyrenemethanol/CNTs.
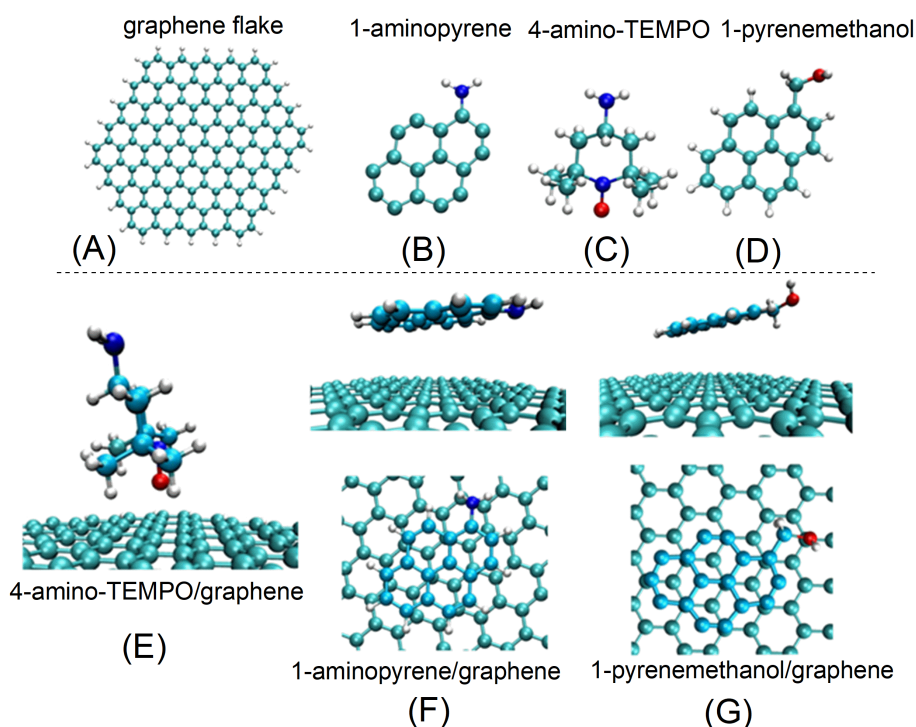
Figure 5.4.: Molecular models of (A) graphene layer, (B) 1-aminopyrene, (C) 4-amino-TEMPO and (D) 1-pyrenemethanol, as well as adsorption geometry of (E) 4-amino-TEMPO/graphene, (F) 1-aminopyrene/graphene and (G) 1-pyrenemethanol/graphene.

Table 5.2.: The interaction energy (ΔE) for graphene/pyrene derivatives and graphene/TEMPO.

Molecules	1-aminopyrene	1-pyrenemethanol	4-amino-TEMPO
ΔE (eV)	-0.022	0.006	0.071

5.4. Electronic Properties and Battery Performance

As the aimed application of TEMPO-containing polymers for the present work is as electrode material, the electronic properties and battery performance of the TEMPO-pyrene copolymers are thus examined. In the following sections, cathode preparation, cyclic voltammetry (CV) and battery performance were introduced.

5.4.1. Cathode Preparation

To eliminate the influence of CNTs on CV measurement (3.2–4.0 V) of coin cells fabricated from P2', P3', P2 and P3 [374], cathodes were prepared without CNTs. Active polymer (10 mg, 10 wt.%), conductive carbon (80 mg, 80 wt.%) and poly(vinylidene fluoride) (PVdF, 10 mg, 10 wt.%) were mixed in N-Methyl-2-pyrrolidone (NMP) overnight to afford a homogeneous slurry, followed by blade coating the slurry onto aluminum foil (thickness 30 μm) and dried in an oven at 80 °C for overnight. The active polymer material (P0-P3, 10 mg) and CNTs (10 mg) were dispersed in a mixture of NMP (0.4 mL) and tetrahydrofuran (THF, 2mL) with the aid of a homogenizer. A suspension of carbon black (70 mg) in NMP (1.3 mL) was prepared as well. Afterwards, the aforementioned two colloidal dispersions were vigorously mixed together and put on a rotary evaporator to degas and remove the THF and part of NMP at 40 °C. In the end, PVdF (10 mg) solution in NMP (10 wt.%) was added and homogenized gently to obtain a bubble-free and uniform slurry.

The composite cathodes were formed by blade coating the above-mentioned slurries onto aluminum foils and dried at room temperature and 80 °C under vacuum sequentially. The typical loading of a PTAm/CNTs hybrid cathode was $\sim$ 1.5 mg cm^{-2}. The thickness of the hybrid electrodes was about 50 μm. The coin cell (CR2032) was fabricated by stacking the polymer-based cathode, lithium metal anode and a separator film with LP30 electrolyte in an argon filled glove box (MBraun) where both O_2 and H_2O content were less than 0.1 ppm.

5.4.2. Cyclic Voltammetry

To gain a better understanding on the structure-electronic property relationship of the two polymeric pyrene derivatives i.e. P2' and P3', CV was conducted. To avoid the influence of CNTs (e.g. faradaic reaction of carbonyls on the surface of CNTs) on CV [374], no CNTs were added in cathodes for CV measurement. Regarding P2', redox peaks at 3.55 V were detected with slightly enhanced intensity as the scan number increased from 1 to 5 (Figure 5.5A). Similarly, redox peaks were observed for P3', while a migrating oxidation peak was detected towards the 5th scan, accompanied with a decrease in the reduction peak (Figure 5.5B). These results emphasize the significant influence of the amide-bonded pyrene moiety on the final electronic properties compared to the methylene-ester pyrene derivative as the redox reaction of amide-bonded pyrene is relatively more stable. Whereas, the CV curves of P1 and P2 showed one pair of redox peak at around 3.6 V, corresponding to the redox reaction between TEMPO and oxoammonium, no apparent redox peaks were detected for the amide-bonded pyrene derivatives (Figure 5.5C). The latter could result from either the overlap of redox peaks for the amide-bonded pyrene and TEMPO derivatives, as both appeared at around 3.6 V, or the low current intensity arising from the amide-bonded pyrene. Nevertheless, a narrow anodic and cathodic peak separation was observed for both P1 and P2, which was 41.5 mV and 26.9 mV, respectively.

5.4.3. Battery Performance

The rate performance for P0-P2 were investigated from 0.1 C to 100 C, as shown in Figure 5.6A. The capacity delivered during discharge at various C-rates were in the order of P1 > P0 > P2. At 0.1 C, P1 delivered a high capacity of 96.1 mAh g^{-1}, which is around 20% ($\sim$19 mAh g^{-1}) higher than P0. With the increase in C-rate, the capacity slowly decreased. At 100 C, as high as 76.8% (73.2 mAh g^{-1}) of the capacity was maintained (Figure 5.6B), which is close to the capacity of P0 at 0.1 C (76.5 mAh g^{-1}). Besides, a distinct voltage plateau at around 3.6 V was observed from the charge-discharge profile of P1 (Figure 5.6C). These results suggest the better rate performance of P1 than P0. With the increase of pyrene content to 10.9%, P2 delivered a capacity of 65.2 mAh g^{-1} at 0.1 C, which is 32% lower than P1, although the TEMPO content of P2 is only about 5% less than P1. As C-rate increased, the capacity retention for P2 exhibited a similar trend as P0. When cycled back at 0.1 C, all samples exhibited a high retention (over 92.5%,) in particularly P2 (96.0%), implying the good rate capability arising from the improved conductivity. Additionally, distinct voltage plateaus at around 3.6 V were observed for P0 and P2 at various C-rates (Figure 5.7). Altogether, the content of amide-bonded pyrene moieties plays
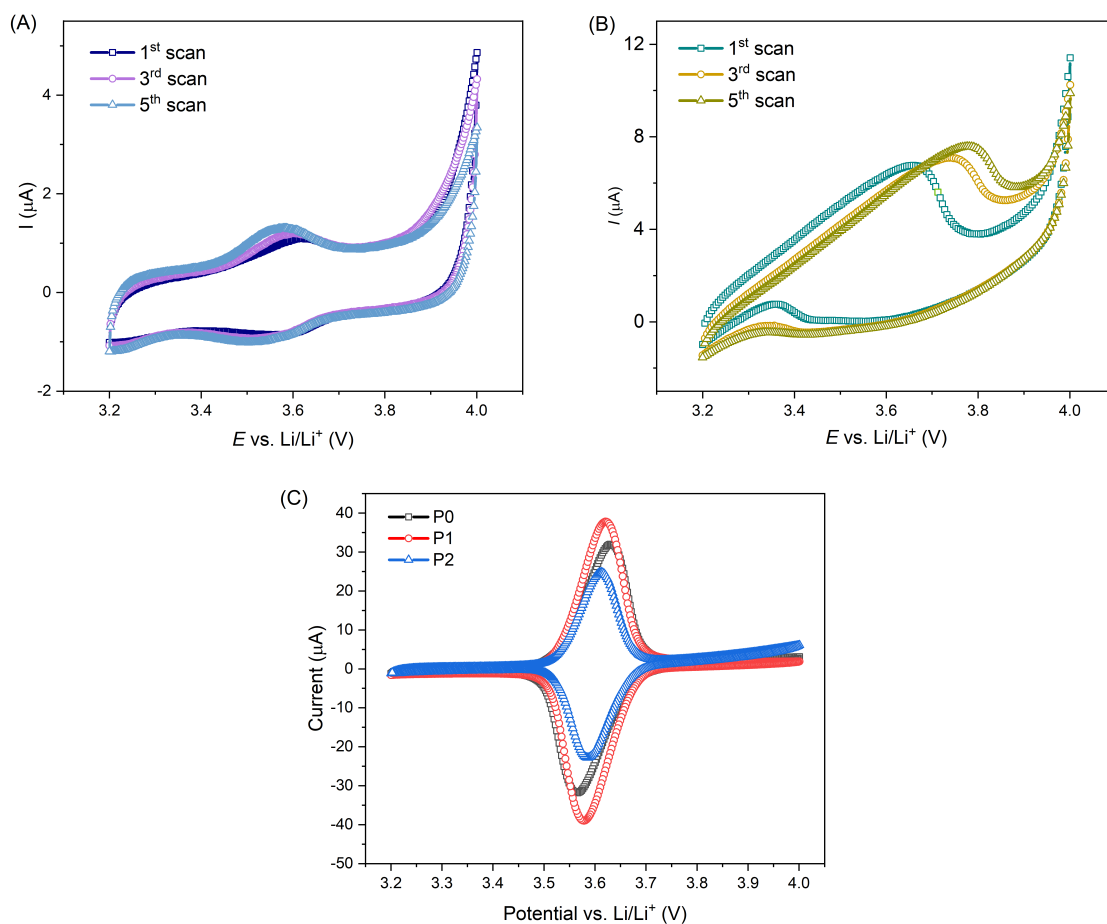
Figure 5.5.: CV curves of (A) P2' and (B) P3' (C) P0–P2 at a scanning rate of 0.1 mV s^{-1} within the potential range of 3.2–4.0 V vs. Li/Li$^+$. The cathode is composed of active polymer/CB/PVdF = 10/80/10 (wt.%)

a critical role in battery performance of TEMPO-containing polymers. In other words, at low content (e.g. 4.3%), the amide-bonded pyrene moieties promote electron transfer and improve rate capability. Whereas, at a relatively high content (e.g. 10.9%), a negative effect on battery performance was observed. When cycled at 1 C for 200 cycles (Figure 5.6D), a relatively fast capacity loss (13.2%) was noted for P0 after the initial 20 cycles, indicating a partial dissolution of P0 in the electrolyte. Intriguingly, the capacity loss for P1 and P2 was only 12.0% and 12.7%, respectively, after the whole 200 cycles, implying the good anchor effect of pyrene moieties on CNTs.

121
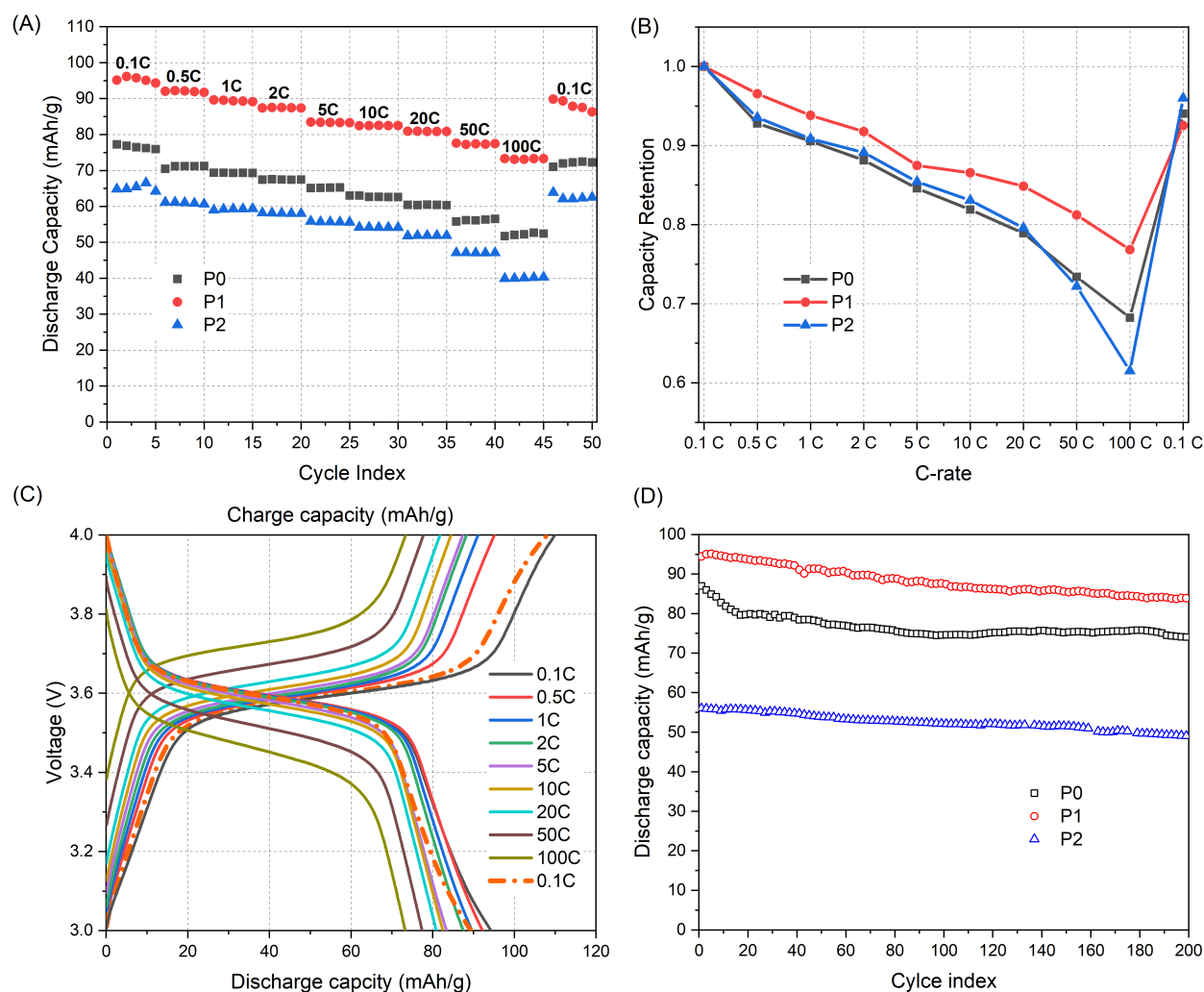
Figure 5.6.: (A) Rate performance of P0-P2 at various C-rates. (B) Capacity retention of P0-P2 at various C-rates. (C) Charge-discharge profile of P1. (D) Cycling performance of P0-P2 at 1 C. Each cathode is composed of active polymer/CNTs/CB/PVdF = 10/10/70/10 (wt.%).

5.4.4. Influence of Pyrene Content

Charge-discharge profile and coulombic efficiency (CE) for P0-P2 at various C-rates were examined in order to figure out why the cathode based on P2 delivered a much lower capacity than P1 by $\sim$30 mAh g^{-1} (Figure 5.8). At 0.1 C, the CE for P0-P2 was 94.6%, 84.5% and 71.6%, respectively, indicating a decrease in CE with the increase in pyrene content of the active material. As C-rate raised to 0.5 C, the CE for P0-P2 got increased, which was 99.0%, 97.1% and 93.2%, respectively, nonetheless CE for P0-P2 still follows the order of P0 > P1 > P2. These results indicate side reactions accompanied at low C-rate, e.g. 0.1 C and 0.5 C, for copolymer P1 and P2, especially the one with high pyrene content, i.e. P2. Moreover, a majority of coin cells based on P2 (10.9%
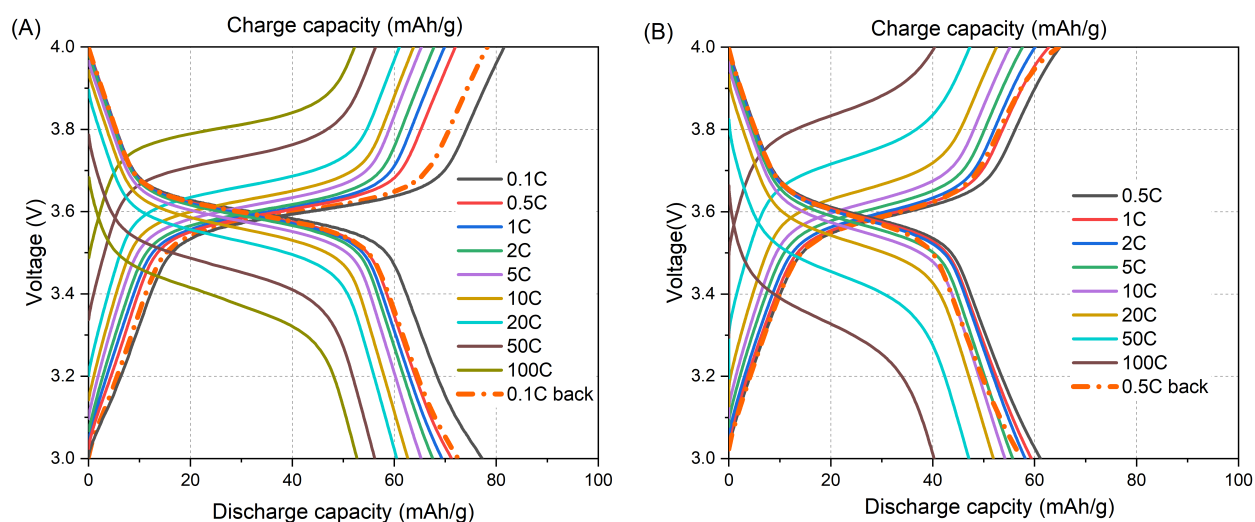
Figure 5.7.: Charge-discharge profiles of (A) P0 and (B) P2 at various C-rates.
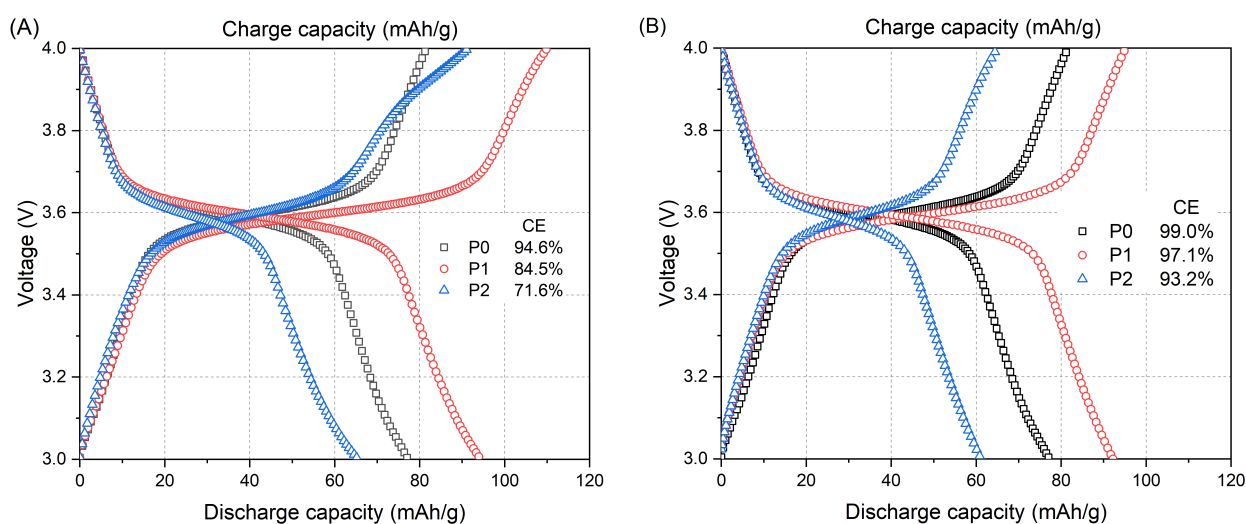
Figure 5.8.: Charge-discharge profile of P0-P2 (A) at 0.1C; (B) 0.5C.

pyrene content) failed when running at 0.1 C due to a plateau at high voltage (3.9–4.0 V) in the voltage profile (Figure 5.9A), while coin cells based on P0 and P1 did not. Besides, CV curve of P2/CNTs cathode at a low scan rate of 0.025 mV s^{-1} in the voltage range of 3.0–4.0 V, which corresponds to a fully charging time of $\sim$ 22 h, exhibited an irreversible oxidation peak at around 3.9 V, while this irreversible anodic peak was absent at a relatively high scan rate of 0.1 mV s^{-1} (Figure 5.9B and 5.9C), demonstrating the existence of side reactions at low C-rate (i.e. 0.1 C). Therefore, the poor battery performance of P2 was assumed to result from the interference of side reactions which probably arise from the irreversible oxidation of pyrene with the participation of TEMPO.

(A)

(B)

(C)
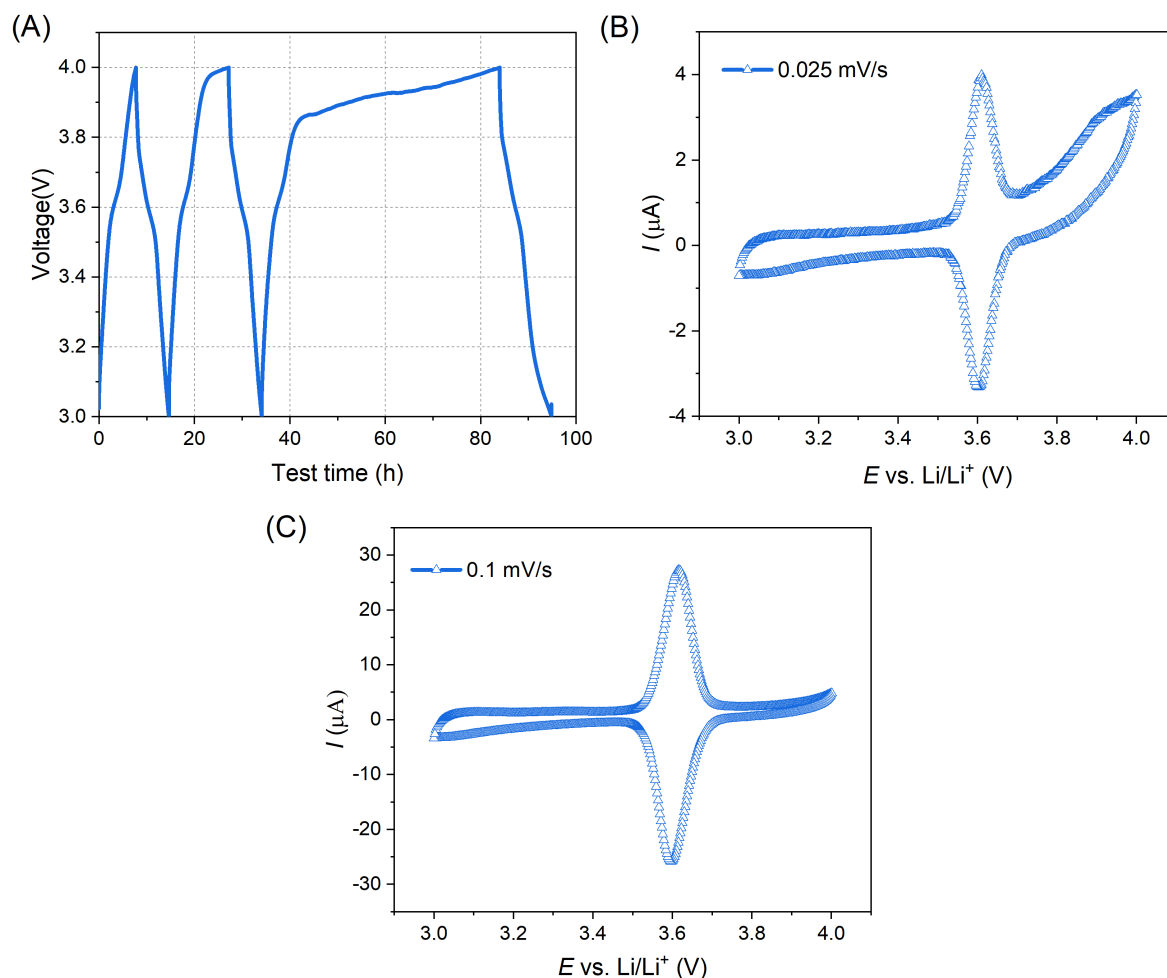
Figure 5.9.: (A) Voltage profile of P2 at 0.1 C. CV curves of P2 (B) at a scan rate of 0.025 mV s^{-1} and (C) at a scan rate of 0.1 mV s^{-1} within the voltage range of 3.0–4.0 V vs. Li/Li$^+$. The cathode is composed of active polymer/CNTs/CB/PVdF = 10/10/70/10 (wt.%).

5.5. Summary

In summary, theory and experiment have been used to study the effect of the structure design of multiple pyrene-functionalized TEMPO-containing polymers to improve battery performance. Through post-polymerization modification via activated ester, amide-bonded pyrene and TEMPO moieties were efficiently incorporated into the same polymer chain. Compared to methylene-ester linked pyrene, the amide-bonded pyrene based polymer, i.e. P1 and P2, showed relatively stable redox peaks at around 3.55 V vs. Li/Li$^+$. Incorporating amide-bonded pyrene moieties into the TEMPO containing polymers improves the battery performance, whereas pyrene content above 10% may induce side reactions, and consequently, impair the redox reaction of TEMPO. Nevertheless, the present work highlighted the often-overlooked role of through-space electrostatic

substituent effects via amide bonded TEMPO-pyrene copolymers, which could assist in the design of nitroxide radical structures for different applications.

6. Conclusion and Outlook

Organic radical batteries (ORB) are a novel promising class for energy storage, particularly featuring a fast charging and extraordinary cycle life. On one hand, nitroxide radicals and their polymer derivatives have found applications in diverse areas in the recent decades. Indeed, the scientific community has seen the revival of such materials due to the development of their applications in organic energy storage and electrochemical catalysis. On the other hand, the representative polymer, i.e. poly(2,2,6,6-tetramethylpiperidinyloxy-4-yl methacrylate) (PTMA), is usually synthesized by a post-oxidation method. As an alternate strategy for developing TEMPO-containing polymers, the present thesis focused on the post-polymerization modification (PPM) via activated ester (namely pentafluorophenyl (PFP) ester) in a one-step or two-step functionalization manner, respectively. Intriguingly, this strategy not only allows a densely populated redox centers along the polymer chain, but also enables the efficient incorporation of other specific functionality, e.g. amide-boned pyrene moiety, to the same polymer chain, thus offering solutions to the critical problems that hindering the development of radical-containing polymers as active materials in organic radical batteries (ORB). Apart from the material aspect, in the present work various processing parameters for PTMA-based cathode were investigated since the fabrication process also plays a significant role in the final battery performance.

Chapter 3 introduced PPM for the synthesis of six types of TEMPO-containing polymers by transesterification or aminolysis reactions of PPFPA and PPFPMA with three types of nucleophilic TEMPO derivatives, i.e. 4-hydroxy-TEMPO, 4-amino-TEMPO and 4-methylamino-TEMPO. Optimizing the reaction conditions by varying different parameters, such as type of nucleophile, catalyst and solvent, feeding ratios of catalysts and nucleophiles, along with reaction time and temperatures, resulted in a library of structurally distinct TEMPO-containing polymers with varying backbone composition. Poly(2,2,6,6-tetramethylpiperidinyloxy-4-yl acrylamide) (PTAm) revealed the highest degree of functionalization with a TEMPO content of 96.2% under considerably mild conditions (TEA, THF, 50 °C within 3 hrs.), while the reaction between PPFPMA and 4-methylamino-TEMPO demonstrated the lowest TEMPO conversion owing to the steric hindrance from methyl group on both the methacrylate chain and the 4-methylamino-TEMPO. All other four

TEMPO-containing polymers exhibited a radical content similar to PTMA (66.6%) synthesized by the conventional post-oxidation methodology. Noteworthy, the choice of catalyst played a critical role in PPM. Compared to TEA, DMAP (4-dimethylaminopyridine) and organo-activator Tz/DBU facilitated an efficient ester bond cleavage independent of the polymer precursor, thus, side reactions such as hydrolysis were increased. Though hydrolysis side reaction occurred, the resulting carboxylic acid group was proven to accelerate ion transfer in a certain way during the redox process. Furthermore, owing to the higher TEMPO content, PTAm exhibited a 12–22 mAh g^{-1} higher specific capacity compared to the PTMA-oxidation when running at 5 C for 500 cycles.

Fabrication of electrodes plays an important role for the final battery performance. Unlike inorganic-based electrodes, organic-based electrodes involve different formulations and configurations due to the chief distinctions in both chemical affinity and electrical conductivity between organic and inorganic compounds. Nevertheless, the processing of organic-based electrodes is less studied compared to that of inorganic-based electrodes. Accordingly, Chapter 4 addressed the influence of various processing parameters on the battery performance with PTMA-oxidation as the model cathode active material. These parameters include slurry viscosity, drying temperature, carbon form and calendering. The performed experiments revealed that cathodes dried at 80 °C exhibited a better battery performance with a more homogeneous and less cracking morphology than the ones dried at 50 °C. Essentially, a modest slurry viscosity is preferable for the fabrication of PTMA-based cathodes, since too high or too low viscosity would worsen the cathode morphology and impair the final battery performance, especially in the case of a slurry with low viscosity. While carbon nanofibers (CNF) and vapor grown carbon fibers (VGCF) improve crack resistance of coated films during drying, the respective cathodes exhibited compromised discharge capacity owing to their lower specific surface area and higher through-plane resistance compared to carbon black (CB). Therefore, a well-suited processing conditions could be summarized as follows: drying temperature of 80 °C and mass ratio between cathode and NMP in the slurry (χ_c), being around 62.5 mg g^{-1} regardless of TEMPO content. Moreover, CB is suggested to be a substantially more favorable conductive agent, not only economically and because of safety concerns, but also electrochemically, compared with VGCF and CNF.

Chapter 5 demonstrated the importance of rational structural design of pyrene-functionalized radical (i.e. TEMPO) copolymers for enhanced electrochemical performance by providing insightful guidelines for designing high-performance polymer-based electrodes for energy storage applications. Through a two-step functionalization of PPM via activated ester, amide-bonded pyrene and TEMPO moieties were efficiently incorporated into the same polymer chain with varying content. Compared to a methylene-ester linked pyrene, the amide-bonded pyrene based polymer, i.e.

P1 and P2, showed relatively stable redox peaks at around 3.55 V vs. Li/Li$^+$. Moreover, quantum mechanical calculations indicated that pyrene moieties preferred to lie almost flat on the surface of CNTS, and a stronger intermolecular interaction was revealed between 1-aminopyrene and a graphene layer than between 1-pyrenemethanol and a graphene layer. Intriguingly, incorporating amide-bonded pyrene moieties into the TEMPO-containing polymers improved the battery performance with 76.8% capacity retention (73.2 mAh g^{-1}) at 100 C, whereas a pyrene content above 10% may induce side reactions, and consequently, impair the redox reaction of TEMPO.

In summary, the current thesis describes PPM via activated ester as a feasible and simple approach for the synthesis of TEMPO-containing polymers targeted for battery application. Due to the high activity of PFP ester, polymers with high TEMPO content as well as bearing other functionalities are readily achievable, hence issues that hinder the development of ORB, such as poor electric conductivity and dissolution of electrode material in conventional electrolyte (e.g. carbonate-based electrolyte) could be well addressed. The results support that the strategies developed in this thesis effectively alter and enhance the electrochemical performance of TEMPO-containing polymers with respect to discharge capacity, cycle stability and rate capability. Noteworthy, the knowledge and methodologies developed in this thesis will not only benefit TEMPO-containing polymers as active materials, but also be applicable to other redox-active organic and polymer materials in energy storage applications.

Nevertheless, with various polymeric structures having been synthesized in chapter 3, the systematic structure-property relationship of TEMPO-containing polymers need further investigation. As TEMPO-containing polymers synthesized by PPM via activated ester are derived from the same parent precursor polymer (e.g. PPFPA), they should possess the same chemical and analytical information in regard to polymer backbone structure with similar degree of polymerization and dispersity. Given the optimized reaction conditions for PPM of TEMPO-containing polymers as well as cathode processing conditions revealed in the present work, a study of the structure-property relationships of the various TEMPO polymers in respect to their electrochemical properties is within easy reach. Moreover, on top of Chapter 5, it is clear that the design of nitroxide radical structures are critical for battery application, therefore the often-overlooked role of through-space electrostatic substituent effects via amide/ester bonded TEMPO-pyrene copolymers need to be further investigated within an expanded polymer pool. Furthermore, except for amide-bonded pyrene group, other functionalities could also be incorporated to TEMPO-containing polymers to serve different purposes with respect to battery application. For instance, the synthesis of cross-linked TEMPO-containing polymers with a well-controlled cross-link density for ORB and

the preparation of aqueous TEMPO-ionic liquid copolymers for aqueous flow batteries. In addition to random copolymers, block copolymers bearing TEMPO pendant groups are also attainable by tuning the structure of the parent polymers, i.e. activated ester-containing polymers, through diverse polymerization techniques (e.g. ATRP, RAFT), followed by PPM with nucleophilic TEMPO derivatives. Such TEMPO-functionalized block copolymers offer a good opportunity to tune the morphology of the resulting electrodes (e.g. nanostructured morphology), thus leading to enhanced battery performance. Last but not least, the fabrication of TEMPO-containing polymers by PPM via activated ester utilized for other applications except energy storage, such as TEMPO-containing hydrogels and microstructured nanocatalyst, are also applicable.

7. Experimental Section

7.1. Materials and Methods

All solvents and regents used in synthetic procedures were purchased from Sigma-Aldrich, Fisher Scientific, ABCR, TCI, and VWR and used as received unless otherwise stated. Deuterated solvents were purchased from Eurisotop. Yields refered to isolated and purified products. Commercially available lithium foil (0.75 mm thick, Alfa Aesar) was used as anode. Solef 6020 poly(vinylidene fluoride) (PVdF, Solvay, Italy) was used as a binder, while CB-SP (Timcal), vapor grown carbon fiber (VGCF, Showa Denko), a mixture of carbon nanofiber (CNF, Sigma-Aldrich) and Super P carbon black (CB-SP: CNF = 9: 1, w/w) were used as conductive additives. All materials and substrates were used as received unless otherwise noted.

Nuclear magnetic resonance (NMR) spectra were recorded on a Bruker Ascend 400 MHz NMR spectrometer in deuterated solvents. Chemical shifts were reported in ppm with TMS as an internal standard. Electron paramagnetic resonance (EPR) spectra were collected on a Bruker EMAXnano. If not otherwise noted, all monomers were measured in dichloromethane (DCM) and all polymers were done in dimethylacetamid (DMAc) using a capillary with an inner diameter of 0.9 mm. FTIR spectroscopy was conducted on a Bruker Vertex70 spectrometer in an attenuated total reflectance (ATR) setup. Size exclusion chromatography (SEC) data were obtained by utilizing a PL-GPC 50 Plus with a sample concentration about 2 mg mL^{-1} in DMAc. For calculating the molecular weight and dispersity, PMMA was used as a calibration. Ultraviolet-visible (UV/vis) absorption measurements were recorded on a JASCO V-630 UV/Vis-photospectrometer at 25 °C except for pyrene-containing polymers which were conducted on a Varian UV-Visible Spectrophotometer CARY 300 BIO for polymers. Fluorescence measurements were performed on a Varian Fluorescence Spectrophotometer CARY Eclipse in the range of 350 to 650 nm in steps of 1 nm with an excitation wavelength of 342 nm. Dynamic light scattering (DLS) analysis was carried out on a Zetasizer Nano ZS light scattering apparatus (Malvern Instruments, UK) with a polymer solution of 1 mg mL^{-1} in DMAc. Thermogravimetric analysis (TGA) was performed on a TGA 55 analyser

(TA instruments) from room temperature to 700 °C at a scan rate of 10 °C min^{-1} under nitrogen atmosphere. Quantification of the pyrene groups within the TEMPO-pyrene copolymers was based on UV/vis absorption data. The extinction coefficient for 1-aminopyrene at 289 nm and for 1-pyrenemethanol at 344 nm were determined by a calibration curve in DMAc to ensure an adequate solvation of the pyrene derivatives, which is a linear line by fitting the absorbance maximum as a function of the solution concentration. The slope of the line corresponds to the extinction coefficient, which was determined to be 22,876 cm^{-1} M^{-1} and 41,167 cm^{-1} M^{-1}, respectively, according to Beer-Lambert Law (see equation 7.1),

$$\xi = \frac{A}{Cl} \tag{7.1}$$

where ξ represents extinction/absorption coefficient, A refers to absorbance of pyrene derivatives at a specific wavelength, C is the concentration of absorbing material, i.e. pyrene derivatives, and l is the path length.

Quantum mechanical calculations based on Mϕller–Plesset perturbation theory were performed by taking the graphene flake, a large aromatic hydrocarbon with 130 carbon atoms, as a model and assuming its edges were terminated with hydrogen atoms. TEMPO, 1-amino-pyrene, and 1-pyrenemethanol molecules were located in the center of the flake to avoid the electronic influence from the edge carbons. Geometry optimization and ground state search were carried out within the TurboMole 7.3 program package [TURBOMOLE V7.3 2018.A Development of University of Karlsruhe and Forschungszentrum Karlsruhe GmbH, 1989-2007. http://www.turbomole.com(TURBOMOLE GmbH, 2007)] at MP2 level of theory with cc-pVDZ basis sets. The interaction energy (ΔE) between the molecular and graphene flake was defined as the energy difference between the graphene/molecular complex and infinitely separated fragments (graphene/ 1-amino-pyrene, 1-pyrenemethanol and TEMPO). As confirmed by literature [375], MP2 methods could give reliable description of the adsorption of small organic molecules on graphene.

Cyclic voltammetry of the polymer solutions (0.5 mg mL^{-1}) were performed on a potentiostat system (PGSTAT128N Metrohm Autolab) in 0.1 M LiClO$_4$ electrolyte in acetonitrile (MeCN) with a scan rate of 100 mV s^{-1} ranging from 0–1.0 V vs Ag/Ag$^+$ at 25 °C. A glass carbon electrode, a Pt-wire electrode and an Ag/AgCl electrode were used as working electrode, counter electrode and reference electrode, respectively. Cyclic voltammetry measurements of coin cells were performed on a potentiostat system (PGSTAT128N Metrohm Autolab) between 3.0–4.1 V vs. Li/Li$^+$ at a scan rate of 0.1 mV s^{-1} or 0.025 mV s^{-1}. Electrode morphology was characterized on an optical microscopy (VHX 900F, Keyence) at 25 °C, and a scanning electron microscopy (SEM,

Zeiss Gemini/LEO 1530 system) with an accelerating voltage of 5 kV and a 20 μm aperture. Through-plane resistance analysis of disk-shaped cathodes ($\phi = 14$ mm) was carried out on a lab-made equipment by applying a constant current of $I = 100$ mA to the cathode disk subjected to a compression force of 70 N. Three cathodes with a mass tolerance less than 0.2 mg were measured for each coating sample. The thickness of the cathode was determined by a micrometer screw gauge. The cells were cycled galvanostatically in the voltage range of 3.0–4.1 V vs. Li/Li$^+$ (PTMA-oxidation system and P$_A$-A_1 system) or 3.0–4.0 V vs. Li/Li$^+$ (TEMPO-pyrene co-polymer system), at a charging and discharging rate of 5 C on a battery tester (BT 2000, Arbin). Rate performance against the cycle number was evaluated for the polymer-based cathodes at variable C-rates of 0.5–10 C (PTMA-oxidation system) or 0.1–100 C (TEMPO-pyrene co-polymer system) in the voltage range of 3.0–4.1 V and 3.0–4.0 V vs. Li/Li$^+$, respectively.

7.2. Synthetic Procedures

7.2.1. Synthesis of TEMPO Derivatives
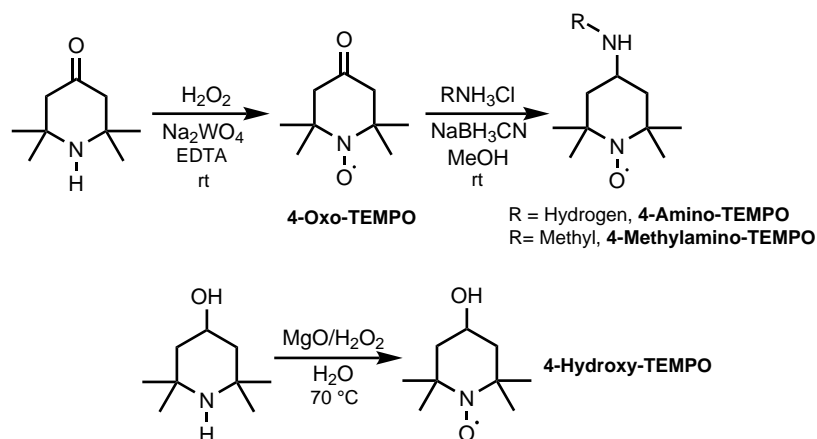
Scheme 7.1: Synthesis of TEMPO derivatives.

4-Oxo-2,2,6,6-tetramethylpiperidooxy (4-Oxo-TEMPO)

4-Oxo-TEMPO was synthesized according to literature [186]. To a solution of 2,2,6,6-tetramethyl-l-piperidone (15.00 g), sodium tungstate (1.50 g) and of ethylenediaminetetraacetic acid (1.50 g) in H$_2$O (100 mL) was added 30% H$_2$O$_2$ (10 mL) dropwise. The reaction mixture was stirred at room temperature for 48 hr. After filtered, pH of the filtrate was lowered to 5, saturated with

NaCl and extracted with diethyl ether, red oil was obtained. Chromatographic separation using neutral Al_2O_3 and DCM/Petroleum ether = 1/1 (v/v) and then 5/1 (v/v) gave a red solid in 67% yield. G factor: 2.0033. FTIR (ATR mode): 1717 cm^{-1} (C=O stretching), 1460 cm^{-1} (N-O stretching). UV-vis (DCM): λ_{max} = 443 nm.

4-Amino-2,2,6,6-tetramethylpiperidmooxy (4-Amino-TEMPO)

To a solution of NH_4Cl (5.70 g, 1.06 mol) in absolute methanol (MeOH) (300 mL) at pH = 7–8 were added $NaBH_3CN$ (0.75 g, 0.11 mol) and 4-oxo-2,2,6,6-tetramethylpiperidinooxy (3.07 g, 0.18 mol). The reaction was stirred at room temperature for 48 hr. and filtered, afterwards the residual solvent was removed in vacuum. The remaining oil was dispersed in H_2O, saturated with NaCl, extracted with diethyl ether, dried over anhydrous $MgSO_4$ and distilled, respectively. The resultant oil was purified by column chromatography (silica gel, DCM/MeOH = 10/1 (v/v) with 1% triethylamine (TEA)) to provide a red solid in 48% yield. G factor: 2.0024. FTIR (ATR mode): 3352 cm^{-1} and 3284 cm^{-1} (N-H 1° amine stretching), 1603 cm^{-1} (NH_2 scissoring), 1460 cm^{-1} (N-O stretching). UV-vis (DCM): λ_{max} = 459 nm.

4-(Methylamino)-2,2,6,6-tetramethyl-1-piperidinyloxy (4-Methylamino-TEMPO)

4-Methylamino-Tempo was synthesized in a similar way as 4-amino-Tempo [187]. To a solution of methylamine hydrochloride (2.50 g, 37.00 mmol) in absolute MeOH (100 mL) were added 4-oxo-TEMPO (1.10 g, 6.20 mmol) and $NaBH_3CN$ (0.27 g, 4.30 mmol) in addition to 5N HCl in MeOH to adjust the pH of the solution to ca. 6. After stirring the reaction at room temperature for additional 48 hr., the solvent was removed in vacuum. The remaining oil was taken up in H_2O, saturated with NaCl, pH adjusted to 9 with sodium hydroxide, extracted with diethyl ether, dried over anhydrous $MgSO_4$ and distilled, respectively. The resultant oil was purified by column chromatography (silica gel, DCM: MeOH = 9.6/0.4 (v/v) with 1% TEA) to provide a red solid with a yield of 92%. G factor: 1.9964. FTIR (ATR mode): 3311 cm^{-1} (N-H 2° amine stretching), 1460 cm^{-1} (N-O stretching). UV-vis (DCM): λ_{max} = 460 nm.

4-Hydroxy-2,2,6,6-tetramethylpiperidinooxy (4-Hydroxy-TEMPO)

To a solution of 2,2,6,6-tetramethylpiperidinol (5.00 g) in 20 mL H_2O stirred at 70 °C was added magnesium oxide (17.50 mg) followed by H_2O_2 (9 mL), which was added in dropwise manner.

After 4 hr., additional H_2O_2 (9 mL) was added dropwise. Finally, MnO_2 was added to the reddish mixture to quench the residual H_2O_2 before filtration. The filtrate was saturated with NaCl and extracted from diethyl ether. After rotary evaporation, the product was recrystallized form *n*-hexane with a yield of 89%. G factor: 2.0054. FTIR (ATR mode): 3406 cm^{-1} (O-H stretching), 1460 cm^{-1} (N-O stretching). UV-vis (DCM): $\lambda_{max} = 460$ nm.

7.2.2. Synthesis of Poly(pentafluorophenyl (meth)acrylate)
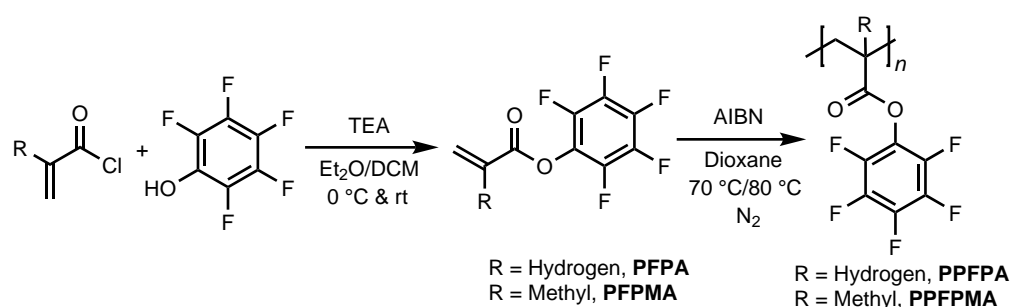
Scheme 7.2: Synthesis of PPFP(M)A.

Poly(pentafluorophenyl acrylate) (PPFPA)

Pentafluorophenyl acrylate (PFPA) was synthesized as literature suggested [376]. To a solution of pentafluorophenol (PFP, 9.20 g, 50.00 mmol) in anhydrous DCM (42 mL) at 0 °C was added TEA (5.57 g, 55.00 mmol) dropwise. Acryloyl chloride (4.98 g, 55.00 mmol) was added dropwise to the cooled reaction mixture under vigorous stirring, after 30 min, the mixed solution was allowed to reach room temperature and stirred for an additional 12 hr. Monitoring of the reaction was performed by thin-layer chromatography (TLC), petroleum ether/ethyl acetate = 15/1, v/v) until complete consumption of PFP was observed. The reaction mixture was filtered prior to two-fold extraction with brine and dried over Na_2SO_4, concentrated by rotary evaporation and suddenly vacuum distilled. The crude product was purified by column chromatography (silica gel, petroleum ether/ethyl acetate = 15/1, v/v). Finally, a colourless liquid was obtained (9.43 g, 79%). The analytical data of pentafluorophenyl acrylate matches published data. ^{1}H NMR (400 MHz, CDCl$_3$): δ 6.72 (dd, J = 17.3, 0.8 Hz, 1H), 6.37 (dd, J = 17.3, 10.6 Hz, 1H), 6.18 (dd, J = 10.6, 0.8 Hz, 1H).

PPFPA was synthesized in accordance with previous reports of the research group [303]. A solution of PFPA (5.00 g, 21.00 mmol) and azobisisobutyronitrile (AIBN), 34.50 mg, 0.21 mmol)

in dry 1,4-dioxane (5 mL) were placed in a Schlenk tube. Three freeze-pump-thaw cycles were performed to degas the solution. The flask was transferred to a preheated oil bath at 70 °C and stirred overnight. The reaction was exposed to air to quench the polymerization. The solution was diluted with chloroform and precipitated from methanol to afford a white solid. It was redissolved in chloroform and reprecipitated from MeOH. The process was repeated thrice. After drying under vacuum at 40 °C for 72 hr., the polymer was given in 90% yield. ^{1}H NMR (400 MHz, CDCl$_3$): δ 3.27–2.70 (m, 1H), 2.55–1.69 (m, 2H). ^{19}F NMR (377 MHz, CDCl$_3$): δ -153.19 (s), -157.14 (d, J = 279.3 Hz), -162.20 (s). FTIR (ATR mode): 1782 cm^{-1} (C=O stretching of PFP-ester), 1516 cm^{-1} (aromatic ring stretching). GPC (PMMA standard, DMAc): M_n = 46.9 kDa, M_w = 102 kDa, $Đ$ = 2.2.

Poly(pentafluorophenyl methacrylate) (PPFPMA)

Pentafluorophenyl methacrylate (PFPMA) was synthesized as it was reported in the literature [377]. To a solution of PFP (18.41 g, 0.10 mol) in diethyl ether (230 mL) at 0 °C, TEA (11.13 g, 0.11 mol) was added. Subsequently, methylacryloyl chloride (11.50 g, 0.11 mol) was added dropwise to the cooled reaction mixture while stirring, and after 3 hr., the mixture was warmed to room temperature and let to stir overnight. Monitoring of the reaction was performed by TLC (petroleum ether) until the complete consumption of PFP was observed. The reaction mixture was filtered prior to two-fold extraction with brine and dried over Na$_2$SO$_4$, and finally concentrated by rotary evaporation. The crude product was purified by column chromatography (silica gel, petroleum ether). Finally, a colourless liquid was obtained with a yield of 91%. The analytical data of PFPMA is in accordance with the published data. ^{1}H NMR (400 MHz, CDCl$_3$): δ 6.60–6.15 (m, 1H), 5.84 (dd, J = 2.8, 1.4 Hz, 1H), 2.01 (t, J = 1.3 Hz, 3H).

A solution of PFPMA (5.00 g, 19.83 mmol) and AIBN (42.30 mg, 0.26 mmol) in dry 1,4-dioxane (5 mL) were placed in a Schlenk tube. Three freeze-pump-thaw cycles were performed to degas the solution. The flask was transferred to a preheated oil bath at 80 °C and stirred overnight. The reaction was exposed to air to quench the polymerization. The solution was diluted with chloroform and precipitated from MeOH to afford a white solid. It was redissolved in chloroform and reprecipitated from MeOH. The process was repeated thrice. After drying under vacuum at 40 °C for 72 hr., a polymer was obtained with a yield of 53%. ^{1}H NMR (400 MHz, CDCl$_3$): δ 3.02 – 1.92 (m, 1H), 1.87–1.06 (m, 2H). ^{19}F NMR (400 MHz, CDCl$_3$): δ -150.54 (t, J = 123.7 Hz), -151.51 (s) -156.97 (s), -16P.10 (s). FTIR (ATR mode): 1782 cm^{-1} (C=O stretching of PFP-ester), 1516 cm^{-1} (aromatic ring stretching). GPC (PMMA standard, DMAc): M_n = 15.4

kDa, M_w = 36.8 kDa, $Đ$ = 2.4.

7.2.3. Synthesis of TEMPO-Containing Polymers by One-Step and Two-Step Post-Polymerization Modification via Activated Esters

TEMPO-Containing Polymers in One-Step Post-Polymerization Modification

Three types of TEMPO derivatives, i.e. 4-amino-TEMPO, 4-methylamino-TEMPO and 4-hydroxy-TEMPO, were used as nucleophiles to react with PPFPA and PPFPMA respectively, in order to yield 6 types of PTEMPOs (Scheme 3.4). In order to optimize the reaction conditions for each PTEMPO derivative, various solvents, catalysts, feeding ratios, temperatures and reaction times were screened, respectively. The general procedures are as follows: to a solution of active ester polymer, catalyst dissolved in solvent under inert condition at a certain temperature, the TEMPO nucleophile dissolved in the same solvent was added dropwise. In specific intervals, samples were withdrawn for FTIR measurements to follow the progress of the reaction. The resulting polymers were purified by precipitation in diethyl ether/*n*-hexane (v/v = 1/1) or dialysis in water, and afterwards freeze dried. For detailed reaction conditions please refer to chapter 3.
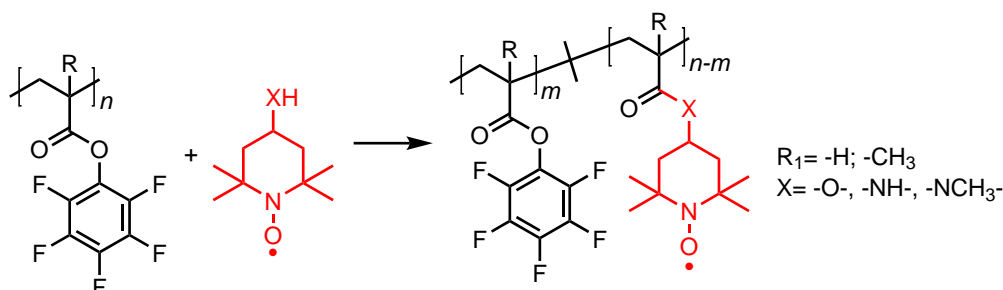
Scheme 7.3: Synthesis of various TEMPO containing polymers by PPM via activated esters.

Polymeric *N*-acylpyridinium Salt

PPFPA (95.40 mg, 0.40 mmol) and dimethylaminopyridine (DMAP, 98.50 mg, 0.80 mmol) were dissolved in 1,2-dimethoxyethane (DME) in a schlenk tube and reacted under nitrogen at 60 °C for 3 hr. The yellowish solution was concentrated and precipitated from cold *n*-hexane/diethylether/MeOH = 2/2/1 (v/v/v, 3 × 20 mL). The yellow solid intermediate was only soluble in DMAc and DMF at room temperature.

Multiple Pyrene-Functionalized TEMPO-Containing Polymers

1) Synthesis of Poly[(1-pyrene acrylamide)-ran-(TEMPO acrylamide)] (P(PyAm-ran-TAm))

P1 and P2 were synthesized in a two-step, one-pot manner via PPM. To a solution of PPFPA (238.1 mg, 1.0 mmol repeating unit) and 1-aminopyrene (434.5 mg, 2.0 mmol) in anhydrous DME (20.0 mL), TEA (202.4 mg, 2.0 mmol) was added under nitrogen atmosphere while stirring, the mixture was heated at different temperatures (50 °C and 70 °C for P1 and P2, respectively) for 20 hr., which resulted in poly[(1-pyrene acrylamide)-ran-PFPA] (P1' and P2') with different pyrene contents. Afterwards, 4-amino-TEMPO (342.5 mg, 2.0 mmol) in DME (5 mL) was added dropwise and the mixture was stirred at 50 °C for another 3 hr. The solution was concentrated under vacuum, precipitated in a mixture of n-hexane and diethyl ether (v/v = 1/1) for three times, and dialysed in methanol and deionized water prior to be freeze-dried.
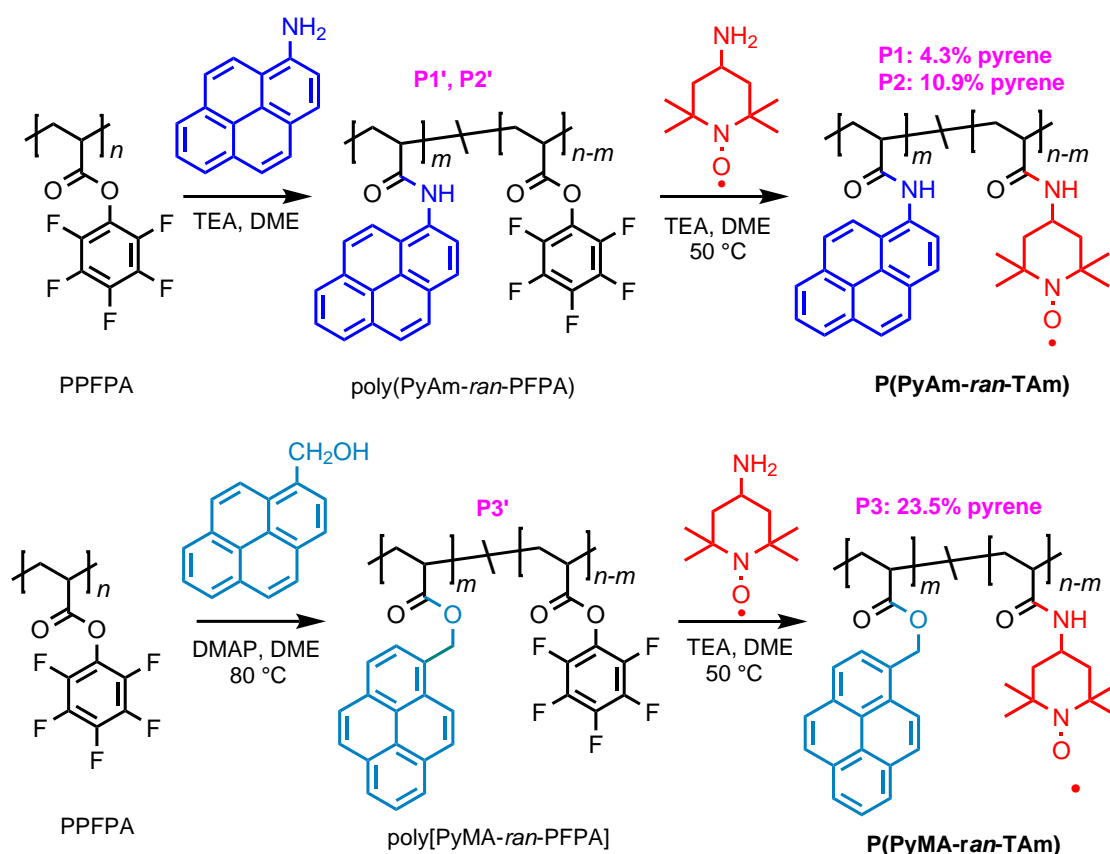
Scheme 7.4: Synthetic routes towards pyrene functionalized TEMPO-containing polymers.

2) Synthesis of Poly[(1-pyrenemethyl acrylate)-ran-(TEMPO acrylamide)] (P(PyMA-

ran-TAm))

P3 was synthesized in a similar procedure as P1 and P2. The first step was conducted with a condition reported previously by our research group [303]. To a solution of PPFPA (238.1 mg, 1.0 mmol repeating unit) and 1-pyrenemethanol (50.0 mg, 0.2 mmol) in anhydrous DME (20.0 mL), DMAP (24.4 mg, 0.2 mmol) was added under nitrogen atmosphere while stirring, the mixture was heated at 80 °C for 15 hr., which resulted in poly[(1-pyrenemethyl acrylate)-*ran*-PFPA] (P3'). Afterwards, 4-amino-TEMPO (342.5 mg, 2.0 mmol) in DME (5 mL) was added dropwise and the mixture was stirred at 50 °C for another 3 hr. The solution was concentrated under vacuum, precipitated in a mixture of *n*-hexane and diethyl ether (v/v = 1/1) for three times, and dialysed in methanol and deionized water prior to be freeze-dried.

7.2.4. Synthesis of PTMA via Post-Oxidation Method
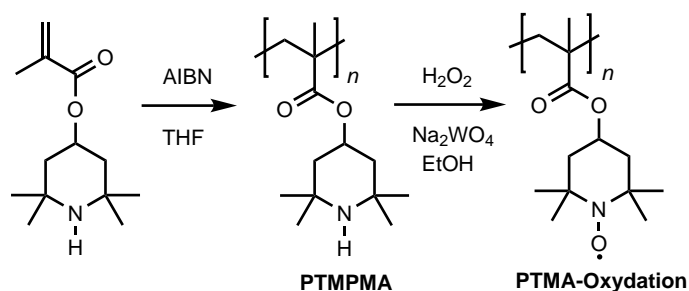
Scheme 7.5: Synthesis of PTMA-Oxydation.

As a reference, PTMA was prepared by traditional post-polymerization oxidation method [25], which was conducted in two steps, first polymerization of PTMA precursor i.e. PTMPMA, and afterwards oxidation of amino groups into ntiroxide radicals. To a solution of monomer 2,2,6,6-Tetramethylpiperidine methacrylate (TMPMA), 4.51 g, 20.00 mmol) in dry tetrahydrofuran (THF, 15 mL) under argon atmosphere, AIBN (0.04 g, 0.26 mmol) was added. After refluxing at 80 °C for 6 hr., the reaction mixture was allowed to cool to room temperature. Polymer was precipitated in *n*-hexane and dried at 40 °C for 24 hr. under vacuum. Yield: 91%. ^{1}H NMR (400 MHz, CDCl$_3$): δ 5.61–4.56 (m, 1H), 2.79–1.61 (m, 4H), 1.58–0.21 (m, 16H).

To a solution of PTMPMA (0.60 g, 2.67 mmol) and sodium tungstate dihydrate (0.15 g, 0.45 mmol) in MeOH (24 mL), solution of H$_2$O$_2$ was added (30 wt.%, 1.5 mL) in a dropwise manner under continuous vigorous stirring. The reaction mixture was stirred at room temperature for additional 48 hr. with protection against light by using aluminium foil. After 48 hr., a red polymer

precipitated from the solution. The residual MeOH was decanted out, and the polymer was washed with MeOH/H$_2$O (1/1, v/v, 2 × 5 mL). Finally, the polymer was dried under vacuum overnight. Yield: 85%. GPC (PMMA standard, DMAc): M_n = 40.1 kDa, M_w = 173 kDa, Đ = 4.3. G factor: 2.0033.

7.3. Cathodes Preparation and Coin Cell Assembly

7.3.1. General Preparative Procedure for Cathodes without Carbon Nanotubes

The cathode slurry was prepared by grinding the TEMPO-containing polymer (10 mg, 10 wt.%) and conductive carbon (80 mg, 80 wt.%) in a mortar for 5 minutes, subsequently transferring the mixed powder into a vial and adding *N*-methyl-2-pyrrolidone (NMP). After mixing on a magnetic stirrer for 2 hrs. to completely dissolve the polymer and coat it on the surface of the conductive carbon, a PVdF (10 mg) solution in NMP (10 wt.%) was added, followed by stirring the mixture overnight. The slurry was blade coated on an aluminium foil (thickness 30 μm) using a film coating applicator (byko-drive V, BYK Gardner) and dried in an oven overnight. Afterwards, the middle area of the coating film was chosen and punched out as disk shaped cathodes (ϕ = 14 mm). Some samples were calendered at 50 °C before punching with a calendering roll (Saueressig, GKL 200) to reduce the porosity of the coating film. The specific mass loading of each specimen was listed in Appendix Table B.1.

7.3.2. Preparation of Cathodes with Carbon Nanotubes

The TEMPO-pyrene co-polymer (10 mg) and carbon nanotubes (CNTs, 10 mg) were dispersed in a mixture of NMP (0.4 mL) and THF (2 mL) with the aid of a homogenizer (IKA, T 10 basic ULTRA-TURRAX). A suspension of CB-SP (70 mg) in NMP (1.3 mL) was homogenized as well. Afterwards, the aforementioned two colloidal dispersion were vigorously mixed together and put on a rotary evaporator to degas and remove the THF and part of NMP at 40 °C. In the end, a PVdF (10 mg) solution in NMP (10 wt.%) was added and homogenized gently to obtain a bubble-free and uniform slurry. Composite cathodes were formed by blade coating the above-mentioned slurries onto an aluminium foil (thickness 30 μm) and dried at room temperature and 80 °C under vacuum sequentially. The typical mass loading of the TEMPO-pyrene copolymer/CNTs hybrid

cathode was $\sim$ 1.5 mg cm^{-2}. The thickness of the hybrid electrodes was about 50 μm.

7.3.3. Coin Cell Assembly

Coin cells (CR2032 type) were assembled by stacking the polymer-based cathode, lithium metal anode and two pieces of separator film (Celgard H2013) with 1.0 M LiPF$_6$ in EC/DMC (50/50, v/v) electrolyte (150 μL) in an argon filled glove box (MBraun), where both O$_2$ and H$_2$O contents were less than 2 ppm.

Bibliography

[1] Staff at BP p.l.c. bp statistical review of world energy june 2020. Technical report, British Petroleum Company, London, UK, 2020.

[2] Staff at U.S. Energy Information Administration. International energy outlook 2019 with projections to 2050. Technical report, USDOE Energy Information Administration (EIA), Washington, DC (United States), 2019.

[3] RENEWABLE POWER GENERATION COSTS IN IRENA. Abu dhabi, 2019, 2018.

[4] A. Olhoff and J. M. Christensen. Emissions gap report 2018. 2019.

[5] A. Zablocki. Fact sheet: energy storage (2019). *Environmental and Energy Study Institute*, 2019.

[6] T. Gül, A. F. Pales, and L. Paoli. Batteries and hydrogen technology: keys for a clean energy future, iea, paris. Technical report, IEA, 2020.

[7] G. Zubi, R. Dufo-López, M. Carvalho, and G. Pasaoglu. The lithium-ion battery: State of the art and future perspectives. *Renewable and Sustainable Energy Reviews*, 89:292–308, 2018.

[8] M. Armand and J. M. Tarascon. Building better batteries. *nature*, 451(7179):652–657, 2008.

[9] K. Turcheniuk, D. Bondarev, V. Singhal, and G. Yushin. Ten years left to redesign lithium-ion batteries. *Nature*, 559:467–470, 2018.

[10] The nobel prize in chemistry 2019. *The Nobel Prize*, Oct 2019.

[11] F. Liu, C. Peng, A. Porvali, Z. Wang, B. P. Wilson, and M. Lundström. Synergistic recovery of valuable metals from spent nickel–metal hydride batteries and lithium-ion batteries. *ACS Sustainable Chemistry & Engineering*, 7(19):16103–16111, 2019.

[12] G. Harper, R. Sommerville, E. Kendrick, L. Driscoll, P. Slater, R. Stolkin, A. Walton, P. Christensen, O. Heidrich, S. Lambert, et al. Recycling lithium-ion batteries from electric vehicles. *Nature*, 575(7781):75–86, 2019.

[13] S. Lee, G. Kwon, K. Ku, K. Yoon, S. K. Jung, H. D. Lim, and K. Kang. Organic electrode materials: Recent progress in organic electrodes for Li and Na rechargeable batteries (adv. mater. 42/2018). *Advanced Materials*, 30(42):1870312, 2018.

[14] Y. Lu and J. Chen. Prospects of organic electrode materials for practical lithium batteries. *Nature Reviews Chemistry*, pages 1–16, 2020.

[15] L. Zhu, G. Ding, L. Xie, X. Cao, J. Liu, X. Lei, and J. Ma. Conjugated carbonyl compounds as high-performance cathode materials for rechargeable batteries. *Chemistry of Materials*, 31(21):8582–8612, 2019.

[16] Y. NuLi, Z. Guo, H. Liu, and J. Yang. A new class of cathode materials for rechargeable magnesium batteries: organosulfur compounds based on sulfur–sulfur bonds. *Electrochemistry Communications*, 9(8):1913–1917, 2007.

[17] K. Nakahara, S. Iwasa, M. Satoh, Y. Morioka, J. Iriyama, M. Suguro, and E. Hasegawa. Rechargeable batteries with organic radical cathodes. *Chemical Physics Letters*, 359(5-6):351–354, 2002.

[18] T. Matsunaga, T. Kubota, T. Sugimoto, and M. Satoh. High-performance lithium secondary batteries using cathode active materials of triquinoxalinylenes exhibiting six electron migration. *Chemistry letters*, 40(7):750–752, 2011.

[19] C. Luo, O. Borodin, X Ji, S. Hou, K. J. Gaskell, X. Fan, J. Chen, T. Deng, R. Wang, J. Jiang, and C. Wang. Azo compounds as a family of organic electrode materials for alkali-ion batteries. *Proceedings of the National Academy of Sciences*, 115(9):2004–2009, 2018.

[20] T. Janoschka, M. D. Hager, and U. S. Schubert. Powering up the future: radical polymers for battery applications. *Advanced Materials*, 24(48):6397–6409, 2012.

[21] C. Friebe and U. S. Schubert. High-power-density organic radical batteries. In *Electrochemical Energy Storage*, pages 65–99. Springer, 2019.

[22] K. Sato, R. Ichinoi, R. Mizukami, T. Serikawa, Y. Sasaki, J. Lutkenhaus, H. Nishide, and K. Oyaizu. Diffusion-cooperative model for charge transport by redox-active nonconjugated polymers. *Journal of the American Chemical Society*, 140(3):1049–1056, 2018.

[23] Y. Hu, K. Zhang, H. Hu, S. Wang, D. Ye, M. J. Monteiro, Z. Jia, and L. Wang. Molecular-level anchoring of polymer cathodes on carbon nanotubes towards rapid-rate and long-cycle sodium-ion storage. *Materials Chemistry Frontiers*, 2(10):1805–1810, 2018.

[24] H. Nishide, S. Iwasa, Y. J Pu, T. Suga, K. Nakahara, and M. Satoh. Organic radical battery:

nitroxide polymers as a cathode-active material. *Electrochimica acta*, 50(2-3):827–831, 2004.

[25] K. Zhang, Y. Hu, L. Wang, J. Fan, M. J. Monteiro, and Z. Jia. The impact of the molecular weight on the electrochemical properties of poly (TEMPO methacrylate). *Polymer Chemistry*, 8(11):1815–1823, 2017.

[26] L. Bugnon, C. J. H. Morton, P. Novak, J. Vetter, and P. Nesvadba. Synthesis of poly (4-methacryloyloxy-TEMPO) via group-transfer polymerization and its evaluation in organic radical battery. *Chemistry of materials*, 19(11):2910–2914, 2007.

[27] T. Sukegawa, H. Omata, I. Masuko, K. Oyaizu, and H. Nishide. Anionic polymerization of 4-methacryloyloxy-TEMPO using an MMA-capped initiator. *ACS Macro Letters*, 3(3):240–243, 2014.

[28] H. A. López-Peña, L. S. Hernández-Muñoz, B. A Frontana-Uribe, F. J. González, I. González, C. Frontana, and J. Cardoso. Tacticity influence on the electrochemical reactivity of group transfer polymerization-synthesized PTMA. *The Journal of Physical Chemistry B*, 116(18):5542–5550, 2012.

[29] Y. Zhang, A. Park, A. Cintora, S. R. McMillan, N. J. Harmon, A. Moehle, M. E. Flatté, G. D. Fuchs, and C. K. Ober. Impact of the synthesis method on the solid-state charge transport of radical polymers. *Journal of Materials Chemistry C*, 6(1):111–118, 2017.

[30] M. Park, X. Zhang, M. Chung, G. B. Less, and A. M. Sastry. A review of conduction phenomena in li-ion batteries. *Journal of Power Sources*, 195(24):7904–7929, 2010.

[31] K. Nakahara, J. Iriyama, S. Iwasa, M. Suguro, M. Satoh, and E. J. Cairns. Cell properties for modified PTMA cathodes of organic radical batteries. *Journal of power sources*, 165(1):398–402, 2007.

[32] A. Das and P. Théato. Activated ester containing polymers: opportunities and challenges for the design of functional macromolecules. *Chemical reviews*, 116(3):1434–1495, 2016.

[33] J. Labskỳ, J. Pilař, and J. Kálal. Spin-label study of the poly (methacrylamide)-type copolymers in solution. *Macromolecules*, 10(5):1153–1157, 1977.

[34] J. Labsky, J. Pilar, and J. Kálal. Effect of the length and structure of the side chain of soluble copolymers of the methacrylamide type on the mobility of the spin label bonded to the chain end. In *Journal of Polymer Science: Polymer Symposia*, volume 66, pages 33–40. Wiley Online Library, 1979.

[35] H. Fu, D. M Policarpio, J. D Batteas, and D. E Bergbreiter. Redox-controlled 'smart'polyacrylamide solubility. *Polymer Chemistry*, 1(5):631–633, 2010.

[36] S. R. A. Devenish, J. B. Hill, J. W. Blunt, J. C. Morris, and M. H. G. Munro. Dual side-reactions limit the utility of a key polymer therapeutic precursor. *Tetrahedron letters*, 47(17):2875–2878, 2006.

[37] P. Schattling, F. D. Jochum, and P. Théato. Multi-responsive copolymers: using thermo-, light-and redox stimuli as three independent inputs towards polymeric information processing. *Chemical Communications*, 47(31):8859–8861, 2011.

[38] T. Suga, K. Aoki, T. Yashiro, and H. Nishide. "click" incorporation of radical/ionic sites into a reactive block copolymer: A facile and on-demand domain functionalization approach toward organic resistive memory. *Macromolecular rapid communications*, 37(1):53–59, 2016.

[39] B. Marinho, M. Ghislandi, E. Tkalya, C. E. Koning, and G. de With. Electrical conductivity of compacts of graphene, multi-wall carbon nanotubes, carbon black, and graphite powder. *Powder Technology*, 221:351–358, 2012.

[40] J. A. Turner. A realizable renewable energy future. *Science*, 285(5428):687–689, 1999.

[41] I. Dincer. Renewable energy and sustainable development: a crucial review. *Renewable and sustainable energy reviews*, 4(2):157–175, 2000.

[42] H. Lund. Renewable energy strategies for sustainable development. *Energy*, 32(6):912–919, 2007.

[43] H. Chen, T. N. Cong, W. Yang, C. Tan, Y. Li, and Y. Ding. Progress in electrical energy storage system: A critical review. *Progress in natural science*, 19(3):291–312, 2009.

[44] Y. Gogotsi and P. Simon. True performance metrics in electrochemical energy storage. *Science*, 334(6058):917–918, 2011.

[45] H. Ibrahim, A. Ilinca, and J. Perron. Energy storage systems—characteristics and comparisons. *Renewable and sustainable energy reviews*, 12(5):1221–1250, 2008.

[46] D. Linden and T. Reddy. *Handbook of Batteries*. McGraw-Hill handbooks. McGraw-Hill Education, 2001.

[47] Y. Liang, C. Z. Zhao, H. Yuan, Y. Chen, W. Zhang, J. Q. Huang, D. Yu, Y. Liu, M. M. Titirici, Y. L. Chueh, et al. A review of rechargeable batteries for portable electronic devices. *InfoMat*, 1(1):6–32, 2019.

[48] María J. Piernas M. and E. Castillo Martínez. *Introduction to Batteries*, pages 1–8. Springer International Publishing, Cham, 2018.

[49] M. A. Hannan, M. S. H. Lipu, A. Hussain, and A. Mohamed. A review of lithium-ion battery state of charge estimation and management system in electric vehicle applications: Challenges and recommendations. *Renewable and Sustainable Energy Reviews*, 78:834–854, 2017.

[50] H. C. Hesse, M. Schimpe, D. Kucevic, and A. Jossen. Lithium-ion battery storage for the grid—a review of stationary battery storage system design tailored for applications in modern power grids. *Energies*, 10(12):2107, 2017.

[51] E. Fan, Li. Li, Z. Wang, J. Lin, Y. Huang, Y. Yao, R. Chen, and F. Wu. Sustainable recycling technology for Li-ion batteries and beyond: Challenges and future prospects. *Chemical Reviews*, 2020.

[52] J. Janek and W. G. Zeier. A solid future for battery development. *Nature Energy*, 1(9):1–4, 2016.

[53] D. Larcher and J. M. Tarascon. Towards greener and more sustainable batteries for electrical energy storage. *Nature chemistry*, 7(1):19, 2015.

[54] R. B. Araujo, A. Banerjee, P. Panigrahi, L. Yang, M. Strømme, M. Sjödin, C. M. Araujo, and R. Ahuja. Designing strategies to tune reduction potential of organic molecules for sustainable high capacity battery application. *Journal of Materials Chemistry A*, 5(9):4430–4454, 2017.

[55] Y. Liang, P. Zhang, S. Yang, Z. Tao, and J. Chen. Fused heteroaromatic organic compounds for high-power electrodes of rechargeable lithium batteries. *Advanced Energy Materials*, 3(5):600–605, 2013.

[56] N. Patil, A. Aqil, F. Ouhib, S. Admassie, O. Inganäs, C. Jérôme, and C. Detrembleur. Bioinspired redox-active catechol-bearing polymers as ultrarobust organic cathodes for lithium storage. *Advanced Materials*, 29(40):1703373, 2017.

[57] Q. Zhao, Z. Zhu, and J. Chen. Molecular engineering with organic carbonyl electrode materials for advanced stationary and redox flow rechargeable batteries. *Advanced Materials*, 29(48):1607007, 2017.

[58] K. Oyaizu, T. Kawamoto, T. Suga, and H. Nishide. Synthesis and charge transport properties of redox-active nitroxide polyethers with large site density. *Macromolecules*, 43(24):10382–10389, 2010.

[59] J. Lutkenhaus, S. Wang, A. M. G. Park, T. Ma, F. Li, A. Easley, and G. D. Fuchs. Solution-

processable thermally crosslinked organic radical polymer battery cathodes. *ChemSusChem*, 2020.

[60] T. Ibe, R. B. Frings, A. Lachowicz, S. Kyo, and H. Nishide. Nitroxide polymer networks formed by michael addition: on site-cured electrode-active organic coating. *Chemical Communications*, 46(20):3475–3477, 2010.

[61] G. Hauffman, A. Vlad, T. Janoschka, U. S. Schubert, and J. F. Gohy. Nanostructured organic radical cathodes from self-assembled nitroxide-containing block copolymer thin films. *Journal of Materials Chemistry A*, 3(38):19575–19581, 2015.

[62] J. Xie, Z. Wang, Z. J. Xu, and Q. Zhang. Toward a high-performance all-plastic full battery with a'single organic polymer as both cathode and anode. *Advanced Energy Materials*, 8(21):1703509, 2018.

[63] Q. Bi, Z.and Kong, Y. Cao, G. Sun, F. Su, X. Wei, X. Li, A. Ahmad, L. Xie, and C. M. Chen. Biomass-derived porous carbon materials with different dimensions for supercapacitor electrodes: a review. *Journal of materials chemistry a*, 7(27):16028–16045, 2019.

[64] L. Zhang, Z. Liu, G. Cui, and L. Chen. Biomass-derived materials for electrochemical energy storages. *Progress in Polymer Science*, 43:136–164, 2015.

[65] C. Friebe, A. Lex-Balducci, and U. S. Schubert. Sustainable energy storage: recent trends and developments toward fully organic batteries. *ChemSusChem*, 12(18):4093–4115, 2019.

[66] G. A. Snook, P. Kao, and A. S. Best. Conducting-polymer-based supercapacitor devices and electrodes. *Journal of power sources*, 196(1):1–12, 2011.

[67] S. I. Tobishima, J. I. Yamaki, and A. Yamaji. Cathode characteristics of organic electron acceptors for lithium batteries. *Journal of The Electrochemical Society*, 131(1):57, 1984.

[68] K. A. See, S. Hug, K. Schwinghammer, M. A. Lumley, Y. Zheng, J. M. Nolt, G. D. Stucky, F. Wudl, B. V. Lotsch, and R. Seshadri. Lithium charge storage mechanisms of cross-linked triazine networks and their porous carbon derivatives. *Chemistry of Materials*, 27(11):3821–3829, 2015.

[69] J. Hong, M. Lee, B. Lee, D. H. Seo, C. B. Park, and K. Kang. Biologically inspired pteridine redox centres for rechargeable batteries. *Nature communications*, 5(1):1–9, 2014.

[70] K. Shimizu, T. Yamamoto, P. Pandit, H. Yoshikawa, and S. Higashibayashi. Application of hydrazine-embedded heterocyclic compounds to high voltage rechargeable lithium organic batteries. *Scientific reports*, 8(1):1–6, 2018.

[71] M. Armand, S. Grugeon, H. Vezin, S. Laruelle, P. Ribière, P. Poizot, and J. M. Tarascon. Conjugated dicarboxylate anodes for Li-ion batteries. *Nature materials*, 8(2):120–125, 2009.

[72] X. Han, G. Qing, J. Sun, and T. Sun. How many lithium ions can be inserted onto fused c6 aromatic ring systems? *Angewandte Chemie International Edition*, 51(21):5147–5151, 2012.

[73] G. S. Vadehra, R. P. Maloney, M. A. Garcia-Garibay, and B. Dunn. Naphthalene diimide based materials with adjustable redox potentials: Evaluation for organic lithium-ion batteries. *Chemistry of Materials*, 26(24):7151–7157, 2014.

[74] H. Chen, M. Armand, G. Demailly, F. Dolhem, P. Poizot, and J. M. Tarascon. From biomass to a renewable $Li_xC_6O_6$ organic electrode for sustainable Li-ion batteries. *ChemSusChem: Chemistry & Sustainability Energy & Materials*, 1(4):348–355, 2008.

[75] A. Ueda, H. Wasa, S. Nishida, Y. Kanzaki, K. Sato, D. Shiomi, T. Takui, and Y. Morita. An extremely redox-active air-stable neutral π radical: Dicyanomethylene-substituted triangulene with a threefold symmetry. *Chemistry–A European Journal*, 18(51):16272–16276, 2012.

[76] Y. Morita, S. Nishida, T. Murata, M. Moriguchi, A. Ueda, M. Satoh, K. Arifuku, K. Sato, and T. Takui. Organic tailored batteries materials using stable open-shell molecules with degenerate frontier orbitals. *Nature materials*, 10(12):947–951, 2011.

[77] J. Y. Shin, T. Yamada, H. Yoshikawa, K. Awaga, and H. Shinokubo. An antiaromatic electrode-active material enabling high capacity and stable performance of rechargeable batteries. *Angewandte Chemie International Edition*, 53(12):3096–3101, 2014.

[78] Y. Hanyu and I. Honma. Rechargeable quasi-solid state lithium battery with organic crystalline cathode. *Scientific reports*, 2:453, 2012.

[79] K. Nakahara, K. Oyaizu, and H. Nishide. Organic radical battery approaching practical use. *Chemistry letters*, 40(3):222–227, 2011.

[80] Y. Yonekuta, K. Oyaizu, and H. Nishide. Structural implication of oxoammonium cations for reversible organic one-electron redox reaction to nitroxide radicals. *Chemistry letters*, 36(7):866–867, 2007.

[81] T. Suga, Y. J. Pu, K. Oyaizu, and H. Nishide. Electron-transfer kinetics of nitroxide radicals as an electrode-active material. *Bulletin of the Chemical Society of Japan*, 77(12):2203–2204, 2004.

[82] T. Suga, H. Ohshiro, S. Sugita, K. Oyaizu, and H. Nishide. Emerging n-type redox-active radical polymer for a totally organic polymer-based rechargeable battery. *Advanced Materials*,

21(16):1627–1630, 2009.

[83] T. Koizumi, H. Ohfuji, S. Tanaka, S. Shigematsu, N. Akutagawa, M. Satoh, and Y. Miura. Charge–discharge behavior of secondary organic radical battery using 2-aryl nitronyl nitroxides as the cathode active material. *Chemistry Letters*, 43(7):1092–1094, 2014.

[84] Y. Imada, H. Nakano, K. Furukawa, R. Kishi, M. Nakano, H. Maruyama, M. Nakamoto, A. Sekiguchi, M. Ogawa, T. Ohta, et al. Isolation of hypervalent group-16 radicals and their application in organic-radical batteries. *Journal of the American Chemical Society*, 138(2):479–482, 2016.

[85] J. E. Nutting, M. Rafiee, and S. S. Stahl. Tetramethylpiperidine *N*-oxyl (TEMPO), phthalimide *N*-oxyl (PINO), and related *N*-oxyl species: electrochemical properties and their use in electrocatalytic reactions. *Chemical reviews*, 118(9):4834–4885, 2018.

[86] J. K. Kim, G. Cheruvally, J. H. Ahn, Y. G. Seo, D. S. Choi, S. H. Lee, and C. E. Song. Organic radical battery with PTMA cathode: Effect of PTMA content on electrochemical properties. *Journal of Industrial and Engineering Chemistry*, 14(3):371–376, 2008.

[87] C. M. Liu, J. Chen, F. Q. Wang, and B. L. Yi. Improvement of electrochemical properties of PTMA cathode by using carbon blacks with high specific surface area. *Russian Journal of Electrochemistry*, 48(11):1052–1057, 2012.

[88] W. Guo, Y. M. Yin, S. Xin, Y. G. Guo, and L. J. Wan. Superior radical polymer cathode material with a two-electron process redox reaction promoted by graphene. *Energy & Environmental Science*, 5(1):5221–5225, 2012.

[89] B. Ernould, M. Devos, J. P. Bourgeois, J. Rolland, A. Vlad, and J. F. Gohy. Grafting of a redox polymer onto carbon nanotubes for high capacity battery materials. *Journal of Materials Chemistry A*, 3(16):8832–8839, 2015.

[90] T. Sukegawa, K. Sato, K. Oyaizu, and H. Nishide. Efficient charge transport of a radical polyether/SWCNT composite electrode for an organic radical battery with high charge-storage density. *RSC Advances*, 5(20):15448–15452, 2015.

[91] E. Lebègue, T. Brousse, J. Gaubicher, R. Retoux, and C. Cougnon. Toward fully organic rechargeable charge storage devices based on carbon electrodes grafted with redox molecules. *Journal of Materials Chemistry A*, 2(23):8599–8602, 2014.

[92] M. Suguro, S. Iwasa, and K. Nakahara. Fabrication of a practical and polymer-rich organic radical polymer electrode and its rate dependence. *Macromolecular rapid communications*, 29(20):1635–

1639, 2008.

[93] W. Choi, S. Ohtani, K. Oyaizu, H. Nishide, and K. E. Geckeler. Radical polymer-wrapped swnts at a molecular level: high-rate redox mediation through a percolation network for a transparent charge-storage material. *Advanced Materials*, 23(38):4440–4443, 2011.

[94] M. Yoshio, R. J. Brodd, and A. Kozawa. *Lithium-ion batteries*, volume 1. Springer, 2009.

[95] Y. Shi, X. Zhou, and G. Yu. Material and structural design of novel binder systems for high-energy, high-power lithium-ion batteries. *Accounts of chemical research*, 50(11):2642–2652, 2017.

[96] S. L Chou, Y. Pan, J. Z. Wang, H. K. Liu, and S. X. Dou. Small things make a big difference: binder effects on the performance of Li and Na batteries. *Physical Chemistry Chemical Physics*, 16(38):20347–20359, 2014.

[97] D. R Nevers, F. R. Brushett, and D. R. Wheeler. Engineering radical polymer electrodes for electrochemical energy storage. *Journal of Power Sources*, 352:226–244, 2017.

[98] S. Komaba, T. Tanaka, T. Ozeki, T. Taki, H. Watanabe, and H. Tachikawa. Fast redox of composite electrode of nitroxide radical polymer and carbon with polyacrylate binder. *Journal of Power Sources*, 195(18):6212–6217, 2010.

[99] N. Casado, G. Hernández, A. Veloso, S. Devaraj, D. Mecerreyes, and M. Armand. PEDOT radical polymer with synergetic redox and electrical properties. *ACS Macro letters*, 5(1):59–64, 2016.

[100] Y. H Wang, M. K Hung, C. H. Lin, H. C. Lin, and J. T. Lee. Patterned nitroxide polymer brushes for thin-film cathodes in organic radical batteries. *Chemical Communications*, 47(4):1249–1251, 2011.

[101] M. K. Hung, Y. H. Wang, C. H. Lin, H. C. Lin, and J. T. Lee. Synthesis and electrochemical behaviour of nitroxide polymer brush thin-film electrodes for organic radical batteries. *Journal of Materials Chemistry*, 22(4):1570–1577, 2012.

[102] T. S. Kim, J. E. Lim, M. S. Oh, and J. K. Kim. Carbon conductor-and binder-free organic electrode for flexible organic rechargeable batteries with high energy density. *Journal of Power Sources*, 361:15–20, 2017.

[103] C. H. Lin, W. J. Chou, and J. T. Lee. Three-dimensionally ordered macroporous nitroxide polymer brush electrodes prepared by surface-initiated atom transfer polymerization for organic radical batteries. *Macromolecular rapid communications*, 33(2):107–113, 2012.

[104] Y. Kim, C. Jo, J. Lee, C. W. Lee, and S. Yoon. An ordered nanocomposite of organic radical

polymer and mesocellular carbon foam as cathode material in lithium ion batteries. *Journal of Materials Chemistry*, 22(4):1453–1458, 2012.

[105] J. K. Kim. Micro-fibrous organic radical electrode to improve the electrochemical properties of organic rechargeable batteries. *Journal of power sources*, 242:683–686, 2013.

[106] J. K. Kim, J. Scheers, J. H. Ahn, P. Johansson, A. Matic, and P. Jacobsson. Nano-fibrous polymer films for organic rechargeable batteries. *Journal of materials chemistry A*, 1(7):2426–2430, 2013.

[107] T. Suga, H. Konishi, and H. Nishide. Photocrosslinked nitroxide polymer cathode-active materials for application in an organic-based paper battery. *Chemical Communications*, (17):1730–1732, 2007.

[108] T. Janoschka, A. Teichler, B. Häupler, T. Jähnert, M. D. Hager, and U. S. Schubert. Reactive inkjet printing of cathodes for organic radical batteries. *Advanced Energy Materials*, 3(8):1025–1028, 2013.

[109] S. Yoshihara, H. Isozumi, M. Kasai, H. Yonehara, Y. Ando, K. Oyaizu, and H. Nishide. Improving charge/discharge properties of radical polymer electrodes influenced strongly by current collector/carbon fiber interface. *The Journal of Physical Chemistry B*, 114(25):8335–8340, 2010.

[110] C. H. Lin, J. T. Lee, D. R. Yang, H. W. Chen, and S. T. Wu. Nitroxide radical polymer/carbon-nanotube-array electrodes with improved c-rate performance in organic radical batteries. *RSC Advances*, 5(42):33044–33048, 2015.

[111] Y. Qian, S. Hu, X. Zou, Z. Deng, Y. Xu, Z. Cao, Y. Kang, Y. Deng, Q. Shi, K. Xu, et al. How electrolyte additives work in li-ion batteries. *Energy storage materials*, 20:208–215, 2019.

[112] J. Kalhoff, G. G. Eshetu, D. Bresser, and S. Passerini. Safer electrolytes for lithium-ion batteries: state of the art and perspectives. *ChemSusChem*, 8(13):2154–2175, 2015.

[113] K. Koshika, N. Sano, K. Oyaizu, and H. Nishide. An ultrafast chargeable polymer electrode based on the combination of nitroxide radical and aqueous electrolyte. *Chemical communications*, (7):836–838, 2009.

[114] H. C. Lin, C. C. Li, and J. T. Lee. Nitroxide polymer brushes grafted onto silica nanoparticles as cathodes for organic radical batteries. *Journal of Power Sources*, 196(19):8098–8103, 2011.

[115] K. Nakahara, K. Oyaizu, and H. Nishide. Electrolyte anion-assisted charge transportation in poly (oxoammonium cation/nitroxyl radical) redox gels. *Journal of Materials Chemistry*, 22(27):13669–13673, 2012.

[116] J. K. Kim, A. Matic, J. H. Ahn, and P. Jacobsson. Improving the stability of an organic battery with an ionic liquid-based polymer electrolyte. *RSC advances*, 2(26):9795–9797, 2012.

[117] Y. Y. Cheng, C. C. Li, and J. T. Lee. Electrochemical behavior of organic radical polymer cathodes in organic radical batteries with *N*-butyl-*N*-methylpyrrolidinium bis (trifluoromethylsulfonyl) imide ionic liquid electrolytes. *Electrochimica acta*, 66:332–339, 2012.

[118] G. Hauffman, Q. Maguin, J. P. Bourgeois, A. Vlad, and J. F. Gohy. Micellar cathodes from self-assembled nitroxide-containing block copolymers in battery electrolytes. *Macromolecular rapid communications*, 35(2):228–233, 2014.

[119] S. Iwasa, T. Nishi, and S. Nakamura. Enhancement of rapid charging capability of organic radical battery using ethylene carbonate-based electrolyte containing LiFSI. *Journal of Power Sources*, 402:157–162, 2018.

[120] P. Gerlach, R. Burges, A. Lex-Balducci, U. S. Schubert, and A. Balducci. The influence of the electrolyte composition on the electrochemical behaviour of cathodic materials for organic radical batteries. *Journal of Power Sources*, 405:142–149, 2018.

[121] D. Aurbach, Y. Talyosef, B. Markovsky, E. Markevich, E. Zinigrad, L. Asraf, J. S. Gnanaraj, and H. J. Kim. Design of electrolyte solutions for li and Li-ion batteries: a review. *Electrochimica Acta*, 50(2-3):247–254, 2004.

[122] S. Wang, F. Li, A. D. Easley, and J. L. Lutkenhaus. Real-time insight into the doping mechanism of redox-active organic radical polymers. *Nature materials*, 18(1):69–75, 2019.

[123] E. P. Roth and C. J. Orendorff. How electrolytes influence battery safety. *Electrochemical Society Interface*, 21(2):45, 2012.

[124] H. Lee, M. Yanilmaz, O. Toprakci, K. Fu, and X. Zhang. A review of recent developments in membrane separators for rechargeable lithium-ion batteries. *Energy & Environmental Science*, 7(12):3857–3886, 2014.

[125] W. Guo, J. Su, Y. H. Li, L. J. Wan, and Y. G. Guo. Nitroxide radical polymer/graphene nanocomposite as an improved cathode material for rechargeable lithium batteries. *Electrochimica acta*, 72:81–86, 2012.

[126] S. Yeşilot, F. Hacıvelioğlu, S. Küçükköylü, K. B. Çelik, G. Sayan, and R. Demir-Cakan. Design, synthesis, and characterization of polyphosphazene bearing stable nitroxide radicals as cathode-active materials in Li-ion batteries. *Macromolecular Chemistry and Physics*, 218(17):1700051, 2017.

[127] J. Zhu, M. Yanilmaz, K. Fu, C. Chen, Y. Lu, Y. Ge, D. Kim, and X. Zhang. Understanding glass fiber membrane used as a novel separator for lithium–sulfur batteries. *Journal of membrane science*, 504:89–96, 2016.

[128] J. K. Kim, G. Cheruvally, J. W. Choi, J. H. Ahn, D. S. Choi, and C. E. Song. Rechargeable organic radical battery with electrospun, fibrous membrane-based polymer electrolyte. *Journal of the Electrochemical Society*, 154(9):A839, 2007.

[129] Q. Liu, J. Sun, H. Lv, S. Long, K. Yin, N. Wan, Y. Li, L. Sun, and M. Liu. Real-time observation on dynamic growth/dissolution of conductive filaments in oxide-electrolyte-based ReRAM. *Advanced Materials*, 24(14):1844–1849, 2012.

[130] Batteries from the printer: Evonik presents a new technology at the LOPEC trade show. *corporate.evonik.com*, Mar 2019.

[131] Evonik and ynvisible introduce technology demonstrator for printed electronics. *corporate.evonik.com*, May 2020.

[132] LOPEC: Printed electronics is conquering numerous application sectors. `https://www.printedelectronicsnow.com/live-from-shows/lopec/2019-03-27/lopec-printed-electronics-conquering-numerous-appl`. Accessed: 2020-08-05.

[133] Z. Shuai, L. Wang, and C. Song. *Theory of charge transport in carbon electronic materials*. Springer Science & Business Media, 2012.

[134] K. Oyaizu and H. Nishide. Radical polymers for organic electronic devices: a radical departure from conjugated polymers? *Advanced Materials*, 21(22):2339–2344, 2009.

[135] K. Oyaizu, Y. Ando, H. Konishi, and H. Nishide. Nernstian adsorbate-like bulk layer of organic radical polymers for high-density charge storage purposes. *Journal of the American Chemical Society*, 130(44):14459–14461, 2008.

[136] T. W. Kemper, R. E. Larsen, and T. Gennett. Relationship between molecular structure and electron transfer in a polymeric nitroxyl-radical energy storage material. *The Journal of Physical Chemistry C*, 118(31):17213–17220, 2014.

[137] D. C. Bobela, B. K. Hughes, W. A. Braunecker, T. W. Kemper, R. E. Larsen, and T. Gennett. Close packing of nitroxide radicals in stable organic radical polymeric materials. *The Journal of Physical Chemistry Letters*, 6(8):1414–1419, 2015.

[138] R. Murry. Molecular design of electrode surfaces. *Techniques of chemistry*, 22, 1992.

[139] M. G. Sullivan and R. W. Murray. Solid state electron self-exchange dynamics in mixed valent poly (vinylferrocene) films. *The Journal of Physical Chemistry*, 98(16):4343–4351, 1994.

[140] D. N. Blauch and J. M. Saveant. Dynamics of electron hopping in assemblies of redox centers. percolation and diffusion. *Journal of the American Chemical Society*, 114(9):3323–3332, 1992.

[141] A. J. Bard and L. R. Faulkner. Fundamentals and applications. *Electrochemical Methods*, 2(482):580–632, 2001.

[142] C. Karlsson, T. Suga, and H. Nishide. Quantifying TEMPO redox polymer charge transport toward the organic radical battery. *ACS applied materials & interfaces*, 9(12):10692–10698, 2017.

[143] R. S. Nicholson. Theory and application of cyclic voltammetry for measurement of electrode reaction kinetics. *Analytical chemistry*, 37(11):1351–1355, 1965.

[144] T. Katsumata, M. Satoh, J. Wada, M. Shiotsuki, F. Sanda, and T. Masuda. Polyacetylene and polynorbornene derivatives carrying TEMPO. synthesis and properties as organic radical battery materials. *Macromolecular rapid communications*, 27(15):1206–1211, 2006.

[145] X. Zhang, H. Li, L. Li, G. Lu, S. Zhang, L. Gu, Y. Xia, and X. Huang. Polyallene with pendant nitroxyl radicals. *Polymer*, 49(16):3393–3398, 2008.

[146] M. Aydın, B. Esat, Ç. Kılıç, M. E. Köse, A. Ata, and F. Yılmaz. A polythiophene derivative bearing TEMPO as a cathode material for rechargeable batteries. *European polymer journal*, 47(12):2283–2294, 2011.

[147] L. Xu, F. Yang, C. Su, L. Ji, and C. Zhang. Synthesis and properties of novel TEMPO-contained polypyrrole derivatives as the cathode material of organic radical battery. *Electrochimica Acta*, 130:148–155, 2014.

[148] T. Suga, K. Yoshimura, and H. Nishide. Nitroxide-substituted polyether as a new material for batteries. In *Macromolecular Symposia*, volume 245, pages 416–422. Wiley Online Library, 2006.

[149] M. Suguro, S. Iwasa, Y. Kusachi, Y. Morioka, and K. Nakahara. Cationic polymerization of poly (vinyl ether) bearing a TEMPO radical: a new cathode-active material for organic radical batteries. *Macromolecular rapid communications*, 28(18-19):1929–1933, 2007.

[150] M. Suguro, A. Mori, S. Iwasa, K. Nakahara, and K. Nakano. Syntheses and electrochemical properties of TEMPO radical substituted silicones: active material for organic radical batteries. *Macromolecular Chemistry and Physics*, 210(17):1402–1407, 2009.

[151] T. Suga, Y. J. Pu, S. Kasatori, and H. Nishide. Cathode-and anode-active poly (nitroxylstyrene) s

for rechargeable batteries: p-and n-type redox switching via substituent effects. *Macromolecules*, 40(9):3167–3173, 2007.

[152] S. B. Sertkol, D. Sinirlioglu, B. Esat, and A. E. Muftuoglu. A novel cathode material based on polystyrene with pendant TEMPO moieties obtained via click reaction and its use in rechargeable batteries. *Journal of Polymer Research*, 22(7):136, 2015.

[153] H. Woehlk, J. Steinkoenig, C. Lang, L. Michalek, V. Trouillet, P. Krolla, A. S. Goldmann, J. P. Barner, L.and Blinco, C. Barner-Kowollik, et al. Engineering nitroxide functional surfaces using bioinspired adhesion. *Langmuir*, 34(10):3264–3274, 2018.

[154] T. Xu, J. Xiong, X. Du, Y. Zhang, S. Song, C. Xiong, and L. Dong. Polytriphenylamine derivative and carbon nanotubes as cathode materials for high-performance polymer-based batteries. *The Journal of Physical Chemistry C*, 122(35):20057–20063, 2018.

[155] J. Qu, F. Z. Khan, M. Satoh, J. Wada, H. Hayashi, K. Mizoguchi, and T. Masuda. Synthesis and charge/discharge properties of cellulose derivatives carrying free radicals. *Polymer*, 49(6):1490–1496, 2008.

[156] J. Qu, R. Morita, M. Satoh, J. Wada, F. Terakura, K. Mizoguchi, N. Ogata, and T. Masuda. Synthesis and properties of DNA complexes containing 2, 2, 6, 6-tetramethyl-1-piperidinoxy (tempo) moieties as organic radical battery materials. *Chemistry–A European Journal*, 14(11):3250–3259, 2008.

[157] R. Hicks. *Stable radicals: fundamentals and applied aspects of odd-electron compounds*. John Wiley & Sons, 2011.

[158] E. G. Rozantsev. *Free Nitroxyl Radicals*. Springer US, 1970.

[159] H. G. Aurich. Nitroxides. *Nitrones, Nitronates and Nitroxides (1989)*, pages 313–370, 1989.

[160] H. Karoui, F. L. Moigne, O. Ouari, and P. Tordo. Nitroxide radicals: properties, synthesis and applications. *Stable Radicals: Fundamentals and Applied Aspects of Odd-Electron Compounds*, pages 173–229, 2010.

[161] I. Novak, L. J. Harrison, B. Kovac, and L. M. Pratt. Electronic structure of persistent radicals: nitroxides. *The Journal of organic chemistry*, 69(22):7628–7634, 2004.

[162] D. F. Bowman, T. Gillan, and K. U. Ingold. Kinetic applications of electron paramagnetic resonance spectroscopy. III. Self-reactions of dialkyl nitroxide radicals. *Journal of the American Chemical Society*, 93(24):6555–6561, 1971.

[163] A. Nilsen and R. Braslau. Nitroxide decomposition: Implications toward nitroxide design for applications in living free-radical polymerization. *Journal of Polymer Science Part A: Polymer Chemistry*, 44(2):697–717, 2006.

[164] M. Amar, S. Bar, M. A. Iron, H. Toledo, B. Tumanskii, L. J. W. Shimon, M. Botoshansky, N. Fridman, and A. M. Szpilman. Design concept for α-hydrogen-substituted nitroxides. *Nature Communications*, 6(1):1–9, 2015.

[165] H. G. Aurich. *Nitroxides*, chapter 4, pages 313–370. John Wiley & Sons, Ltd, 2010.

[166] E. Fremy. Sur une nouvelle série d'acides formés d'oxygène, de soufre, d'hydrogène et d'azote. *Annales de chimie et de physique*, 15(3):408–488, 1845.

[167] J. F. w. Keana. Newer aspects of the synthesis and chemistry of nitroxide spin labels. *Chemical reviews*, 78(1):37–64, 1978.

[168] D. Bardelang, K. Banaszak, H. Karoui, A. Rockenbauer, M. Waite, K. Udachin, J. A. Ripmeester, C. I. Ratcliffe, O. Ouari, and P. Tordo. Probing cucurbituril assemblies in water with TEMPO-like nitroxides: a trinitroxide supraradical with spin- spin interactions. *Journal of the American Chemical Society*, 131(15):5402–5404, 2009.

[169] E. Finkelstein, G. M. Rosen, E. J. Raukman, and J. Paxton. Spin trapping of superoxide. *Molecular pharmacology*, 16(2):676–685, 1979.

[170] Y. Wu, L. Bi, W. Bi, Z. Li, M. Zhao, C. Wang, J. Ju, and S. Peng. Novel 2-substituted nitronyl nitroxides as free radical scavengers: synthesis, biological evaluation and structure–activity relationship. *Bioorganic & medicinal chemistry*, 14(16):5711–5720, 2006.

[171] S. Wertz and A. Studer. Nitroxide-catalyzed transition-metal-free aerobic oxidation processes. *Green chemistry*, 15(11):3116–3134, 2013.

[172] J. P. Lomont, S. C. Nguyen, and C. B. Harris. Reactivity of TEMPO toward 16-and 17-electron organometallic reaction intermediates: a time-resolved IR study. *Journal of the American Chemical Society*, 135(30):11266–11273, 2013.

[173] J. Nicolas, Y. Guillaneuf, C. Lefay, D. Bertin, D. Gigmes, and B. Charleux. Nitroxide-mediated polymerization. *Progress in Polymer Science*, 38(1):63–235, 2013.

[174] O.A. Lebedev and S.N. Kazarnovskii. Catalytic oxidation of aliphatic amines with hydrogen peroxide. *Trudy po khimii i khim technologii (Gorkii)*, 8:649–652, 1959.

[175] F. Francis. Preparation of triacetonamine hydrate. *J. Chem. Soc*, 2897:1927, 1927.

[176] H. K. Hall Jr. Steric effects on the base strengths of cyclic amines1. *Journal of the American Chemical Society*, 79(20):5444–5447, 1957.

[177] T. Haruna, A. Nishimura, and K. Sugibuchi. Method for preparing 2, 2, 6, 6-tetramethyl-4-oxopiperidine, May 5 1987. US Patent 4,663,459.

[178] A. Wu, W. Yang, and X. Pan. Preparation of triacetoneamine, an improved method. *Synthetic communications*, 26(19):3565–3569, 1996.

[179] Y. C. Son, S. L. Suib, and R. E. Malz. A selective process to prepare triacetone amine. *Chemical Industries-New York-Marcel Dekker*, pages 559–564, 2003.

[180] W. Heintz. Triacetondiamin. *Justus Liebigs Annalen der Chemie*, 203(3):336–350, 1880.

[181] G. Sosnovsky, J. Lukszo, R. C. Brasch, U. G. Eriksson, and T. N. Tozer. Evaluation of spin labeled tartaric and galactaric diamides as potential MRI contrast enhancing agents. *European journal of medicinal chemistry*, 24(3):241–247, 1989.

[182] K. Murayama, S. Morimura, T. Toda, E. Yamao, T. Tsuzi, S. Higashida, and O. Amakasu. Preparation of 2, 2, 6, 6-tetramethyl-4-oxopiperidine, May 19 1970. US Patent 3,513,170.

[183] G. K. Friestad and B. P. Branchaud. *Ammonium Tetrafluoroborate*. American Cancer Society, 2001.

[184] G. M. Rosen, E. Schneider, S. Shortkroff, P. Tsai, and C. S. Winalski. Use of sodium triacetoxyborohydride in the synthesis of nitroxide biradicals. *Journal of the Chemical Society, Perkin Transactions 1*, (23):2663–2667, 2002.

[185] E. E. Anggard and A. I. Haj-Yehia. Piperidine and pyrrolidine derivatives comprising a nitric oxide donor for treating stress, September 10 2002. US Patent 6,448,267.

[186] G. M. Rosen. Use of sodium cyanoborohydride in the preparation of biologically active nitroxides. *Journal of Medicinal Chemistry*, 17(3):358–360, 1974.

[187] S. Nakatsuji, T. Ojima, H. Akutsu, and J. Yamada. Anthracene derivatives and the corresponding dimers with TEMPO radicals. *The Journal of organic chemistry*, 67(3):916–921, 2002.

[188] N. Koga, S. Karasawa, H. Hayashi, A. Tanaka, and K. Odoi. Hyperbranched polymer having nitroxyl group, August 9 2011. US Patent 7,994,258.

[189] E. W. Baxter and A. B. Reitz. Reductive aminations of carbonyl compounds with borohydride and borane reducing agents. *Organic reactions*, 59:1–714, 2004.

[190] C. Wang, L. Zhang, and J. You. Nickel-catalyzed aminoxylation of inert aliphatic C (sp^3)–H bonds with stable nitroxyl radicals under air: One-pot route to α-formyl acid derivatives. *Organic letters*, 19(7):1690–1693, 2017.

[191] J. A. Hendricks, S. V. Gullà, D. E. Budil, and R. N. Hanson. Synthesis of a spin-labeled anti-estrogen as a dynamic motion probe for the estrogen receptor ligand binding domain. *Bioorganic & medicinal chemistry letters*, 22(4):1743–1746, 2012.

[192] W. R. Couet, R. C. Brasch, C. Sosnovsky, J. Lukszo, I. Prakash, C. T. Gnewech, and T. N. Tozer. Influerce of chemical structure of nitroxyl spin labels on their reduction by ascorbic acid. *Tetrahedron*, 41(7):1165–1172, 1985.

[193] M. L. Smythe, C. R. Nakaie, and G. R. Marshall. α-helical versus 310-helical conformation of alanine-based peptides in aqueous solution: An electron spin resonance investigation. *Journal of the American Chemical Society*, 117(42):10555–10562, 1995.

[194] C. R. Toppin, G. T. Pauly, P. Devanesan, D. Kryak, and A. M. Bobst. Three novel spin-labeled substrates for enzymatic incorporation into nucleic acid lattices. *Helvetica chimica acta*, 69(2):345–349, 1986.

[195] H. Schlude. Oxidation of hydroxylamines to nitroxyl radicals with fremy's salt: Nitroxyl aldehydes. *Tetrahedron*, 29(23):4007–4011, 1973.

[196] T. Kálai, J. Jekő, Z. Berente, and K. Hideg. Palladium-catalyzed cross-coupling reactions of paramagnetic vinyl bromides and paramagnetic boronic acids. *Synthesis*, 2006(03):439–446, 2006.

[197] L. A. Krinitskaya and L. B. Volodarskii. 3-monohalo derivatives of triacetoneamine, 1-hydroxy-2, 2, 6, 6-tetramethyl-4-oxopiperidine, and 2, 2, 6, 6-tetramethyl-4-oxopiperidin-1-oxyl. *Bulletin of the Academy of Sciences of the USSR, Division of chemical science*, 31(2):401–404, 1982.

[198] G. Salinas, M. Aguilar-Martínez, and I. González. Electrochemical characterization of stable nitroxyl radical, intermediaries in the synthesis of 3-methacryloylamin-proxyl. *ECS Transactions*, 36(1):483, 2011.

[199] G. Z Zhu, S. P. Xu, and C. Y. Li. 3, 5-dibromo-4-oxo-2, 2, 6, 6-tetramethylpiperidin-1-yl oxide. *Acta Crystallographica Section E: Structure Reports Online*, 67(12):o3262–o3262, 2011.

[200] P. I. Dmitriev, A. B. Shapiro, L. G. Kuz'mina, and Yu. T. Struchkov. Synthesis and structure of cyclometalated nitroxyl radicals of piperidine. *Doklady Akademii Nauk SSSR*, 271(3):645–649, 1983.

[201] E. Sh. Kagan, V. I. Mikhailov, V. V. Pavlikov, A. B. Shapiro, V. D. Sholle, and E. G. Rozantsev. Unusual product of aminomethylation. *Izvestiya Akademii Nauk SSSR, Seriya Khimicheskaya*, (9):2187, 1978.

[202] A. D. Malievskii, A. B. Shapiro, I. V. Yakovleva, and S. V. Koroteev. Quantitative study of nucleophilic addition of secondary amines to 3, 5-dimethylene-2, 2, 6, 6-tetramethyl-4-oxopiperidine-1-oxyl. *Bulletin of the Academy of Sciences of the USSR, Division of chemical science*, 37(3):542–548, 1988.

[203] R. M. Moriarty, I. Prakash, and R. Penmasta. Hypervalent iodine oxidation. synthesis of spin labeled, 1-oxyl-2, 2, 6, 6-tetramethylpiperidine derivatives. *Journal of heterocyclic chemistry*, 22(6):1581–1582, 1985.

[204] D. L. Marshall, M. L. Christian, G. Gryn'ova, Michelle L. C., P. J. Barker, and S. J. Blanksby. Oxidation of 4-substituted TEMPO derivatives reveals modifications at the 1-and 4-positions. *Organic & biomolecular chemistry*, 9(13):4936–4947, 2011.

[205] G. T. Cunkle, M. E. Gande, and R. Seltzer. Derivatives of 1-oxyl-4-amino-2, 2, 6, 6-tetramethylpiperidine as polymerization inhibitors for (meth) acrylate monomers, July 27 1999. US Patent 5,928,558.

[206] L. A. Oparina, A. V. Artem'ev, O. V. Vysotskaya, I. V. Sterkhova, S. S. Khutsishvili, V. I. Smirnov, and B. A. Trofimov. Hydroalkoxylation of alkynes by a nitroxyl containing alcohol, 4-hydroxy-2, 2, 6, 6-tetramethylpiperidin-1-oxyl: synthesis of spin-labeled enol ethers. *ARKIVOC: Online Journal of Organic Chemistry*, 2015, 2015.

[207] F. Ge, Y. Xu, J. Chen, Z. Zhu, and H. Zhang. Rhodamine B-type free radical fluorescent probe, its preparation method and application in detection of free radical in production process of acrylic acid and ester, September 10 2018. CN 2018-11111971.

[208] T. Noda and F. Nakaya. Calcination material containing polymer with good low temperature thermal decomposition performance, and pattern formed with it, January 22 2013. JP 2014141549A.

[209] B. A. Trofimov, L. A. Oparina, I. V. Yakovleva, V. I. Lavrov, and A. B. Shapiro. Vinyl ether of 2, 2, 6, 6-tetramethyl-4-hydroxypiperidine-1-oxyl and its oligomers. *Bulletin of the Academy of Sciences of the USSR, Division of chemical science*, 35(12):2522–2526, 1986.

[210] D. Li, X. Shen, L. Chen, H. Jiang, and J. Wang. The stability of covalently immobilization of TEMPO on the polymer surface through ionic liquid linkage: a comparative and model research. *e-Polymers*, 15(1):39–44, 2015.

[211] Z. Zhang, Y. Gao, Y. Liu, J. Li, H. Xie, H. Li, and W. Wang. Organocatalytic aerobic oxidation of benzylic sp^3 C–H bonds of ethers and alkylarenes promoted by a recyclable TEMPO catalyst. *Organic letters*, 17(21):5492–5495, 2015.

[212] W. Zhang, D. Liu, C. Hua, J. Zhao, B. Chen, and X. Gou. Synthesis and properties of multifunctional nitroxyl radical hindered-amine light stabilizers. *Heterocyclic Communications*, 21(2):77–81, 2015.

[213] J. H. Guo, R. W. Jiang, J. L. Andersen, M. Esmann, and N. U. Fedosova. Spin-labeled derivatives of cardiotonic steroids as tools for characterization of the extracellular entrance to the binding site on Na$^+$, K$^+$-ATP ase. *The FEBS journal*, 285(12):2292–2305, 2018.

[214] C. Song, K. N. Hu, C. G. Joo, T. M. Swager, and R. G. Griffin. Totapol: a biradical polarizing agent for dynamic nuclear polarization experiments in aqueous media. *Journal of the American Chemical Society*, 128(35):11385–11390, 2006.

[215] S. Hashimoto, Y. Kono, Y. Kinpara, and K. Fujita. Dye-sensitized solar cell and electrolysis solution for dye-sensitized solar cell, April 2018. US Patent App. 15/568,437.

[216] N. Mittal, G. M. Nisola, J. G. Seo, S. P. Lee, and W. J. Chung. Organic radical functionalized sba-15 as a heterogeneous catalyst for facile oxidation of 5-hydroxymethylfurfural to 2, 5-diformylfuran. *Journal of Molecular Catalysis A: Chemical*, 404:106–114, 2015.

[217] F. Behrends, H. Wagner, A. Studer, O. Niehaus, R. Pöttgen, and H. Eckert. Polynitroxides from alkoxyamine monomers: structural and kinetic investigations by solid state NMR. *Macromolecules*, 46(7):2553–2561, 2013.

[218] T. Siu, S. Yekta, and A. K. Yudin. New approach to rapid generation and screening of diverse catalytic materials on electrode surfaces. *Journal of the American Chemical Society*, 122(48):11787–11790, 2000.

[219] S. Bothe, J. Nowag, V. Klimavičius, M. Hoffmann, T. I Troitskaya, E. V. Amosov, V. M. Tormyshev, I. Kirilyuk, A. Taratayko, A. Kuzhelev, et al. Novel biradicals for direct excitation highfield dynamic nuclear polarization. *The Journal of Physical Chemistry C*, 122(21):11422–11432, 2018.

[220] X. E. Wu, L. Ma, M. X. Ding, and L. X. Gao. TEMPO-derived task-specific ionic liquids for oxidation of alcohols. *Synlett*, 2005(04):607–610, 2005.

[221] W. L. Matier and G. Patil. Esterified N-hydroxypiperidine compounds for the amelioration of the development of cataracts and other opthalmic diseases, preparation thereof, and compositions containing them, October 15 2003. WO 2003096991A2.

[222] J. Zakrzewski and M. Krawczyk. Reactions of nitroxides. Part XII [1].–2, 2, 6, 6-tetramethyl-1-oxyl-4-piperidyl chloroformate–a new reactive nitroxyl radical. A one-pot synthesis of 2, 2, 6, 6-tetramethyl-1-oxyl-4-piperidyl *N*, *N*-dialkyl-carbamates. *Zeitschrift für Naturforschung B*, 66(5):493–498, 2011.

[223] F. Caffy and R. Nicolaÿ. Transformation of polyethylene into a vitrimer by nitroxide radical coupling of a bis-dioxaborolane. *Polymer Chemistry*, 10(23):3107–3115, 2019.

[224] L. Zhang, Y. B. Vogel, B. B. Noble, V. R. Goncales, N. Darwish, A. L. Brun, J. J. Gooding, G. G. Wallace, M. L. Coote, and S. Ciampi. TEMPO monolayers on Si (100) electrodes: electrostatic effects by the electrolyte and semiconductor space-charge on the electroactivity of a persistent radical. *Journal of the American Chemical Society*, 138(30):9611–9619, 2016.

[225] V. Strehmel, H. Rexhausen, and P. Strauch. Synthesis of 4-sulfonatooxy-2, 2, 6, 6-tetramethylpiperidine-1-yloxyl derivatives for investigation of ionic liquids. *Tetrahedron Letters*, 49(4):586–588, 2008.

[226] B. Huras, J. Zakrzewski, and M. Krawczyk. Reactions of nitroxides. Part IXa. Reactive (thio) phosphoryl mono-chlorides bearing a nitroxyl moiety and nitroxyl derivatives of coumarin. *Letters in Organic Chemistry*, 7(7):545–551, 2010.

[227] B. Huras, J. Zakrzewski, and M. Krawczyk. Reactions of nitroxides, part XI: *O*-aryl phenylselenophosphonates bearing a nitroxyl moiety. *Heteroatom Chemistry*, 22(2):137–147, 2011.

[228] J. Zakrzewski, B. Huras, A. Kiełczewska, M. Krawczyk, J. Hupko, and K. Jaszczuk. Reactions of nitroxides, part 17. synthesis, fungistatic and bacteriostatic activity of novel five-and six-membered nitroxyl selenoureas and selenocarbamates. *Molecules*, 24(13):2457, 2019.

[229] M. Tsunaga, C. Iwakura, and H. Tamura. Electrode reactions of nitroxide radicals at platinum in acetonitrile. *Electrochimica Acta*, 18(3):241–245, 1973.

[230] J. R. Fish, S. G. Swarts, M. D. Sevilla, and T. Malinski. Electrochemistry and spectroelectrochemistry of nitroxyl free radicals. *The Journal of Physical Chemistry*, 92(13):3745–3751, 1988.

[231] Y. Kato, Y. Shimizu, Y. Lin, K. Unoura, H. Utsumi, and T. Ogata. Reversible half-wave potentials of reduction processes on nitroxide radicals. *Electrochimica acta*, 40(17):2799–2802, 1995.

[232] S. Kishioka, S. Ohki, T. Ohsaka, and K. Tokuda. Reaction mechanism and kinetics of alcohol oxidation at nitroxyl radical modified electrodes. *Journal of Electroanalytical Chemistry*, 452(2):179–186, 1998.

[233] J. B. Gerken, Y. Q. Pang, M. B. Lauber, and S. S. Stahl. Structural effects on the pH-dependent redox properties of organic nitroxyls: Pourbaix diagrams for TEMPO, ABNO, and three TEMPO analogs. *The Journal of organic chemistry*, 83(14):7323–7330, 2017.

[234] S. Kishioka, M. Umeda, and A. Yamada. Effect of oxygen on the electrochemical reduction of nitroxyl radical: Interpretation of the mechanism for a redox probe in biological systems. *Analytical sciences*, 18(12):1379–1381, 2002.

[235] R. C. Engstrom. Electrochemical pretreatment of glassy carbon electrodes. *Analytical Chemistry*, 54(13):2310–2314, 1982.

[236] T. Fukushima, W. Drisdell, J. Yano, and Y. Surendranath. Graphite-conjugated pyrazines as molecularly tunable heterogeneous electrocatalysts. *Journal of the American Chemical Society*, 137(34):10926–10929, 2015.

[237] S. Nigam, K. D. Asmus, and R. L. Willson. Electron transfer and addition reactions of free nitroxyl radicals with radiation induced radicals. *Journal of the Chemical Society, Faraday Transactions 1: Physical Chemistry in Condensed Phases*, 72:2324–2340, 1976.

[238] A. Israeli, M. Patt, M. Oron, A. Samuni, R. Kohen, and S. Goldstein. Kinetics and mechanism of the comproportionation reaction between oxoammonium cation and hydroxylamine derived from cyclic nitroxides. *Free Radical Biology and Medicine*, 38(3):317–324, 2005.

[239] D. P. Hickey, D. A. Schiedler, I. Matanovic, P. V. Doan, P. Atanassov, S. D. Minteer, and M. S. Sigman. Predicting electrocatalytic properties: modeling structure–activity relationships of nitroxyl radicals. *Journal of the American Chemical Society*, 137(51):16179–16186, 2015.

[240] S. Kishioka, T. Ohsaka, and K. Tokuda. Electrochemical studies of acid-promoted disproportionation of nitroxyl radical. *Electrochimica acta*, 48(11):1589–1594, 2003.

[241] A. M. Janiszewska and M. Grzeszczuk. Mechanistic–kinetic scheme of oxidation/reduction of TEMPO involving hydrogen bonded dimer. RDE probe for availability of protons in reaction environment. *Electroanalysis: An International Journal Devoted to Fundamental and Practical Aspects of Electroanalysis*, 16(20):1673–1681, 2004.

[242] V. D. Sen', I. V. Tikhonov, L. I. Borodin, E. M. Pliss, V. A. Golubev, M. A. Syroeshkin, and A. I. Rusakov. Kinetics and thermodynamics of reversible disproportionation–comproportionation in redox triad oxoammonium cations–nitroxyl radicals–hydroxylamines. *Journal of Physical Organic Chemistry*, 28(1):17–24, 2015.

[243] G. Thomas and J. G. Mohanty. Oxidation-reduction of nitroxyl radicals: cyclic voltammetric

response in aqueous media. 1982.

[244] S. Morris, G. Sosnovsky, B. Hui, C. O. Huber, N. U. M. Rao, and H. M. Swartz. Chemical and electrochemical reduction rates of cyclic nitroxides (nitroxyls). *Journal of pharmaceutical sciences*, 80(2):149–152, 1991.

[245] K. Zhang, B. B. Noble, A. C. Mater, M. J. Monteiro, M. L. Coote, and Z. Jia. Effect of heteroatom and functionality substitution on the oxidation potential of cyclic nitroxide radicals: role of electrostatics in electrochemistry. *Physical Chemistry Chemical Physics*, 20(4):2606–2614, 2018.

[246] K. Chabita and P. C. Mandal. Electrochemical oxidation and reduction of nitroxides: A cyclic voltammetric and simulation study. *Indian Journal of Chemistry Section A-Inorganci Bio-Inorganic Physical Theoretical & Analytical Chemistry*, 41(11):2231–2237, 2002.

[247] R. Barhdadi, C. Comminges, A. P. Doherty, J. Y. Nédélec, S. O'Toole, and M. Troupel. The electrochemistry of TEMPO-mediated oxidation of alcohols in ionic liquid. *Journal of applied electrochemistry*, 37(6):723–728, 2007.

[248] W. Zhou, W. Liu, M. Qin, Z. Chen, J. Xu, J. Cao, and J. Li. Fundamental properties of TEMPO-based catholytes for aqueous redox flow batteries: effects of substituent groups and electrolytes on electrochemical properties, solubilities and battery performance. *RSC Advances*, 10(37):21839–21844, 2020.

[249] Y. Maruyama, K. Nagamine, A. Nomura, S. Iwasa, and S. Tokito. Electrochemical characterization of TEMPO radical in ionic liquids. *Electrochemistry*, 88(1):34–38, 2020.

[250] E. D. Carlson and M. Majda. Electrochemistry of TEMPO: an assessment of the water diffusion constant in the aqueous liquid/vapor interfacial region. *Journal of Solid State Electrochemistry*, 17(12):3083–3091, 2013.

[251] T. Kurosaki, K. W. Lee, and M. Okawara. Polymers having stable radicals. I. Synthesis of nitroxyl polymers from 4-methacryloyl derivatives of 2, 2, 6, 6-tetramethylpiperidine. *Journal of Polymer Science Part A-1: Polymer Chemistry*, 10(11):3295–3310, 1972.

[252] T. Janoschka, A. Teichler, A. Krieg, M. D. Hager, and U. S. Schubert. Polymerization of free secondary amine bearing monomers by RAFT polymerization and other controlled radical techniques. *Journal of Polymer Science Part A: Polymer Chemistry*, 50(7):1394–1407, 2012.

[253] N. Hergué, B. Ernould, A. Minoia, R. Lazzaroni, J. F. Gohy, P. Dubois, and O. Coulembier. Improving the performance of batteries by using multi-pyrene PTMA structures. *Batteries &*

Supercaps, 1(3):102–109, 2018.

[254] L. Rostro, A. G. Baradwaj, and B. W. Boudouris. Controlled radical polymerization and quantification of solid state electrical conductivities of macromolecules bearing pendant stable radical groups. *ACS Applied Materials & Interfaces*, 5(20):9896–9901, 2013.

[255] Lizbeth Rostro, Si Hui Wong, and Bryan W Boudouris. Solid state electrical conductivity of radical polymers as a function of pendant group oxidation state. *Macromolecules*, 47(11):3713–3719, 2014.

[256] O. Bertrand, B. Ernould, F. Boujioui, A. Vlad, and J. F. Gohy. Synthesis of polymer precursors of electroactive materials by SET-LRP. *Polymer Chemistry*, 6(33):6067–6072, 2015.

[257] J. A. Cella, J. A. Kelley, and E. F. Kenehan. Nitroxide-catalyzed oxidation of alcohols using m-chloroperbenzoic acid. new method. *The Journal of Organic Chemistry*, 40(12):1860–1862, 1975.

[258] B. Ganem. Biological spin labels as organic reagents. oxidation of alcohols to carbonyl compounds using nitroxyls. *The Journal of Organic Chemistry*, 40(13):1998–2000, 1975.

[259] K. A. Hansen, L. C. Chambers, M. Eing, C. Barner-Kowollik, K. Fairfull-Smith, and J. P. Blinco. A methoxyamine-protecting group for organic radical battery materials–an alternative approach. *ChemSusChem*, 2020.

[260] O. H. Griffith, J. F. W. Keana, S. Rottschaefer, and T. A. Warlick. Preparation and magnetic resonance of nitroxide polymers. *Journal of the American Chemical Society*, 89(19):5072–5072, 1967.

[261] T. Michinobu, J. Inui, and H. Nishide. Magnetic force microscopic images of nanometer-sized polyradical particles. *Polymer journal*, 35(1):71–75, 2003.

[262] C. Liedel and C. K. Ober. Nanopatterning of stable radical containing block copolymers for highly ordered functional nanomeshes. *Macromolecules*, 49(16):5884–5892, 2016.

[263] T. Endo, K. Takuma, T. Takata, and C. Hirose. Synthesis and polymerization of 4-(glycidyloxy)-2, 2, 6, 6-tetramethylpiperidine-1-oxyl. *Macromolecules*, 26(12):3227–3229, 1993.

[264] K. Oyaizu, T. Suga, K. Yoshimura, and H. Nishide. Synthesis and characterization of radical-bearing polyethers as an electrode-active material for organic secondary batteries. *Macromolecules*, 41(18):6646–6652, 2008.

[265] Z. Jia, Q. Fu, and J. Huang. Synthesis of poly (ethylene oxide) with pending 2, 2, 6, 6-

tetramethylpiperidine-1-oxyl groups and its further initiation of the grafting polymerization of styrene. *Journal of Polymer Science Part A: Polymer Chemistry*, 44(12):3836–3842, 2006.

[266] J. Qu, T. Katsumata, M. Satoh, J. Wada, and T. Masuda. Poly (7-oxanorbornenes) carrying 2, 2, 6, 6-tetramethylpiperidine-1-oxy (TEMPO) radicals: synthesis and charge/discharge properties. *Polymer*, 50(2):391–396, 2009.

[267] T. Sukegawa, I. Masuko, K. Oyaizu, and H. Nishide. Expanding the dimensionality of polymers populated with organic robust radicals toward flow cell application: synthesis of TEMPO-crowded bottlebrush polymers using anionic polymerization and ROMP. *Macromolecules*, 47(24):8611–8617, 2014.

[268] T. Katsumata, J. Qu, M. Shiotsuki, M. Satoh, J. Wada, J. Igarashi, K. Mizoguchi, and T. Masuda. Synthesis, characterization, and charge/discharge properties of polynorbornenes carrying 2, 2, 6, 6-tetramethylpiperidine-1-oxy radicals at high density. *Macromolecules*, 41(4):1175–1183, 2008.

[269] M. E. Hay, S Hui Wong, S. Mukherjee, and B. W Boudouris. Controlling open-shell loading in norbornene-based radical polymers modulates the solid-state charge transport exponentially. *Journal of Polymer Science Part B: Polymer Physics*, 55(20):1516–1525, 2017.

[270] D. Le, M. Dilger, V. Pertici, S. Diabaté, D. Gigmes, C. Weiss, and G. Delaittre. Ultra-fast synthesis of multivalent radical nanoparticles by ring-opening metathesis polymerization-induced self-assembly. *Angewandte Chemie International Edition*, 58(14):4725–4731, 2019.

[271] K. Oyaizu, H. Tatsuhira, and H. Nishide. Facile charge transport and storage by a TEMPO-populated redox mediating polymer integrated with polyaniline as electrical conducting path. *Polymer Journal*, 47(2):212–219, 2015.

[272] T. Suga, M. Sakata, K. Aoki, and H. Nishide. Synthesis of pendant radical-and ion-containing block copolymers via ring-opening metathesis polymerization for organic resistive memory. *ACS Macro Letters*, 3(8):703–707, 2014.

[273] Y. Xia, Y. Li, A. O. Burts, M. F. Ottaviani, D. A Tirrell, J. A. Johnson, N. J. Turro, and R. H. Grubbs. EPR study of spin labeled brush polymers in organic solvents. *Journal of the American Chemical Society*, 133(49):19953–19959, 2011.

[274] L. Dulog and S. Lutz. Polymerization of acetylene derivatives with nitroxyl radical pendant groups. *Die Makromolekulare Chemie, Rapid Communications*, 14(3):147–153, 1993.

[275] J. Qu, T. Katsumata, M. Satoh, J. Wada, J. Igarashi, K. Mizoguchi, and T. Masuda. Synthesis and charge/discharge properties of polyacetylenes carrying 2, 2, 6, 6-tetramethyl-1-piperidinoxy

radicals. *Chemistry–A European Journal*, 13(28):7965–7973, 2007.

[276] J. Qu, T. Fujii, T. Katsumata, Y. Suzuki, M. Shiotsuki, F. Sanda, M. Satoh, J. Wada, and T. Masuda. Helical polyacetylenes carrying 2, 2, 6, 6-tetramethyl-1-piperidinyloxy and 2, 2, 5, 5-tetramethyl-1-pyrrolidinyloxy moieties: Their synthesis, properties, and function. *Journal of Polymer Science Part A: Polymer Chemistry*, 45(23):5431–5445, 2007.

[277] P. Nesvadba, L. Bugnon, P. Maire, and P. Novák. Synthesis of a novel spirobisnitroxide polymer and its evaluation in an organic radical battery. *Chemistry of Materials*, 22(3):783–788, 2010.

[278] S. Shi, R. Pelton, Q. Fu, and S. Yang. Comparing polymer-supported TEMPO mediators for cellulose oxidation and subsequent polyvinylamine grafting. *Industrial & Engineering Chemistry Research*, 53(12):4748–4754, 2014.

[279] Q. Fu, Z. R. Gray, A. van der Est, and R. H Pelton. Phase behavior of aqueous poly (acrylic acid-*g*-TEMPO). *Macromolecules*, 49(13):4935–4939, 2016.

[280] H. Tokue, K. Kakitani, H. Nishide, and K. Oyaizu. Electrochemical current rectification with cross reaction at a TEMPO/viologen-substituted polymer thin-layer heterojunction. *RSC advances*, 6(101):99195–99201, 2016.

[281] G. Huang, X. Liu, Y. Bei, and H. Ma. Facile TEMPO immobilization onto poly (acrylic acid)-modified magnetic nanoparticles: Preparation and property. *International Journal of Polymer Science*, 2017, 2017.

[282] J. Wang, Z. Wu, H. Shen, and G. Wang. Synthesis, characterization and the paramagnetic properties of bottle-brush copolymers with shielding TEMPO radicals. *Polymer Chemistry*, 8(45):7044–7053, 2017.

[283] Y. Chen, Y. Zhang, X. Liu, X. Fan, B. Bai, K. Yang, Z. Liang, Z. Zhang, and K. Mai. Long-life and high-power binder-free cathode based on one-step synthesis of radical polymers with multi-pendant groups. *Macromolecular rapid communications*, 39(12):1800195, 2018.

[284] D. P. Hickey, R. D. Milton, D. Chen, M. S. Sigman, and S. D. Minteer. TEMPO-modified linear poly (ethylenimine) for immobilization-enhanced electrocatalytic oxidation of alcohols. *ACS Catalysis*, 5(9):5519–5524, 2015.

[285] K. Zhang, M. J. Monteiro, and Z. Jia. Stable organic radical polymers: synthesis and applications. *Polymer Chemistry*, 7(36):5589–5614, 2016.

[286] W. Xue, H. Mutlu, and P. Théato. Post-polymerization modification of polymeric active esters

towards TEMPO containing polymers: A systematic study. *European Polymer Journal*, page 109660, 2020.

[287] K. Koshika, N. Sano, K. Oyaizu, and H. Nishide. An aqueous, electrolyte-type, rechargeable device utilizing a hydrophilic radical polymer-cathode. *Macromolecular Chemistry and Physics*, 210(22):1989–1995, 2009.

[288] J. H. Ku, S. S. Hwang, D. J. Ham, M. S. Song, J. K. Shon, S. M. Ji, J. M. Choi, and S. G. Doo. Poly (isobutylene-alt-maleic anhydride) binders containing lithium foráhigh-performance Li-ion batteries. *Journal of Power Sources*, 287:36–42, 2015.

[289] I. Seok. Chae, M. Koyano, K. Oyaizu, and H. Nishide. Self-doping inspired zwitterionic pendant design of radical polymers toward a rocking-chair-type organic cathode-active material. *Journal of Materials Chemistry A*, 1(4):1326–1333, 2013.

[290] J. Zhu, T. Zhu, H. Tuo, and W. Zhang. Synthesis of a TEMPO-substituted polyacrylamide bearing a sulfonate sodium pendant and its properties in an organic radical battery. *Polymers*, 11(12):2076, 2019.

[291] H. Tokue, T. Murata, H. Agatsuma, H. Nishide, and K. Oyaizu. Charge–discharge with rocking-chair-type Li^+ migration characteristics in a zwitterionic radical copolymer composed of TEMPO and trifluoromethanesulfonylimide with carbonate electrolytes for a high-rate Li-ion battery. *Macromolecules*, 50(5):1950–1958, 2017.

[292] Y. Joo, V. Agarkar, S. H. Sung, B. M. Savoie, and B. W. Boudouris. A nonconjugated radical polymer glass with high electrical conductivity. *Science*, 359(6382):1391–1395, 2018.

[293] A. G Baradwaj, S. H. Wong, J. S. Laster, A. J. Wingate, M. E. Hay, and B. W. Boudouris. Impact of the addition of redox-active salts on the charge transport ability of radical polymer thin films. *Macromolecules*, 49(13):4784–4791, 2016.

[294] A. Vlad, J. Rolland, G. Hauffman, B. Ernould, and J. F. Gohy. Melt-polymerization of TEMPO methacrylates with nano carbons enables superior battery materials. *ChemSusChem*, 8(10):1692–1696, 2015.

[295] Y. Li, Z. Jian, M. Lang, C. Zhang, and X. Huang. Covalently functionalized graphene by radical polymers for graphene-based high-performance cathode materials. *ACS applied materials & interfaces*, 8(27):17352–17359, 2016.

[296] K. Zhang, Y. Hu, L. Wang, M. J. Monteiro, and Z. Jia. Pyrene-functionalized PTMA by NRC for greater π–π stacking with rGO and enhanced electrochemical properties. *ACS applied materials &*

interfaces, 9(40):34900–34908, 2017.

[297] N. Sano, W. Tomita, S. Hara, C. M. Min, J. S. Lee, K. Oyaizu, and H. Nishide. Polyviologen hydrogel with high-rate capability for anodes toward an aqueous electrolyte-type and organic-based rechargeable device. *ACS applied materials & interfaces*, 5(4):1355–1361, 2013.

[298] K. Hatakeyama-Sato, H. Wakamatsu, R. Katagiri, K. Oyaizu, and H. Nishide. An ultrahigh output rechargeable electrode of a hydrophilic radical polymer/nanocarbon hybrid with an exceptionally large current density beyond 1 A cm^{-2}. *Advanced Materials*, 30(26):1800900, 2018.

[299] K. Hatakeyama-Sato, H. Wakamatsu, K. Yamagishi, T. Fujie, S. Takeoka, K. Oyaizu, and H. Nishide. Ultrathin and stretchable rechargeable devices with organic polymer nanosheets conformable to skin surface. *Small*, 15(13):1805296, 2019.

[300] G. Hauffman, J. Rolland, J. P. Bourgeois, A. Vlad, and J. F. Gohy. Synthesis of nitroxide-containing block copolymers for the formation of organic cathodes. *Journal of Polymer Science Part A: Polymer Chemistry*, 51(1):101–108, 2013.

[301] S. Iwasa, T. Nishi, H. Sato, and S. Nakamura. Flexibility and high-rate discharge properties of organic radical batteries with gel-state electrodes. *Journal of The Electrochemical Society*, 164(4):A884, 2017.

[302] P. Théato and H. A. Klok. *Functional polymers by post-polymerization modification: concepts, guidelines and applications*. John Wiley & Sons, 2013.

[303] A. Das and P. Théato. Multifaceted synthetic route to functional polyacrylates by transesterification of poly (pentafluorophenyl acrylates). *Macromolecules*, 48(24):8695–8707, 2015.

[304] H. G. Batz, G. Franzmann, and H. Ringsdorf. Pharmakologisch aktive polymere, 5. modellreaktionen zur umsetzung von pharmaka und enzymen mit monomeren und polymeren reaktiven estern. *Die Makromolekulare Chemie: Macromolecular Chemistry and Physics*, 172(1):27–47, 1973.

[305] P. Ferruti, A. Bettelli, and A. Feré. High polymers of acrylic and methacrylic esters of *N*-hydroxysuccinimide as polyacrylamide and polymethacrylamide precursors. *Polymer*, 13(10):462–464, 1972.

[306] A. Godwin, M. Hartenstein, A. H. E. Müller, and S. Brocchini. Narrow molecular weight distribution precursors for polymer–drug conjugates. *Angewandte Chemie*, 113(3):614–617, 2001.

[307] M. Eberhardt, R. Mruk, R. Zentel, and P. Théato. Synthesis of pentafluorophenyl (meth) acrylate polymers: New precursor polymers for the synthesis of multifunctional materials. *European Polymer*

Journal, 41(7):1569–1575, 2005.

[308] Y. Liu, L. Wang, and C. Pan. Synthesis of block copoly (styrene-*b*-*p*-nitrophenyl methacrylate) and its derivatives by atom transfer radical polymerization. *Macromolecules*, 32(25):8301–8305, 1999.

[309] N. Metz and P. Théato. Controlled synthesis of poly (acetone oxime acrylate) as a new reactive polymer: Stimuli-responsive reactive copolymers. *European polymer journal*, 43(4):1202–1209, 2007.

[310] E. Pedone, X. Li, N. Koseva, O. Alpar, and S. Brocchini. An information rich biomedical polymer library. *Journal of Materials Chemistry*, 13(11):2825–2837, 2003.

[311] S. Y. Wong and D. Putnam. Overcoming limiting side reactions associated with an nhs-activated precursor of polymethacrylamide-based polymers. *Bioconjugate chemistry*, 18(3):970–982, 2007.

[312] X. Yang and V. B. Birman. Acyl transfer catalysis with 1, 2, 4-triazole anion. *Organic letters*, 11(7):1499–1502, 2009.

[313] R. Kakuchi, K. Wongsanoh, V. P Hoven, and P. Théato. Activation of stable polymeric esters by using organo-activated acyl transfer reactions. *Journal of Polymer Science Part A: Polymer Chemistry*, 52(9):1353–1358, 2014.

[314] K. A. Hansen and J. P. Blinco. Nitroxide radical polymers–a versatile material class for high-tech applications. *Polymer Chemistry*, 9(13):1479–1516, 2018.

[315] R. Ye, D. Henkensmeier, S. J. Yoon, Z. Huang, D. K. Kim, Z. Chang, S. Kim, and R Chen. Redox flow batteries for energy storage: a technology review. *Journal of Electrochemical Energy Conversion and Storage*, 15(1), 2018.

[316] Z. Song and H. Zhou. Towards sustainable and versatile energy storage devices: an overview of organic electrode materials. *Energy & Environmental Science*, 6(8):2280–2301, 2013.

[317] N. Chikushi, H. Yamada, K. Oyaizu, and H. Nishide. TEMPO-substituted polyacrylamide for an aqueous electrolyte-typed and organic-based rechargeable device. *Science China Chemistry*, 55(5):822–829, 2012.

[318] M. I. Gibson, E. Fröhlich, and H. A. Klok. Postpolymerization modification of poly (pentafluorophenyl methacrylate): Synthesis of a diverse water-soluble polymer library. *Journal of Polymer Science Part A: Polymer Chemistry*, 47(17):4332–4345, 2009.

[319] S. Tang and H. Zhao. Glymes as versatile solvents for chemical reactions and processes: from the

laboratory to industry. *RSC advances*, 4(22):11251–11287, 2014.

[320] S. Tang, H. Zhao, Z. Song, and O. Olubajo. Glymes as benign co-solvents for cao-catalyzed transesterification of soybean oil to biodiesel. *Bioresource technology*, 139:107–112, 2013.

[321] H. Mutlu, C. W. Schmitt, N. Wedler-Jasinski, H. Woehlk, K. E. Fairfull-Smith, J. P. Blinco, and C. Barner-Kowollik. Spin fluorescence silencing enables an efficient thermally driven self-reporting polymer release system. *Polymer Chemistry*, 8(40):6199–6203, 2017.

[322] S. Noree, V. Tangpasuthadol, S. Kiatkamjornwong, and V. P. Hoven. Cascade post-polymerization modification of single pentafluorophenyl ester-bearing homopolymer as a facile route to redox-responsive nanogels. *Journal of colloid and interface science*, 501:94–102, 2017.

[323] R. M. Arnold, G. R. Sheppard, and J. Locklin. Comparative aminolysis kinetics of different active ester polymer brush platforms in postpolymerization modification with primary and aromatic amines. *Macromolecules*, 45(13):5444–5450, 2012.

[324] S. Xu, I. Held, B. Kempf, H. Mayr, W. Steglich, and H. Zipse. The DMAP-catalyzed acetylation of alcohols—a mechanistic study (DMAP= 4-(dimethylamino) pyridine). *Chemistry–A European Journal*, 11(16):4751–4757, 2005.

[325] V. Lutz, J. Glatthaar, C. Würtele, M. Serafin, H. Hausmann, and P. R. Schreiner. Structural analyses of *N*-acetylated 4-(dimethylamino) pyridine (DMAP) salts. *Chemistry–A European Journal*, 15(34):8548–8557, 2009.

[326] F. M. Winnik, M. F. Ottaviani, S. H. Bossmann, M. Garcia-Garibay, and N. J. Turro. Consolvency of poly (*N*-isopropylacrylamide) in mixed water-methanol solutions: a look at spin-labeled polymers. *Macromolecules*, 25(22):6007–6017, 1992.

[327] Y. Zhang, H. Feng, X. Wu, L. Wang, A. Zhang, T. Xia, H. Dong, X. Li, and L. Zhang. Progress of electrochemical capacitor electrode materials: A review. *International journal of hydrogen energy*, 34(11):4889–4899, 2009.

[328] J. K. Kim, Y. Kim, S. Park, H. Ko, and Y. Kim. Encapsulation of organic active materials in carbon nanotubes for application to high-electrochemical-performance sodium batteries. *Energy & Environmental Science*, 9(4):1264–1269, 2016.

[329] K. B. Singh and M. S. Tirumkudulu. Cracking in drying colloidal films. *Physical review letters*, 98(21):218302, 2007.

[330] A. Kraytsberg and Y. Ein-Eli. Conveying advanced li-ion battery materials into practice the impact

of electrode slurry preparation skills. *Advanced Energy Materials*, 6(21):1600655, 2016.

[331] Z. Du, K. M. Rollag, J. Li, S. J. An, M. Wood, Y. Sheng, P. P. Mukherjee, C. Daniel, and D. L. Wood Iii. Enabling aqueous processing for crack-free thick electrodes. *Journal of Power Sources*, 354:200–206, 2017.

[332] H. Zheng, L. Zhang, G. Liu, X. Song, and V. S. Battaglia. Correlationship between electrode mechanics and long-term cycling performance for graphite anode in lithium ion cells. *Journal of Power Sources*, 217:530–537, 2012.

[333] C. S. Tang, B. Shi, Y. J. Cui, C. Liu, and K. Gu. Desiccation cracking behavior of polypropylene fiber–reinforced clayey soil. *Canadian Geotechnical Journal*, 49(9):1088–1101, 2012.

[334] N. Yousefieh, A. Joshaghani, E. Hajibandeh, and M. Shekarchi. Influence of fibers on drying shrinkage in restrained concrete. *Construction and Building Materials*, 148:833–845, 2017.

[335] M. Gaberscek, R. Dominko, and J. Jamnik. Is small particle size more important than carbon coating? an example study on lifepo4 cathodes. *Electrochemistry Communications*, 9(12):2778–2783, 2007.

[336] G. Oberdörster, V. Castranova, B. Asgharian, and P. Sayre. Inhalation exposure to carbon nanotubes (CNT) and carbon nanofibers (CNF): Methodology and dosimetry. *Journal of Toxicology and Environmental Health, Part B*, 18(3-4):121–212, 2015.

[337] C. Pramanik, J. R. Gissinger, S. Kumar, and H. Heinz. Carbon nanotube dispersion in solvents and polymer solutions: mechanisms, assembly, and preferences. *ACS nano*, 11(12):12805–12816, 2017.

[338] J. Zhao, D. W. Schaefer, D. Shi, J. Lian, J. Brown, G. Beaucage, L. Wang, and R. C. Ewing. How does surface modification aid in the dispersion of carbon nanofibers? *The Journal of Physical Chemistry B*, 109(49):23351–23357, 2005.

[339] P. Ma, N. A. Siddiqui, G. Marom, and J. K. Kim. Dispersion and functionalization of carbon nanotubes for polymer-based nanocomposites: a review. *Composites Part A: Applied Science and Manufacturing*, 41(10):1345–1367, 2010.

[340] H. Jiang, S. Wang, W.g. Deng, Y. Zhang, Y. Tan, Q. Xie, and M. Ma. Graphene-like carbon nanosheets as a new electrode material for electrochemical determination of hydroquinone and catechol. *Talanta*, 164:300–306, 2017.

[341] N. Yabuuchi, M. Takeuchi, S. Komaba, S. Ichikawa, T. Ozaki, and T. Inamasu. Synthesis and

electrochemical properties of $Li_{1.3}Nb_{0.3}v_{0.4}o_2$ as a positive electrode material for rechargeable lithium batteries. *Chemical Communications*, 52(10):2051–2054, 2016.

[342] L. Sieuw, A. Jouhara, É. Quarez, C. Auger, J. F. Gohy, P. Poizot, and A. Vlad. A H-bond stabilized quinone electrode material for Li–organic batteries: the strength of weak bonds. *Chemical science*, 10(2):418–426, 2019.

[343] J. Pu, Z. Shen, J. Zheng, W. Wu, C. Zhu, Q. Zhou, H. Zhang, and F. Pan. Multifunctional Co_3S_4@ sulfur nanotubes for enhanced lithium-sulfur battery performance. *Nano energy*, 37:7–14, 2017.

[344] J. Meng, H. Guo, C. Niu, Y. Zhao, L. Xu, Q. Li, and L. Mai. Advances in structure and property optimizations of battery electrode materials. *Joule*, 1(3):522–547, 2017.

[345] Y. Pan. First-principles investigation of the new phases and electrochemical properties of MoSi2 as the electrode materials of lithium ion battery. *Journal of Alloys and Compounds*, 779:813–820, 2019.

[346] J. Xie, P. Gu, and Q. Zhang. Nanostructured conjugated polymers: toward high-performance organic electrodes for rechargeable batteries. *ACS Energy Letters*, 2(9):1985–1996, 2017.

[347] G. W. Lee, J. H. Ryu, W. Han, K. H. Ahn, and S. M. Oh. Effect of slurry preparation process on electrochemical performances of $LiCoo_2$ composite electrode. *Journal of Power Sources*, 195(18):6049–6054, 2010.

[348] D. Liu, L. C. Chen, T. J. Liu, T. Fan, E. Y. Tsou, C. Tiu, et al. An effective mixing for lithium ion battery slurries. *Advances in Chemical Engineering and Science*, 4(04):515, 2014.

[349] Z. Liu, V. Battaglia, and P. P. Mukherjee. Mesoscale elucidation of the influence of mixing sequence in electrode processing. *Langmuir*, 30(50):15102–15113, 2014.

[350] K. Kuratani, K. Ishibashi, Y. Komoda, R. Hidema, H. Suzuki, and H. Kobayashi. Controlling of dispersion state of particles in slurry and electrochemical properties of electrodes. *Journal of The Electrochemical Society*, 166(4):A501, 2019.

[351] S. Jaiser, M. Müller, M. Baunach, W. Bauer, P. Scharfer, and W. Schabel. Investigation of film solidification and binder migration during drying of Li-Ion battery anodes. *Journal of Power Sources*, 318:210–219, 2016.

[352] M. Baunach, S. Jaiser, S. Schmelzle, H. Nirschl, P. Scharfer, and W. Schabel. Delamination behavior of lithium-ion battery anodes: Influence of drying temperature during electrode processing.

Drying Technology, 34(4):462–473, 2016.

[353] M. Müller, L. Pfaffmann, S. Jaiser, M. Baunach, V. Trouillet, F. Scheiba, P. Scharfer, W. Schabel, and W. Bauer. Investigation of binder distribution in graphite anodes for lithium-ion batteries. *Journal of Power Sources*, 340:1–5, 2017.

[354] B. Westphal, H. Bockholt, T. Günther, W. Haselrieder, and A. Kwade. Influence of convective drying parameters on electrode performance and physical electrode properties. *ECS Transactions*, 64(22):57, 2015.

[355] K. Rollag, D. Juarez-Robles, Z. Du, D. L. Wood III, and P. P. Mukherjee. Drying temperature and capillarity-driven crack formation in aqueous processing of li-ion battery electrodes. *ACS Applied Energy Materials*, 2(6):4464–4476, 2019.

[356] J. Ahn, S. Yoon, S. G. Jung, J. H. Yim, and K. Y. Cho. A conductive thin layer on prepared positive electrodes by vapour reaction printing for high-performance lithium-ion batteries. *Journal of Materials Chemistry A*, 5(40):21214–21222, 2017.

[357] N. C. Rosero-Navarro, T. Kinoshita, A. Miura, M. Higuchi, and K. Tadanaga. Effect of the binder content on the electrochemical performance of composite cathode using li_6ps_5cl precursor solution in an all-solid-state lithium battery. *Ionics*, 23(6):1619–1624, 2017.

[358] M. S. Balogun, Y. Luo, W. Qiu, P. Liu, and Y. Tong. A review of carbon materials and their composites with alloy metals for sodium ion battery anodes. *Carbon*, 98:162–178, 2016.

[359] S. Li, B. Jin, X. Zhai, H. Li, and Q. Jiang. Review of carbon materials for lithium-sulfur batteries. *ChemistrySelect*, 3(8):2245–2260, 2018.

[360] J. W. Kim, G. Cheruvally, J. W. Choi, J. H. Ahn, S. H. Lee, D. S. Choi, and C. E. Song. Effect of radical polymer cathode thickness on the electrochemical performance of organic radical battery. *Solid State Ionics*, 178(27-28):1546–1551, 2007.

[361] W. Mei, H. Chen, J. Sun, and Q. Wang. The effect of electrode design parameters on battery performance and optimization of electrode thickness based on the electrochemical–thermal coupling model. *Sustainable energy & fuels*, 3(1):148–165, 2019.

[362] S. Sridhar and U. B. Pal. Effects of slurry properties on anode cermets for solid oxide fuel cells. *Powder technology*, 88(2):173–178, 1996.

[363] F. Ma, Y. Fu, V. Battaglia, and R. Prasher. Microrheological modeling of lithium ion battery anode slurry. *Journal of Power Sources*, 438:226994, 2019.

[364] S. Lim, S. Kim, K. H. Ahn, and S. J. Lee. The effect of binders on the rheological properties and the microstructure formation of lithium-ion battery anode slurries. *Journal of Power Sources*, 299:221–230, 2015.

[365] H. Luo, C. M. Cardinal, L. E. Scriven, and L. F. Francis. Ceramic nanoparticle/monodisperse latex coatings. *Langmuir*, 24(10):5552–5561, 2008.

[366] E. D. Manev and J. K. Angarska. Critical thickness of thin liquid films: comparison of theory and experiment. *Colloids and Surfaces A: Physicochemical and Engineering Aspects*, 263(1-3):250–257, 2005.

[367] G. F. Yang and S. K. Joo. Calendering effect on the electrochemical performances of the thick Li-ion battery electrodes using a three dimensional Ni alloy foam current collector. *Electrochimica Acta*, 170:263–268, 2015.

[368] W. Haselrieder, S. Ivanov, D. K. Christen, H. Bockholt, and A. Kwade. Impact of the calendering process on the interfacial structure and the related electrochemical performance of secondary lithium-ion batteries. *ECS Transactions*, 50(26):59, 2013.

[369] X. Bian, Q. Fu, C. Qiu, X. Bie, F. Du, Y. Wang, Y. Zhang, H. Qiu, G. Chen, and Y. Wei. Carbon black and vapor grown carbon fibers binary conductive additive for the $Li_{1.18}Co_{0.15}Ni_{0.15}Mn_{0.52}O_2$ electrodes for Li-ion batteries. *Materials Chemistry and Physics*, 156:69–75, 2015.

[370] Q. Huang, D. Choi, L. Cosimbescu, and J. P. Lemmon. Multi-electron redox reaction of an organic radical cathode induced by a mesopore carbon network with nitroxide polymers. *Physical Chemistry Chemical Physics*, 15(48):20921–20928, 2013.

[371] S. Bose, A. R. Bhattacharyya, A. R. Kulkarni, and P. Pötschke. Electrical, rheological and morphological studies in co-continuous blends of polyamide 6 and acrylonitrile–butadiene–styrene with multiwall carbon nanotubes prepared by melt blending. *Composites Science and Technology*, 69(3-4):365–372, 2009.

[372] N. Karousis, N. Tagmatarchis, and D. Tasis. Current progress on the chemical modification of carbon nanotubes. *Chemical reviews*, 110(9):5366–5397, 2010.

[373] E. M. Espinoza, J. A. Clark, J. B. Derr, D. Bao, B. Georgieva, F. H. Quina, and V. I Vullev. How do amides affect the electronic properties of pyrene? *ACS omega*, 3(10):12857–12867, 2018.

[374] Z. Song, T. Xu, M. L. Gordin, Y. B. Jiang, I. T. Bae, Q. Xiao, H. Zhan, J. Liu, and D. Wang. Polymer–graphene nanocomposites as ultrafast-charge and-discharge cathodes for rechargeable lithium batteries. *Nano letters*, 12(5):2205–2211, 2012.

[375] P. Lazar, F. Karlicky, P. Jurecka, M. Kocman, E. Otyepkova, K. Safarova, and M. Otyepka. Adsorption of small organic molecules on graphene. *Journal of the American Chemical Society*, 135(16):6372–6377, 2013.

[376] R. De Coen, N. Vanparijs, M. D. P. Risseeuw, L. Lybaert, B. Louage, S. De Koker, V. Kumar, J. Grooten, L. Taylor, N. Ayres, et al. pH-degradable mannosylated nanogels for dendritic cell targeting. *Biomacromolecules*, 17(7):2479–2488, 2016.

[377] Q. Zhang, P. Schattling, P. Théato, and R. Hoogenboom. UV-tunable upper critical solution temperature behavior of azobenzene containing poly (methyl methacrylate) in aqueous ethanol. *European Polymer Journal*, 62:435–441, 2015.

Appendix

The following sections provide additional characterization data of the chemical structures, cathodes and thermal stabilities of resulting polymers developed in the present thesis, if not displayed in chapter 3–5.

A. Additional Figures of Chapter 3
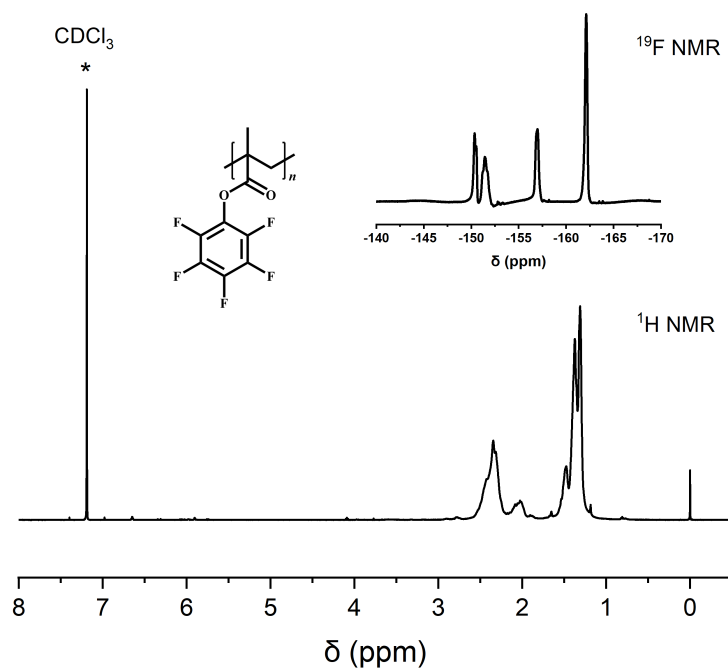
Figure A.1.: NMR spectrum (400 MHz, CDCl$_3$, 298K) of PPFPMA.
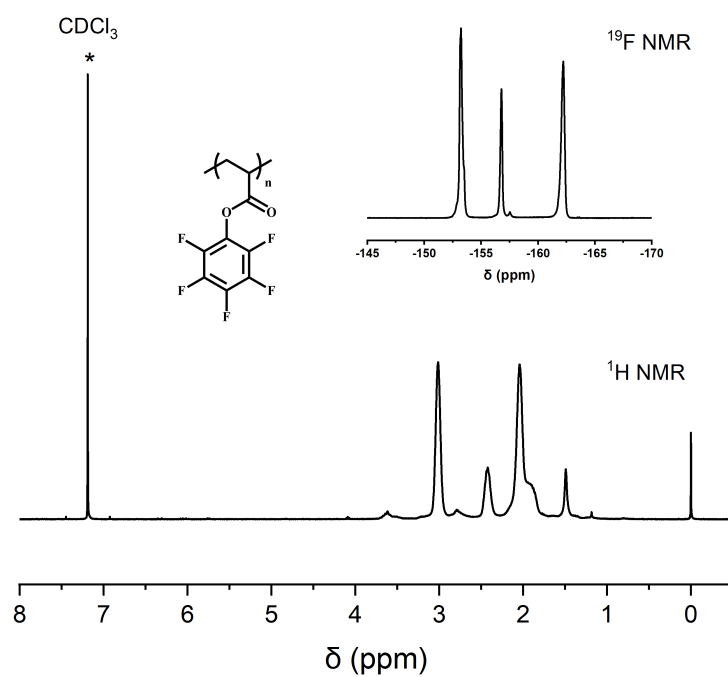
Figure A.2.: NMR spectrum (400 MHz, CDCl$_3$, 298K) of PPFPA.
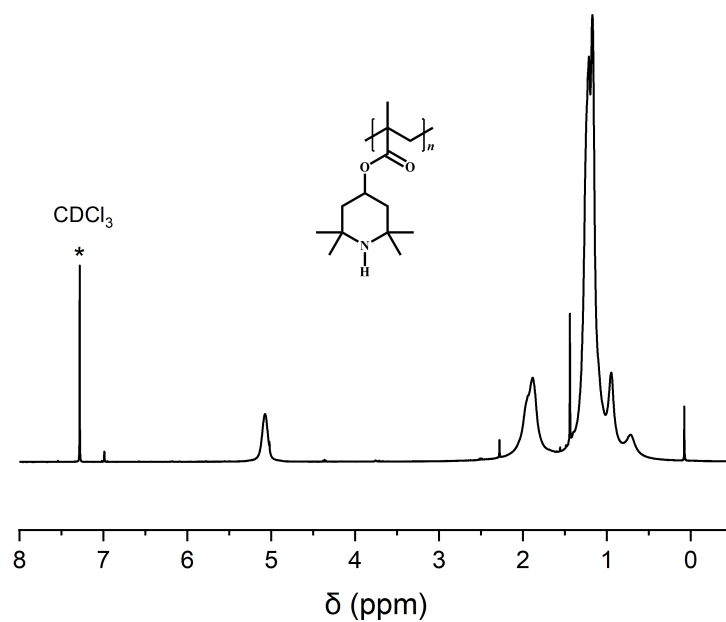
Figure A.3.: NMR spectrum (400 MHz, CDCl$_3$, 298K) of PTMPM
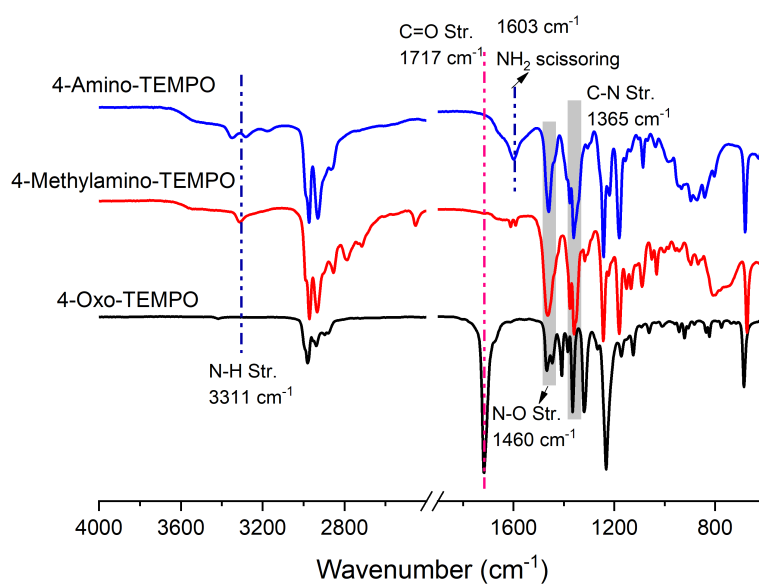
Figure A.4.: Comparative IR spectra of 4-Oxo-TEMPO, 4-Amino-TEMPO and 4-Methylamino-TEMPO, respectively.
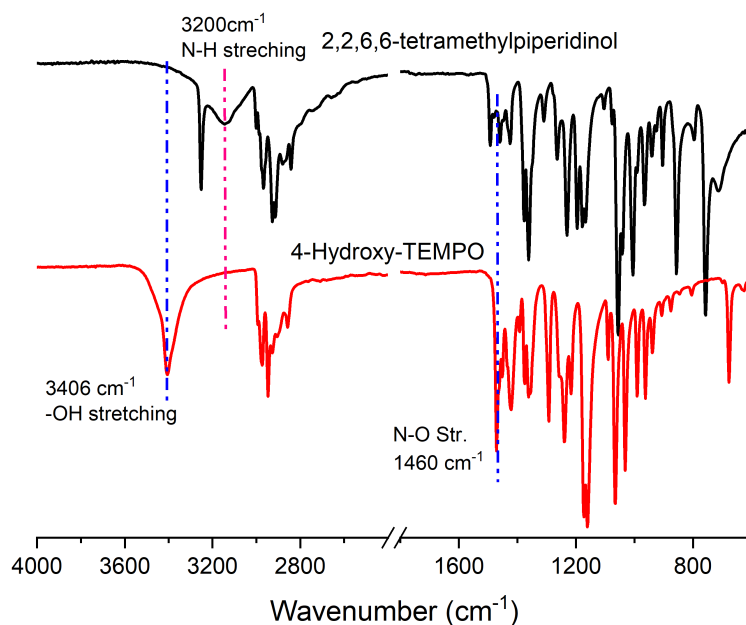
Figure A.5.: Comparative IR spectra of 4-Hydroxy-TEMPO and 2,2,6,6-tetramethylpiperidinol.
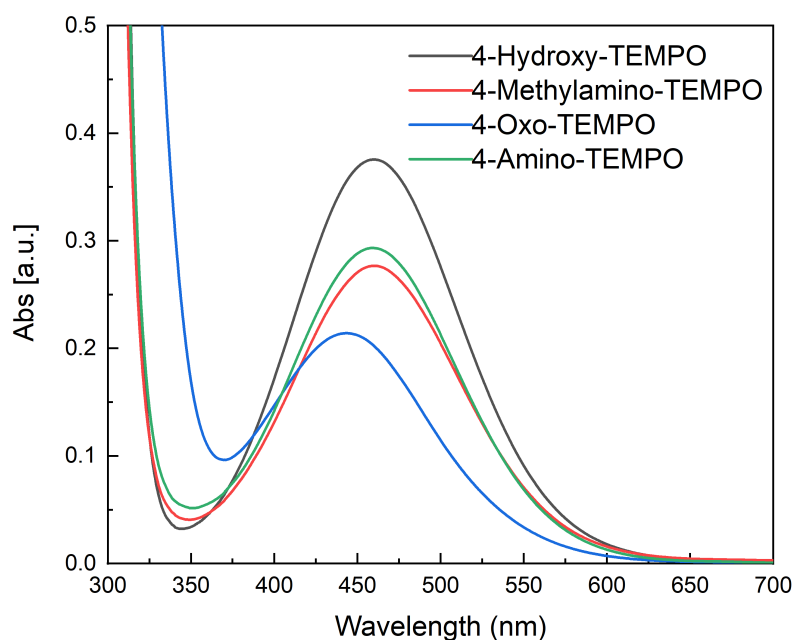
Figure A.6.: Comparative UV/vis spectra of 4-Amino-TEMPO, 4-Methylamino-TEMPO, 4-Hydroxy-TEMPO and 4-Oxo-TEMPO in DCM (33.5 mM), respectively.
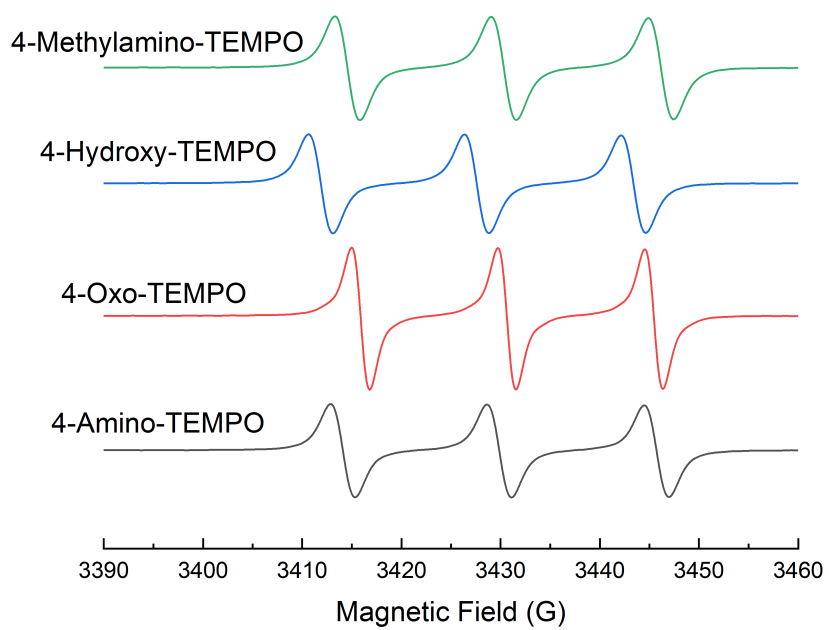
Figure A.7.: Comparative EPR spectra of 4-Amino-TEMPO, 4-Methylamino-TEMPO, 4-Hydroxy-TEMPO and 4-Oxo-TEMPO, respectively

B. Additional Table of Chapter 4

Table B.1.: Loading mass (mg cm^{-2}) of cathodes.

Sample ID	Mass$_{\textbf{cathodes}}$(mg) specimen				Average mass loading (mg cm^{-2})
	1	2	3	4	
#1 PTMA66-T50	2.7	2.7	3.1	-	1.82
#2 PTMA66-T80	3.2	2.9	3.2	-	2.01
#3 PTMA66-χ76.5	2.6	2.4	2.6	-	1.62
#4 PTMA66-χ70.8	2.4	2.0	2.3	-	1.43
#5 PTMA66-χ62.5	2.1	2.3	2.3	-	1.43
#6 PTMA66-χ54	1.5	1.5	1.5	-	0.97
#7 PTMA66-χ46.2	0.7	0.5	0.6	-	0.39
#8 PTMA66-CB&CNF	3.3	3.5	3.6	-	2.21
#9 PTMA55-NC	3.1	3.1	3.1	3.1	2.01
#10 PTMA55-C	3.2	3.3	3.2	3.5	2.14
#11 PTMA55-VGCF	3.4	3.2	3.6	-	2.21

C. Additional Figures and Tables of Chapter 5
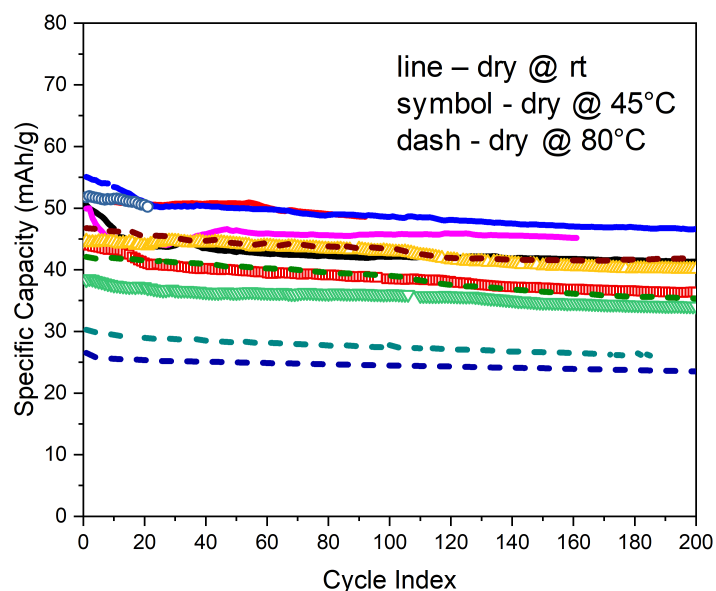
Figure C.1.: Cycle performance of cathodes based on P0 dried at various temperatures.
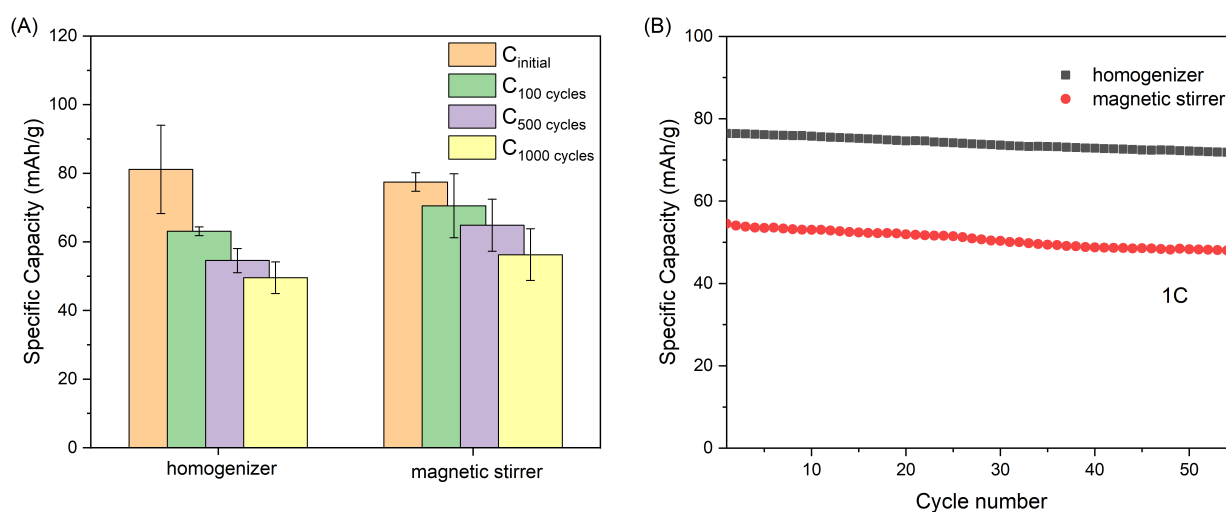
Figure C.2.: Cycle performance of cathodes based on (A) PTMA-Oxidation and (B) PTAm prepared with different mixing methods.
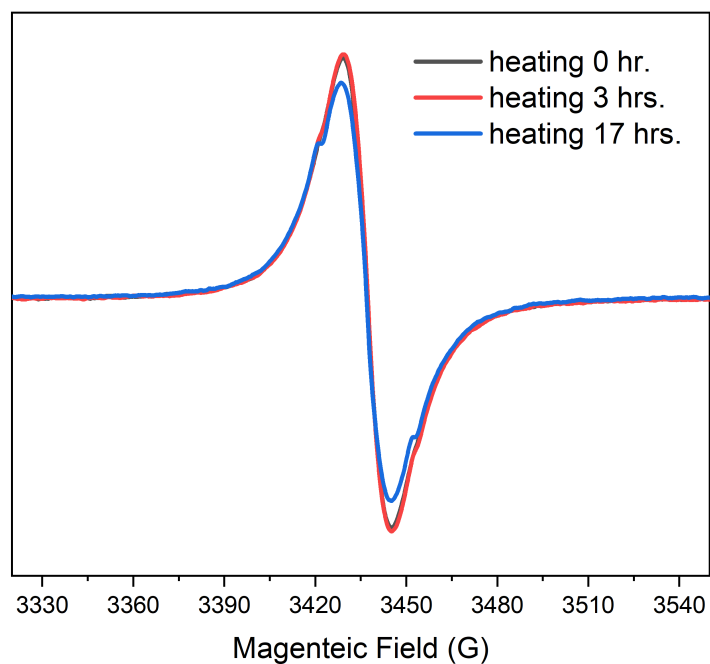
Figure C.3.: EPR spectra of P0 solution (1.035 mg mL^{-1}) in NMP heating at 80 °C under ambient conditions for various times.

Table C.1.: Coulombic efficiency for P0-P2 at different C-rates.

Sample	Coulombic Efficiency (CE,%)									
	0.1 C	0.5 C	1 C	2 C	5 C	10 C	20 C	50 C	100 C	0.1 C
P0	94.6	99	99.4	99.7	99.9	99.9	99.8	99.8	100	91.3
P1	84.5	97.1	98.4	99.2	95.4	97.6	98.9	99.6	99.8	82.7
P2	71.6	93.2	94.7	96.6	96.6	98.2	98.8	99.5	99.6	80.7

List of Abbreviations

3DOM	three-dimensional ordered macroporous
4-allyl-TEMPO ether	4-allyl-2,2,6,6-tetramethylpiperidine-*N*-oxyl ether
4-amino-TEMPO	4-amino-2,2,6,6-tetramethylpiperidinyloxyl
4-carboxy-TEMPO	4-carboxy-2,2,6,6-tetramethylpiperidine-1-oxyl
4-glycidyloxy-TEMPO	4-(glycidyloxy)-2,2,6,6-tetramethylpiperidine-1-oxyl
4-hydroxy-TEMPO	4-hydroxy-2,2,6,6-tetramethylpiperidinooxy
4-methylamino-TEMPO	4-(methylamino)-2,2,6,6-tetramethyl-1-piperidinyloxy
4-NPE	4-nitrophenyl ester
4-oxo-TEMPO	4-oxo-2,2,6,6-tetramethyl-1-piperidinyloxy
4-vinyloxyl-TEMPO	2,2,6,6-tetramethylpiperidine-*N*-oxyl-4-vinyl ether
AB	acetylene black
ACT	4-(acetylamino)-2,2,6,6-tetramethyl-1-piperidinyloxy
AIBN	azobisisobutyronitrile
AMT	4-amino-2,2,6,6-tetramethyl-piperidinyloxy
ATR	attenuated total reflectance
BMPTFSI	*N*-butyl-*N*-methylpyrrolidinium bis(trifluoromethylsulfonyl)imide
BP-2000	Black Pearl 200
CB	carbon black
CB-SP	carbon black-super P
CMC	carboxyl methyl cellulose
CNF	carbon nanofibers
CNTs	carbon nanotubes
CE	coulombic efficiency
CuAAC	copper-catalyzed azide/alkyne cycloaddition
CV	cyclic voltammogram
DBU	1,8-diazabicyclo [5.4.0] undec-7-ene
DCM	dichloromethane

DCM	dichloromethane
DFT	density-functional theory
DLS	dynamic light scattering
DMAc	dimethylacetamid
DMAP	4-dimethylaminopyridine
DME	1,2-dimethoxyethane
DMF	dimethylformamide
DMSO	dimethyl sulfoxide
DPHLi	1,1-diphenylhexyllithium
DPHLi/MMA	methyl methacrylate-capped 1,1-diphenylhexyllithium
DPV	differential pulse voltammogram
EC/DEC	ethylene carbonate/diethyl carbonate
EC/DMC	ethylene carbonate/dimethyl carbonate
EDC	1-ethyl-3-(3-(dimethylamino)propyl)carbodiimide
EDTA	ethylenediaminetetraacetic acid
emf	electromotive force
EPR	electron paramagnetic resonance
EQCM-D	electrochemical quartz crystal microbalance with dissipation monitoring
Et_4NTFSI	tetraethylammoniumbis(trifluoromethylsulfonyl)imide
FRP	free radical polymerization
GC-MS	gas chromatography coupled to mass spectrometry
GMA	glycidyl methacrylate
GTP	group-transfer polymerization
HCA	highly conductive carbon agent
LCST	the lower critical solution temperature
$LiBF_4$	lithium tetrafluoroborate
LIBs	Lithium ion batteries
$LiCF_3SO_3$	lithium trifluoromethanesulfonate
$LiClO_4$	lithium perchlorate
LiFSI	lithium bis(fluorosulfonyl) imide
$LiPF_6$	lithium hexafluorophosphate
LiTFSI	lithium bis(trifluoromethanesulfony)imide
LPEI	linear poly(ethylenimine)
LRP	living/controlled radical polymerization
*m*CPBA	m-chloroperbenzoic acid

MeCN	acetonitrile
MeOH	methanol
MO	molecular orbitals
MPEOT	4-methacryloyloxy-1-((1′-phenylethyl)oxy)-2,2,6,6-tetramethylpiperidine
MTS	(1-methoxy-2-methyl-1-propenyloxy)-trimethylsilane
MWCNTs	multiwalled carbon nanotubes
NCM	$LiNi_1/3Co_1/3Mn_1/3O_2$
NHS	*N*-hydroxysuccinimide
NiMH	Nickel metal hydride
NMP	nitroxide-mediated radical polymerization
NMP	*N*-Methyl-2-pyrrolidone
ORB	organic radical batteries
PAA	poly(acrylic acid)
PAQE	poly(anthraquinone-substituted ethyleneimine)
PC	propylene carbonate
PEDOT	poly(3,4-ethylenedioxythiophene)
MCF	mesocellular carbon foam
PEM	poly(ethylene-*alt*-maleic anhydride)
PET	poly(ethylene terephthalate)
PFP	pentafluorophenyl
PFPA	Pentafluorophenyl acrylate
PFPMA	Pentafluorophenyl methacrylate
PMHS	poly(methylhydrosiloxane)
PMMA	poly(methyl methacrylate)
PMPEOT	polyMPEOT
PNAS	poly(*N*-hydroxysuccinimide acrylate)
PNIPAM	poly(*N*-isopropylacrylamide)
PNMAS	poly(*N*-hydroxysuccinimide methacrylate)
PPFPA	poly(pentafluorophenyl acrylate)
PPFPMA	poly(pentafluorophenyl methacrylate)
PPM	post-polymerization modification
PS	polystyrene
PTAm	poly(2,2,6,6-teteramethylpiperidine-4–yl acrylamide)
PTEO	poly(4-glycidyloxy-2,2,6,6-tetramethylpiperidine-1-oxyl)
PTFE	polytetrafluoroethylene

PTMA	poly(2,2,6,6-tetramethyl- piperidenyloxyl-4-yl methacrylate)
PTMPMA	poly(2,2,6,6-tetramethyl-4-piperidyl methacrylate)
PTNB	poly[2,3-bis(2′,2′,6′,6′-tetramethylpiperidin-1′-oxyl-4′-oxycarbonyl)-5-norbornene]
PTPM	poly(tripyridiniomesitylene)
p-TSA	p-toluenesulfonic acid
PTVE	poly(2,2,6,6-tetramethylpiperidine-Noxyl-4-vinyl ether)
PVdF	poly(vinylidene fluoride)
PVDF-HFP	poly(vinylidene fluoride-co-hexafluoropropylene)
Py$_{14}$TFSI	*N*-butyl-*N*-methyl-pyrrolidiniumbis(trifluoromethanesulfonyl)imide
RAFT	reversible addition–fragmentation chain transfer mediated polymerization
RCP	radical-containing polymers
ROMP	ring-opening metathesis polymerization
SBR	styrene butadiene rubber
SCE	saturated calomel electrode
SEC	size exclusion chromatography
SET-LRP	single electron transfer-living radical polymerisation
SI-ATRP	surface-initiated atom transfer polymerization
SOMO	single occupied molecular orbital
sulfo-NHS	*N*-hydroxysulfosuccinimide sodium salt
SWCNTs	single-walled carbon nanotubes
TBABF4	tetrabutylammonium tetrafluoroborate
TBFA	tetrabutylammonium fluoride
TEA	triethyl amine
TEAP	tetraethylammonium perchlorate
TEMPO	2,2,6,6-tetramethylpiperidin-1-oxyl-4-yl
TGA	thermogravimetric analysis
THF	tetrahydrofuran
TLC	thin-layer chromatography
TMPMA	2,2,6,6-tetramethyl-4-piperidyl methacrylate
Tz	1,2,4-triazole
UV/vis	ultraviolet-visible
VGCF	vapor grown carbon fiber

List of Publications

Submitted Manuscripts

1. <u>Wenwen Xue</u>, Hatice Mutlu, Hongjiao Li, Wolfgang Wenzel and Patrick Théato. Influence of Pyrene Amide moieties on the electronic properties of TEMPO containing polymers, *Polymer Chemistry*, under revision.
2. <u>Wenwen Xue</u>, Hatice Mutlu, Frieder Scheiba, Marcus Müller, Yunji Xie, Jessica Pfisterer and Patrick Théato. Processing of radical polymer-based electrodes, *Batteries & Supercaps*, in resubmission.
3. Christina M. Geiselhart, <u>Wenwen Xue</u>, Christopher Barner-Kowollik and Hatice Mutlu. Degradable Redox-Responsive Polyethylene Mimics, *ACS Macro Letters*, submitted.

Peer Reviewed Publications during Candidature

4. <u>Wenwen Xue</u>, Hatice Mutlu and Patrick Théato. Post-polymerization modification of polymeric active esters towards TEMPO containing polymers: A systematic study, *European Polymer Journal*, 130, **2020**: 109660.
5. <u>Wenwen Xue</u>, Xiao Lei Gong and Patrick Théato. Functional polymer surfaces via post-polymerization modification. Responsive Polymer Surfaces, book chapter, *Responsive Polymer Surfaces: Dynamics in Surface Topography*, John Wiley & Sons, **2017**.
6. Tao Zhou, Weize Jin, <u>Wenwen Xue</u>, Bin Dai, Chun Feng, Xiaoyu Huang, Patrick Théato and Yongjun Li. Radical polymer grafted carbon nanotubes with two-stage redox reaction as high-capacity cathode materials for lithium organic batteries. *Journal of Power Sources*, 483, **2020**: 229136.

Previous Publications

7. <u>Wenwen Xue</u>, Lisheng Zhang, Haizhen Chen, Jinggang Wang, Haining Na and Jin Zhu. Synthesis of polyurethane containing carbon–carbon double bonds to prepare functionalizable ultrafine fibers via electrospinning. *Polymer Chemistry*, 6, **2015**: 3858-3864.

8. <u>Wenwen Xue</u>, Lisheng Zhang, Jinping Ni, Hainign Na and Jin Zhu. Fabrication of ultrafine polyurethane fibers containing carbon-carbon double bonds. *CN. 201510105671.9 [P]*, **2015**.

9. Jinping Ni, Haining Na, Zhen She, Jinggang Wang, <u>Wenwen Xue</u> and Jin Zhu. Responsive behavior of regenerated cellulose in hydrolysis under microwave radiation. *Bioresource Technology*, 167, **2014**: 69-73.

10. Haizhen Chen, Jinping Ni, Jing Chen, <u>Wenwen Xue</u>, Jinggang Wang, Haining Na and Jin Zhu. Activation of corn cellulose with alcohols to improve its dissolvability in fabricating ultrafine fibers via electrospinning. *Carbohydrate Polymers*, 123, **2015**: 174-179.

Conference Contribution

11. <u>Wenwen Xue</u> and Patrick Théato, Post-polymerization modification for the synthesis of radical containing polymers, Poster, *Organic Battery Days **2019***, Jena, Germany.

Acknowledgments

Declaration of Authorship

I hereby declare on oath, that the dissertation presented is entirely written by me based on my own original research. All direct or indirect sources used are acknowledged. I further declare that I have not submitted, either in part or whole, for a doctorate (Ph.D. studies) at this or any other university.

Karlsruhe, 04.09.2020